THE EFFECTS OF FE AND AL ON THE COMPOSITION, PROCESSING, MICROSTRUCTURE, AND PROPERTY RELATIONSHIPS OF TI-11AT.%CR

By

JoAnn Ballor

A DISSERTATION

Submitted to
Michigan State University
in partial fulfillment of the requirements
for the degree of

Materials Science and Engineering – Doctor of Philosophy

2022

ABSTRACT

THE EFFECTS OF FE AND AL ON THE COMPOSITION, PROCESSING, MICROSTRUCTURE, AND PROPERTY RELATIONSHIPS OF TI-11AT.%CR

By

JoAnn Ballor

Beta-titanium (β-Ti) alloys contain elements that promote enhanced retention of the β phase, termed β-stabilizers. This class of Ti alloys can exhibit a range of mechanical properties, making them suitable for applications requiring low Young's moduli, such as biomedical implants, as well as applications that require high Young's moduli and strengths, such as aerospace engine components. The mechanical properties of β-Ti alloys can be tuned to meet the needs of specific applications by changing the microstructure.

As the β-phase is metastable, phase transformations to other metastable and stable phases can be induced by thermomechanical processing. Aging β-Ti alloys in the 300 °C to 500 °C temperature range allows certain β-Ti alloys to undergo the β-to-ω and β-to-α phase transformations, both of which promote strengthening. The ω phase in particular is known to significantly increase Young's modulus and strength, but is generally avoided because it also severely decreases elongation-to-failure (ϵ_f). Recently, the ω phase has been shown to assist in the formation of a nanoscale α phase.

Composition and processing affect both the β-to-ω and β-to-α transformations. In this dissertation, four β-Ti alloys, Ti-11Cr, Ti-11Cr-0.85Fe, Ti-11Cr-5.3Al, and Ti-11Cr-0.85Fe-5.3Al (all in at.%) were investigated to determine how Fe and Al additions affect the phase transformations, phase volume fractions, and phase lattice parameters during aging, and how the microstructural changes affect the mechanical properties. Each alloy underwent 400 °C aging treatments to induce the β-to-ω and β-to-α phase transformations.

A microstructural characterization of the β-homogenized condition of each alloy was performed. Each alloy was found to contain only the β phase with randomly distributed alloying elements using X-ray diffraction (XRD), scanning electron microscopy (SEM), and atom probe tomography (APT).

The Fe and Al additions did not affect the hardness of the alloys, but reduced the shear and Young's moduli of the alloys. The alloys' yield strength (σ_y) and ultimate tensile strength (UTS) increased with decreased grain size and ϵ_f increased as the grain size approached that necessary for the minimum critical stress for stress-induced martensite.

A microstructural characterization of each alloy during and after aging was also performed to determine the effects of Fe and Al on the microstructural evolution. Ti-11Cr underwent the β-to-ω and β-to-α transformations. The Fe addition reduced the volume fraction of the ω phase and increased the lattice parameter of the β phase. The Al addition inhibited the β-to-ω phase transformation and increased the volume fraction of the α phase. When Fe and Al were both added, Al prevented the β-to-ω transformation and Fe reduced the α-phase volume fraction.

Cr and Fe diffused from the ω and α precipitates into the β matrix during the β-to-ω and β-to-α transformations. Al diffused from the β matrix into the α precipitates. The β-phase lattice parameter decreased with increasing Cr and Fe contents, and an empirical relationship between the β-phase lattice parameter and the β-phase stability, involving the molybdenum equivalency, was proposed. The β-phase lattice parameter also affect the c/a ratios of the α and ω phases, which has implications for the ω-assisted α-phase transformation. Higher contents of impurity element O were measured in the α and ω phases.

Each alloy exhibited an increase in σ_y and UTS with precipitation of the α and ω phases. The aged alloys containing Fe exhibited larger ϵ_f values than the Fe-free alloys. The alloys containing ω-phase microstructures exhibited significantly higher shear moduli than the ω-free alloys.

Through this work, the composition-processing-microstructure-property relationships of the Ti-Cr-Fe-Al system were revealed. The relationships established between processing, β-phase stability, microstructure, and mechanical properties are expected to be applicable to β-Ti alloys outside of the Ti-Cr-Fe-Al system.

This work is dedicated to my family.

ACKNOWLEDGEMENTS

I would like to thank my advisor, Dr. Carl J. Boehlert, for introducing me to the Materials Science program at MSU. Without him I may not have chosen to enter graduate school, and I would not have entered into the materials science field. I cannot thank him enough for pushing me towards opportunities I may not have otherwise considered, and for helping me form connections with researchers across the country. I would also like to extend thanks to my committee, Dr. Martin Crimp, Dr. Philip Eisenlohr, Dr. Patrick Kwon, and Dr. Arun Deveraj, for their invaluable input, expertise, and advice towards my academic and professional career. Without them, I would have met many more roadblocks in my research and graduate career.

I would also like to thank Dr. Per Askeland, Dr. Alexandra Zevalkink, Dr. Elizabeth Kautz, Dr. Bharat Gwalani, Dr. Jonathan Poplawsky, Dr. Scott Misture, Dr. Takeshi Sunaoshi, Dr. Jane Howe, Mr. A K M Ashiquzzaman Shawon, and Mr. Robert "Bob" Passeri for their contributions towards the work presented in this dissertation, and Dr. Masahiko Ikeda for providing the materials studied in this work.

I extend my thanks to my friends that have supported me through this time: Dr. Adam Marsh, Dr. Madeline Mackinder, and Dr. Young Kim, who were always willing and available to answer a question, proofread an email, or meet up to hang out when I needed it, and Ms. Meridith Murley, who was always there to listen to my problems, get me outside and take a walk, and who provided very needed pet therapy with cats Martha, Schnapps, and Apollo, and dogs Charlie and Nala.

Finally, I would like to thank my family, without whom I would not be the person I am today, and whose support has been incredible. To my parents, Mr. Richard Ballor and Mrs. Lee Ballor, who have supported me, listened to me complain, and let me talk through research problems that they weren't necessarily interested in, and to my sister, Ms. Elizabeth Ballor, who has always been available to sit on a couch and watch a new TV show or funny video when I really needed it, I will forever be grateful. I would also like to thank all of my extended family who have provided me with words of encouragement over the years, and who never doubted that I would make it this far.

TABLE OF CONTENTS

LIST OF TABLES

LIST OF FIGURES

KEY TO ABBREVIATIONS

α alpha

β beta

δ delta

$\epsilon_{\mathbf{f}}$ elongation-to-failure

λ lambda

μ mu

$\sigma_{\mathbf{y}}$ Yield stress

θ theta

ω omega

$\omega_{\mathbf{ath}}$ Athermal omega phase

$\omega_{\mathbf{iso}}$ Isothermal omega phase

Al Aluminum

at.% Atomic percent

APF Atomic packing factor

APT Atom probe tomography

BCC Body centered cubic

BSE Back-scattered electron

C Carbon

Co Cobalt

Cr Chromium

Cu Copper

D Diffusion coefficient

Da Dalton

E Young's modulus

EDS Energy dispersive X-ray spectroscopy

EDM Electro-discharge machine

Fe Iron

FEG Field emission gun

FIB Focused-ion beam

G Shear modulus

h Hour

HAADF High-angle annular dark-field

HCP Hexagonal close packed

HF Hydrofluoric acid

Hf Hafnium

HPT High-pressure torsion

HRSEM High-resolution scanning electron microscopy

HTXRD High temperature X-ray diffraction

Hv Vickers microhardness unit

ICP-AES Inductively coupled plasma atomic emission spectroscopy

IVAS Interactive Visualization and Analysis Software

K Bulk modulus

LEAP Local electrode atom probe

Mn Manganese

Mo Molybdenum

Mo-Eq Molybdenum equivalency

Nb Niobium

N Nitrogen

NDIR Non-dispersive infrared spectroscopy

Ni Nickel

O Oxygen

ORNL Oak Ridge National Laboratory

PDBSE Photodiode backscattered electron

PNNL Pacific Northwest National Laboratory

Pt Platinum

R Stress ratio

RDF Radial distribution function

Re Rhenium

ROM Rule of mixtures

RT Room temperature

RUS Resonance ultrasound spectroscopy

SAD Selected area diffraction

SAED Selected area electron diffraction

SE Secondary electron

SEM Scanning electron microscopy

SiC Silicon carbide

SIM Stress-induced martensite

STEM Scanning transmission electron microscopy

Sn Tin

Ta Tantalum

TC Ti-11Cr(at%)

TCA Ti-11Cr-5.3Al (at%)

TCF Ti-11Cr-0.85Fe (at%)

TCFA Ti-11Cr-0.85Fe-5.3Al (at%)

TEM Transmission electron microscopy

Ti Titanium

TRIP Transformation induced plasticity

TTT Time-temperature-transformation

TWIP Twinning induced plasticity

UTS Ultimate tensile strength

V Vanadium

W Tungsten

wt.% Weight percent

XRD X-ray diffraction

Zr Zirconium

CHAPTER 1

RATIONALE AND RESEARCH OBJECTIVE AND INTRODUCTION

Titanium (Ti) and Ti alloys exhibit high specific strength, biocompatibility, good fracture toughness and fatigue resistance, and excellent corrosion resistance. This has led to their use in various industries requiring a range of material property requirements. The class of Ti alloys known as β-Ti alloys is distinct from other classes of Ti alloys because it retains the body centered cubic (BCC) β phase after quenching from above the β-transus temperature. β-Ti alloys are particularly useful because they can display a wide range of microstructures and mechanical properties. The high strengths attainable by β-Ti alloys allow them to be used for structural applications. For example, Ti-5553 (Ti-5Al-5V-5Mo-3Cr) is used in the landing gear of the Boeing 777 [1–4]. The composition of β-Ti alloys can be tuned to produce a low Young's modulus (E), which is ideal for biomedical implants as the low Young's modulus favors less stress-shielding of the bone, thereby decreasing the likelihood of implant failures [5, 6]. β-Ti alloys exhibit flexibility for use in both high-strength structural applications and lower-strength biomedical applications because their mechanical properties can be tailored to meet the needs of specific applications through judicious control of the microstructure and phase transformations.

One way to control the microstructure in β-Ti alloys is by controlling the alloy composition, as different alloying elements tend to stabilize different phases. All β-Ti alloys contain alloying elements that stabilize the BCC β phase. These elements are called β-stabilizers and they lower the β-transus temperature. The binary phase diagrams of β-Ti alloys can be either isomorphous or eutectoid-type [2, 7, 8]. Vanadium (V), molybdenum (Mo), niobium (Nb), tantalum (Ta), hafnium (Hf), and rhenium (Re) are β-stabilizers that exhibit isomorphous phase diagrams, and chromium (Cr), manganese (Mn), iron (Fe), cobalt (Co), nickel (Ni), copper (Cu), and tungsten (W) are β-stabilizers that exhibit eutectoid-type phase diagrams. The isomorphous Ti-Mo and the eutectoid Ti-Cr phase diagrams are provided in Figure 1.1.

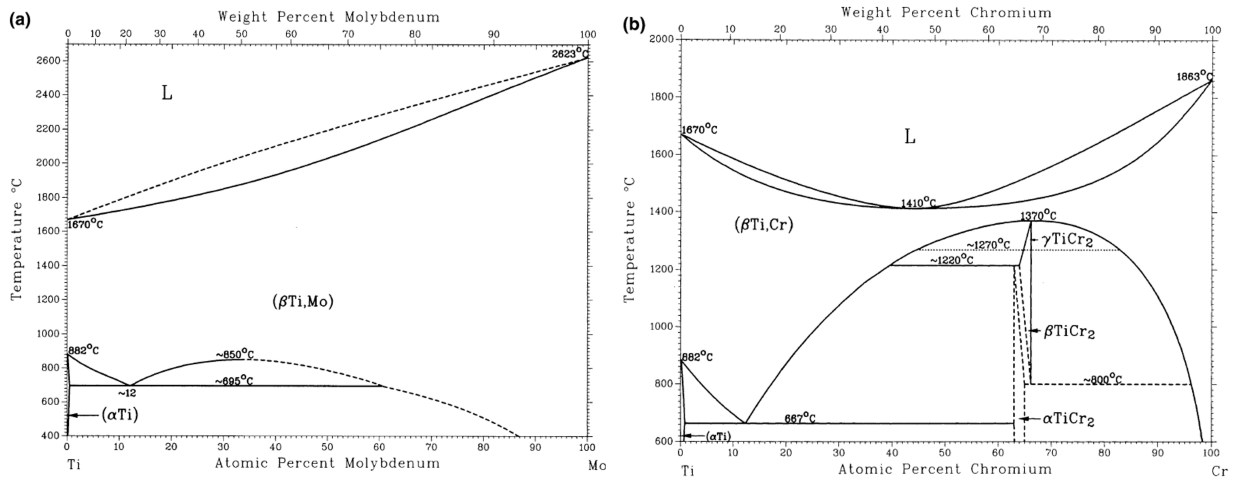

Figure 1.1: Binary phase diagrams of (a) Ti-Mo (isomorphous) and (b) Ti-Cr (eutectoid). Adopted from J. D. Cotton, R. D. Briggs, R. R. Boyer, S. Tamirisakandala, P. Russo, N. Shchetnikov and J. C. Fanning, "State of the Art in β Titanium Alloys for Airframe Applications," JOM, vol. 67, no. 6, pp. 1281–1303, May 2015.

Elements that stabilize the hcp α phase are sometimes included in β-Ti alloys to help promote the β-to-α transformation during processing. Strong α-stabilizers, such as aluminum (Al), oxygen (O), nitrogen (N), and carbon (C), promote the α-phase formation in β-Ti alloys. Al is the most commonly used α-stabilizer [7]. O, N, and C are intentionally or unintentionally included in β-Ti alloys. Some elements included in β-Ti alloys such as tin (Sn) and zirconium (Zr) are neutral to both α and β phases. Processing is also used to control the microstructure and phase transformations in β-Ti alloys [7]. The β-to-ω phase transformation has been of significant interest to researchers because of its influence on both the mechanical properties and the β-to-α phase transformation [9, 10].

The synergistic effects of processing and composition can affect the microstructure of β-Ti alloys. These complex interactions are important to understand in order to tailor the microstructure and mechanical properties of β-Ti alloys. Processing-microstructure-property relationships are also important to consider when designing new β-Ti alloys or new processing routes. The main research objective of this dissertation was accomplished by studying the effects of small alloying additions on the microstructural evolution, phase transformations, and mechanical properties of β-Ti alloys during processing.

Main research objective: Determine the composition-processing-microstructure-mechanical property relationships of the β-eutectoid Ti-Cr alloy system modified with small Fe and Al additions.

To accomplish this main research objective, the following tasks were performed.

1. Investigate how additions of 0.85at.% Fe and 5.3at.% affect the β-to-ω and β-to-α transformations of a base Ti-11at.%Cr alloy using X-ray diffraction (XRD), scanning electron microscopy (SEM), and atom probe tomography (APT).

2. Determine how 400°C aging affects the volume fractions and lattice parameters of the phases using 400°C XRD and SEM.

3. Use APT to investigate the composition of the phases in each alloy during the β-to-ω and β-to-α transformations.

4. Use 400°C resonance ultrasound spectroscopy (RUS) to determine the evolution of the shear modulus (G) with aging time.

5. Use tensile, fatigue, and Vickers hardness testing to investigate how the microstructural changes affect the mechanical properties of each alloy.

This dissertation is divided into 9 chapters. Chapter 1 above outlines the rationale and provides the main research objective. Chapter 2 provides background information on β-Ti alloys, the β, α, and ω phases, the alloying elements chosen for this investigation, and lists the research gaps associated with the main research objective. Information on the alloys, experiments, and analysis techniques used in this dissertation is provided in Chapter 3. Chapter 4 provides the results of all experiments performed on the β-homogenized alloys, which were characterized using SEM, EDS, APT, XRD, RUS, hardness, and tensile testing. A discussion of those results is provided in Chapter 5. Chapter 6 provides the SEM, TEM, EDS, APT, XRD, RUS, hardness, and tensile testing results of the alloys during and after aging. Chapter 7 contains a discussion of those results. The conclusions about the β-homogenized and aged alloys are provided in Chapter 8. The recommended future work is presented in Chapter 9.

The results (Chapter 4) and discussion (Chapter 5) of the β-homogenized material are presented separately from the results and discussion of the aged material to establish the condition of the β-homogenized alloys before aging. Without firm understanding of the composition, microstructure, and mechanical properties of the β-homogenized alloys, the effect of aging on the microstructure and mechanical properties of each alloy cannot be conclusively determined. Chapters 4 and 5 are separated into two sections: microstructure and mechanical properties. These sections are further divided by experiment.

Chapters 6 and 7 provide the results and discussion of the aged alloys, respectively, where the microstructure and mechanical property sections are separated similarly to that for Chapters 4 and 5. Within the microstructure section of Chapter 7, the discussion is organized according to the phase transformations and phase morphology evolution, the phase volume fraction evolution, the phase lattice parameter evolution (including the composition changes that occur during the transformations), and the locations of the impurity elements (O and H) as measured using APT. This allows the results from several experiments to be discussed together in the context of the microstructural changes observed with increased aging time. The mechanical property section of Chapter 7 is organized by experiment, but includes information from the Chapter 7 microstructure section to discuss the changes in mechanical properties with aging.

At the end of this work, a standard operating procedure for the FIB-based lift out procedure is provided in Appendix A. Supplemental 400 °C XRD data are provided in Appendix B. Supplemental BSE-SEM photomicrographs of the microstructure of each alloy are provided in Appendix C. Supplemental SEM photomicrographs of the fracture surfaces of the tensile samples are provided in Appendix D.

CHAPTER 2

BACKGROUND

To understand processing-microstructure-property relationships of Fe- and Al-modified Ti-11Cr alloys, an understanding of the crystal structures and the driving factors behind the β-to-ω, β-to-α, and ω-assisted-α phase transformations is necessary. This chapter discusses the β, α, and ω phases, followed by a discussion of the effects of Cr, Fe, and Al on the phase transformations and mechanical properties of β-Ti alloys.

2.1 β-Titanium alloys

β Titanium (β-Ti) alloys are used in several industries, such as the aerospace, biomedical, chemical, and automotive industries, where high strength-to-weight ratios and corrosion resistance are desired [2, 3, 11, 11–14]. The mechanical property requirements of components used in these industries vary. For example, biomedical applications require a low Young's modulus (E) to prevent the stress-shielding and promote healing [5], while aerospace applications require high tensile strength and adequate elongation-to-failure (ϵ_f) values [2]. Processing can transform the metastable BCC β phase into other metastable or equilibrium phases, affecting the mechanical properties. This allows the mechanical properties of β-Ti alloys to be tuned for specific applications.

Recently, research into improving the mechanical properties of β-Ti alloys has been driven by the need to replace heavier automotive and aerospace components with lighter parts of equivalent or higher strength to improve energy efficiency. This concept is known as "lightweighting." An example of lightweighting in aircraft is the replacement of 4.35 kg steel springs with springs made of Ti alloy "Beta C" that weigh 1.45 kg, as well as the replacement of fasteners with equivalent "Beta C" fasteners [2,11]. In the automotive industry, lightweighting of race cars using Ti alloys has been shown to improve performance [13]. However, β-Ti alloy usage in commercial automobiles is limited due to its higher cost in comparison to cheaper steel and Al alloys [13, 15].

One reason for the higher cost of Ti is its affinity for oxygen (O), nitrogen (Ni), hydrogen (H),

and carbon (C). Because of this affinity, manufacturing processes to extract Ti metal from naturally occurring Ti oxides must be performed in a vacuum or inert gas, and most high-temperature processing leads to significant scale loss due to oxidation [7, 16]. Subsequent processing of Ti into usable forms (such as bars, ingots, sheets, etc.) is also difficult, as are additional machining processes needed to manufacture usable Ti parts [7, 15, 16].

One avenue to cut the cost of β-Ti is by changing the alloying elements from the relatively expensive and commonly used vanadium (V), niobium (Nb), and molybdenum (Mo) to low-cost alternatives [2]. Low-cost alternative alloying elements that provide equivalent β-phase stability can help lower the cost of the β-Ti alloys thereby making them more feasible for lightweighting applications. Before substitutions of low-cost alloying elements can be made, the impacts of such elements on the microstructure and mechanical properties of the alloys must be identified.

To begin studying the relationships between alloy composition and microstructure, a comprehensive understanding of the possible phases and phase transformations in β-Ti alloys is necessary. This understanding is also necessary to investigate the microsctructure-property relationships of β-Ti alloys. To that end, a review of the β, α, and ω phases is now presented.

2.2 The β phase

The β phase is a BCC structure with two atoms in its unit cell at (0,0,0) and (1/2,1/2,1/2), and belongs to the space group Im-3m. Its BCC crystal structure has an atomic packing factor (APF) of 0.68, and in pure β Ti at 900°C the lattice parameter is 3.32Å [7]. The BCC structure is not an equilibrium structure at room temperature (RT) in pure Ti, so alloying elements that stabilize the β phase, called β-stabilizers, are added. To keep the β phase at RT, the alloy is typically raised above the β-transus temperature and then quenched, freezing in the BCC microstructure [7]. The β phase formed through this process is metastable and its stability can be affected by the concentration of β-stabilizers in the alloy [7, 17]. To compare the stability between alloys with different amounts of β-stabilizing alloying elements, the Mo Equivalency equation (Mo-Eq) was developed [8, 17]. Mo-Eq compares the β-phase stability by calculating the equivalent concentration of Mo that, if

alloyed instead, would provide an equivalent amount of β-phase stability. The Mo-Eq equation is:

$$\text{Mo-Eq} = \text{Mo} + 0.67\,\text{V} + 0.44\,\text{W} + 0.28\,\text{Nb} + 0.22\,\text{Ta} + 2.9\,\text{Fe} + 1.6\,\text{Cr} + 0.77\,\text{Cu} - 1.0\,\text{Al} \quad (2.1)$$

where the elemental symbol is the amount of that element in weight percent [17]. While not a perfect way to compare β-Ti alloys, because some of the elements are isomorphous stabilizers and some are eutectoid stabilizers, Mo-Eq provides a reference point for comparison. Even using the Mo-Eq, it is still difficult to compare β-phase stability between alloys.

As the β-phase microstructure is metastable, it can transform into other metastable and/or stable phases through thermomechanical processing. Alloys containing β-isomorphous stabilizers tend to decompose into the α and β phases with no other compounds formed [17]. While β-eutectoid alloys form the α phase, they also tend to form other compounds, such as $TiCr_2$ in Ti-Cr alloy systems [17]. In all types of β-Ti alloys, a common transformation, which increases strength, is the β-to-α phase transformation.

2.3 The α phase

The α phase is an equilibrium hexagonal close packed (HCP) phase in pure Ti and Ti alloys at temperatures below the β-transus. In Figure 2.1, the temperature and concentration combinations where the α phase can form are highlighted. The RT lattice parameters in pure Ti are 2.95Å for a and 4.68Å for c, with a resulting c/a ratio of 1.587 [7]. The unit cell contains two atoms at (0,0,0) and (1/3,2/3,1/2), and belongs to the space group P63/mmc.

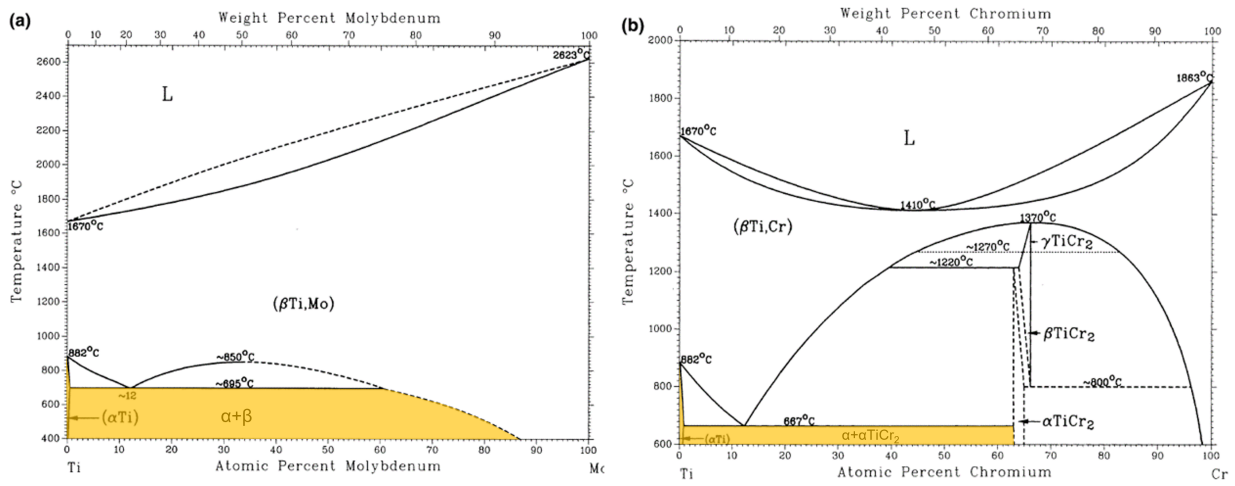

Figure 2.1: Phase diagrams of binary β-Ti (a) Ti-Mo and (b) Ti-Cr alloys with α-phase containing regions highlighted. Adopted from J. D. Cotton, R. D. Briggs, R. R. Boyer, S. Tamirisakandala, P. Russo, N. Shchetnikov and J. C. Fanning, "State of the Art in β Titanium Alloys for Airframe Applications," JOM, vol. 67, no. 6, pp. 1281–1303, May 2015.

The α phase forms in β alloys during heat treatment [18–20] according to the Burgers relationship between the β and the α phases:

$$(1\,1\,0)_\beta \parallel (0\,0\,0\,1)_\alpha$$
$$(1\,\bar{1}\,1)_\beta \parallel (1\,1\,\bar{2}\,0)_\alpha$$

The Burgers relationship has been verified [18, 21], and 12 variants are possible between a β grain and an α grain [22]. The α phase prefers to form in variant pairs or 3-variant clusters with an axis–angle pair relationship of $\langle 1\,1\,\bar{2}\,0\rangle/60°$ [23]. Formation of α phase is encouraged in β-Ti alloys by the inclusion of α-phase stabilizing elements Al, O, and/or N [2]. Reducing the amount of β-stabilizing elements will also promote α-phase formation, however a threshold level of β-stabilizers (i.e. a Mo-Eq of ∼10) must remain to retain the β phase upon quenching for the alloy to be considered as a β-Ti alloy [2].

The α phase can form as laths [24, 25], needles [26], or plates [18], or can have a globular [27] morphology, and form both inside β grains and along β-grain boundaries. Along with the location of the α phase, the size, distribution, and morphology of the α phase in the β-phase matrix can

significantly influence the tensile properties of β-Ti alloys [7, 27]. In particular, microstructures containing fine α-phase have exhibited a desirable combination of high strength and ϵ_f [27].

The α phase can form with the assistance of the metastable ω phase [24, 28]. Although less is known about the ω-assisted α-phase transformation than the β-to-α phase transformation, because the tensile strength tends to increase with increased fine-grained α phase, a considerable amount of work has been done to understand how the ω phase affects the formation, growth, and morphology of the α phase.

2.4 The ω phase

2.4.1 Crystal structure

To understand how the ω phase can affect the α phase transformation, a thorough understanding of the ω phase is necessary.

Discovered in 1954 by Frost et al. [29], the ω phase is defined as a hexagonal crystal structure that can exist in pure Ti and zirconium (Zr) at high pressures [30,31], in shock-deformed polycrystalline Ta and Ta-W alloys [32], or in β-Ti alloys [2,33]. The hexagonal structure is not close-packed [34] and forms by the collapse of a pair of (1 1 1) BCC planes into a single plane [7, 33–36]. This collapse occurs when linear defects of vacancies and crowdions in the ⟨1 1 1⟩ direction align so that the ω structure is created from the BCC structure, thereby changing the stacking pattern of the (1 1 1) planes from ABCABC in the BCC structure to AB'AB' in the ω structure [37, 38]. Because there are four ⟨1 1 1⟩ directions in the BCC unit cell, four variants of the ω phase can be formed [7, 39, 40]. The ω phase has three atoms in the primitive unit cell and the lattice points are (0,0,0), (2/3,1/3,1/2), and (1/3,2/3,1/2), belonging to the space group $D1/6_h$, P6/mmm [30, 35]. Figure 2.2 shows the BCC (β phase), HCP (α phase), and hexagonal ω-phase structures. The crystallographic orientation relationship between the β, α, and ω phases has been determined as:

$$\langle 0\,0\,0\,1\rangle_\omega \parallel \langle 1\,1\,\bar{2}\,0\rangle_\alpha \parallel \langle 1\,1\,1\rangle_\beta$$
$$\langle 1\,\bar{2}\,1\,0\rangle_\omega \parallel \langle 0\,0\,0\,1\rangle_\alpha \parallel \langle 0\,1\,1\rangle_\beta$$
$$(0\,0\,0\,1)_\omega \parallel (\bar{1}\,2\,\bar{1}\,0)_\alpha \parallel (1\,1\,1)_\beta$$
$$(\bar{1}\,0\,1\,0)_\omega \parallel (1\,0\,\bar{1}\,0)_\alpha \parallel (2\,1\,1)_\beta$$
$$(\bar{1}\,\bar{1}\,2\,0)_\omega \parallel (0\,0\,0\,1)_\alpha \parallel (0\,\bar{1}\,1)_\beta$$

These relationships have been verified through multiple independent studies [7,9,10,32,39,41–54]. A representation of the $(\bar{1}\,0\,1\,0)_\omega \| (2\,1\,1)_\beta$ relationship is shown in Figure 2.2 (e), showing that the $(\bar{1}\,0\,1\,0)_\omega$ planes have a d-spacing of 3 times that of the $(2\,1\,1)_\beta$ planes.

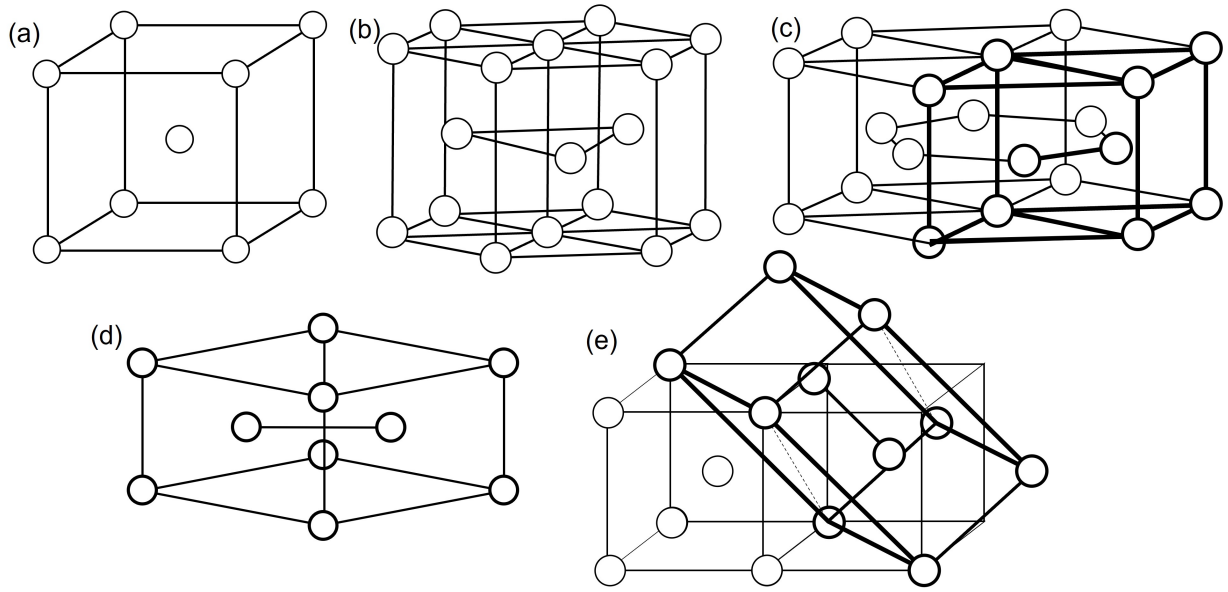

Figure 2.2: The (a) BCC β phase, (b) HCP α phase, (c) hexagonal ω phase with the primitive unit cell bolded, (d) ω phase primitive unit cell with corresponding highlighted atoms, and (e) relationship between the β and ω phase unit cells, with the primitive ω unit cell bolded.

The ω phase in a Ti-16Vwt.% alloy was reported to have a lattice parameter 'a' value of 460 pm and a 'c' value of 282 pm [33,35]. Calculating the c/a ratio from these parameters gives a value of 0.613 and a calculated APF of 0.68. The ω-phase APF was calculated assuming the radius of each atom in the unit cell was equivalent. In the case of the α phase, an 'a' value of 295 pm, a 'c' value of 468 pm, a c/a ratio of 1.587, and an APF of 0.74 has been reported [7,8]. Even though the reported

Table 2.1: Lattice parameters, volumes, and APFs of the β, ω , and α phases.

	β phase	**ω phase**	**α phase**
Lattice parameters	a=328pm	a=460pm c=282pm	a=295pm c=466pm
c/a ratio		0.613	1.588
Volume	$\frac{64r^3}{3\sqrt{3}} \cong 12.3168r^3$	$\frac{32r^3}{\sqrt{3}} \cong 18.4752r^3$	$8r^3\sqrt{2} \cong 11.3137r^3$
Volume per atom	$\frac{32r^3}{3\sqrt{3}} \cong 6.1584r^3$	$\frac{32r^3}{3\sqrt{3}} \cong 6.1584r^3$	$4r^3\sqrt{2} \cong 5.6569r^3$
APF	$\frac{\pi\sqrt{3}}{8} \cong 0.68$	$\frac{\pi\sqrt{3}}{8} \cong 0.68$	$\frac{\pi\sqrt{2}}{6} \cong 0.74$

ω-phase lattice parameters are for Ti-16V and Aurelio and Guillermet [55] and Bönisch et al. [56] found that the ω-phase lattice parameters change with alloy content, the c/a ratio is consistently 0.613 [33, 55]. In Zr alloys, Hatt and Roberts found that the ω-phase c/a ratio was 0.622 [51], and a shock-induced ω phase in polycrystalline Ta had a c/a ratio of 0.611 [32].

Table 2.1 contains a comparison of the lattice parameters, volumes, and APFs of the ω , α , and β phases. These APF calculations illustrate that if the β and ω phases are made up of atoms with the same radii, the β-to-ω transformation would not change the overall volume of the material; the APFs for the β and ω phases are both 0.68. The APF also helps clarify that even though the ω phase is sometimes misidentified in the literature as HCP [8, 52, 57], it is not close-packed.

Selected area electron diffraction (SAED) patterns are commonly used to analyze the presence of the ω phase. ω-phase diffraction spots can be imaged along the $[1\,1\,0]_\beta$ or $[1\,1\,3]_\beta$ zone axes, appearing at the $1/3\langle 1\,1\,2\rangle_\beta$ or $2/3\langle 1\,1\,2\rangle_\beta$ positions. Figure 2.3 (a) and (b) show example diffraction patterns of the β and ω phases. These patterns have assisted in identification of the crystallographic orientation relationships between the β and ω phases (detailed above). These patterns have also allowed the morphology of the ω phase to be studied using dark-field imaging. Ellipsoidal and cuboidal are two morphologies exhibited by the ω phase (see Figure 2.3) [37,58,59]. The morphology of the ω phase depends on alloying elements and processing and is covered in more detail in Section 2.4.2.3.

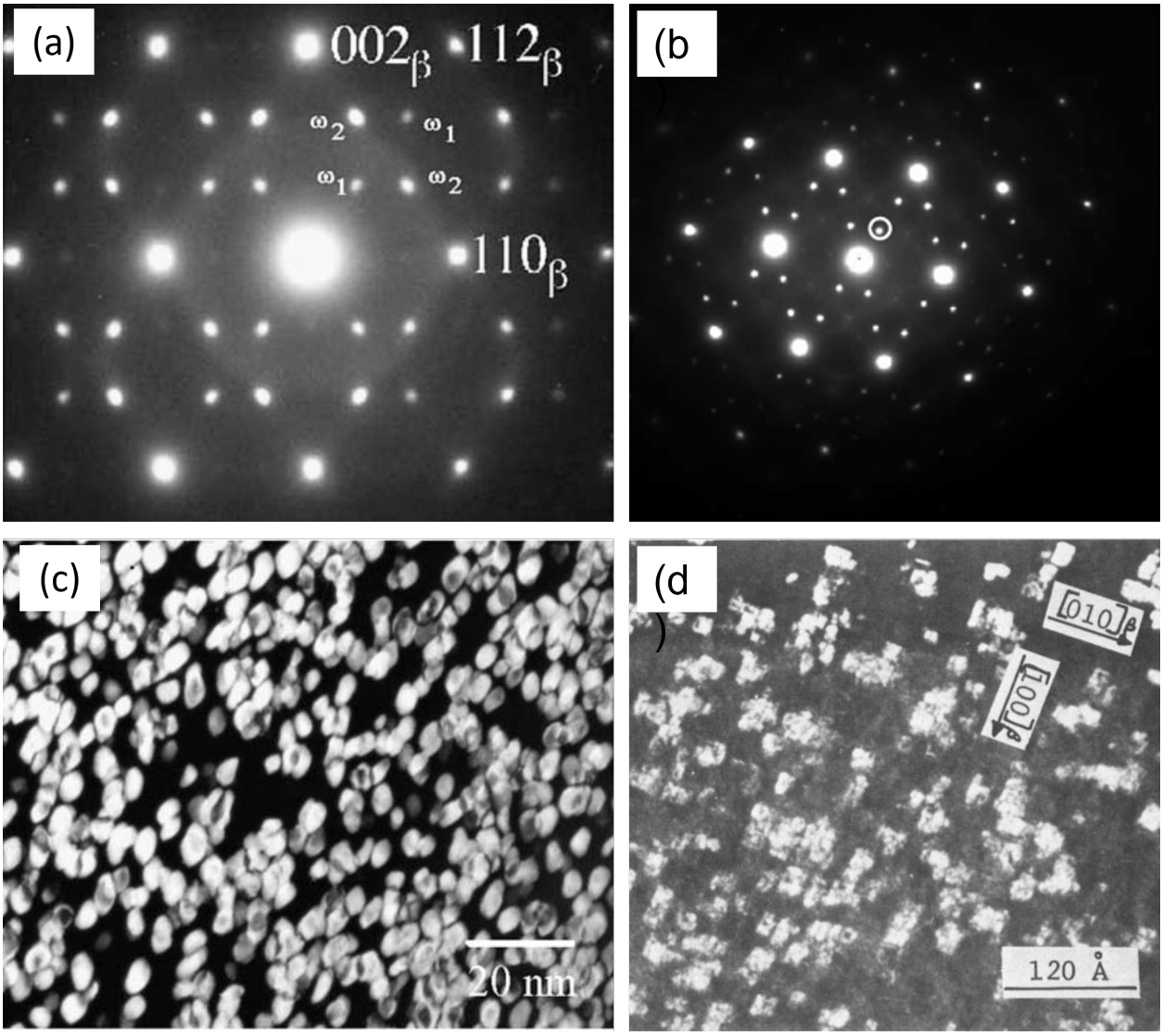

Figure 2.3: Examples of SAED patterns containing the β and ω phases taken from the (a) $[1\,1\,0]_\beta$ and (b) $[1\,1\,3]_\beta$ zone axes, as well as dark-field images obtained using the ω reflections in SAED patterns showing the (c) ellipsoidal and (d) cuboidal morphologies of the ω phase. ((a, c) adapted from F. Prima et. al., *Scripta Materialia*, vol. 54, pp. 645–648, 2006. (b) from J. I. Qazi et. al., *Materials Science and Engineering C*, vol. 25, pp. 389–397, 2005. (d) from V. Chandrasekaran et. al. *Metallography*, vol. 11, pp. 183–198, 1978).

2.4.2 Classification of ω phases

The plane collapse that creates the ω phase in β-Ti alloys is triggered by pressure/plastic deformation, quenching from above the β-transus, or thermal energy. Compositional differences in the β phase affect these triggers [39, 60, 61], which create different types of the ω phase. While the

types of ω phase have the same crystal structure, they are differentiated in the literature to help the reader distinguish between their formation mechanisms. These distinctions are useful because the formation mechanism can affect the size, morphology, and composition of the ω phase. The generally recognized types of ω phase are the (1) **deformation-induced ω phase,** (2) **athermal ω phase (ω_{ath}),** and (3) **isothermal ω phase (ω_{iso})**. A detailed analysis of the state of the knowledge of each type of ω phase is provided below.

2.4.2.1 Deformation-induced ω phase

The deformation-induced ω phase can be studied in pure Ti and Zr through the application of high static pressures because the structure remains stable after the pressure is removed [30, 31, 62–65]. This is true of β-Ti alloys as well as pure α-Ti. β-Ti alloys have four stress-induced transformations: the α' and α" martensites, the ω phase, and mechanical twins [36]. Low concentrations of β-stabilizing elements favor α'- and α"-martensitic transformations (decreasing the M_s temperature). Higher concentrations of β-stabilizing elements suppress the α' and α" transformations, allowing the ω phase and twins to form instead [36, 66], with the ω phase forming in both the β matrix and inside of the twins [66, 67]. If the β-stabilizer concentration is high enough, the ω-phase transformation will also be suppressed and only twins will form [36, 68]. Clear cutoffs for low, medium, and high β-stabilizer concentrations are not well defined in the deformation-induced ω-phase literature. Comparing the β-phase stability can be difficult because different alloys are often used, such as Xing and Sun's Ti-23Nb-0.7Ta-2Zr-0.2O (at.%) alloy [69] and Ahmed et al.'s Ti-10V-3Fe-3Al alloy [67], so Mo-Eq is used to help the comparisons. Each multiplier in the Mo-Eq is determined by taking the critical minimum level of β-stabilizer content (β_c)needed to retain the β phase and dividing it by the β_c of Mo (10) [17]. A higher β_c value is associated with a lower amount of β stability imparted by the element, while a lower β_c value is associated with a higher amount of β stability [17]. Table 2.2 gives the β_c values and the multipliers from the Mo-Eq (Equation 2.1) as given by Bania [17].

Table 2.2: β-stabilizing elements with their associated β_c values and Mo-Eq multipliers. The β_c wt.% values are the concentration of each alloying element needed to retain 100% of the β phase upon quenching.

Elements	**β_c (wt.%)**	**Mo-Eq multiplier**
Mo	10.0	1.0
V	15.0	0.67
W	22.5	0.44
Nb	35.7	0.28
Ta	45.0	0.22
Fe	3.5	2.9
Cr	6.5	1.6
Cu	13.0	0.77

In general, a low β-stabilizer concentration seems to refer to alloys with a Mo-Eq of less than 10 [70]. The β-phase stability range where the ω phase forms is a Mo-Eq of approximately 10–12.5 [67–71]. A range of ~12 to 15 supports deformation-induced twin formation, with or without the ω phase [71, 72]. A Mo-Eq higher than ~15 supports slip as the dominant deformation mechanism [70]. These ranges are only general guidelines for β-Ti alloys and exceptions to these ranges can be found, such as twins and ω phase forming along with α" martensite in a cold-rolled Ti-24Nb-4Zr-8Sn alloy (Mo-Eq of ~6.7) [66].

However, β-stabilizer concentration is not the only variable that affects deformation-induced ω-phase formation. Grain size [44], processing route [67], and the existence of deformation twins [65] have been shown to affect the volume fraction of the ω phase. In static-pressure experiments, impurities such as O or N increased the pressure required to initiate the deformation-induced ω-phase [62].

Severe shear plastic deformation during high-pressure torsion (HPT) has been shown to induce the ω phase in Ti and its alloys. The torsion that the samples experience lowers the incubation time for ω-phase formation at RT in Ti by approximately 27 h compared to static pressure alone [73] and reduces the amount of pressure needed to generate the ω phase [74]. β-stabilizer concentration affects the amount of ω phase in the material after HPT processing [75, 76]. However, Tane et al. [77] and Panigrahi et al. [78] demonstrated that HPT processing can lead to the formation of a

deformation-induced ω-phase in pure Ti and Ti-16.1Nb. The starting microstructure can affect the number of turns needed to start the ω-phase transformation [75] as well as the amount of ω phase in the material formed after HPT [79]. HPT can also induce an α-to-ω phase transformation [73, 79] through atomic shuffles in the $(0\,0\,0\,1)_\alpha$ planes [75]. However, the α-to-ω transformation is not guaranteed to form in all Ti alloys during HPT [79]. Wang et al. [44] and Edalati and Horita [80] found that grain size is an important variable that influences the ω-phase formation in both β-Ti and pure Ti, with smaller grains lowering the amount of ω phase in the material, although temperature was also a variable in the Edalati and Horita study [80].

Multiple morphologies are reported for the deformation-induced ω phase. In compression testing, long, thin lamellar ω phases were generated [67]. During hot deformation in the β+α region, a thin lamellar-like ω phase was reported to form [52]. Impact testing formed a plate-like ω phase [81, 82]. Cold-rolling produced plate-like ω phase [66]. In polycrystalline Ta and Ta-W alloys, the shock-generated ω phase had a zigzag structure with multiple interconnected ω-phase variants [32]. Also, alloying Ta with the β-stabilizer W increased both the volume fraction and the size of the ω phase [32].

2.4.2.2 Athermal ω phase

The athermal ω phase forms as well-dispersed particles during the quenching of β-Ti alloys from above the β transus temperature, when the $(1\,1\,1)_\beta$ plane collapse occurs as a result of the instability of the β phase with respect to a specific mode of phonon [25, 40, 83]. ω_{ath} particles are less than 10 nm in size—usually between ~2 and 5 nm [7, 39, 45, 66, 84–86], and are generally reported as spheroidal [39, 52, 67, 85, 87] or ellipsoidal [45, 52, 84, 86]. Because quenching does not allow diffusion to occur, ω_{ath} theoretically has the same composition as the surrounding β matrix [88], with higher volume fractions forming in β alloys with β stabilizer concentrations close to the lower limit of β-phase retention [33, 48, 89]. Hydrogen is known to limit the amount of ω_{ath} formed [8].

Rather than discrete diffraction spots, ω_{ath} is observed to lead to diffuse streaking in SAD patterns as a result of the small size of ω_{ath}, local strain fields around ω_{ath}, and/or short-range

correlated displacements in the β lattice [25, 51, 83, 90, 91]. Diffuse streaking in SAD patterns is also observed when there is an incomplete collapse of the $(1\,1\,1)_\beta$ planes during the β-to-ω transformation. Instead of being located at (0,0,0), (1/3,2/3,1/2), and (2/3,1/3,1/2), the atoms have positions at (0,0,0), (1/3,2/3,1/2+δ), and (2/3,1/3,1/2-δ), where $0<\delta<1/6$. The value of δ depends on the degree of plane collapse, which seems to be correlated with the β-stabilizer concentration [34]. Although the existence of the partially collapsed ω phase has been debated [83], high-resolution STEM (HRSTEM) images have verified that this occurs [39, 43, 60]. Sometimes referred to as "rumpled" ω [32], "rumpled-plane" ω [51], trigonal ω [34], "modulated" ω [92], or "embryonic" ω [10, 39, 43, 93], these "incommensurate" structures have also been reported with the fully collapsed "commensurate" ω_{ath} after quenching [25, 39, 90]. However, it is important to note that these ω structures can also form during heat treatments, causing diffuse streaking in selected area diffraction patterns of quenched and isothermally aged samples [10, 94]. Figure 2.4 shows an example of the incommensurate ω phase as seen in high resolution transmission electron microscopy (HRTEM), along with graphical representations of the incommensurate and commensurate ω-phase structures.

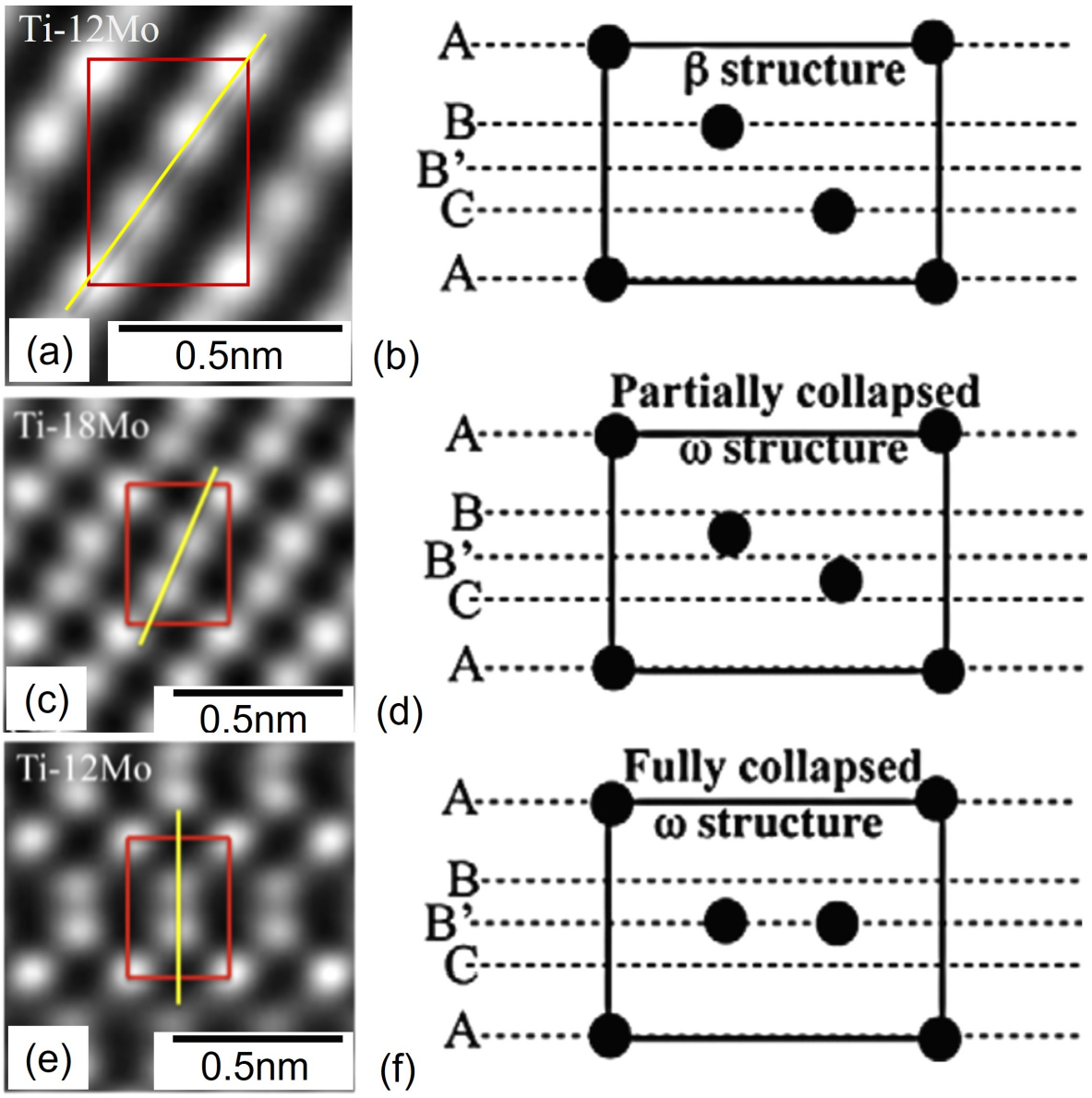

Figure 2.4: (a) Fully collapsed and (b) partially collapsed ω structures in Ti-Mo alloys as shown in HRTEM images and (c) a schematic of the structures. (All images adopted from A. Devaraj et al. *Acta Materialia*, vol. 60, no. 2, pp. 596–609, November 2011).

The different types of ω phase (deformation-induced, athermal, and isothermal) are differentiated via their formation pathway (deformation, quenching, heat treatment). Because the incommensurate ω phase can form through either quenching or heat treatment, labeling it as solely an athermal or isothermal type of ω phase is not sufficient, and the literature to date has been inconsistent with its nomenclature. Therefore, in the remainder of this work, the terminology "athermal ω phase" or

"ω_{ath}" is used to mean a commensurate ω phase that forms through quenching and "isothermal ω phase" or "ω_{iso}" is used to mean a commensurate ω phase that forms during isothermal aging. To refer to incommensurate ω phase formed through the athermal pathway, "incommensurate athermal ω phase" or "incommensurate ω_{ath}" is used. Similarly, "incommensurate isothermal ω phase" or "incommensurate ω_{iso}" is used to refer to incommensurate ω phase formed through the isothermal pathway.

2.4.2.3 Isothermal ω phase

The isothermal ω phase precipitates homogeneously in metastable β-Ti alloys during low-temperature heat treatments that favor the β-toω transformation over the β-to-α transformation [8, 25, 28, 33, 95–97]. Depending on the alloy, the lowest temperature that initiates the β-to-ω_{iso} transformation is between 150°C [42] and 280°C [98]. Most researchers use a temperature range of 300°C–400°C to generate the isothermal ω phase [10, 41–43, 47, 49, 50, 58, 93, 98–100], and 500°C is the highest temperature reported to form ω_{iso} [56, 101]. Using in situ synchrotron diffraction experiments, Bönisch et al. [56] found that the ω phase lattice parameters remained relatively constant in both Ti−28.5Nb and Ti−36Nb as they were heated from 300°C to 500°C.

ω_{iso} has been found to nucleate at defects in the β matrix left by ω_{ath} after ω_{ath} reverts to β phase during heat treatment [42, 102]. ω_{iso} has also been found to grow from ω_{ath} [9, 40, 88]. Locations in the β matrix with lower concentrations of β-stabilizers due to nanoscale chemical fluctuations are also favorable sites for ω_{iso} nucleation [39, 43, 60].

During the growth of ω_{iso} particles, alloying elements diffuse from the ω phase into the surrounding β matrix [7, 33, 34, 98, 103]. APT is a powerful technique for investigating at the sub-nanometer scale and provides spatially resolved composition of precipitate phases [104], and APT studies of multiple binary β-Ti alloys clearly show that the ω phase is solute−lean (shown in 2.5) [39, 49, 60, 84, 104]. For example, in a binary Ti-9.9Mo (at.%) alloy, the ellipsoidal ω phase was found to have a Mo concentration near 2 at.% [39, 105]. More complex alloys have also been studied using APT, showing that ω_{iso} is depleted of both β- and α-stabilizing

elements [9, 10, 47, 85, 93, 95, 96, 99, 106, 107].

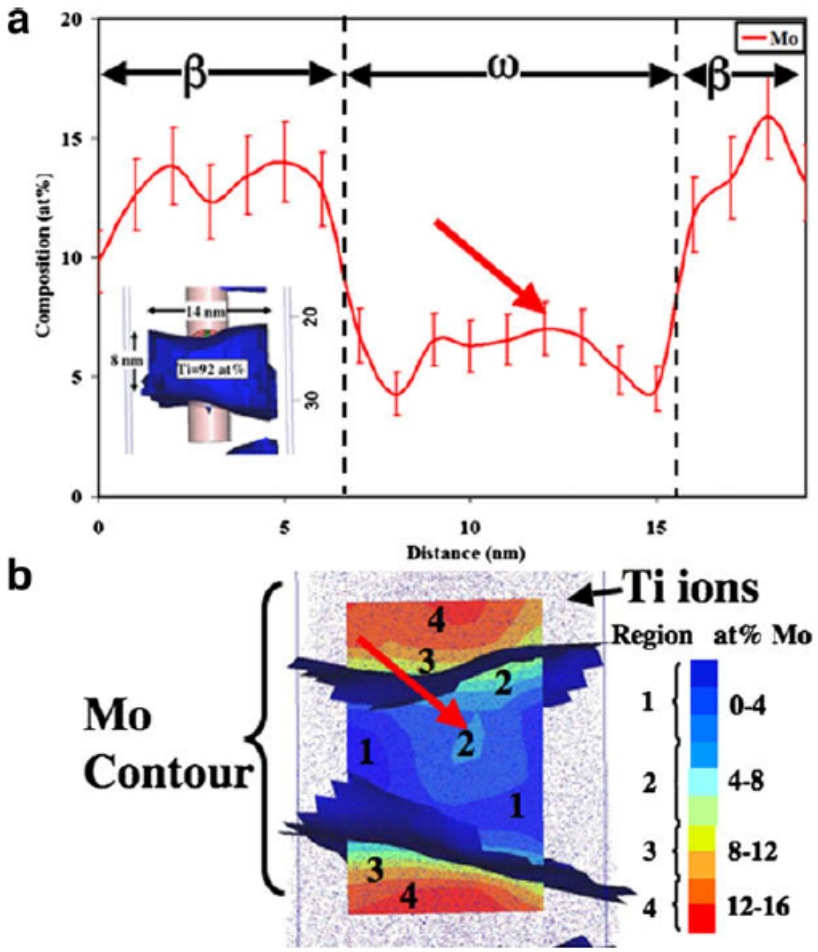

Figure 2.5: (a) A Mo composition plot taken from a 1-D cylinder showing the Mo composition difference between the β matrix and an ω-phase particle and (b) the associated Mo contour plot. (Figure adopted from A. Devaraj, et al., "Three−dimensional morphology and composition of ω precipitates in a binary titanium−molybdenum alloy," *Scripta Materialia*, vol. 61, pp. 701–704, June 2009).

The size of ω_{iso} particles depends on the time spent at the heat treatment temperature because the particles coarsen with time. A range of 2–100 nm has been reported for ω_{iso} particles generated using various temperatures and times [39, 41, 43, 45, 59, 84, 85, 88, 95, 96, 100, 105, 108]. Moffat and Larbalestier [108] have also shown that higher aging temperatures produce larger precipitates for the same amount of time. Because of the small size of ω_{iso}, transmission electron microscopy (TEM) is the most effective microscopy technique for detecting the ω phase, although some studies

have detected the presence of the ω phase using X-ray diffraction (XRD) [48, 101, 106, 109].

The morphology of the ω phase is determined by the elastic strain energy in the crystal that is due to the difference between the radii of alloying elements and Ti [40, 105] or by elastic interactions between the ω_{iso} particles [110]. ω_{iso} particles in high-misfit systems, such as Ti-Cr, have a cuboidal morphology with the flat surfaces parallel to the $(1\,1\,0)_\beta$ planes [7, 105, 108]. ω_{iso} particles in low-misfit systems, such as Ti-Mo, have an ellipsoidal morphology in which the major axis is parallel to the $\langle 1\,1\,1\rangle_\beta$ directions [7, 53, 105, 108] as a result of the elastic anisotropy of the β phase, and an average ratio of the major to the minor axis of 3.56 [104]. With enough time, the ellipsoidal ω_{iso} particles in low-misfit systems become cuboidal because the elastic interactions between the particles affect the morphology with increasing growth of ω_{iso} [110]. Blackburn and Williams [53] show this transformation from ellipsoidal morphology to a cuboidal morphology of ω_{iso} in a high-misfit Ti-V alloy. Figure 2.3 shows dark-field TEM images of ω_{iso} particles with the two morphologies. Furthermore, for a low-misfit Ti-6554 alloy, the morphology of ω_{iso}—which grew from an ellipsoidal incommensurate isothermal ω phase—was observed to evolve from more lath-like to a mixed plate- and rod-like morphology as the annealing time increases at 300°C [10].

Because of the effects of ω_{iso} on mechanical properties (covered in detail below), methods have been developed to avoid precipitation of ω_{iso}. Precipitation of the isothermal ω phase can be avoided through the addition of alloying elements that increase the stability of the β phase [101, 111, 112] or the α phase (such as oxygen or aluminum) [46, 112–114]. Heat treatment temperatures above 500°C can be used to precipitate the α phase without precipitating the ω phase [25, 28, 33]. However, the ω phase might still be precipitated if the heating rate to reach temperatures above 500°C is slow enough to allow ω-phase precipitation or if the α ” phase was present before heating and a fast heating rate is used [57, 115, 116]. Increasing the amount of time the alloy stays at lower heat treatment temperatures (100°C–500°C) can cause the α phase to grow into the ω phase, leaving only the α crystal structure and no ω crystal structure [10, 41, 43, 59]; in some alloys, however, ω_{iso} can coexist with α after heat treatments of 192 h [43, 47]. ω-phase formation can also be suppressed by large quantities of grain boundaries or dislocations that prevent

$(1\,1\,1)_\beta$ plane collapse [28].

2.4.3 β-to-ω phase transformation mechanism

ω_{ath} and deformation-induced ω are formed through a displacive mechanism via atomic shuffling. Driven by quenching or stress, the $(1\,1\,1)_\beta$ plane collapse occurs without diffusion. The displacive collapse is reversible, as De Fontaine et al. showed through in situ TEM ω_{ath} formation and reversion in the temperature range of $-171°C$ to $5°C$, which prevented diffusion [83]. The combination of temperature increase from electron irradiation and oscillations from inelastic scattering in a TEM can also reverse the displacive collapse [87].

Current debate about the β-to-ω transformation centers around the athermal and incommensurate ω_{iso} phases (which are early stages of ω_{iso}). Nag et al. [60] and Devaraj et al. [39] found evidence that incommensurate ω_{iso} particles formed in pockets of slight Mo-depletion in a binary Ti-Mo alloy during quenching, and Li et al. [10,43] found that the incommensurate ω_{iso} particles in Ti-6Cr-5Mo-5V-4Al were Mo lean. However, they clarified that the Mo-lean pockets were created by second-order spinodal decomposition of the β phase and that the incommensurate ω_{iso} phase forms via a displacive mechanism within these Mo-lean regions [43]. Tane et al. [117] came to a similar conclusion with their work in a Ti-V alloy system, showing that the ω phase can form without diffusion in quenched-in V-lean pockets while aging at RT. In contrast, Ahmed et al. [57] and Ng et al. [85] have found no change between the matrix composition and the composition of the athermal ω phase. Coakley et al. [99] also did not observe the formation of ω_{ath} in Mo-lean pockets in Ti-5Al-5Mo-5V-3Cr. Sun et al. [118] and Mantri et al. [119] both found no compositional variation in a Ti-12Mo alloy associated with the formation of ω_{ath}, but both recorded sharp diffraction spots—this suggests a lack of the incommensurate ω phase, which Nag et al. [60], Devaraj et al. [39], and Li et al. [10] all observed forming in the Mo-lean pockets.

Recent work by Li and Min [120] appears to resolve the debate about the relationship between the displacive collapse forming the athermal and incommensurate ω_{iso} phases. Although independent of diffusion, the displacive collapse that forms the athermal ω phase is not totally independent of

composition. Li and Min [120] have shown in a Ti-Mo alloy that, although the ω phase can still form in areas with Mo, stacking fault energy and charge density difference drive the ω phase to form in Mo-depleted areas. This supports predictions by Gullberg et al. [121] and earlier findings by McCabe and Sass [122] that ω_{ath} is Ti rich, as well as with observations by Fan and Miodownik [61] that the ω phase forms in solute-lean β phase areas more readily. Li and Min's [120] work also supports findings by Nag et al. [123] that suggested ω_{ath}/incommensurate ω phase particles were associated with fluctuations in stabilizer concentrations. However, while ω_{ath} and incommensurate ω phase prefer Mo-lean areas, their formation is still a displacive collapse and is not dependent on diffusion to occur.

In contrast, ω_{iso} is known to form via a diffusion mode. That is, elemental partitioning occurs along with the $(1\,1\,1)_\beta$ plane collapse, creating an ω phase with a lower energy than the ω phase generated through displacive collapse [111]. While ω_{iso} has been shown to grow rapidly without diffusion for short times (60 seconds) at the start of nucleation [40, 85, 118], the rejection of the β stabilizers is important for ω_{iso} growth because it stabilizes the ω phase by lowering the energy of the structure and making the ω transformation irreversible [83]. Quenching before the heat treatment and heating during isothermal aging are necessary to make the β-to-ω transition more energetically favorable than the β-to-α transition, with faster quenching rates increasing the number of ω_{iso} precipitates formed [108, 114, 124]. This is attributed to the relationship between ω_{ath} and ω_{iso} because ω_{ath} locations in the β matrix have been shown to act as nucleation sites for ω_{iso} [34, 102]. However, the exact mechanism behind ω_{ath}-assisted precipitation of ω_{iso} is not known. Additionally, a slow heating rate is found to allow nucleation and growth of ω_{iso} particles from the β phase during heating [57, 115, 116], although Barriobero-Vila et al. [116] have shown that if α" martensite is present, a faster heating rate increases the volume fraction of ω_{iso} compared to slower heating rates by activating the α"-to-ω_{iso} transformation along with the β-to-ω_{iso} transformation.

2.4.4 ω-assisted precipitation of the α phase

Another important phase transformation is the ω-to-α phase transformation. ω_{iso} is known to affect the precipitation of the α and α" phases [24, 28, 40, 54]. The finely distributed α platelets formed by ω-assisted precipitation were noted by Ohmori et al. [54] to have a significantly deviated habit plane compared to the coarse α plates formed without ω-assistance. It should be clarified that ω_{ath} and the incommensurate ω_{iso} phases do not assist in α-phase formation [10, 49, 125, 126], but they can coexist with the α phase [10, 25]. The commensurate ω_{iso} phase promotes the formation of refined α-phase precipitates, thereby providing attractive mechanical properties for high-strength applications [9, 24]. A fine-grained α-phase also formed in high-pressure torsion (HPT) samples composed of the deformation-induced ω-phase when heated above 320°C, although the mechanical properties of this α-phase have not been investigated [78].

Understanding ω-assisted precipitation of the α phase is key for tuning processing conditions and/or alloy content to achieve desired mechanical properties. In the last 20 years, this topic has been an active area of research, and APT has expanded the field of knowledge considerably.

In high-misfit systems where the ω phase has a cuboidal morphology, ledges between the β and ω phases drive the ω-to-α transformation [49]. In low-misfit systems, the nucleation sites for the α phase have been the subject of debate for years. Historically, three locations of α precipitation have been considered:

1. The α phase precipitates at some distance from the ω/β boundary [97].

2. The α phase precipitates in the core of the ω phase [59].

3. The α phase precipitates at the ω/β boundary [57].

Azimzadeh and Rack [97] proposed that Al diffuses away from the ω phase into the β matrix in a low-cost β-Ti alloy, providing an α phase nucleation point at some distance from the ω phase, where it then grows toward—and looks like it is precipitating "in association" with—the ω phase. Against this view, Prima et al. [59] have presented concurrent ω/α phase images that

suggest the α phase forms in the core of the ω precipitate. The α phase might prefer nucleating in the core of the ω phase as a result of the low amounts of β stabilizers present in the ω phase compared to the heavily stabilized surrounding β phase, and the transformation would most likely be a purely displacive reaction [42, 59]. TEM images of α particles with ω super cells at both boundaries—which could provide evidence that the α phase nucleates in the ω phase core—have been presented by Ahmed et al [57]. Ahmed et al.'s [57] TEM images could also provide evidence for the α phase nucleating at the ω/β boundary because the α particles were coherent with both the β and ω particles. HRTEM images by Furuhara et al. [127] also suggest that the α phase nucleates at the ω/β boundary, although the α phase growing toward the boundary cannot be ruled out. Li et al. [43] presented images similar to Furuhara et al. [127], but they determined that the α phase did not nucleate in the β phase and grow toward the boundary through composition analysis. If the α phase had nucleated in the β phase, the β stabilizer concentrations in the α phase would be expected to decrease with time, which does not match experimental observations [43]. Chemical driving force calculations by Shi et al. [128] indicate that the cuboidal ω/β interface is the most favorable nucleation site for α phase, and subsequent HRSTEM work showed the presence of the α phase at the cuboidal ω/β interface as predicted. Li et al. [10] and Zheng et al. [49] have also presented images of the α phase that nucleated at the ω/β boundary, and the 3-D APT results in the work of Zheng et al. [49] show the association of the ω and α phases.

Another much-disputed topic is the dominant nucleation driving force for ω-assisted α formation. Recent studies proposed that the elastic stress associated with the coherent ω/β interface, compositional variation between ω_{iso} and the surrounding β phase, and/or dislocations migrating to or forming at the ω/β boundary could provide additional driving force to promote the precipitation of the α phase [9, 40, 128]. A combination of those reasons could also influence α precipitation. To ascertain the key nucleation driving force for ω-assisted α formation, the transitional stage before and after the α phase forms must be identified. Li et al. [10] captured the transitional stage by analyzing samples aged for 2, 4, 8, 12, 16, 24, 32, 48, and 192 h, respectively, at 573 K using HRTEM and APT. They found that high elastic stress and O-rich regions present around the coher-

ent incommensurate-ω/β interface (at 12 h) do not assist α formation (see Figure 2.6) [10]. The α phase forms only when the coherent interface becomes semi-coherent, suggesting that increased interfacial energy serves as the dominant factor in triggering ω-assisted α precipitation [10]. In addition, O trapped by ledges at the semi-coherent interfaces could provide an additional nucleation driving force for ω-assisted α formation. These results are supported by the chemical driving force calculations of Shi et al. [128] which indicate that a semi-coherent β/ω interface provides a lower energy barrier to α phase nucleation than a coherent interface. However, while Shi et al. [128] indicate that local enrichment of O at the ω/β interface could provide another chemical driving force for α nucleation, they also argue that the energy associated with other factors could outweigh the contribution of O and that more study is needed. Similarly to Shi et al. [128], Nag et al. [123] concluded that coherency strains and local enrichment of Zr both played a role in the nucleation and growth of α precipitates at the ω/β interface. Zheng et al. [9] also conclude from CALPHAD studies that composition variance and coherency stress between the β and ω phases both play a role in α nucleation. Thus, there is a lack of current consensus and more experimental evidence combined with modeling studies are required to determine the key nucleation driving force behind ω-assisted α formation.

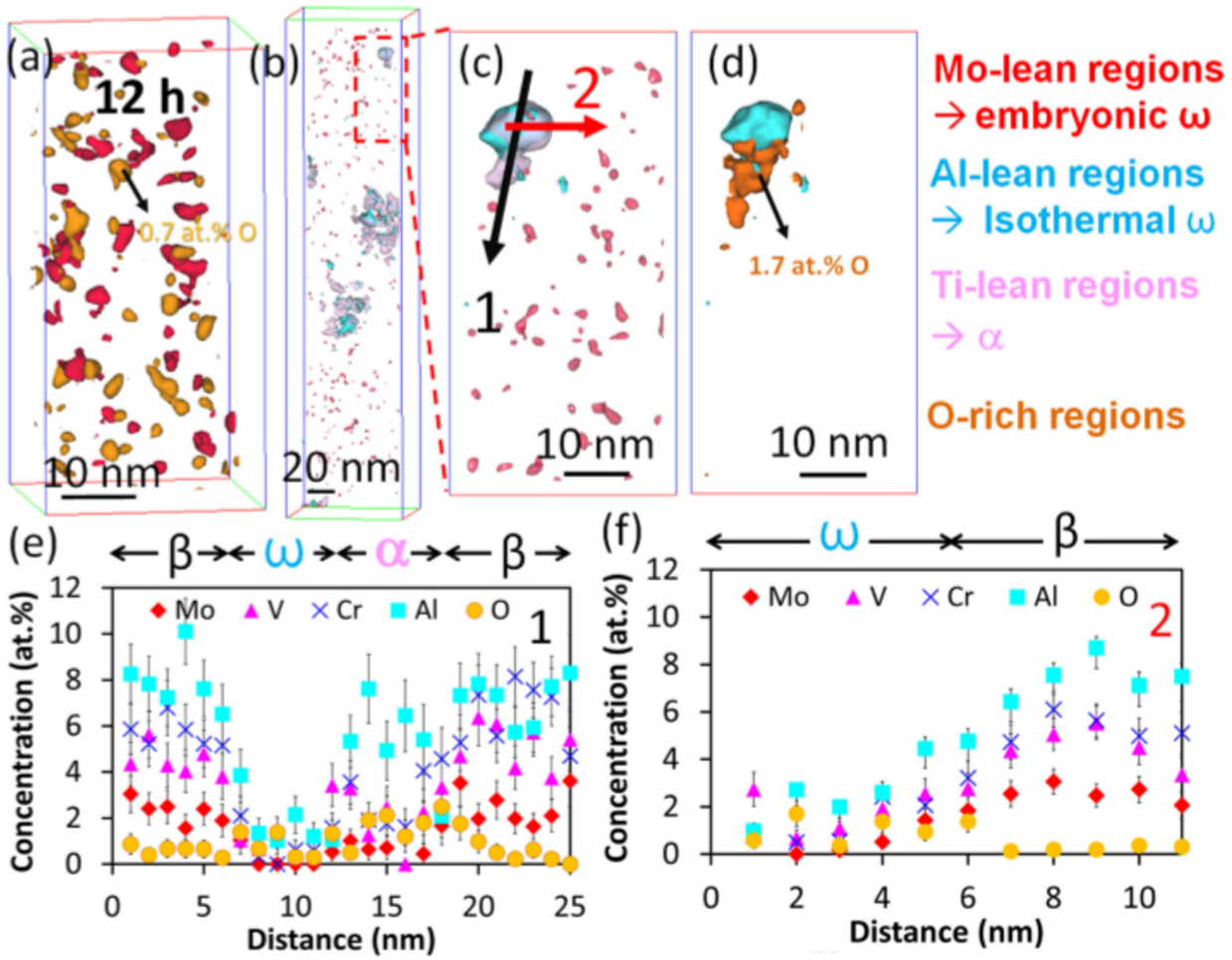

Figure 2.6: APT reconstructions of a Ti-6554 sample showing the relative positions of orange O-rich regions compared to (a) Mo-lean regions in red (embryonic ω phase) and (b) Al-lean regions in blue (isothermal ω phase) and Ti-lean regions in pink (α phase). A close-up region of (b) is shown in (c) and (d) highlighting the Al-lean and Ti-lean regions in (c) and the same Al-lean regions along with the O-rich regions in (d). The concentration profile in (e) was made using Arrow 1 in (c), and the profile in (f) was made using Arrow 2 in (c).

Furthermore, conclusions about O's role in α phase nucleation have led to debate on O's significance in ω-assisted α nucleation. While O increases the range of α phase stability in Ti alloys [7], it also suppresses the formation of ω_{iso}. O suppresses ω_{iso} by pinning the linear defects that initiate the $(1\,1\,1)_\beta$ plane collapse [46] and/or by increasing the relative energy of the ω phase and the energy barrier for the β-to-ω transition [129]. Therefore, Li et al.'s [47] analysis that O-rich regions were near the ω phase, and that those O-rich regions could drive α-phase nucleation, was novel. Li et al.'s [47] claims are supported by Coakley et al.'s [130] results of a 27% higher

concentration of O at the ω/β boundary compared to the β matrix. O-rich regions have also been found near Mo-lean embryonic ω particles [93], and Coakley et al. [99] observed O-enrichment at the ω/β boundary starting after 1 h of 300°C heat treatment of Ti-5Al-5Mo-5V-3Cr. Within ω-phase particles, Niinomi et al. [106] have found a higher concentration of O than in the surrounding β matrix, although the association between O, the ω phase, and the α phase was not reported. Contradictory to those results, Zheng et al. [9, 49, 107] did not find a significant difference in O concentration moving from the β phase to the ω phase. Instead, compositional differences of the other alloying elements and strains at the ω/β boundary are presented as the driving force by these studies.

The differing results about O's role in α phase formation, along with the differing results about the composition of athermal and incommensurate ω_{iso} phase outlined above, could be because of the varying alloy compositions used by the different studies and lack of worldwide standardized approaches for APT data analysis procedures, especially when it comes to analyzing minor impurity element concentrations. Comparing the alloys used in 22 studies by Mo-Eq, 15 different Mo-Eq's were investigated as shown in 2.3. It is clear that comparisons of mechanisms are not usually made between alloys with similar Mo-Eq's. For example, Ahmed et al. [57] compared their ω_{ath} composition results from a Ti-5Al-5Mo-5V-2Cr-1Fe (Mo-Eq of 9.45) alloy to Devaraj et al.'s [39] results for a Ti-18Mo alloy (Mo-Eq of 18). Along with different Mo-Eq's, Ahmed et al.'s [57] alloy is more complex than the binary Ti-18Mo alloy. Stabilizer types are not consistent either, with some studies using alloys of four or more alloying elements of isomorphous- and eutectoid-type stabilizers, while others use binary isomorphous systems.

Table 2.3: Molybdenum equivalencies of alloys used in APT studies.

Alloy	**Mo-Eq**	**Reference**
Ti-1Al-8V-5Fe	18.86	[4]
Ti-18Mo	18	[39, 60, 86, 105, 107]
Ti-6Cr-5Mo-5V-4Al	13.95	[10, 43, 47, 93]
Ti-20V	13.4	[49]
Ti-18Mo-5Al	13	[107]
Ti-5Al-5Mo-5V-3Cr-0.5Fe	12.8	[131]
Ti-12Mo	12	[86]
Ti-10V-6Cu	11.3	[85]
Ti-38Nb-2Ta-3Zr	11.08	[96]
Ti-29Nb-13Ta-4.6Zr	10.98	[106]
Ti-24Nb-3Mo-3Zr-2Sn	9.72	[132]
Ti-5Al-5Mo-5V-2Cr-1Fe	9.45	[67, 133]
Ti-5Al-5Mo-5V-3Cr	8.15	[9, 95, 99]
Ti-24Nb-4Zr-8Sn	6.72	[134–137]
Ti-6Al-4V	−3.32	[61]

Along with alloy composition, the APT experimental procedure can affect the reported compositions and spatial accuracy of APT results. Coakley et al. [130] have addressed this by comparing their results to those of Li et al. [43], explaining how higher sample temperatures and laser energies make quantitative concentration analysis more difficult and increase the potential for surface diffusion, which affects spatial accuracy. Other studies, however, have not addressed how experimental procedures can affect results. This can be seen in Ahmed et al.'s [57] comparison to Devaraj et al.'s [39] work; Ahmed et al. [57] did not mention that they used pulsed-laser-assisted APT and that Devaraj et al.'s [39] work used pulsed-voltage APT. In APT studies of the ω phase, the biggest differences in experimental procedure are the pulsing mode (pulsed laser vs. pulsed voltage), operating temperature, and laser pulse energies. The APT experimental parameters used for a selection of ω phase studies in β-Ti alloys are shown in Table 2.4. Unfortunately, not all settings are reported in the literature for pulsed-laser-assisted APT.

Table 2.4: Experimental procedure settings used for 16 different APT studies of the ω phase.

APT mode	Operating temperature (K)	Evaporation rate	Voltage pulse fraction	Laser wavelength (nm)	Pulse rate (kHz)	Pulse energy (pJ)	Laser spot size (μm)	Reference
Voltage	60	0.2-1.0%	20%					[9, 49]
Voltage	60	0.5-0.7%	20%					[107]
Voltage	70	0.2-1.0%	20%					[39, 60, 85, 105]
Voltage	70	0.2-1.0%	30%					[131]
Voltage	80	0.5-0.8%	10%					[106]
Laser	60		0.005 ions/pulse	355		20		[4]
Laser	50		0.005 ions/pulse	355	250	70	2	[67]
Laser	50		0.005 ions/pulse		250	70	2	[43]
Laser	50		0.005 ions/pulse			80		[10]
Laser	50					80		[47, 93]
Laser	40			355		50		[95]
Laser	40			512		200		[95]

Both voltage pulsing and laser pulsing of APT have been used to analyze β-Ti alloys. In both voltage and laser modes, higher specimen temperatures or higher laser energies can provide better yield but poorer spatial resolution as a result of surface migration. Coakley et al. [99] found that higher laser pulse energies reduced the volume fraction of the ω phase that is identified in a sample, as shown in Figure 2.7. Coakley et al. [99] have also found that laser direction can influence detection of the ω phase in Ti samples, with ω-phase particles on the same side as the laser being more difficult to detect.

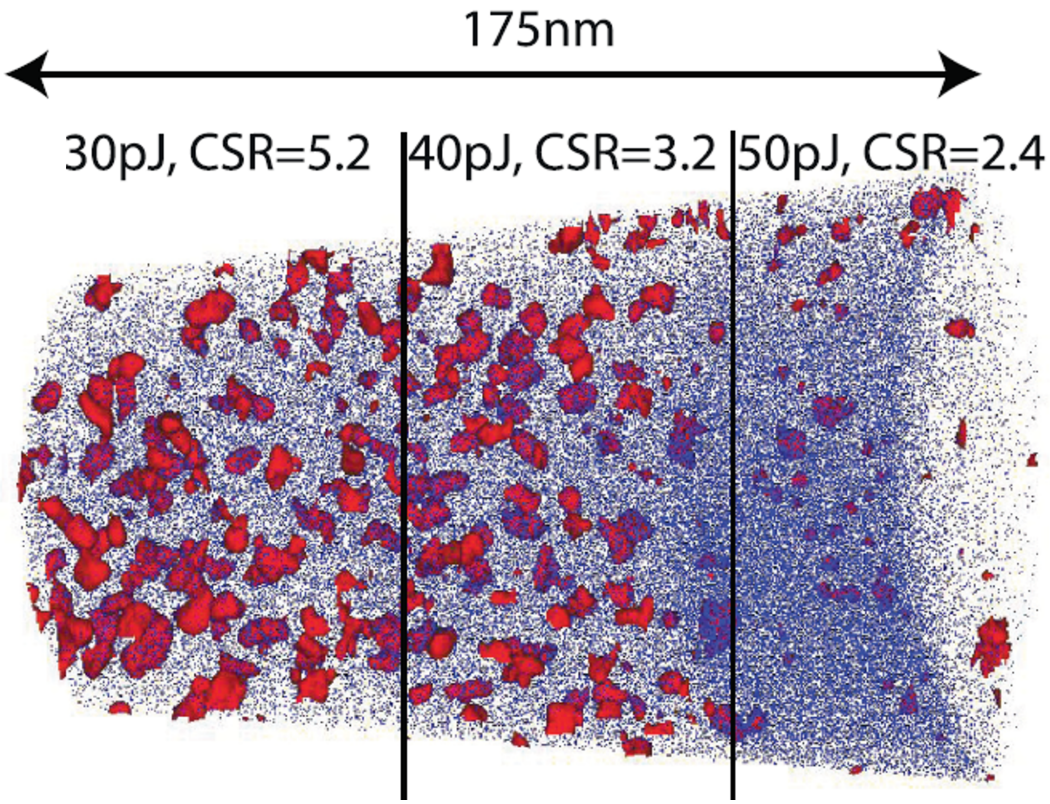

Figure 2.7: An APT sample reconstruction showing how laser energy affects the detection of the ω phase in β-Ti alloys. Adopted from J. Coakley, A. Radecka, D. Dye, P. A. Bagot, T. L. Martin, T. J. Prosa, Y. Chen, H. J. Stone, D. N. Seidman and D. Isheim, "Characterizing nanoscale precipitation in a titanium alloy by laser-assisted atom probe tomography," Materials Characterization, vol. 141, pp. 129–138, 2018.

Finally, when it comes to using APT to analyze the composition of ω , β, and α phases, the procedure selected for ranging the mass-to-charge spectra peaks of minor impurity elements such as O can induce a significant amount of statistical variability. For example, the O^{1+} peak at 16 Da can overlap with the Ti^{3+} peak, requiring a detailed peak deconvolution. TiO molecular peaks are often minor and may not be indexed if the mass-to-charge spectra ranging is not conducted using a log scale for the counts. Such variability in data analysis procedures must be accounted for to facilitate accurate interpretation of the roles of minor impurity elements such as O in key phase transformation mechanisms in alloys.

Thus, the different alloy compositions, variabilities in APT experimental parameters used, and APT mass-to-charge spectra ranging procedures used in the research for ω-phase transformation

Table 2.5: The Young's modulus (E) and shear modulus (G) of the ω and β phases.

Phase	Temperature	E_{iso} (GPa)	G_{iso} (GPa)	Reference
ω (simulation)	0	155	61	[77]
ω (polycrystalline)	RT	152.8±0.6	60.1±0.3	[77]
β	1293 K	65	23	[140]
β (as-quenched)	RT	78-103	34-43	[8]
β (aged)	RT	100-124	40.7-43.3	[8]

in β-Ti alloys can make it difficult to conclusively use only the current body of work to resolve the debates around the ω-phase transformation.

2.4.5 Effect of the ω phase on mechanical properties

A single crystal of ω phase is difficult to grow without high pressures, so the mechanical properties of a single crystalline ω phase have been determined using simulations and polycrystalline material. Tane et al. [77] used HPT to create a polycrystalline ω microstructure to determine the mechanical properties of the ω phase because the elastic tensor was calculated using simulations but had never been verified experimentally. The ω phase was anisotropic, with the $\langle 0\,0\,0\,1 \rangle$ direction modulus equal to 201 ± 7.4 GPa and the $\langle 1\,1\,\bar{2}\,0 \rangle$ direction modulus being 70 GPa lower at 129 ± 3.9 GPa [77]. The experimental ω-phase elastic tensor agreed well with the simulated elastic tensor calculated using the tight-binding model [138] (shown in Table 2.5), and an experimental isotropic elastic modulus was calculated to compare to the β phase [77]. The experimental and calculated ω-phase shear moduli (G) also agree with the ω-phase G values calculated for pure Ti by Salloom et al. [139]. While direct comparison to pure Ti with the BCC structure at RT is not possible, the β values at 1293 K are included. Also included are a range of property values compiled from multiple β alloys (β III, β C, Ti-1023, Ti-13V-11Cr-3Al, Ti-15V-3Cr-3Al-3Sn, Ti-8Mo-8V-2Fe-3Al, Ti-15Mo-5Zr, Ti-15Mo-5Zr-3Al, Ti-8V-5Fe-1Al, and Ti-16V-2.5Al) at RT, both as-quenched and aged, since processing can significantly affect the mechanical properties of β alloys. More detail on aging treatments and corresponding modulus values for specific alloys can be found in the Materials Properties Handbook: Titanium Alloys [8].

While it is difficult to compare these moduli because of the variability in temperatures, the experimental ω phase Young's modulus (E) is approximately 30 GPa higher than the highest E reached for β-Ti alloys, and the shear modulus (G) is approximately 17 GPa higher than the highest β-Ti G. Therefore, the E and G values of the ω phase should contribute to an increase in the E of β-Ti alloys when the ω phase is present. Hsu et al. [141] and Ho et al. [142] have observed this, recording increases in the bending elastic modulus of ~35 GPa and ~20–40 GPa, respectively. Coakley et al. [99] and Hsu et al. [109] also report an E increase as indicated by the increase in slope in the elastic region of their tensile and bending tests, given in Figure 2.8 [142]. However, this apparent increase is not observed for athermal ω microstructures. ω_{ath} tends to be neglected in studies on the mechanical influence of the ω phase because it is generally thought not to affect the mechanical properties of β-Ti alloys [8, 25, 40]. Unfortunately, because ω_{ath} cannot be prevented during quenching of metastable or near-β alloys without changing the alloy composition to stabilize the β phase [45, 143], the mechanical properties of β alloys with and without ω_{ath} (such as Ti-15Mo with ω_{ath} and Ti-15Mo without ω_{ath}) cannot be compared [40]. It is possible that ω_{ath} does affect mechanical properties—one study by Ho [143] reports an increase in microhardness from 263 Hv to 337 Hv associated with the presence of ω_{ath}. No extensive studies on the mechanical effects of the incommensurate ω phase have been done so far.

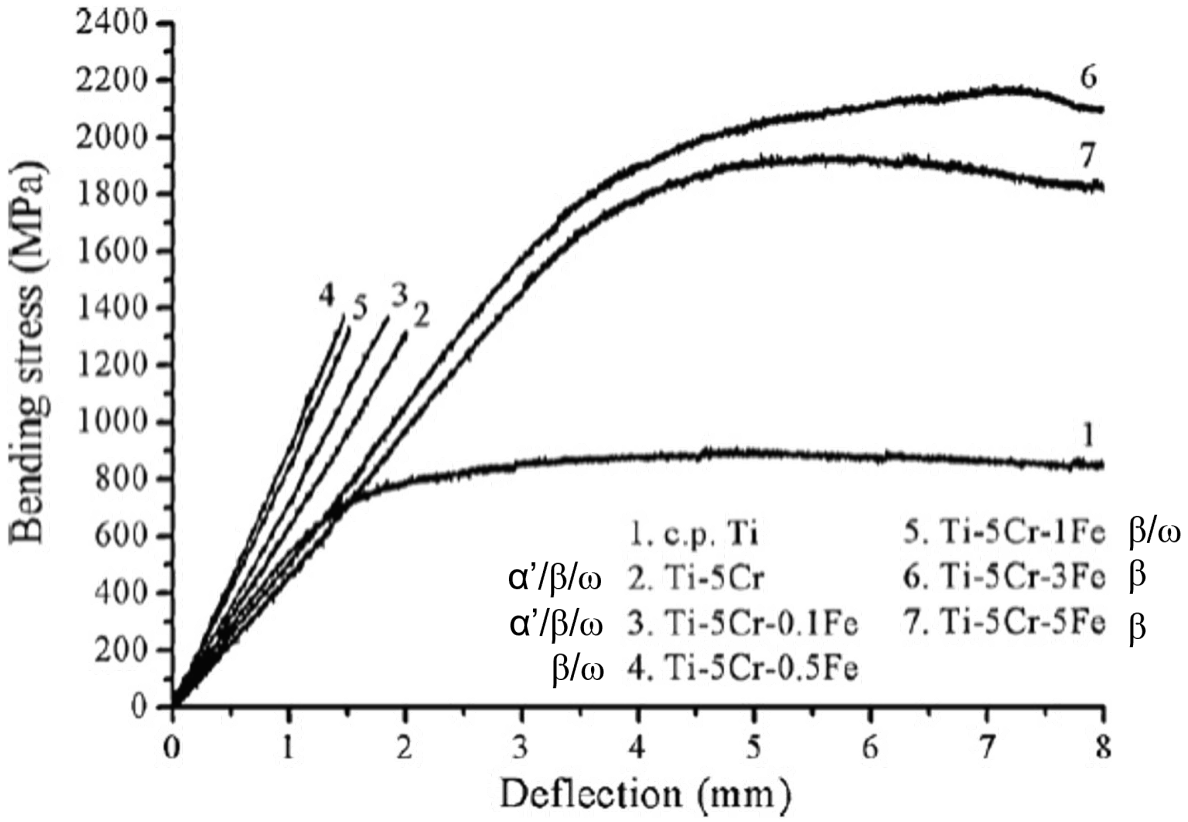

Figure 2.8: Bending test results showing the elastic modulus increase in β-Ti with ω-phase microstructures. Adopted from Ho, W.-F., Pan, C.-H., Wu, S.-C., et al. "Mechanical properties and deformation behavior of Ti–5Cr–xFe alloys," Journal of Alloys and Compounds, V. 472, Nos. 1–2, 2009, pp. 546–50.

The ω phase also increases the microhardness of β-Ti alloys. Multiple studies have reported an increase in microhardness after precipitation of the isothermal ω phase, regardless of alloy composition [88, 90, 99, 101, 109, 115, 141, 144–147]. Although Jones et al. [25] attribute the microhardness increase to precipitation of the nanoscale α phase, Coakley et al. [88] counter that the observed hardness increase from 280 Hv to 400 Hv was due to the rapid precipitation of ω_{iso} during a 400°C heat treatment. ω phase microstructures have also exhibited higher microhardness than martensitic α" microstructures by approximately 100 Hv [109], although the hardness of α" martensite is not wholly intrinsic and is partly due to sliding interfaces. Hida et al. [90] found that hardness increased with precipitation of the commensurate ω phase, as shown in Figure 2.9. The results in Figure 2.9 also support the assumption stated above that the incommensurate ω phase

does not affect the mechanical properties of β alloys because the incommensurate ω phase did not appear to affect microhardness [90]. Figure 2.9 is also a typical example of the scale of hardness increase, as most hardness values were reported to start around 300 Hv and increase to 400–550 Hv [88, 90, 101, 109, 141, 145–147].

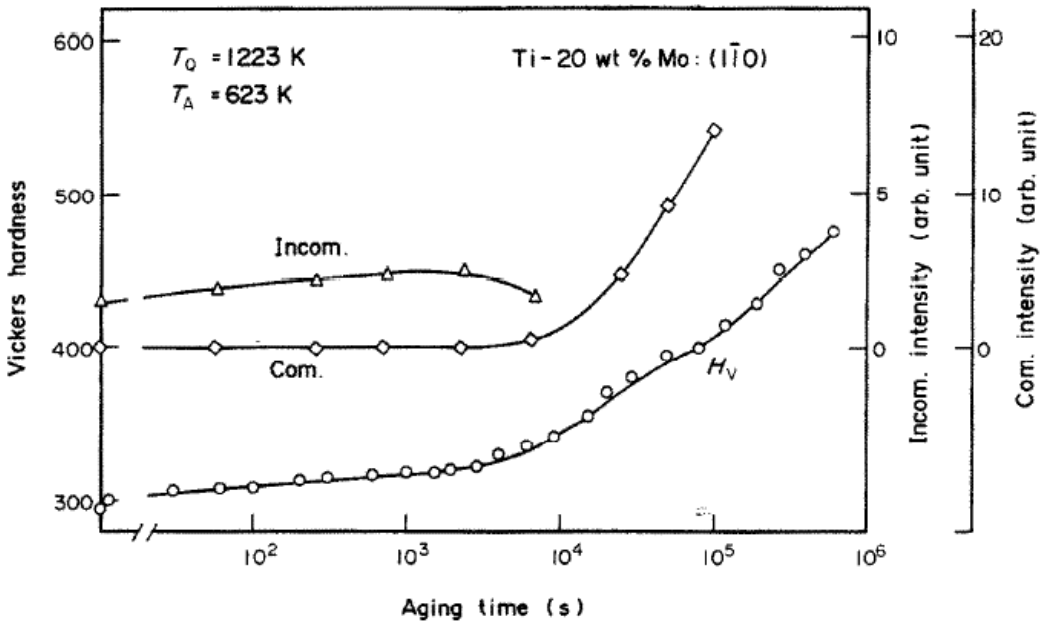

Figure 2.9: The effects of incommensurate and commensurate ω phases on the microhardness of a Ti-20Mo alloy. Adapted from M. Hida, E. Sukedai and H. Terauchi, "Microscopic approaches to isothermal transformation of incommensurate ω phase zones in Ti-20wt%Mo alloy studied by XDS, HREM and EXAFS," Acta Metallurgica, vol. 36, no. 6, pp. 1429–1441, 1988.

The ω-phase microstructure also increases the tensile strength of alloys. Chandrasekaran et al. [148] found that precipitating ω_{iso} in a Ti-15Cr (at.%) alloy increased the yield strength (σ_y) of the alloy by ~186 MPa, and Mantri et al. [119] found that ω_{iso} precipitation increased the ultimate tensile strength (UTS) of Ti-12Mo by ~525 MPa. Feeney and Blackburn [149] found that β + ω microstructures in a Ti-11.5Mo-6Zr-4.5Sn alloy exhibited strengths up to 1500 MPa. Williams et al. [150] found that the yield stress σ_y of Ti-10Mo (at.%), Ti-25V (at.%), Ti-8Mn (at.%), and β III alloys increased when the ω phase was present and decreased when the α phase became the dominant phase. Alloys that deform via the ω-phase transformation also exhibit higher σ_y than alloys that deform via twins [68].

The increase in elastic modulus and tensile strength due to the ω phase is accompanied by embrittlement. In tension, embrittlement is shown by a decrease in ϵ_f when ω microstructures are present, as Zhao et al. [48], Mantri et al. [119], Williams et al. [150], and Feeney and Blackburn [149] documented in alloys that had precipitated the isothermal ω phase. The decrease can be seen the most clearly in the Ti-18V alloy used by Zhao et al. [48] in Table 2.6 and is also demonstrated by the drop in ϵ_f from ~35% to < 5% with ω_{iso} precipitation in the Ti-12Mo alloy used by Mantri et al. [119]. Li et al. [100] has shown that ϵ_f in tensile deformation varies with ω_{iso}, with higher ω_{iso} volume fractions corresponding to lower elongation to failure values. A drop in ϵ_f from 6.1% to ~1.7% in a Ti-24Nb-4Zr-8Sn alloy was associated with the presence of isothermal ω-phase microstructures [144]. Chandrasekaran et al. [58] also observed a drop in ϵ_f from 17% to 2% when ω_{iso} was precipitated. When the ω phase was removed from the β matrix using heat treatments, the ϵ_f increased from 2% to 6% [148]. These embrittling effects are only true for ω_{iso} microstructures because ω_{ath} does not embrittle alloys as does ω_{iso}; Wang et al. [151] and Sun et al. [118] observed no embrittling effects in binary Ti-Mo alloys. Chandrasekaran et al. [148] have also found that ω_{ath} microstructures reach an ϵ_f of 13%, while ω_{iso} microstructures reached 2%. Salloom et al. suggest that the embrittling effects of ω_{iso} are due to the increase in shear modulus (G) as the ω_{iso} precipitates become more Ti-rich, making them less plastically deformable and more embrittling [139].

Table 2.6: The strengths and ϵ_f of the β and β+ω microstructures [48].

Alloy	**Microstructure**	**Approximate σ_y (MPa)**	**Approximate UTS (MPa)**	**Approximate ϵ_f (%)**
Ti-18V	β+ω_{ath}	730	830	28
Ti-18V	β+ω_{ath}+deformation ω	750	1080	6
Ti-20V	β+ω_{ath}	880	910	17
Ti-20V	β+ω_{ath}+deformation ω	900	1050	10
Ti-22V	β	910	900	11
Ti-22V	β+deformation ω	950	980	10

Bending tests also illuminate the embrittling effects of the ω phase. Hsu et al. [109] and Ho et al. [142] found that alloys with ω-phase microstructures fractured during bending at significantly lower deflections than alloys containing the ω + α or no ω phase microstructures. This can be seen in the low deflections at the fracture of ω-phase microstructures (Alloys 2–5) in Figure 2.8, compared to Alloys 1, 6, and 7, which completed the bending test without fracture [142]. Cleavage facets were found on the fracture surfaces of the ω-phase microstructures [109, 142], which are characteristic of decreased ϵ_f.

The embrittling effects of the ω phase are thought to be because dislocations stop or bend around ω particles, leaving high dislocation densities in the β matrix [150]. When dislocations do move through the ω phase, they shear the ω phase, creating slip bands that can lead to crack nucleation at low macroscopic strains [152], as shown in Figure 2.10. Recently, Lai et al. [96] have shown that high densities of nanometer-sized (~1.23 nm) ω phases suppress TWIP and TRIP effects. TWIP and TRIP deformations have been shown to lead to a desirable balance of strength and ϵ_f in β alloys [153], and the ω phase suppression of these effects leads to localized plasticity in dislocation channels and reduction of ϵ_f values [96]. Sun et al. [118] have used low heat-treatment temperatures and 60 second heat treatment times to avoid embrittlement while strengthening their Ti-12Mo alloy through precipitation of ω_{iso}. Their study pointed to diffusion being another cause of embrittlement because the processing route was meant to precipitate ω_{iso} without allowing significant diffusion between the ω and β phases [118]. When diffusion did not occur, strengthening of the alloy from ω_{iso} was achieved but the true strain at fracture was still over 40%. When diffusion occurred, the tensile strength of the alloys was observed to be highest, but the embrittling effects were also seen manifested by the reduction of true strain at fracture to ~3% [118].

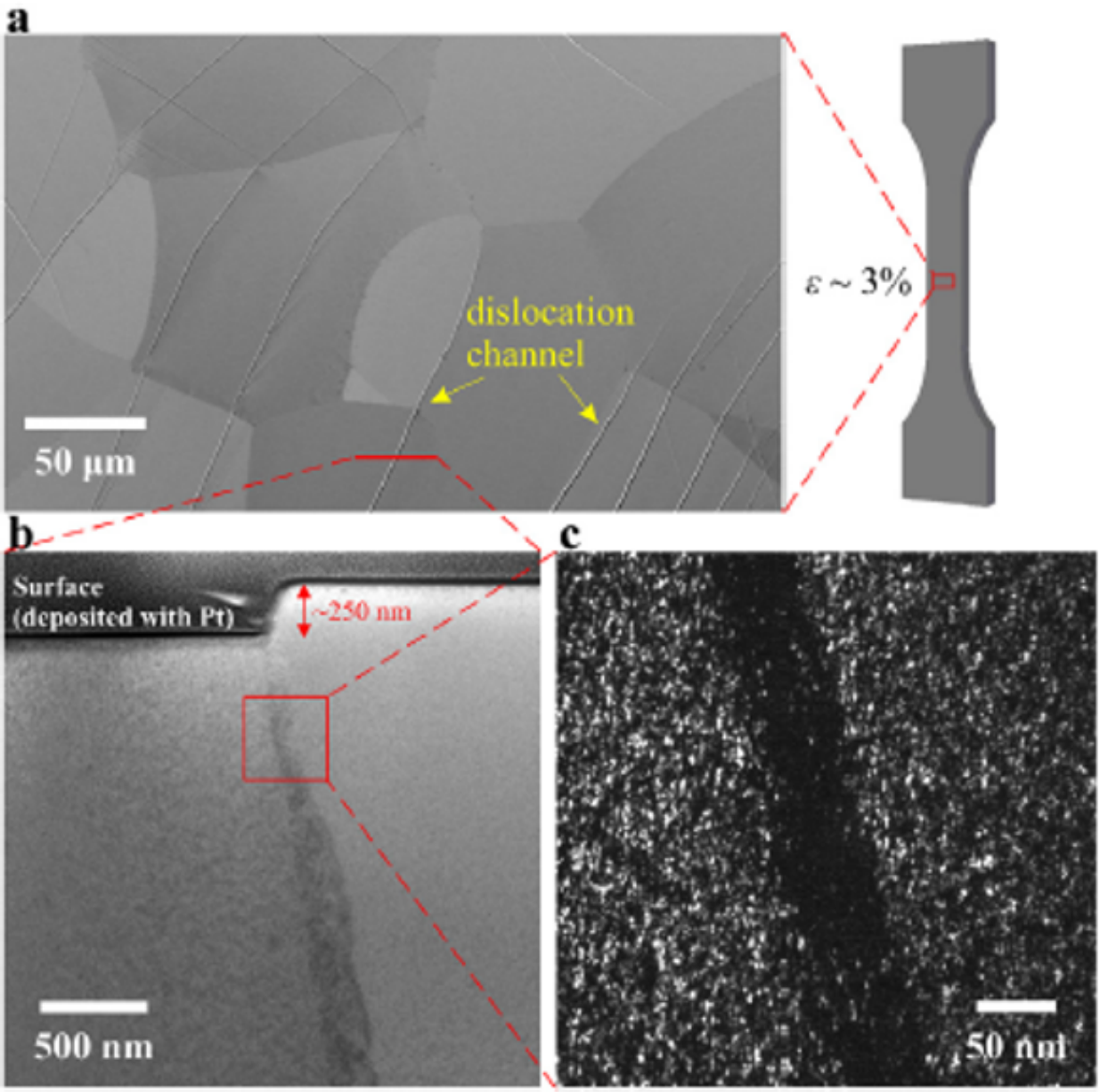

Figure 2.10: TEM micrographs of deformed β alloys showing dislocation channels that are ω-phase free. Adapted from M.J. Lai, T. Li, and D. Raabe, "ω phase acts as a switch between dislocation channeling and joint twinning- and transformation-induced plasticity in a metastable β titanium alloy," *Acta Materialia*, vol. 151, pp. 67–77, 2018.

Because the ω phase allows crack nucleation at low macroscopic strains, it can be detrimental to fatigue properties [152]. However, ω_{iso} microstructures have been found to retard fatigue crack propagation significantly more than α-phase microstructures [154]. Nakai et al. [146] have also found that the maximum cycle stress of their TNTZ alloy increased by ~200 MPa after precipitation

of the ω phase through a combination of cold-rolling and aging. In Feeney and Blackburn's [149] study, the fracture toughness of the β-Ti alloy was independent of ω particle size once the particles were larger than ~10 nm.

Although crack nucleation and embrittlement are reasons why processing routes and alloy compositions are designed to avoid precipitation of the ω phase, ω-assisted α-phase microstructures have attractive mechanical properties. The ω phase can also influence the mechanical properties of β alloys by preventing the formation of the martensitic α" phase [35, 41], which is detrimental to the formability of β alloys [155].

The tensile behavior of β alloys is heavily affected by the size, morphology, and distribution of α-phase particles in the β matrix, and fine-grained α-phase microstructures have exhibited high strengths with higher ϵ_f than ω-phase microstructures [27]. Azimzadeh and Rack [97] found that the hardness of a Ti-6.8Mo-4.5Fe-1.5Al alloy (TIMET LCB alloy) was highest with a combination ω phase and α phase microstructures. Hsu et al. [109] and Ho et al. [142] found that alloys with ω + α phase microstructures could withstand more deflection before fracture in bending tests than alloys with only ω-phase microstructures. ω-assisted α-phase microstructures have been found to be weaker than ω_{iso} microstructures, as Williams et al. [150] showed when the σ_y of Ti-10Mo (at.%) dropped by ~275 MPa with precipitation of the α phase; however, the strength was still relatively high at ~965 MPa, and the ϵ_f increased from 6% to 8%. The mechanical property benefits of the ω-assisted α phase are driving research of processing routes that encourage ω_{iso} to form the ω-assisted α phase [9, 10, 49, 57, 59, 125].

2.5 The novel Ti-Cr-Fe-Al alloy system

As stated in Section 2.2, the use of β-Ti alloys in commercial applications is limited due to its higher cost in comparison to cheaper steel and Al alloys [13, 15]. Low-cost alloying elements, which can be substituted for the relatively expensive and commonly used vanadium (V), niobium (Nb), and molybdenum (Mo), can help reduce the costs associated with β-Ti alloys and expand their commercial applications [2]. Out of the elements that can be alloyed with Ti to create a β-Ti

alloying elements Cr, Fe, and Al are all low-cost options. Cr and Fe are both lower-cost options to Mo or V, and stabilize the β phase more than Mo or V, requiring less Cr and Fe to be used to achieve the same β stability [17]. Al is a common low-cost α-stabilizer already used in alloys like Ti-6Al-4V to promote α-phase formation.

Cr and Fe are both eutectoid-type β-stabilizers [17], and are known to affect the mechanical properties of β-Ti alloys as well as the β-to-ω phase transformation. Increasing the concentration of the β-eutectoid element Cr in binary Ti-Cr alloys affects E, σ_y, and UTS through solution strengthening and athermal ω-phase formation [156]. Binary Ti-Cr alloys can also exhibit 5% of the isothermal ω phase after short heating times (15 minutes) at 400 °C [157]. The eutectoid β-stabilizer Fe can affect ω-phase formation by altering the β-phase lattice parameter [74]. However, Fe exhibits a strong stabilizing effect on the β phase and promotes the ω-to-β phase transformation [17, 158, 159]. Fe is also thought to inhibit the α-phase transformation by preventing long-range diffusion of the β-stabilizing elements needed to undergo the β-to-α transformation [160]. The α-stabilizer Al suppresses the athermal ω phase [161] and provides solid solution strengthening for the α phase [2].

To understand the effects of how low-cost β-stabilizing and α-stabilizing alloying elements affect the β-to-ω and β-to-α transformations, the novel Ti-Cr-Fe-Al alloy system was created for this work.

Fe and Al were added to a base Ti-Cr alloy to determine their individual and synergistic effects on the phase transformations. A 400 °C aging treatment was also chosen since it is within the 300 °C to 500 °C range of stability for the ω phase [10, 41–43, 47, 49, 50, 56, 58, 93, 98–101], and an aging range of 0 to 24 h was chosen to allow precipitation of the ω and α phases.

2.6 Research gaps

After the above review of β-Ti alloys and their phase transformations, and the review of how the alloying elements Cr, Fe, and Al affect the physical metallurgy of β-Ti alloys, the following research gaps were identified:

1. How do the β- and α-phase stabilizers affect the microstructure and mechanical properties of the Ti-Cr alloy system after a β-homogenization treatment?

2. How do the β- and α-phase stabilizers affect the microstructural evolution during the phase transformations in the Ti-Cr alloy system?

3. Where do such alloying elements (and interstitials) diffuse and how do they affect the phase transformations?

4. How do the microstructural changes during the phase transformations affect the mechanical properties of the Ti-Cr alloy system?

Understanding these research gaps can aid alloy and processing route design in β-Ti alloys. Such understanding may be applicable to other materials that transform from the BCC structure to other structures.

To investigate these research gaps, a baseline alloy containing nominally 12wt.% (11at.%) Cr was chosen. Fe was the model β-stabilizer used in this study, at 1wt.% (0.85at.%) nominally. Cr and Fe are both eutectoid-type β-stabilizers. Al was the model α-stabilizer used in this study, at 3wt.% (5.3at.%) nominally. All transformations were induced by a 400 °C treatment.

2.6.1 Research gap 1: how do the β- and α-phase stabilizers affect the microstructure and mechanical properties of the Ti-Cr alloy system after a β-homogenization treatment?

Determining whether the small alloying additions of 0.85% Fe and 5.3% Al caused changes to the microstructure and mechanical properties of the Ti-Cr system after undergoing a β-homogenization treatment is important for understanding how alloying element additions affect the β-phase microstructure in β-Ti alloys. As the β-phase microstructure can affect the subsequent phase transformations, understanding the β-homogenized microstructure before the 400 °C treatment was also critical for understanding the phase transformations and microstructural evolution detailed in Chapter 6.

As each alloy underwent the same levitation melting, hot forging, homogenization annealing, and quenching processes, it was reasonable to assume that the microstructure of each alloy would be similar. Also, the β-phase lattice parameters (a_β) of each alloy were expected to be less than those for pure Ti, as a_β has been shown to decrease with increasing Cr content [162]. Similarly, since each alloy contained similar Cr contents, the lattice parameters of each alloy were not expected to differ significantly. Thus, the following hypotheses about the β-homogenized microstructures of the Ti-Cr alloy system were made:

- The alloys were fully β-homogenized. If the α phase was present, it would appear at the grain boundaries due to greater diffusion rates at the boundaries.
- The alloys would possess similar grain sizes.
- The alloying elements would be randomly distributed in the microstructure.
- The alloys' β-phase lattice parameters would be less than that of pure Ti.
- The small additions of Fe and Al would not affect the β-phase lattice parameters significantly.

Investigating these predictions was important since any α phase in the microstructure would increase the strength, moduli, and hardness of the material compared to a fully β-homogenized microstructure, and areas of compositional variation could affect the β-to-ω and β-to-α transformations during the 400 °C treatment. Different lattice parameters in each alloy could also affect the β-to-ω and β-to-α transformations as well as the ω-assisted α-phase transformation, since different a_β values could affect the strain at the ω/β boundary.

To test these hypotheses, diffraction was necessary to determine the phases present in the microstructure and to determine the lattice parameters. XRD was chosen, as XRD could measure a larger volume of material than other diffraction techniques, such as TEM selected area diffraction or EBSD. However, if the α phase was present in volumes of less than 5 mass%, XRD would not be able to detect it [163], so BSE SEM imaging was chosen to supplement the XRD measurements. BSE SEM imaging would be able to view the β-stabilizer lean α phase because BSE imaging is

sensitive to atomic number, and thus the α phase and β phases would have a contrast difference. APT was chosen to measure the compositions of each alloy, as the sub-nanometer resolution of the technique would be able to determine whether the alloying elements were randomly distributed within the microstructure or whether nanoscale compositional variation existed. The resolution of APT could also determine whether there was local ordering of the alloying elements, which could affect the transformations or mechanical properties.

Assuming that each alloy exhibited similar β-phase microstructures after the β-homogenization process, no significant differences between the hardness, σ_y, UTS, ϵ_f values, and fracture mechanisms of each alloy were predicted. To test this hypothesis, Vickers microhardness and Rockwell B hardness were used to determine the hardness values of each alloy, and tensile testing was used to determine the σ_y, UTS, and ϵ_f values of each alloy. After tensile testing, the fracture surface of each alloy was investigated using SE SEM imaging to determine the fracture mechanism. It was expected that each alloy would experience ductile fracture, as the β phase is the most ductile phase in Ti. Unlike the hardness, σ_y, UTS, ϵ_f values, and fracture mechanisms, the elastic moduli of the alloys were expected to change with the Fe and Al additions. Considering that the Bo values of Ti, Cr, Fe, and Al in BCC Ti were 2.790, 2.779, 2.651, and 2.426, respectively, adding Fe and Al should reduce the bond strengths in the Ti-Cr alloys [164]. Reducing the bond strengths in the Ti-Cr alloys should reduce the E and G values of the alloys as well. Overall, the following hypotheses regarding the mechanical properties were proposed:

- The alloying element additions will not significantly affect the hardness, σ_y, UTS, ϵ_f values, or fracture mechanisms of the alloys.
- The 0.85% Fe addition will reduce the bond strengths and moduli in TCF compared to TC.
- The 5.3% Al addition will reduce the bond strengths in TCA more than the 0.85% Fe addition in TCF, and TCA will exhibit lower moduli than TCF.
- Adding both Fe and Al will reduce the bond strengths in TCFA the most, and TCFA will exhibit the lowest moduli of TC, TCF, and TCA.

These hypotheses could be tested using tensile testing to determine the E of each alloy and RUS testing to determine the G of each alloy.

By utilizing XRD, SEM, APT, hardness, tensile, and RUS testing, the effect of Fe and Al additions on the microstructure and mechanical properties of the Ti-Cr alloy system could be investigated.

2.6.2 Research gap 2: how do the β- and α-phase stabilizers affect the microstructural evolution during the phase transformations in the Ti-Cr alloy system?

The question of how the β- and α-stabilizers affect the microstructural evolution during the phase transformations in the Ti-Cr alloy system is very broad. The β-stabilizer Fe and the α-stabilizer Al have the potential to affect which phase transformations occur during the 400 °C treatment. The ω and α phases are known to affect the strength, ϵ_f, and moduli of β-Ti alloys. The volume fraction of each phase can also affect the strength, ϵ_f, and moduli, as phase volume fraction and mechanical properties are related and can be predicted using techniques such as the rule of mixtures (ROM). The composition of each phase can also affect the phase lattice parameters. Lattice parameters can affect interfacial strain between phases, phase misfit, and transformations such as the ω-assisted α-phase transformation. Thus, the question of how the alloying elements affect the microstructural evolution during the phase transformations was narrowed to two specific questions:

1. How do the phase volume fractions change?
2. How do the phase lattice parameters change?

Since Fe is the strongest β-stabilizing element in the Mo-Eq, and since Al is an α-stabilizer, the following effects of Fe and Al on the phase volume fractions were hypothesized:

- Fe would suppress α- and ω-phase formation, therefore lower α-and ω-phase volume fractions would be expected in the Fe-containing alloys.
- The α-phase stabilizer Al would promote α-phase formation, and higher α-phase volume fractions would be expected in the Al-containing alloys.

To test these hypotheses, diffraction was needed to determine the phase transformations that occurred in each alloy. 400 °C XRD was chosen to investigate the phase transformations in the bulk material. The in-situ measurements allowed the phase transformations to be determined as they occurred at 400 °C. To evaluate the phase volume fractions, Rietveld analysis and threshold analysis were used. Rietveld analysis is a technique that can deconvolute the individual contributions from each phase towards the measured XRD profile. This deconvolution allows the volume fraction of each phase to be calculated, and applying the Rietveld analysis technique to the 400 °C XRD profiles would determine the volume fractions of each phase as the transformations occurred. Threshold analysis is a technique which determines what fraction of a darker contrast phase is present in a BSE SEM image. By setting a threshold contrast value, summing the pixels in the image that are darker than the set value, and dividing that sum by the total pictures in the image, the fraction of the darker precipitates in the image is determined. Both techniques have benefits and limitations towards calculating accurate volume fractions.

One strength of Rietveld analysis is that it can determine the volume fractions of individual phases. The volume fractions calculated using Rietveld analysis are also bulk measurements, as a larger volume of material is measured using XRD than can be measured using other techniques. However, overlapping or broad peaks in the XRD profile can decrease the accuracy of the analysis. Compared to Rietveld analysis, threshold analysis has more limitations, such as providing local measurements, with many images needed to achieve a statistically significant result for the bulk material. Also, if the contrast of two or more phases is similar, the threshold analysis cannot distinguish between the phases. Contrast differences between β-phase grain could also affect the accuracy of the measurement. Finally, threshold analysis is a 2D area measurements that can be used to estimate the fraction of phases in a 3D volume. The benefit of threshold analysis over Rietveld analysis is that the spatial distribution and morphology of the precipitate volume fractions can be determined, i.e., it can be used to determine whether the precipitates form mainly along grain boundaries, whether the volume fractions are coming from a few large precipitates or many small precipitates, and whether the precipitates are randomly distributed throughout the β grains.

To balance the benefits and limitations of each technique, Rietveld analysis was used to calculate the volume fractions of the individual phases, and threshold analysis was used to verify the Rietveld analysis and provide more information about the size, morphology, and distribution of the phases within the microstructure through the BSE SEM images. To determine the phase transformations and volume fractions, XRD measurements were taken every 0.5 h during the 12 h 400 °C treatment. BSE SEM images were taken after 0.75, 1.5, 3, and 6 h of treatment. The measurement times and relationships are provided in Figure 2.11 at the end of this section.

While the phase transformations occurred in each alloy, the alloying elements were expected to diffuse. This diffusion could affect the phase lattice parameters, as the a_β of binary β alloys tend to decrease with increasing β-stabilizer content [162, 165, 166]. The change in lattice parameters of all three phases during the β-to-ω and β-to-α transformations is not well understood. Considering the trend of binary β alloys and the radius differences between Ti and Cr, Fe, and Al, the following changes in β-, ω-, and α- phase lattice parameters were hypothesized:

- The diffusion of the β-stabilizers from the α and ω phases into the β phase would increase the stability of the β phase. The relative β-phase stability of the alloying elements would decrease the β-phase lattice parameter.

- The diffusion of the α-stabilizer Al from the β phase into the α phase would affect the lattice parameter of the α phase in the Al-containing alloys differently than the Al-free alloys.

- The rejection of all alloying elements except Ti from the ω phase would cause the ω-phase lattice parameter to remain constant throughout the transformation. The Fe and Al additions could affect the ω-phase lattice parameter, as different ω-phase lattice parameters have been reported in different compositions of β-Ti alloys.

To test these hypotheses, diffraction was needed to determine the phase transformations and calculate the phase lattice parameters during the phase transformations, and composition measurements of each phase were needed. The phase transformations and lattice parameters were investigated during the phase transformations using 400 °C XRD. Rietveld analysis was used with the 400 °C

XRD data to determine each phase's peak locations and their associated lattice parameters. To measure the compositions of the nanoscale α and ω phases, a composition measurement technique with high spatial resolution was necessary. APT, with its sub-nanometer 3D spatial resolution, was ideal for determining the phase compositions in each alloy. The evolution of the phase lattice parameters as a function of composition could be determined by combining the lattice parameter results from the Rietveld analysis with the composition results from APT. To determine the phase lattice parameters, XRD measurements were taken every 0.5 h during the 12 h 400 °C treatment. APT measurements were taken after 0.75, 1.5, 3, 6, and 12 h of treatment. The measurement times and relationships are provided in Figure 2.11.

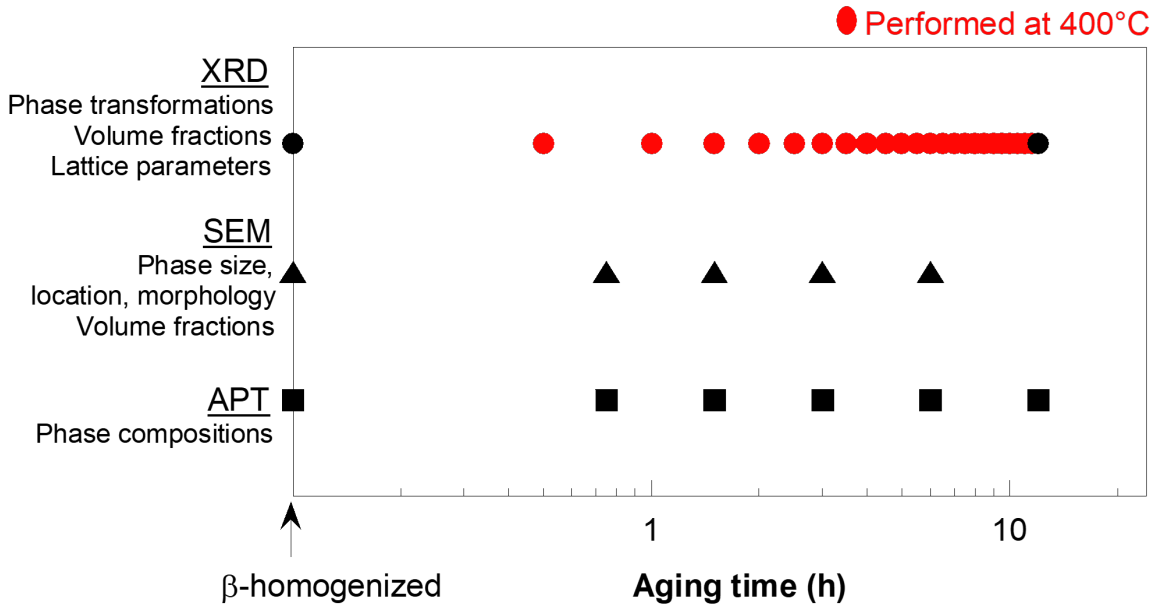

Figure 2.11: The experiment matrix detailing the length of time the alloys spent at 400 °C before each experiment.

2.6.3 Research gap 3: where do such alloying elements (and interstitials) diffuse and how do they affect the phase transformations?

Diffusion of the β-stabilizers and α-stabilizers during the phase transformations could affect the phase stability and phase lattice parameters. Phase stability could affect how likely the ω and α phases are to nucleate and grow, which could affect phase size and volume fraction. The location of

the alloying elements could also affect the where the ω and α phases precipitate, as they may prefer β-stabilizer lean volumes, and the α phase may prefer Al- or O-rich volumes. The diffusion of the β- and α-stabilizers during the phase transformations could also affect how quickly the ω and α phases nucleate and grow, as the β-to-ω and β-to-α transformations use a displacive/diffusive mechanism. These fundamental relationships between composition and microstructure can be used to understand how local diffusion is related to the transformation from the BCC to other crystal structures, and can be applied to alloy and thermomechanical treatment design to achieve desired microstructures.

Since β-stabilizers increase the stability of the β phase, α stabilizers increase the stability of the α phase, and the ω phase is known to reject all alloying elements, the alloying elements were hypothesized to diffuse in the following ways:

- The β-stabilizers Cr and Fe would diffuse from the α and ω phases into the β phase.
- The α-stabilizer Al would diffuse from the β phase into the α phase.
- The ω-phase would reject any elements except Ti.

Since the β-to-ω, β-to-α, and ω-assisted α transformations tend to form fine microstructures, APT was chosen to determine the compositions of each phase in the microstructure as it can be used to measure compositions in 3D volumes with subnanometer resolution. With its sensitivity to all elements in the periodic table, APT could also determine the location of the low atomic number impurity elements, particularly O and H, in the microstructure.

O and H occupy interstitial sites in Ti lattices, and in high enough concentrations can form oxides and hydrides with Ti [7, 167]. The impurity element O is an α-phase stabilizer, and could play an important role in the ω-assisted α-phase transformation, as explored above in Section 2.4.4. O can also promote the formation of an α-phase layer known as "α case" along the surface of β-Ti alloys. Along with changing the microstructure, interstitial O can also increase the hardness of the α phase [7]. Thus, the following hypotheses regarding were made:

- The interstitial O would be present in higher concentrations in the α phase than the other phases.
- The interstitial O would be rejected from the ω phase and cluster at the ω/β boundaries, which would promote the ω-assisted α-phase transformation.

The impurity element H is known for being detrimental to the strength and ϵ_f of β-Ti alloys through hydrogen embrittlement [167, 168]. H can affect the fracture mode of β-Ti alloys at concentrations below that needed to form hydrides in the β phase [167], thereby reducing the strength of the alloys. Thus, studies of H in β-Ti alloys are important. H can also cause complex fracture mechanisms such as hydrogen-induced decohesion in metastable β-Ti alloys with small amounts of α phase [169–171]. The ratio of the solubility of H in the β phase to the solubility of H in the α phase is 20:1 due to the higher number of interstitial sites in the BCC lattice compared to the HCP lattice [168, 172]. Because of the advantages of APT in measuring H, significant work has been done to quantify H in materials using APT [173–176]. In Ti specifically, APT has successfully measured the composition of titanium hydrides for comparison to phase diagram predictions [177]. H can be picked up in significant quantities during the FIB-based lift-out process for APT samples. The platinum (Pt) precursor, used to protect the surface of the sample during the lift-out process and to weld the sample to the microtip array for the APT experiments, was identified as a likely source of H in APT samples [178, 179]. H was hypothesized to behave in the following ways:

- The interstitial H would be present in higher concentrations in the β phase than in any other phase. If enough H was present in the sample, equilibrium hydrides would form.
- During the FIB-based lift-out process for APT samples, a higher electron-beam accelerating voltage during the decomposition of the Pt precursor would cause more gaseous H to be released, and this would result in an increase in the H concentration in the APT samples.

The diffusion of the alloying elements, and the locations of O and H in the microstructure, were investigated using APT after 0.75, 1.5, 3, 6, and 12 h of 400 °C treatment. Figure 2.11 in Section

2.6.2 above provides a graphical representation of the APT experiments, and how they relate to other microstructural characterization experiments.

2.6.4 Research gap 4: how do the microstructural changes during the phase transformations affect the mechanical properties of the Ti-Cr alloy system?

The β-to-ω and β-to-α transformations are known to increase the strength and hardness of β-Ti alloys [7]. The ω and α phases also affect the elastic moduli of β-Ti alloys, as the moduli of the β, ω, and α phases are all different [77]. Since the β phase is the most ductile of the Ti phases, any phase transformations are also expected to decrease the ϵ_f of β-Ti alloys. Out of all the phase transformations, the ω phase is known to reduce ϵ_f the most, and microstructures containing the ω phase tend to undergo brittle failure [48, 119, 149, 150]. Thus, the following hypotheses about the mechanical properties of the Ti-Cr alloy system were made:

- The elastic moduli would increase with increasing volume fractions of the ω and α phases according to the rule of mixtures.
- The σ_y and UTS values would increase with increasing volume fractions of the ω and α phases.
- The hardness values would increase with increasing volume fractions of the ω and α phases.
- Increasing the ω-phase volume fraction would increase E, G, σ_y, UTS, and the hardness more than increasing the α-phase volume fraction.
- Alloys containing any amount of the ω-phase microstructure would fail before yielding.

To test these hypotheses, various mechanical testing of the alloying after the β-to-ω and β-to-α transformations had occurred was needed. Vickers microhardness testing could determine the change in hardness after the β-to-ω and β-to-α phase transformations, and tensile testing could determine the change in E, σ_y, UTS, and ϵ_f after the phase transformations. Resonance ultrasound spectroscopy (RUS) could determine G as the phase transformations were occurring, as it could

be performed during the 400 °C treatment. The tensile testing could determine whether samples containing the ω-phase microstructure failed before yielding via the tensile curves. In addition, the fracture surfaces could provide information about the failure mode of the alloys, to determine whether the ω phase affected the failure mode of the sample differently than the α phase.

The results of the mechanical testing could be coordinated with the results from the microstructural characterization. Through that coordination, the effects of the microstructural evolution on the mechanical properties could be determined. Figure 2.12 shows the experimental matrix for the mechanical testing experiments.

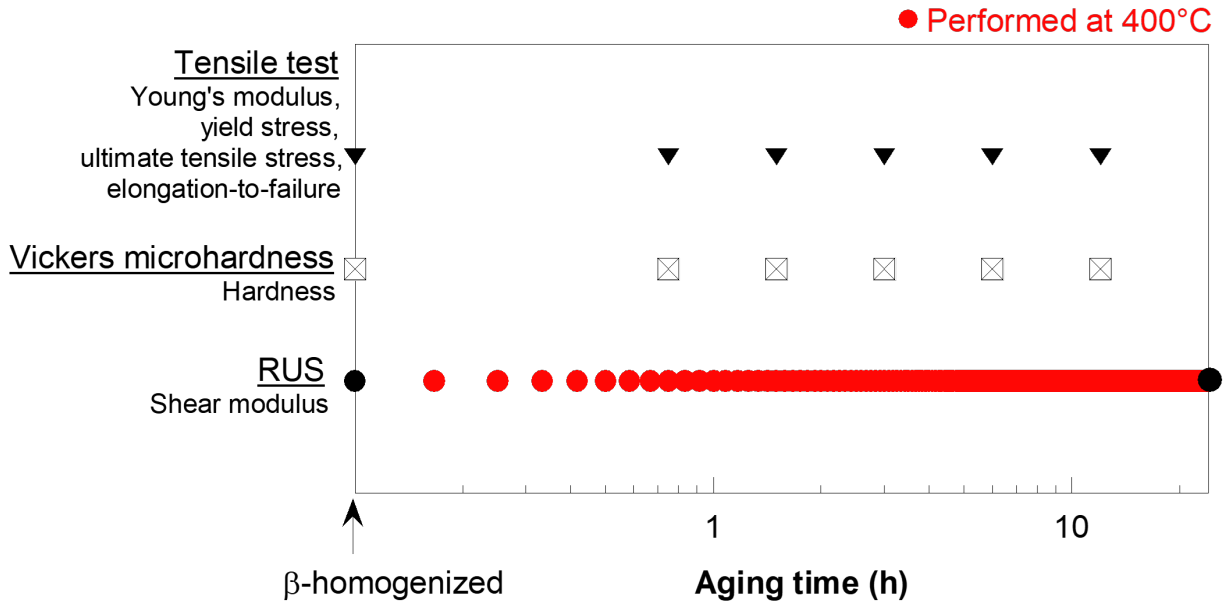

Figure 2.12: The experiment matrix detailing the length of time the alloys spent at 400 °C before each mechanical property characterization experiment.

CHAPTER 3

EXPERIMENTAL METHODS

This chapter presents the alloys investigated in this work, as well as the processing, sample preparation, characterization techniques, and experiments that were employed to complete this dissertation research. Details on the alloy processing, including the information provided by Daido Steel Corporation (Nagoya, Japan), are provided first, followed by a description of the aging treatments used to induce the phase transformations in the alloys. Metallographic sample preparation and microstructural characterization are listed next, followed by a description of the mechanical property experiments. Because much of the necessary sample preparation was experiment specific, sample preparation is not provided in a separate section and is instead included with information on the individual experiments. Schematics and photos are provided to assist anyone interested in reproducing each experiment.

3.1 Alloys

The four alloys investigated in this dissertation work were nominally Ti-11Cr, Ti-11Cr-0.85Fe, Ti-11Cr-5.3Al, and Ti-11Cr-0.85Fe-5.3Al (at.%). All of the alloys were levitation melted in a 2kg, 90Dx80L LEV levitation induction furnace and hot forged at approximately 1047 °C into 25mmx60mmx250mm blocks. After hot forging, the alloys were subjected to a homogenization anneal at 900 °C for 1 hour in a vacuum, then quenched in ice water at an estimated cooling rate of 34.7 °C s^{-1}. This cooling rate was necessary to prevent the formation of the α phase [180]. The bulk chemical compositions of Cr, Fe, and Al in the alloys were measured using inductively coupled plasma atomic emission spectroscopy (ICP-AES) and the compositions of the impurity elements C, O, and N were measured using non-dispersive infrared spectroscopy (NDIR) by the Daido Steel Corporation (Nagoya, Japan). These bulk composition measurements are presented together as ICP-AES/NDIR. The measured compositions are provided in both wt.% and at.% in Table 3.1 as published in [181].

Table 3.1: The chemical compositions of each alloy measured using ICP-AES/NDIR as provided by Daido Steel Corporation.

Alloy		Chemical composition						
		Ti	**Cr**	**Fe**	**Al**	**C**	**O**	**N**
TC	wt.%	Bal.	12.1	0.02	0.01	0.004	0.059	0.004
	at.%	Bal.	11.2	0.02	0.02	0.02	0.18	0.01
TCA	wt.%	Bal.	12.3	0.02	3.06	0.003	0.062	0.004
	at.%	Bal.	11.2	0.02	5.35	0.01	0.18	0.01
TCF	wt.%	Bal.	12.5	0.93	0.02	0.003	0.069	0.004
	at.%	Bal.	11.6	0.8	0.04	0.01	0.21	0.01
TCFA	wt.%	Bal.	12.4	0.93	3.02	0.003	0.11	0.004
	at.%	Bal.	11.3	0.79	5.28	0.01	0.32	0.01

3.2 Processing

The β-homogenized alloys were subjected to a 400 °C aging treatment to induce the β-to-ω and β-to-α phase transformations. Each aging was performed in a quartz vacuum tube furnace. One thermocouple was wrapped around the samples to monitor the sample temperature during the aging treatment and another thermocouple was wrapped around the outside of the quartz tube to monitor the surrounding temperature. A reliable connection between the sample and the thermocouple was ensured before starting the furnace.

Samples were heated at a rate of 15 °C min^{-1}. The aging time was measured from when the sample temperature reached 400 °C. The aging times were for 0.75, 1.5, 3, 6, and 12 h. Once the treatment time had elapsed, the quartz tube was removed from the furnace and atmospheric air was allowed into the tube to air-quench the samples to RT.

3.3 Microstructural characterization

The microstructural characterization was accomplished according to the experimental matrices in Figures 2.11 and 2.12 in Sections 2.6.2 and 2.6.4, respectively.

3.3.1 Scanning electron microscopy

β-homogenized and 12 h aged samples for SEM imaging were cut from the forged blocks using a diamond wheel cutter. The aged samples were mounted in a Conductomet conductive resin so that three different perpendicular orientations, referred to as the cross-section, thickness, and top orientations, could be polished using the same mount. Figure 3.1 shows these orientations with respect to the original forged blocks. The mounted samples were ground and polished to a mirror finish using standard metallographic procedures including SiC paper up to 1200 grit and water, with a final polish containing a 50/50 mix of Struers OP-S Colloidal silica (0.02-0.04 micron) and 30% hydrogen peroxide. Samples from the β-homogenized and 12 h 400 °C aged conditions were etched using Kroll's reagent (2ml HF, 6ml nitric acid, 92ml distilled water).

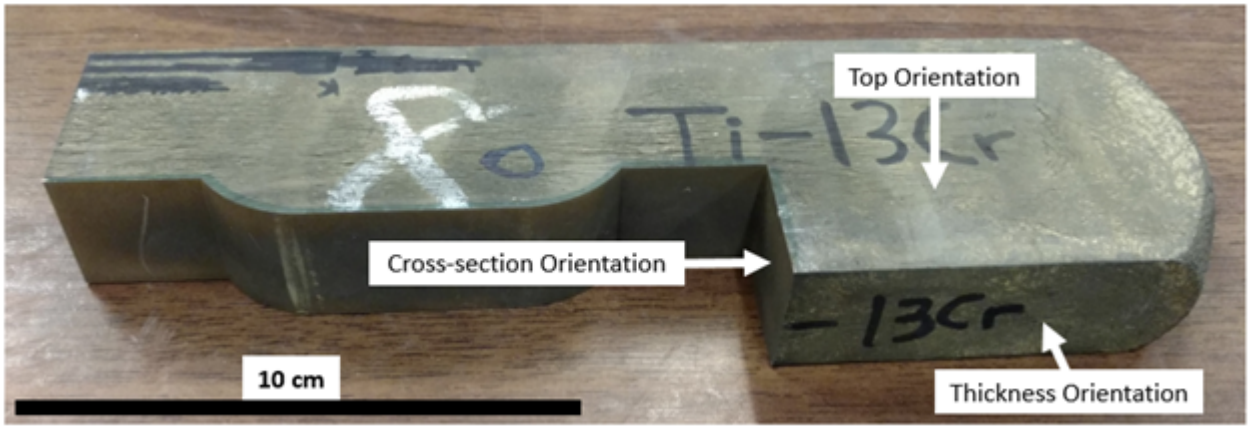

Figure 3.1: The cross-section, top, and thickness orientations of the forged TC alloy block. These orientations are consistent for all forged alloy blocks. The forged block is missing material that was removed using electro-discharge machining to make dogbone-shaped tensile samples (see Figure 3.4 for reference).

The FEI Quanta 3D field emission gun (FEG) dual beam focused ion beam/scanning electron microscope (FIB/SEM) at the Pacific Northwest National Laboratory (PNNL) was used to obtain back-scattered electron (BSE) images and energy dispersive X-ray spectroscopy (EDS) measurements of the β-homogenized and 12 h aged samples. EDS measurements were taken with a 30 kV accelerating voltage.

0.75, 1.5, 3, and 6 h aged samples for BSE-SEM imaging were cut from the grip sections of the

aged tensile samples and polished using 320 grit SiC paper and water. The samples were then ion milled using a Hitachi IM4000Plus at 6 kV to reveal the microstructure. BSE photomicrographs were taken using a Hitachi Regulus 8230 using 5.0 kV accelerating voltage and a photodiode backscattered electron (PDBSE) detector at 70x, 10kx, and 80kx magnifications. A threshold analysis was conducted using ImageJ software to estimate the volume fractions of the precipitating phases in the HRSEM photomicrographs. For the threshold analysis, subsets of each image were isolated and a threshold saturation value was set. Pixels that were darker than a set threshold value were counted to determine the volume fraction of the precipitates.

The grain size of the β-homogenized samples was measured according to the method detailed in ASTM standard E112-12 [182].

Fracture surfaces were cut from tensile samples using a diamond wheel cutter without damaging the fracture surfaces and were imaged using a Tescan Mira III FEG SEM. Surfaces were imaged using an accelerating voltage of 20 kV and beam current of 3 nA.

3.3.2 Transmission electron microscopy

Samples for scanning TEM (STEM) imaging were prepared from the 12 h aged and etched SEM sample of TCFA. General procedures from Muehle et al. [183] were followed to manufacture the FIB-liftouts for TEM imaging using a FEI Quanta 3D FEG dual beam FIB/SEM equipped with an Omniprobe nanomanipulator at PNNL. STEM imaging of the 400 °C 12 h samples was completed with a probe-corrected FEI Titan 80-300 operated at 300 kV with a high-angle annular dark-field (HAADF) detector. The probe convergence angle was 18 mrad and the inner detection angle on the HAADF detector was three times higher than the probe convergence angle.

3.3.3 Energy Dispersive X-ray Spectroscopy

The FEI Quanta 3D field emission gun (FEG) dual beam focused ion beam/scanning electron microscope (FIB/SEM) at the Pacific Northwest National Laboratory (PNNL) was used to obtain

BSE photomicrographs and energy dispersive X-ray spectroscopy (EDS) measurements of the β-homogenized samples. EDS measurements were taken with a 30 kV accelerating voltage.

3.3.4 Atom probe tomography

Needle specimens for APT were taken from samples cut from the forged blocks using a diamond wheel cutter and polished to a mirror finish using SiC paper up to 1200 grit with a final polish of 50/50 mix of Struers OP-S Colloidal silica (0.02-0.04 µm) and 30% hydrogen peroxide. The β-homogenized and 12 h 400 °C aged SEM samples were etched using Kroll's reagent (2 mL HF, 6 mL nitric acid, and 92 mL distilled water).

Specimens from the β-homogenized and 12 h 400 °C aged conditions were prepared from the polished bulk metallographic samples using a FEI Quanta 3D FEG dual beam FIB/SEM equipped with an Omniprobe nanomanipulator at PNNL. The FIB-based lift-out and annular milling method described in Thompson et al. [184] and Devaraj et al. [104] was followed. Associated images and the standard operating procedure for the needle specimen manufacturing process can be found in Appendix A. During the FIB-based lift-out and annular milling process, accelerating voltages and beam currents were kept consistent for each sample, with the exception of the electron-beam accelerating voltage during platinum (Pt) deposition. The accelerating voltage during Pt deposition was either 30 kV or 5 kV. Each deposited Pt capping layer was approximately 1 µm thick on all samples, regardless of accelerating voltage. Needle samples from the 0.75, 1.5, 3, and 6 h 400 °C samples were made using the same standard procedures on a FEI Nova200 FIB at ORNL.

The CAMECA local electrode atom probe (LEAP) 4000X HR system was used for all APT data collection. Pulsed-voltage mode with a 200 kHz pulse frequency, 50 K specimen temperature, pulse fraction of 0.2, and a detection rate of 0.5% was used for all alloys in the β-homogenized and 12 h 400 °C aged conditions, for the TC 0.75 h and 1.5 h condition samples, and for some of the TCFA 0.75 h and 1.5 h condition samples. Pulsed-laser mode with a 50 pJ laser energy, 200 kHz pulse frequency, 30 K specimen temperature, and a detection rate of 0.5% was used for the TCA and TCF 0.75 h and 1.5 h aged samples, and for some of the TCFA 0.75 h and 1.5 h aged samples. All

data sets were analyzed using the Interactive Visualization and Analysis Software (IVAS) version 3.8.2.

3.3.5 X-ray diffraction

XRD samples were cut from the grips of the dogbone mechanical testing samples in the β-homogenized condition and top orientation, and were polished using 320 grit SiC paper and water to remove any macroscopic surface defects or oxidation-affected surface layers. The final sample dimensions were 17 mmx17 mmx1.1 mm.

RT XRD was performed at Alfred University (AU) on a D8 Advance with an automatic sample changer. Cu-Kα X-ray radiation was used and data was collected over a 2θ range of 25° to 75° .

400 °C XRD was performed using a Bruker-AXS (Madison, WI) D8 diffractometer with an automatic sample changer, a Vantec linear position-sensitive detector, Cu-Kα radiation, and an Anton-Paar HTK1200 furnace with ultra-high-purity nitrogen gas to prevent oxidation during heating. The heating rate was 30 °C min^{-1} except for the beginning and ending of the heating process, which had an exponential and logarithmic character, respectively. Data was collected in situ over a 2θ range of 25° to 75° every 0.5 h during the 12 h 400 °C exposure. Along with analyzing the XRD scans for peaks associated with Ti oxides, samples were visually inspected after the HTXRD tests to determine if oxidation occurred during testing. No evidence of oxidation was found in the data or during the visual inspection.

For each alloy, Rietveld analysis was performed on the 400 °C XRD data to determine the volume fractions and lattice parameters of the β, α, and ω phases at each 0.5 h time step. The Rietveld refinement and lattice parameter calculations were performed using the Topas software package (Bruker-AXS). The Rietveld lattice parameter refinement for TC was accomplished using software suite PDXL version 2 [185], and the weighted-profile residual for each Rietveld analysis was between 4.87% and 7.85%. Table 3.2 contains the crystallographic information of the phases considered for Rietveld refinement as cited in the ICSD database, and Figure 3.2 contains the phase peaks and relative intensities considered for Rietveld refinement.

Table 3.2: The crystallographic data of the β, α, and ω phases used for Rietveld refinement.

Phase	a (Å)	b (Å)	c (Å)	Structure	Space Group	Atom Positions (x,y,z)	Reference
β	3.2100	-	-	Cubic	$Im\bar{3}m(229)$	(0,0,0) (1/2,1/2,1/2)	[186]
α	2.9508	-	4.6855	Hexagonal	$P6_3/mmc(194)$	(0,0,0) (1/3,2/3,1/2)	[187]
ω	4.6000	-	2.82	Hexagonal	P6/mmm(191)	(0,0,0) (1/3,2/3,1/2) (2/3,1/3,1/2)	[188]

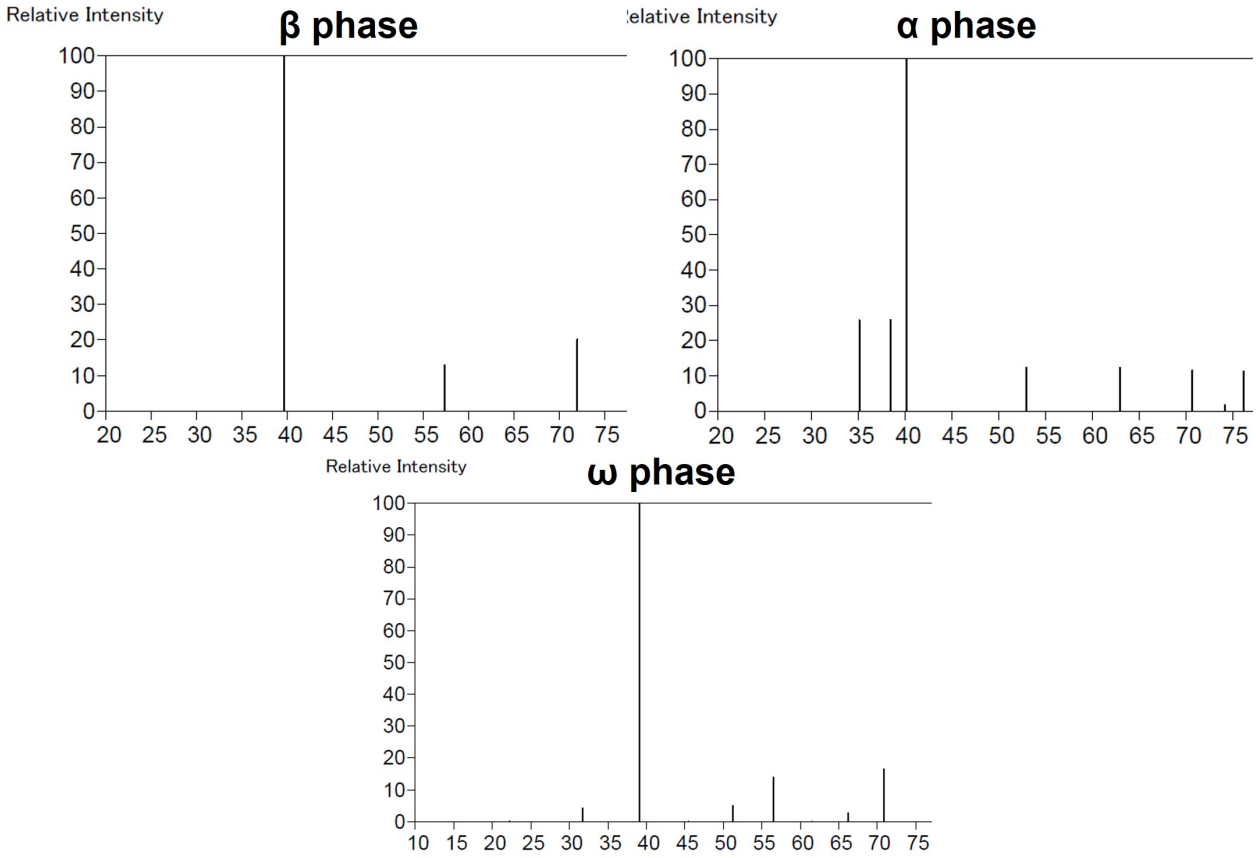

Figure 3.2: The peak locations and relative peak intensities for the β, α, and ω phases, from [186], [187], and [188], respectively.

3.4 Mechanical testing

The E, σ_y, UTS, and ϵ_f were determined using tensile testing. The shear modulus was determined using RUS. The hardness was determined using Vickers microhardness and Rockwell B hardness testing for the β-homogenized condition, and Vickers microhardness testing for the 400 °C treated conditions.

The Vickers microhardness and tensile tests on the aged samples were performed after holding

the samples at 400 °C for 0.75, 1.5, 3, 6, and 12 h. RUS testing was performed at RT before heating to 400 °C, at 400 °C where measurements were taken every 5 minutes during a 24 h test, and after cooling from 400 °C to RT.

3.4.1 Tensile testing

Samples for tensile testing were electro-discharge machine (EDM) cut from the forged blocks into one of 2 'dogbone-shaped' geometries according to the schematic in Figure 3.4(a). A photo of the larger dogbone geometry samples with accompanying forged block is shown in Figure 3.4(b). After being EDM cut, aged samples were subjected to the 400 °C aging described in Section 3.2 above. Before tensile or fatigue testing, surface defects and oxidation-affected surface layers were removed using 320 grit SiC paper and water. The larger dogbone geometry in 3.3(a) was used for tensile testing and fatigue testing. The smaller dogbone geometry illustrated in 3.3(b) was only used for tensile testing.

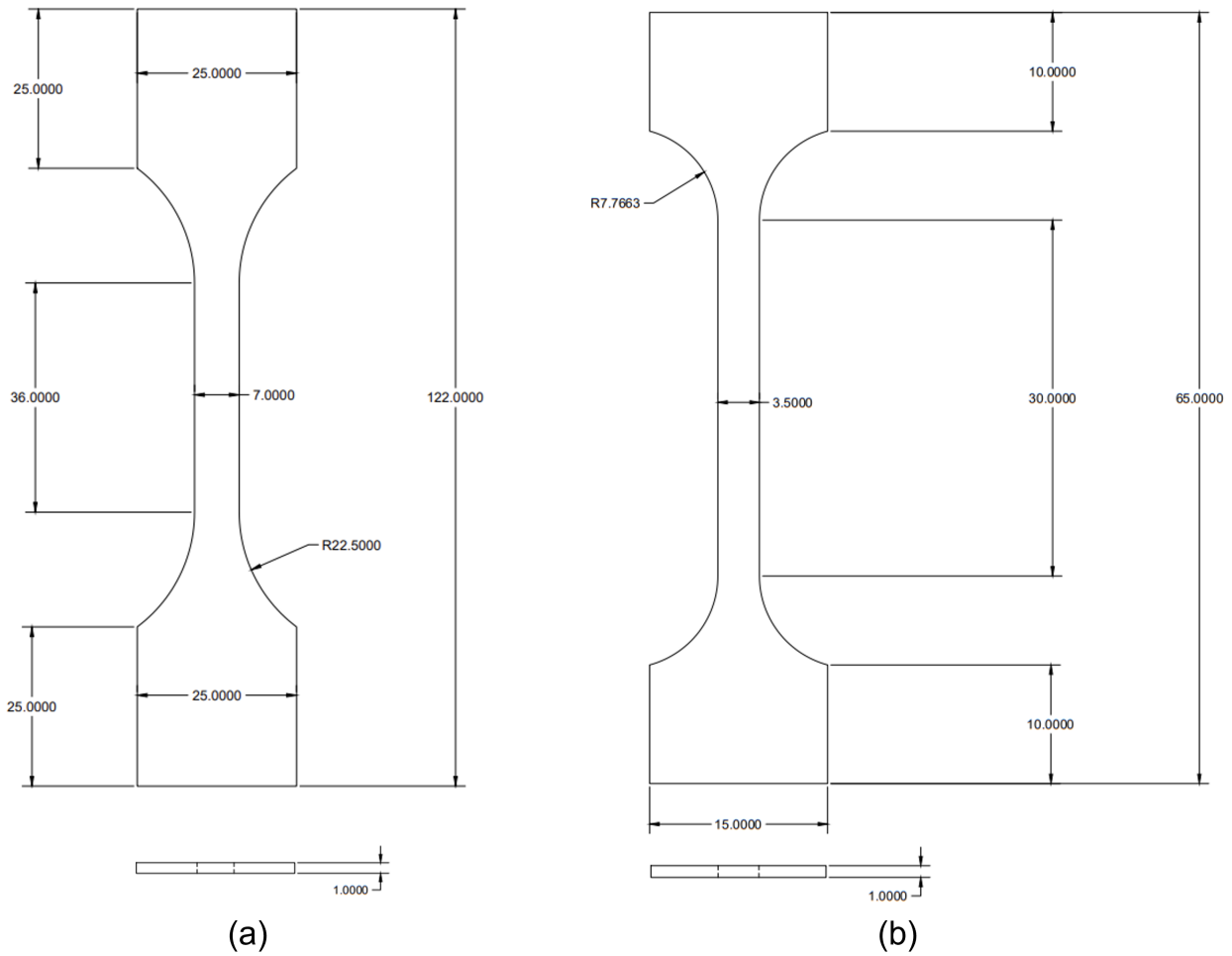

Figure 3.3: Schematic drawings of the (a) 122 mm long dogbone and (b) 65 mm long dogbone geometries used in tensile and fatigue testing. All measurements are given in mm.

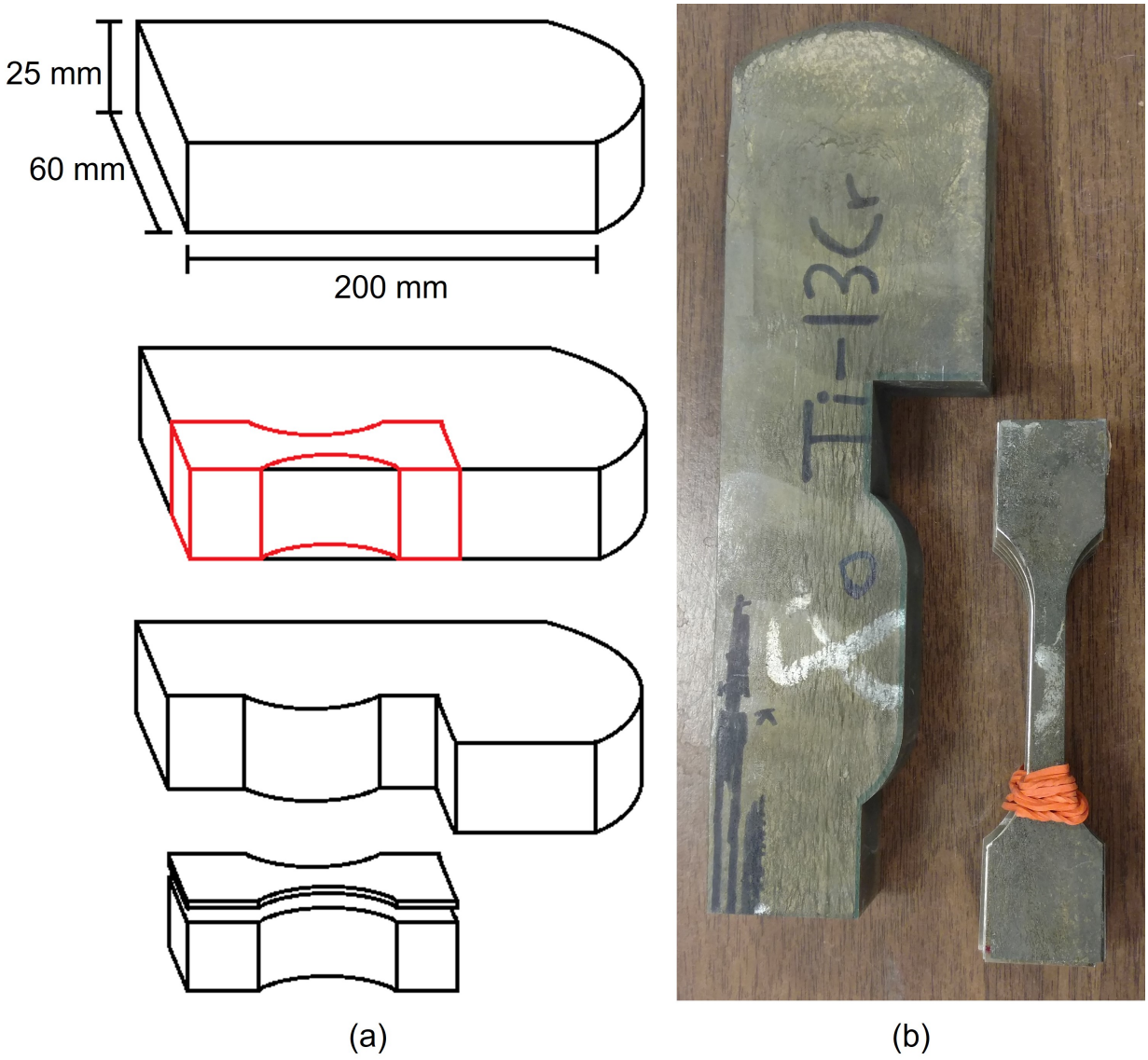

Figure 3.4: A schematic of how the larger dogbone geometries were EDM cut from the forged alloy blocks (a) and a photo of the larger dogbone geometry extracted from the TC forged block (b).

Prior to tensile testing, specimens were mechanically polished using 60 grit SiC paper and water to remove any oxidation-affected surfaces that occurred during the 400 °C aging. After the initial polish with the 60 grit SiC paper, the used paper was saved and reused to provide a final surface polish. The used 60 grit SiC paper efficiently removed surface oxides and defects.

Conventional uniaxial tensile tests were performed using a MTS® servo-hydraulic testing machine, shown in Figure 3.5, equipped with an MTS® Flex Test 40 controller. All tests were performed in an open-air environment at approximately 25 °C using a displacement rate of 0.025 mm

per second. Strain was measured using an alumina-arm extensometer with a 12mm gage length spring-pressed to the side of the gage section, as shown in Figure 3.6. σ_y, UTS, and ϵ_f were calculated using sections 7.7.1, 7.10, and 7.11.5 of ASTM standard E8-E8M-13a, respectively, and the σ_y and UTS values were reported according to section 7.13.1. The E was calculated using the slope of the elastic portion of the engineering stress versus engineering strain curves. Two samples were tensile tested per condition to evaluate the data reproducibility.

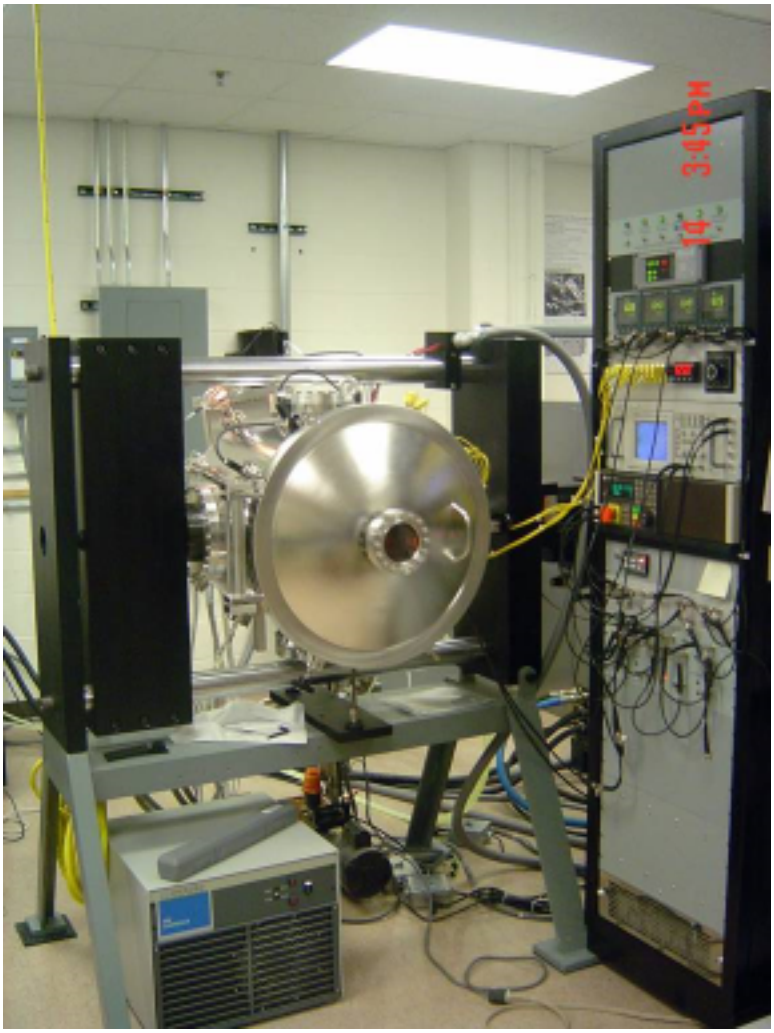

Figure 3.5: A digital image of the MTS® servo-hydraulic testing machine (with the chamber door closed) used for the tensile and fatigue testing.

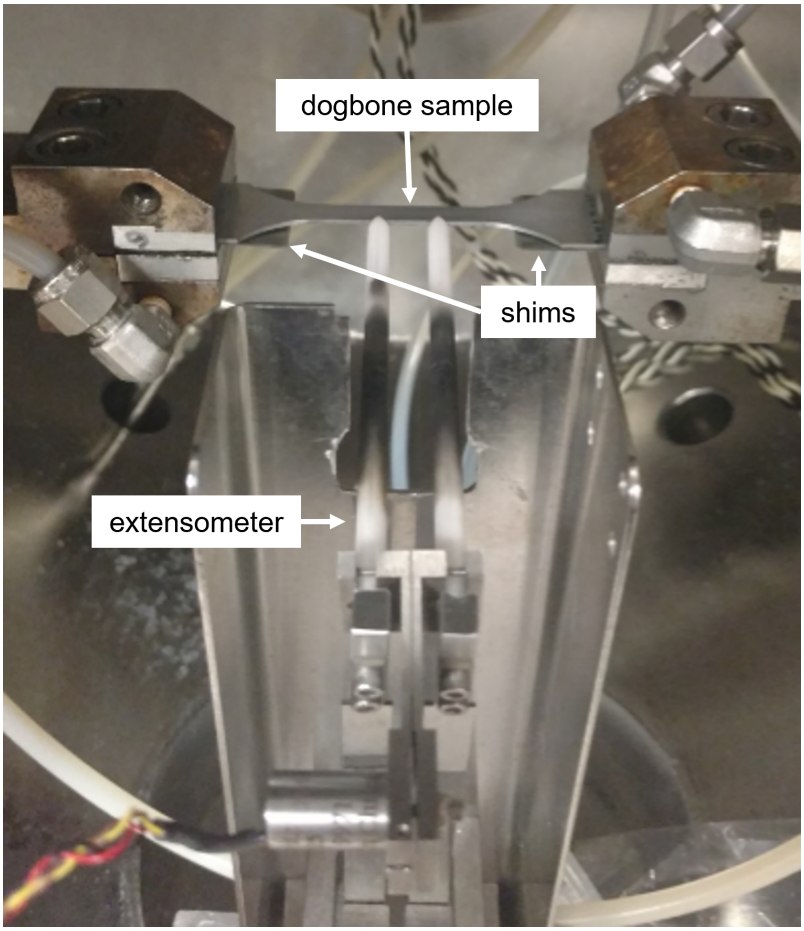

Figure 3.6: A digital image of the mechanical testing setup with a larger dogbone geometry sample. Shims were placed under the dogbone to facilitate gripping of the sample, and the alumina-arm extensometer was spring-pressed to the side of the gage sample.

3.4.2 Hardness testing

Hardness testing was performed according to ASTM Standards E92-17 and E18-18a for Vickers microhardness and Rockwell B hardness, respectively. Vickers microhardness testing was performed using a 500 gram-force load and a dwell time of 15 seconds.

For the β-homogenized condition, tests were performed for each alloy on the undeformed grip sections of tensile test samples polished according to the procedures described in Section 3.4.1. A total of 6 Vickers microhardness measurements were taken per alloy, with two measurements taken on three separate samples. A total of 9 Rockwell B hardness measurements were taken per alloy, with three measurements taken on three separate samples.

For the aged samples, Vickers hardness tests were performed on samples prepared for SEM imaging according to Section 3.3.1. 10 measurements were obtained per alloy and aging condition, and all 10 measurements were taken on the same sample.

3.4.3 Resonance ultrasound spectroscopy

Resonance ultrasound spectroscopy (RUS) is a nondestructive vibration-based technique used to measure the elastic properties of solid samples [189]. Samples for RUS measurements were EDM cut from the forged blocks into cubes with dimensions of 4.5 mmx5 mmx5.5 mm, and polished using 320 grit SiC paper and water to remove any surface defects or oxidation.

A commercial room temperature RUS (RUS008) was used to determine G before and after heat treatment [189]. In situ RUS measurements were taken using a high-temperature stage employing alumina buffer rods attached to piezoelectric transducers in a sealed chamber. Samples were mounted with the diagonally opposite corners in contact with the piezoelectric transducers to approximate free boundary conditions. Samples were heated at a rate of 45 °C min^{-1} to 400 °C, followed by a 24 h heat treatment at 400 °C in flowing argon gas. Resonance spectra were collected every 15 seconds for the first 2 h of the 24 h test, then every 5 minutes thereafter. The excitation frequencies were between 170 to 194 kHz. This range contained the first peak in the vibrational spectrum, the location of which was solved using the Los Alamos National Laboratory-based software [189]. Since the first peak was almost entirely c44 dependent, the G could be determined by converting the frequency of the peak positions into c44 using Equation 3.1, where F was the frequency of the first peak and A was a multiplication factor determined from the fit of the RT RUS scan after the 24 h aging and cooling. The A values used for TC, TCF, TCA, and TCFA were 9.878×10^{-10} MPa Hz^{-2}, 1.007×10^{-9} MPa Hz^{-2}, 1.012×10^{-9} MPa Hz^{-2}, and 9.9055×10^{-10} MPa Hz^{-2}, respectively. Texturing of the sample prevented any peaks other than the first peak from being fit.

$$c44 = A * (F^2) \tag{3.1}$$

CHAPTER 4

RESULTS OF β-HOMOGENIZED ALLOYS

In this chapter, the results of testing the hypotheses concerning the β-homogenized condition of each alloy is presented. This chapter is divided into two sections, the first containing the microstructural characterization of the β-homogenized alloys, and the second containing the mechanical property characterization of the β-homogenized alloys.

The microstructural characterization in the first section includes the investigation of whether the microstructure of each alloy was fully β-homogenized. Because each alloy underwent the same levitation melting, hot forging, and β-homogenization process, the following hypotheses were proposed:

- The alloys were fully β-homogenized. If this hypothesis is incorrect and the α phase was present, it would appear at the grain boundaries due to greater diffusion rates at the boundaries.
- The alloys would possess similar grain sizes.
- The alloying elements would be randomly distributed in the microstructure.
- The alloys' β-phase lattice parameters would be less than that for pure Ti.
- The small Fe and Al additions would not affect the β-phase lattice parameters significantly.

XRD was used to determine the phases present and the a_β of each alloy. BSE SEM was used to observe the grain boundaries and grain interiors of each alloy, since XRD would not detect the α phase if it was present in amounts less than 5 mass% [163]. SEM was also used to determine the grain size of each alloy. The composition of the alloys and the distribution of the alloying elements at the nanoscale was investigated using APT. The XRD, SEM, and APT results are presented in separate subsections.

The mechanical property characterization in the second section includes the investigation of how the small additions of Fe and Al affected the hardness, tensile properties, and shear modulus

of each alloy. While the alloys were not expected to have significant microstructural differences, the moduli were expected to change as Ti, Cr, Fe, and Al each have different bond orders in Ti, 2.790, 2.779, 2.651, and 2.426, respectively. The following hypotheses regarding the mechanical properties were proposed:

- As the microstructure of each alloy was hypothesized to be similar, the σ_y, UTS, ϵ_f values, and fracture mechanisms should also be similar.
- The 0.85% Fe addition will reduce the bond strengths and moduli in TCF more than in TC.
- The 5.3% Al addition will reduce the bond strengths in TCA more than the 0.85% Fe addition in TCF, and TCA will exhibit lower moduli than TCF.
- Adding both Fe and Al will reduce the bond strengths in TCFA the most, and TCFA will exhibit the lowest moduli of TC, TCF, and TCA.

Vickers microhardness testing was used to determine the effect of the alloying element additions on the hardness of each alloy. RUS was used to determine the effect of the alloying element additions on G. Tensile testing was used to determine the E, σ_y, UTS, and ϵ_f of each alloy, and SE SEM imaging of the tensile test fracture surfaces was used to investigate the fracture mechanisms of each alloy. The Vickers microhardness, RUS, tensile testing, and SE SEM images of the fracture surfaces are presented in separate subsections.

4.1 Characterization of the β-homogenized microstructure

The microstructures of each alloy were investigated using XRD, BSE SEM imaging, and APT, to determine the phases present in each alloy and their lattice parameters, the grain sizes of each alloy, the composition of each alloy, and the alloying element distribution within each alloy.

The XRD and BSE SEM results indicated that each alloy was fully β-homogenized. XRD results showed only peaks associated with the β phase in each alloy, and no α phase was observed along the grain boundaries using BSE SEM imaging. The Fe and Al additions did not affect a_β significantly.

Even though the alloys underwent the same processing, TC exhibited the smallest grain size. TCF and TCFA exhibited similar grain sizes, and the grains were twice as large as those in TC. TCA exhibited the largest grain size, at nearly triple the size of those in TC.

The APT analysis indicated that the alloying elements were randomly distributed throughout the material. The Ti and Cr atoms exhibited a greater association than Ti and Ti, Ti and Fe, or Ti and Al. This was most prevalent in TC.

The results of the XRD, SEM, and APT experiments are presented below. The discussion of why the hypotheses were verified or not can be found in Section 5.1.

4.1.1 XRD

RT XRD scans of the top face of each β-homogenized alloy revealed peaks corresponding to the (1 0 1), (2 0 0), and (2 1 1) β-phase crystallographic planes, see Figure 3.1. No other phase peaks were visible, indicating that the microstructure was purely β phase, or that any other phases were present in amounts less than 5 mass% [163].

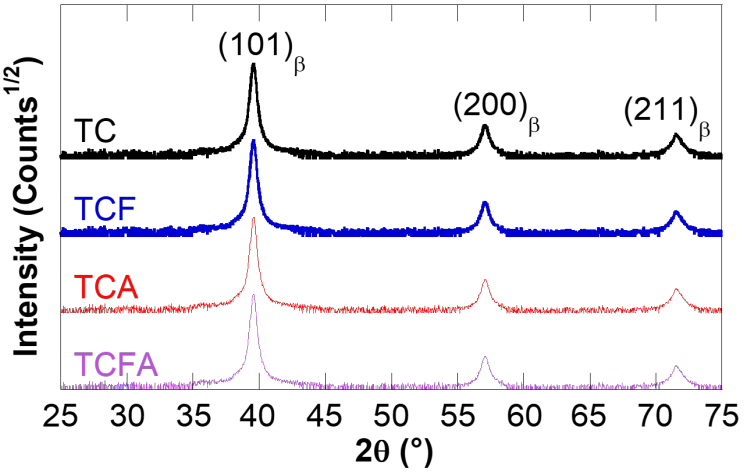

Figure 4.1: Intensity versus 2θ XRD plots of the top face of the β-homogenized TC, TCF, TCA, and TCFA alloys, showing the (1 0 1), (2 0 0), (2 1 1), and (2 0 2) β peaks.

Bragg's Law, provided in Equation 4.1, was used to calculate the BCC lattice parameter (a_β) for each alloy. For each alloy, d was the spacing between the $(2\,0\,0)_\beta$ planes, λ was the monochromatic wavelength of Cu-Kα radiation (1.54Å), and θ was the angle of the incident X-ray on the sample.

As a_β is the distance between the $(1\,0\,0)_\beta$ planes, and d was the spacing between the $(2\,0\,0)_\beta$ planes, a_β was twice the value of d. Table 4.1 lists the calculated a_β values. The pure Ti RT lattice parameter was calculated because the β phase does not exist in equilibrium in pure Ti at RT [166]. As expected, adding Cr reduced the lattice parameter from the theoretical Pure Ti lattice parameter. Also as expected, the small additions of Fe and Al did not significantly affect a_β.

$$\lambda = 2\,d\,\sin\theta \tag{4.1}$$

Table 4.1: The calculated β-phase lattice parameters of the TCFA alloys. *Calculated value from [166]

Alloy	D8 Advance lattice parameter (Å)
Pure Ti*	3.282±0.003
TC	3.22
TCF	3.22
TCA	3.22
TCFA	3.22

4.1.2 SEM

Each alloy was characterized using SEM imaging in three orientations, which were referred to as cross section, thickness, and top, see 3.1 in 3.3.1. The α phase rejects β-stabilizing elements such as Cr and Fe during precipitation and growth [131], which allows the α phase to be identified using Z-sensitive BSE imaging. Thus, high-magnification BSE imaging was used to help identify the α phase, which would appear as a darker contrast phase within the lighter-contrast β-phase grains or along the β-phase grain boundaries. The samples were imaged before and after etching. Representative images of the etched samples of each alloy are provided in Figure 4.2. The α phase was not observed in any orientation of the alloys.

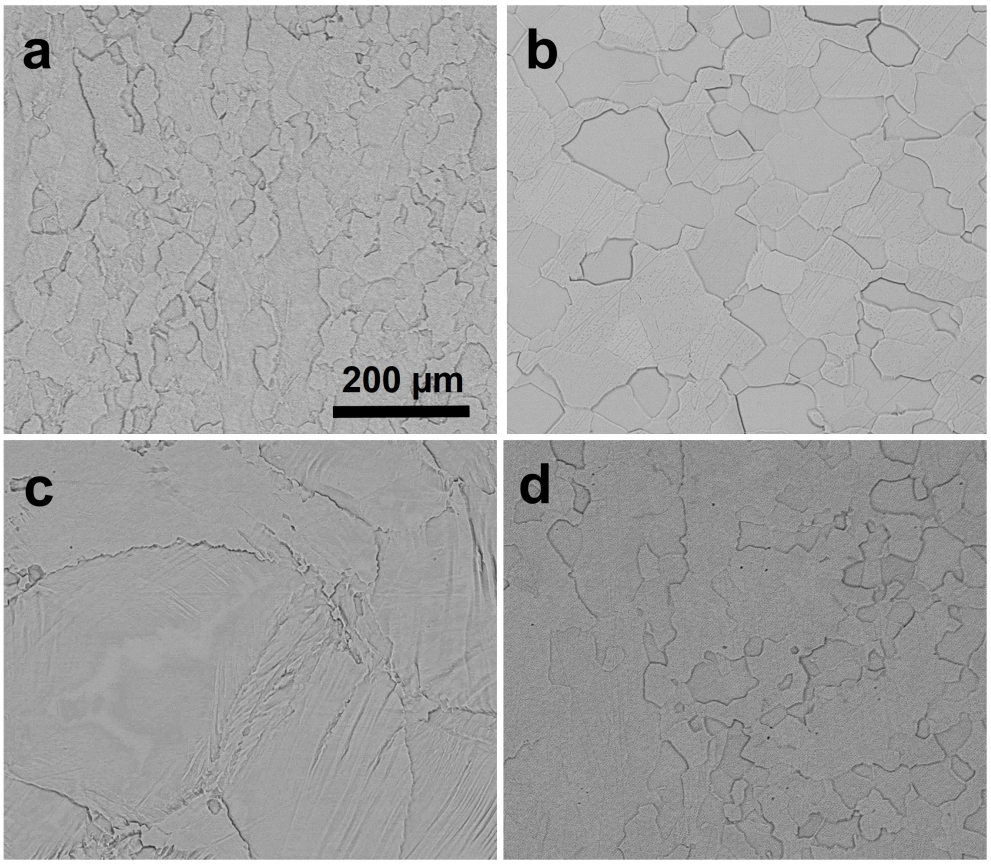

Figure 4.2: Representative BSE-SEM photomicrographs of the cross-section of the (a) TC, (b) TCF, (c) TCA, and (d) TCFA alloys.

While the α phase was not observed within the bulk of the alloys, a darker phase was observed in areas of each alloy that were previously the surfaces of the forged blocks. The darker phases extended between 200 µm and 300 µm from the surface, and EDS element maps of the phases found that they were Cr-poor, see Figure 4.3. Higher amounts of impurity elements O, C, and N were also present at the surfaces of the forgings, see Figure 4.3. The size, morphology, lack of Cr, and presence of O and N suggests that the darker phase at the surface of the forging is a layer of α-phase precipitates known as "α case," and most likely was formed when O and N were absorbed into the surface of the forged block during the elevated temperature thermo-mechanical processing steps or during the 900 °C homogenization anneal, as described in Gammon et al. [190]. Since no APT or mechanical testing samples were taken from the edges of the forgings, this α case layer could not have affected any of the experimental results in this work.

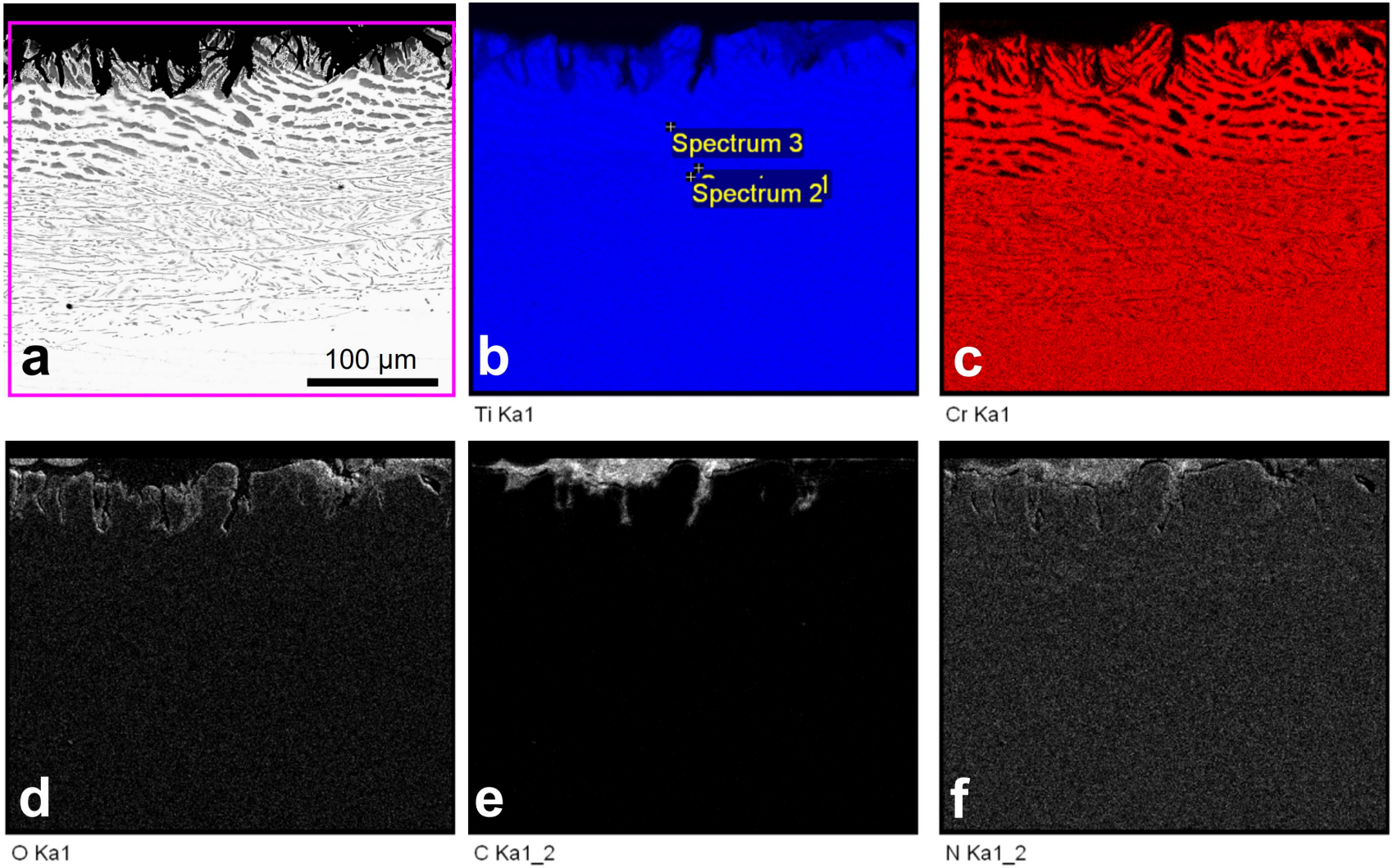

Figure 4.3: A (a) BSE-SEM photomicrograph of a β-homogenized TC sample showing the α case, and the element maps of (b) Ti, (c) Cr, (d) O, (e) C, and (f) N.

Each forged block was evaluated in the top, thickness, and cross-section orientations in order to estimate the average β-phase grain size. The β-homogenized SEM samples were etched with Kroll's reagent, as described in Section 3.3.1, to make each grain visible. The grains were visible after etching in all alloys and orientations, and representative images of the cross-section orientation of all alloys can be found in Figure 4.2. In some grains, plate- or needle-shaped lamella appeared. To determine whether the lamella were a secondary phase, EDS measurements were taken to determine their composition, see Figure 4.4. The EDS element maps indicated that the alloy composition did not vary within the lamella. As such, the lamella were considered to be surface topography, and an artefact of the etching process.

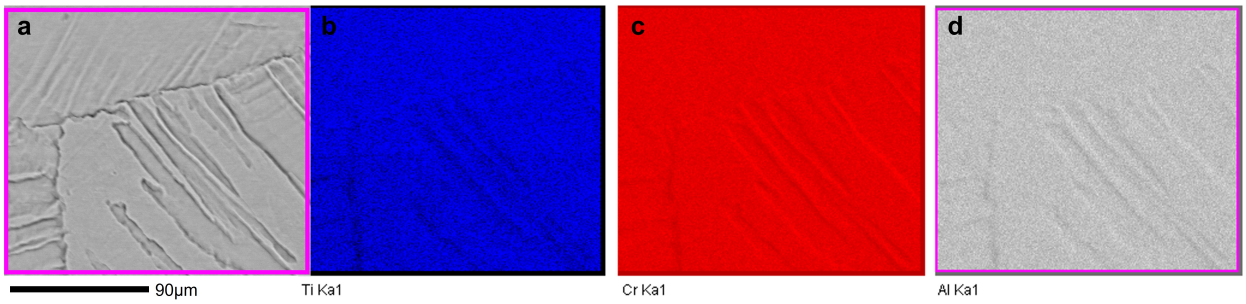

Figure 4.4: Representative BSE photomicrograph of the lamella visible on the surface of TCA (a) with EDS element maps of (b) Ti, (c) Cr, (d) and Al. The lack of compositional variation suggested that the lamella in (a) were the result of surface topography from etching and not a different phase.

The β-phase grain sizes were measured from the etched samples for each orientation according to ASTM standard E112-12 [182]. Three images, taken at 120x, 200x, and 500x, were used to measure the grain size. Procedures for measuring the intercept length, outlined in section 16.3 of ASTM E112-12 [182], were used with the randomly placed test line method. The mean lineal intercept lengths ($\bar{l}$) were calculated from the total test line length (L), the magnification of the image (M), and the total number of intersections (N) according to Equation 4.2 (developed from equations 10 and 12 in ASTM E112-12 [182]):

$$\bar{l} = \bar{N}_L^{-1} = \frac{L/M}{N} \tag{4.2}$$

and the values are provided for each orientation in Table 4.2. To calculate the overall mean lineal

intercept length ("Overall Mean" in Table 4.2), $\bar{N}_L$ was calculated according to Equation 4.3:

$$\bar{N} = (\bar{N}_{Lthickness} * \bar{N}_{Ltop} * \bar{N}_{Lcross-section})^{1/3} \tag{4.3}$$

The average $\bar{N}$ was used to calculate the grain size number, also reported in Table 4.2, according to ASTM E112 [182].

Adding Fe or Al resulted in an increased grain size in all three orientations, see Table 4.2. The addition of Fe approximately doubled the grain size while the addition of Al nearly tripled the average grain size. However, when 5.3% Al was added to TCF, the average grain size only increased by 20%. Thus, Fe appears to limit the ability of Al to increase the grain size. Overall, by adding both Fe and Al to TC, a greater than doubling of the average grain size resulted.

Table 4.2: Summary of the measured grain sizes for TC, TCF, TCA, and TCFA.

Orientation	**TC**	**TCF**	**TCA**	**TCFA**
$\bar{l}$, Cross-section (μm)	33.9	50.9	84	57
$\bar{l}$, Top (μm)	46	86.8	134.2	78.4
$\bar{l}$, Thickness (μm)	27.1	52.3	94.2	89.1
Overall mean (μm)	34.9	61.3	102	73.6
Grain size number (G)	6.4	4.8	3.3	4.2

4.1.3 APT

APT was used to investigate nanoscale compositional fluctuations because the relatively large interaction volume of the 30-keV electron beam limits the sensitivity of the BSE image contrast to composition fluctuations above 1 μm [191]. Nanoscale α-phase precipitation, which could not be resolved by SEM BSE imaging, has been reported in other β-Ti alloys depending on specific thermomechanical treatments [4]. If such nanoscale α-phase precipitation occurred in any of the alloys, it would induce a nanoscale compositional partitioning that APT is able to measure.

Since the composition of each β-homogenized alloy was measured using APT and ICP-AES/NDIR, the measured composition from each technique was compared, see Table 4.3.

Table 4.3: Alloy composition measured via APT, with ±1 standard deviation, compared with composition measured via ICP-AES/NDIR and SEM-EDS. All SEM-EDS measurements were taken from a sample area of approximately 1200 µm by 1200 µm (see Figure 4.3 for an example region from which the EDS measurement was taken). * indicates no standard deviation.

Alloy	Method	Ti (at.%)	Cr (at.%)	Fe (at.%)	Al (at.%)	C (at.%)	O (at.%)	N (at.%)
TC	APT	84.7 ± 1.1	14.1 ± 1.3	0.03 ± 0.005	0.01*	0.91 ± 0.31	0.21 ± 0.04	0.02 ± 0.02
	ICP-AES/NDIR	88.5	11.2	0.02	0.02	0.02	0.18	0.01
TCF	APT	83.9 ± 0.1	14 ± 0.05	0.94 ± 0.11	0.08 ± 0.04	0.68 ± 0.08	0.32 ± 0.05	0.03 ± 0.001
	ICP-AES/NDIR	87.3	11.6	0.8	0.04	0.01	0.21	0.01
TCA	APT	79.7 ± 0.2	13.7 ± 0.1	0.04 ± 0.02	5.71 ± 0.26	0.49 ± 0.09	0.23 ± 0.03	0.13 ± 0.13
	ICP-AES/NDIR	83.3	11.2	0.02	5.35	0.01	0.18	0.01
TCFA	APT	79 ± 0.14	13.3 ± 0.14	1.1 ± 0.16	4.48 ± 1.39	0.85 ± 0.54	0.32 ± 0.05	0.93 ± 0.79
	ICP-AES/NDIR	82.3	11.3	0.79	5.28	0.01	0.32	0.01

The Cr concentrations of the alloys measured from APT are approximately 2-3% higher than the bulk Cr concentrations reported by Daido Steel using ICP-AES/NDIR. The concentrations of Al in TCA and TCFA differ, with TCA containing 0.36 at.% more Al than the ICP-AES/NDIR measurement, and TCFA containing 0.8 at.% less. Higher amounts of C were also measured in the APT tips than in the bulk ICP-AES/NDIR samples. Gallium, which can be implanted during the FIB/SEM lift-out process, was present at concentrations of less than 0.07% in all samples used for this study.

The difference between the APT and ICP-AES/NDIR concentrations could be because APT measured the dissolved H concentration in the alloys while ICP-AES/NDIR did not. To directly compare APT to ICP-AES/NDIR, the APT results in Table 4.3 were also calculated while excluding the H ions from the analysis. However, this could lead to skewed concentration values. The elemental concentrations of TC and TCFA including H were significantly different than when H was excluded, see Table 4.4. TC and TCFA contained 32.7% and 15.4% H, respectively. In contrast, TCA and TCF contained between 2% and 4% H, and the concentrations with and without H are similar. Because the compositions of TC and TCFA do not significantly differ from TCF and TCA when H is not included in the analysis, the H-free calculations are still considered reliable. It is believed that the H in TC and TCFA was introduced during the sample preparation process, and more detailed results and discussion of H are provided in Sections 6.1.3.3 and 7.1.3.3, respectively.

APT was also used to investigate the presence of nanoscale compositional fluctuations not easily seen in the elemental distribution maps. To check for local elemental ordering/clustering in these alloys, a frequency distribution analysis was performed using 100 atom bins [192], and the results are provided in Figure 4.5(b-e). For a homogeneous solid solution, the observed frequency distribution should match a calculated binomial distribution [193]. All observed measurements seem to match well to the binomial distributions, see Figure 4.5(b-e), suggesting that the compositions are homogeneous in the volumes analyzed via APT. The largest visible difference between the observed and binomial distributions was in the Ti distribution of the TC alloy, suggesting order/clustering of the Ti atoms.

Table 4.4: Alloy composition measured via APT (calculated with and without H included, ±1 standard deviation). * indicates no standard deviation available.

Alloy	H (at.%)	Ti (at.%)	Cr (at.%)	Fe (at.%)	Al (at.%)	C (at.%)	O (at.%)	N (at.%)
TC	-	84.7 ± 1.1	14.1 ± 1.3	0.03 ± 0.005	0.01*	0.91 ± 0.31	0.21 ± 0.04	0.02 ± 0.02
	32.7 ± 16.7	57.1 ± 14.6	9.40 ± 1.7	0.02 ± 0.003	0.01*	0.65 ± 0.3	0.14 ± 0.05	0.02 ± 0.01
TCF	-	83.9 ± 0.1	14.0 ± 0.05	0.94 ± 0.11	0.08 ± 0.04	0.68 ± 0.08	0.32 ± 0.05	0.03 ± 0.001
	2.57 ± 0.3	81.7 ± 0.4	13.7 ± 0.1	0.92 ± 0.11	0.07 0.04	0.66 ± 0.08	0.31 ± 0.05	0.03 ± 0.001
TCA	-	79.7 ± 0.2	13.7 ± 0.1	0.04 ± 0.02	5.71 ± 0.26	0.49 ± 0.09	0.23 ± 0.03	0.13 ± 0.13
	3.47 ± 3.1	76.9 ± 2.2	13.2 ± 0.6	0.04 ± 0.02	5.52 0.4	0.48 ± 0.08	0.22 ± 0.03	0.12 ± 0.12
TCFA	-	79.0 ± 0.14	13.3 ± 0.14	1.1 ± 0.16	4.48 ± 1.39	0.85 ± 0.54	0.32 ± 0.05	0.93 ± 0.79
	15.4 ± 14.0	66.7 ± 10.4	11.3 ± 1.77	0.94 ± 0.26	3.93 1.69	0.76 ± 0.54	0.27 ± 0.06	0.70 ± 0.48

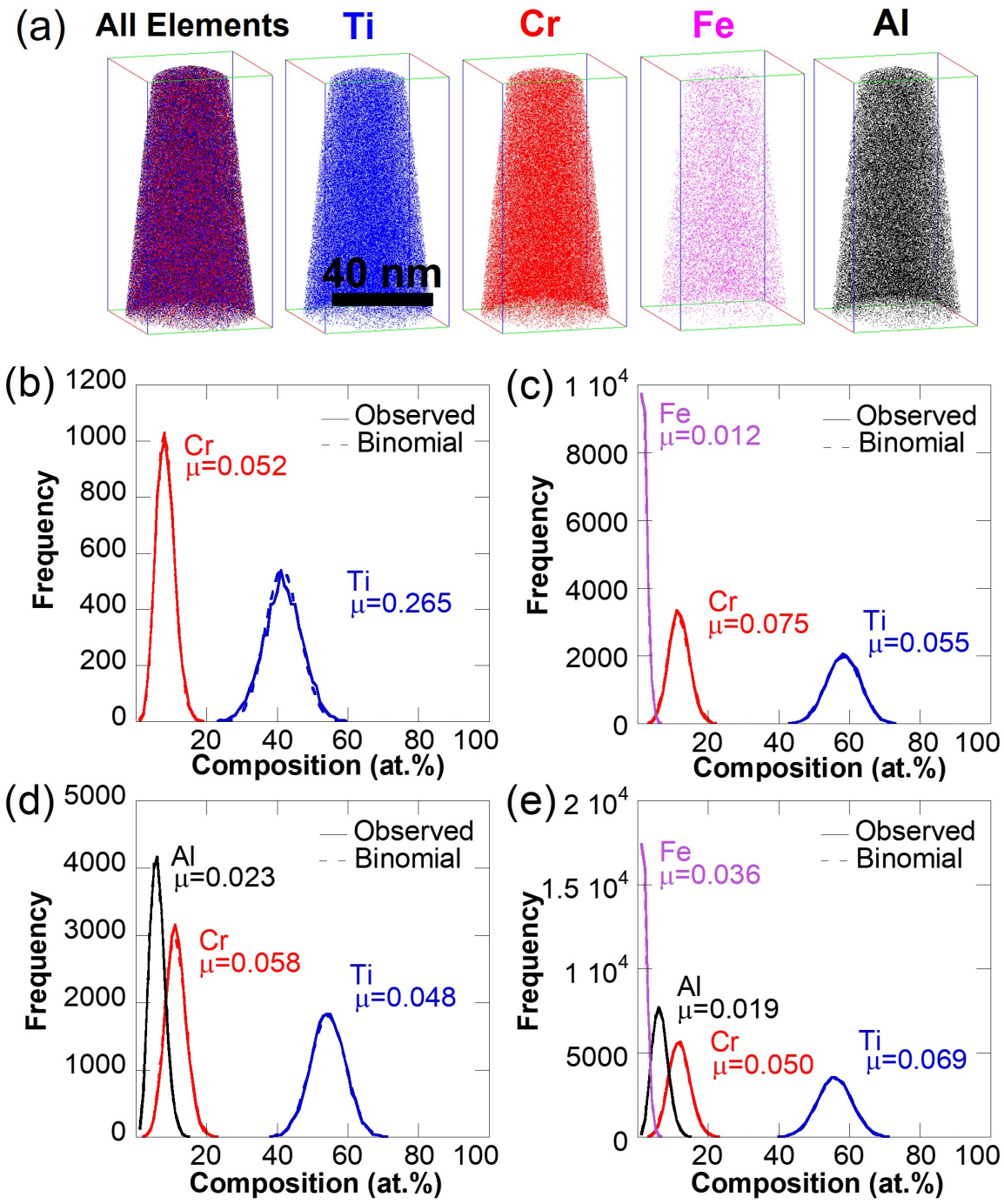

Figure 4.5: The (a) APT elemental distribution maps of a TCFA sample, which are representative of the elemental distributions in each alloy, showing a uniform distribution of ions. The frequency distribution functions for (b) TC, (c) TCF, (d) TCA, and (e) TCFA. The functions are representative of all samples studied, and include the Pearson coefficients (μ) for each distribution.

To quantitatively evaluate the composition distributions, the Pearson correlation coefficient (μ), which measures deviance from a random solid solution [194, 195], were calculated. μ was used instead of a χ^2 value because μ is independent of dataset size [193, 196]. A μ equal to 0 indicates a binomial distribution, while a μ equal to 1 indicates complete association between the chosen atoms [196]. Agreeing with the observation that the Ti distribution was less random in TC, the calculated μ of 0.265 for Ti in TC was the highest for Ti in each alloy. This μ value suggests that Ti is distributed more non-uniformly in TC than in the other alloys, which could affect the mechanical properties and phase transformations of the alloy. While other smaller deviations are visible in the frequency distributions in TCF, TCA, and TCFA, μ was <0.1 for all other distributions, indicating a closer to ideal homogeneous distribution in those alloys.

While the element distribution maps provided qualitative visual information regarding any partitioning of the elements and the frequency distribution analysis gives quantitative information on overall compositional segregation, radial distribution function (RDF) analysis can provide information on the spatial relationships of atoms [192]. RDF analysis provides information on the local neighborhood of the specified atoms in a radial direction, which allows for the determination of local ordering/clustering that other techniques cannot identify. RDFs for each alloy were created with respect to the ions from the Ti^{2+} peak at 24 Daltons (Da). This peak was selected because there was no overlap with other peaks in the Ti-Cr-Fe-Al alloy mass spectrum. Similarly, the 26 Da Cr^{2+}, 28 Da Fe^{2+}, and 13.5 Da Al^{2+} peaks were used in the analysis. The shell thickness for RDF was kept at 0.1 nm and RDF analysis was conducted for a maximum distance of 2 nm from the center Ti atoms. Because the first and second nearest neighbors can affect the E and G values in BCC metals, such as Ti, which show an allotropic transformation to the FCC or HCP phase [164], the distances from the center Ti atoms were normalized by a_β (3.22Å), which is the distance of the second nearest neighbor, see Figure 4.6. The RDFs were then normalized with the bulk concentration of each alloy to obtain the bulk normalized concentration shown in Figure 4.7. Each bulk normalized concentration plateaued after reaching a_β.

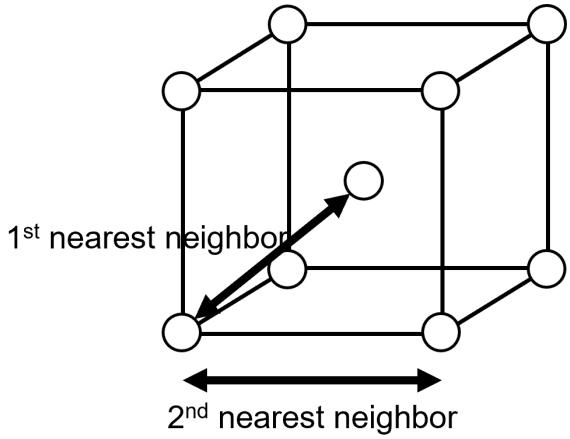

Figure 4.6: The BCC unit cell with a lattice parameter of 3.22Å, showing the distance between the first and second nearest neighbors.

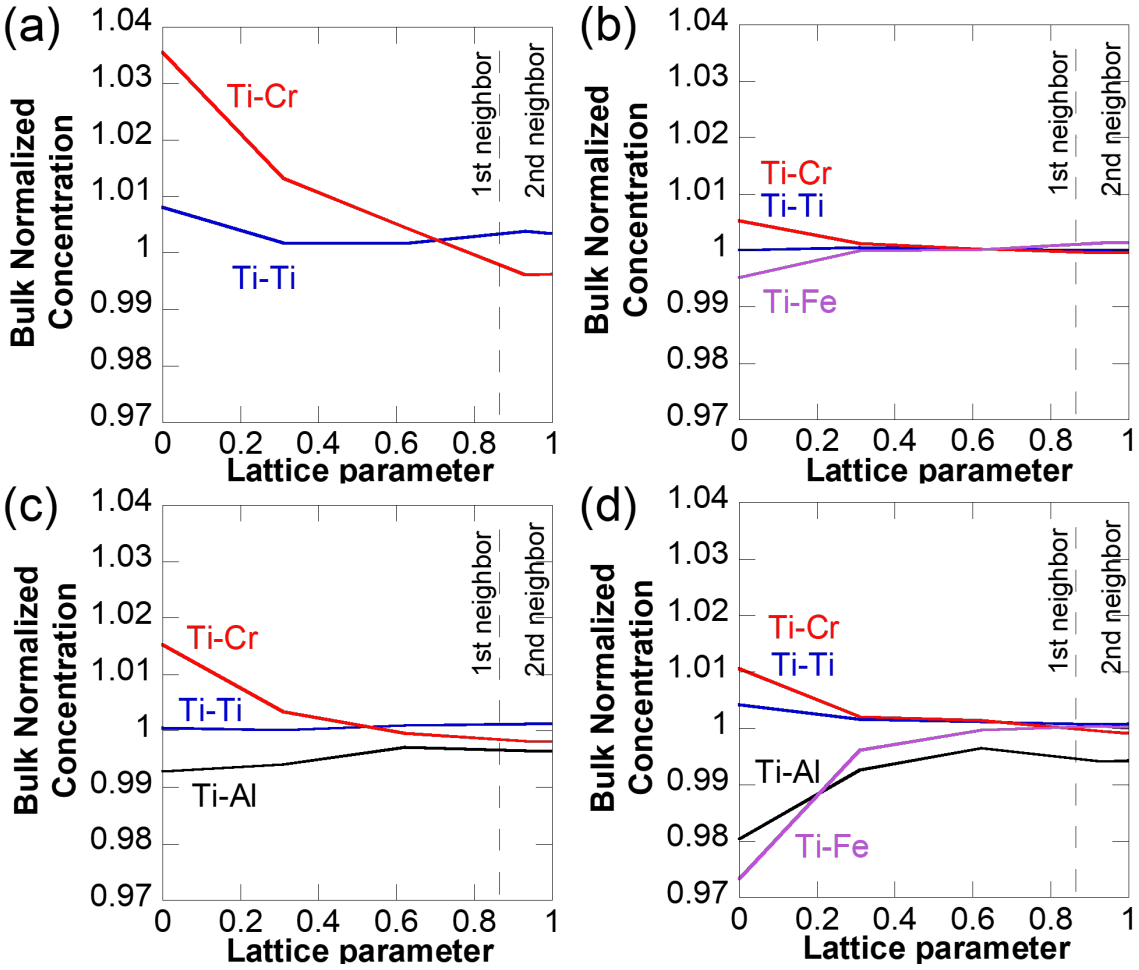

Figure 4.7: APT radial distribution functions of elemental concentrations for (a) TC, (b) TCF, (c) TCA, and (d) TCFA.

When the bulk normalized concentration of two atoms are greater than 1, there is a positive correlation, while a value of 1 indicates no correlation, and a value less than 1 means anti-correlation. At distances greater than 0.5 nm, the RDFs settle into constant values close to 1 for all alloys. However, within the first 0.5 nm, specific correlation trends are observed between center Ti atoms and all the other elements in all alloys. Ti had a positive correlation with Cr for each alloy. Ti also shows a slight positive correlation for other Ti atoms in TC. Fe has an anti-correlation in TCA and TCFA, with bulk normalized concentration being less than 1 in both alloys, although a correlation of 1 is approached as the distance increases to that of the first nearest neighbor. Al has an anti-correlation up to the second nearest neighbor in TCA and TCFA.

Although Ti-Cr and Ti-Ti showing a greater than 1 value appears to be contradictory, it is possible since each sample contained impurity elements such as O, H, or Ga, see Table 4.4, that were not included in the RDF analysis. Since the impurity elements were not included, it is not expected that the average bulk normalized concentration of each alloy be 1 for all distances.

4.2 Characterization of the β-homogenized mechanical properties

Tensile testing, RUS, and Vickers microhardness and Rockwell B hardness were used to investigate the E, σ_y, UTS, ϵ_f, G, and hardness values of each alloy. SE SEM imaging was used to investigate the fracture surfaces of the tensile samples.

No significant difference was found in the Vickers microhardness or Rockwell B hardness values of each alloy.

Although each alloy underwent the same processing, TC exhibited the highest average σ_y and UTS values, TCF and TCFA exhibited similar intermediate σ_y and UTS values, and TCA exhibited the lowest σ_y and UTS values. TCF and TCFA exhibited higher ϵ_f values than TC and TCA. Even though the ϵ_f values of each alloy were different, evidence of only ductile failure was found on every fracture surface.

TC exhibited the highest E and G values. TCF exhibited a lower E and G than TC, and TCA exhibited a lower E and G value than TCF, as hypothesized. However, TCFA did not exhibit the

lowest E and G values as hypothesized, and instead exhibited similar E and G values to TCF.

The results of the hardness, RUS, tensile testing, and fracture surface experiments are presented below. The discussion of why the hypotheses were verified or not can be found in Section 5.2.

4.2.1 Vickers microhardness

Vickers hardness and Rockwell B hardness were used to test the hardness of each alloy, and the results are shown in Figure 4.8(a) and (b), respectively. No significant difference in either Vickers or Rockwell B hardness values was exhibited between the alloys.

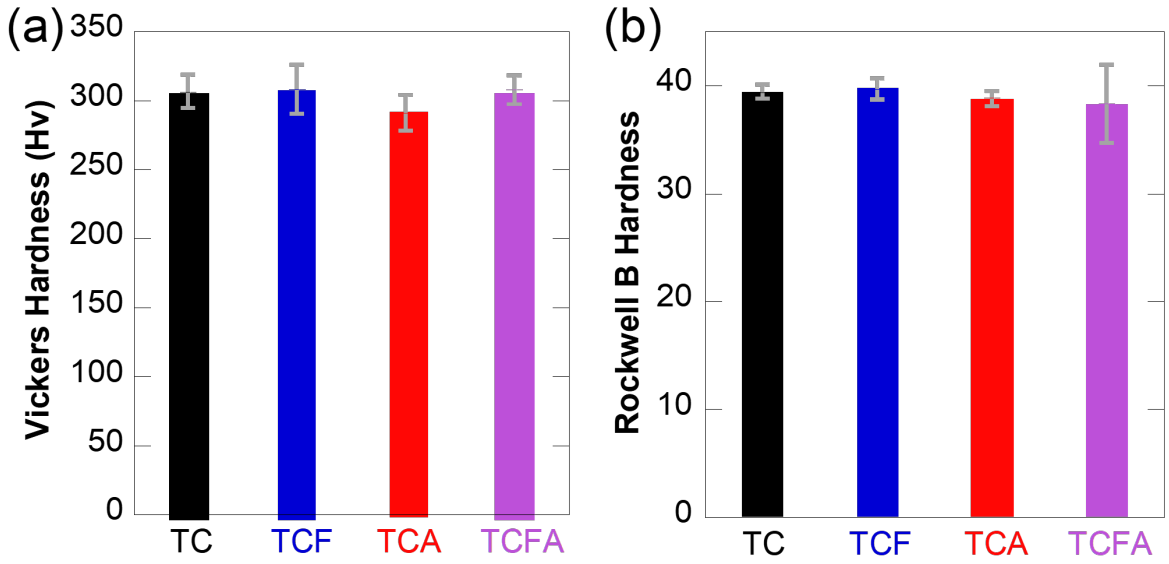

Figure 4.8: The average (a) Vickers microhardness values and (b) Rockwell B hardness values measured for each alloy. The error bars show ±1 standard deviation from the average.

4.2.2 RUS

RUS was used to determine the G of each alloy at RT. The G values for TCF, TCA, and TCFA were 33 GPa, 30 GPa, and 33 GPa, respectively, measured from 1 sample each. For TC, two samples were measured, and the G values were 37 GPa and 40 GPa.

4.2.3 Tensile testing

Two tensile tests were performed per alloy, and the RT stress-strain curves are shown in Figure 4.9. In both tests, TC exhibited the highest E while TCA exhibited the lowest E. TC exhibited higher average σ_y and UTS values than TCF, TCA, and TCFA. TCF, TCA, and TCFA exhibited similar σ_y and UTS values, seen in Figure 4.9. TC and TCA exhibited similar ϵ_f values, which were less than the ϵ_f values of TCF and TCFA. TCF exhibited the highest ϵ_f at 12.4%.

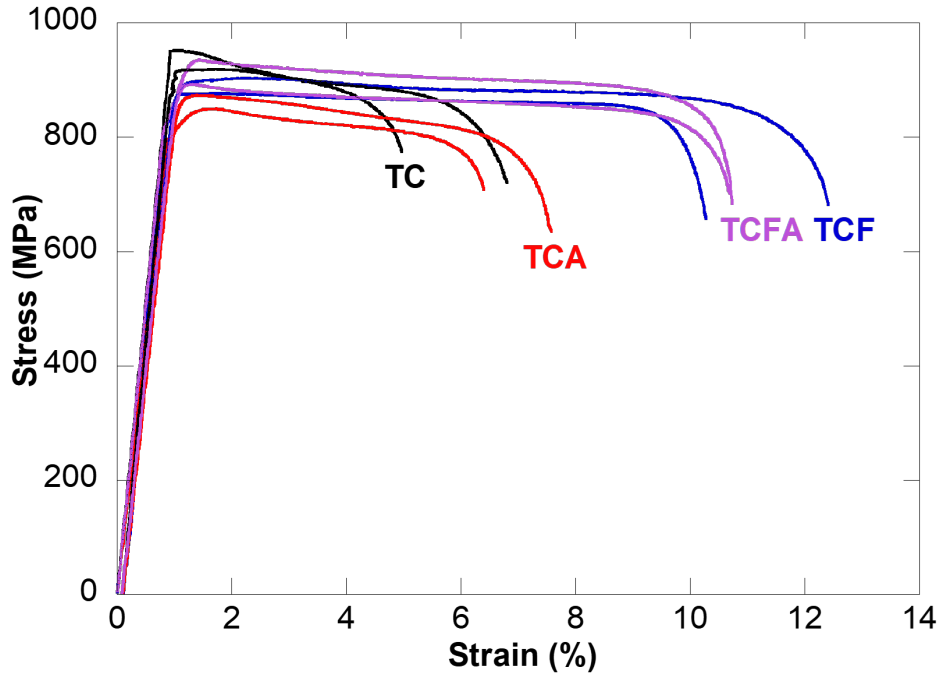

Figure 4.9: Engineering stress versus strain curves for the β-homogenized TC, TCF, TCA, and TCFA. Two tests per alloy were performed.

From the tensile curves shown in Figure 4.9, the tensile properties in Table 4.5 were calculated. The E, σ_y, UTS, and ϵ_f values were calculated using sections 7.7.1, 7.10, and 7.11.5 of ASTM standard E8-E8M-13a.

4.2.4 Fracture surface imaging

A single fracture surface per alloy was viewed in the SEM to examine the fracture features. These surfaces are shown in Figures 4.10, 4.11, 4.12, and 4.13 for TC, TCF, TCA, and TCFA respectively. Each alloy exhibited dimples on its fracture surface, indicative of ductile fracture.

Table 4.5: Summary of the tensile properties of the β-homogenized alloys.

Alloy	**E (GPa)**	σ_y **(MPa)**	**UTS (MPa)**	ϵ_f **(%)**
TC	102, 105	917, 955	919, 955	5.0, 6.7
TCF	96, 99	873, 886	876, 903	10.2, 12.4
TCA	89, 92	825, 860	849, 872	6.4, 7.5
TCFA	93, 101	871, 885	892, 935	10.6, 10.7

Higher magnification SEM images of the dimples are provided in Figures 4.10(b-d), 4.11(b,c), 4.12(b), and 4.13(b,c) for TC, TCF, TCA, and TCFA, respectively.

Tearing ridges were also observed on the fracture surfaces, another characteristic of ductile fracture, see Figures 4.10(b,d), 4.11(b), and 4.13(c). The different angles and ridges on the fracture surfaces could be related to the crystallographic orientations of the β-grains with respect to the direction of force on the tensile samples.

Dimples of multiple sizes were observed on each fracture surface. The larger microvoids on the surfaces could be from smaller grain within the microstructure, where the grain could have pulled and fractured along the axis of the grain. The larger microvoids are not expected to be related to any precipitates in the microstructure, as the alloys were fully β-homogenized.

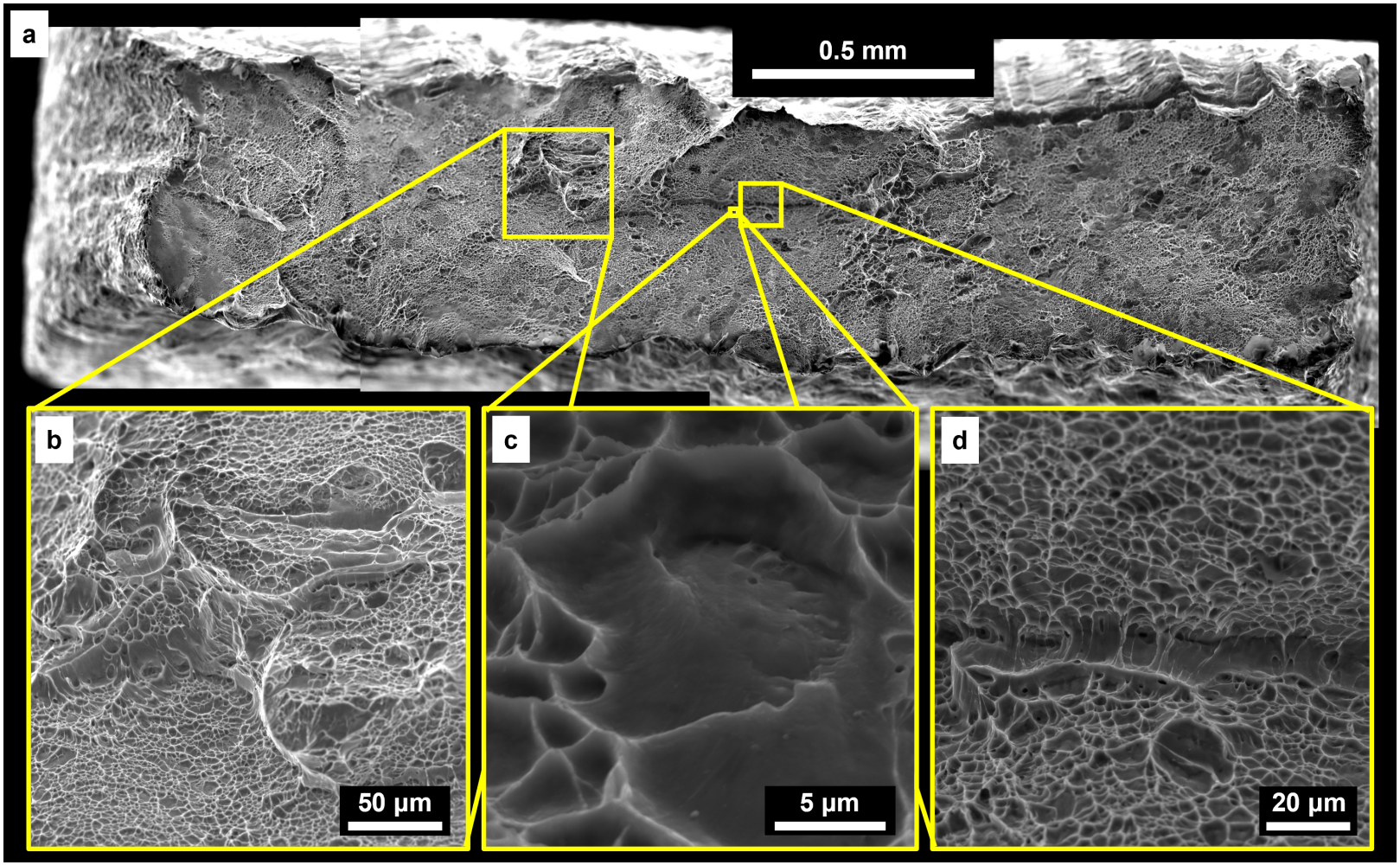

Figure 4.10: (a) SE SEM photomicrographs of the fracture surface from a β-homogenized TC tensile test sample, stitched together using multiple photomicrographs. (b-d) Higher magnification SE SEM photomicrographs illustrating dimples and tearing.

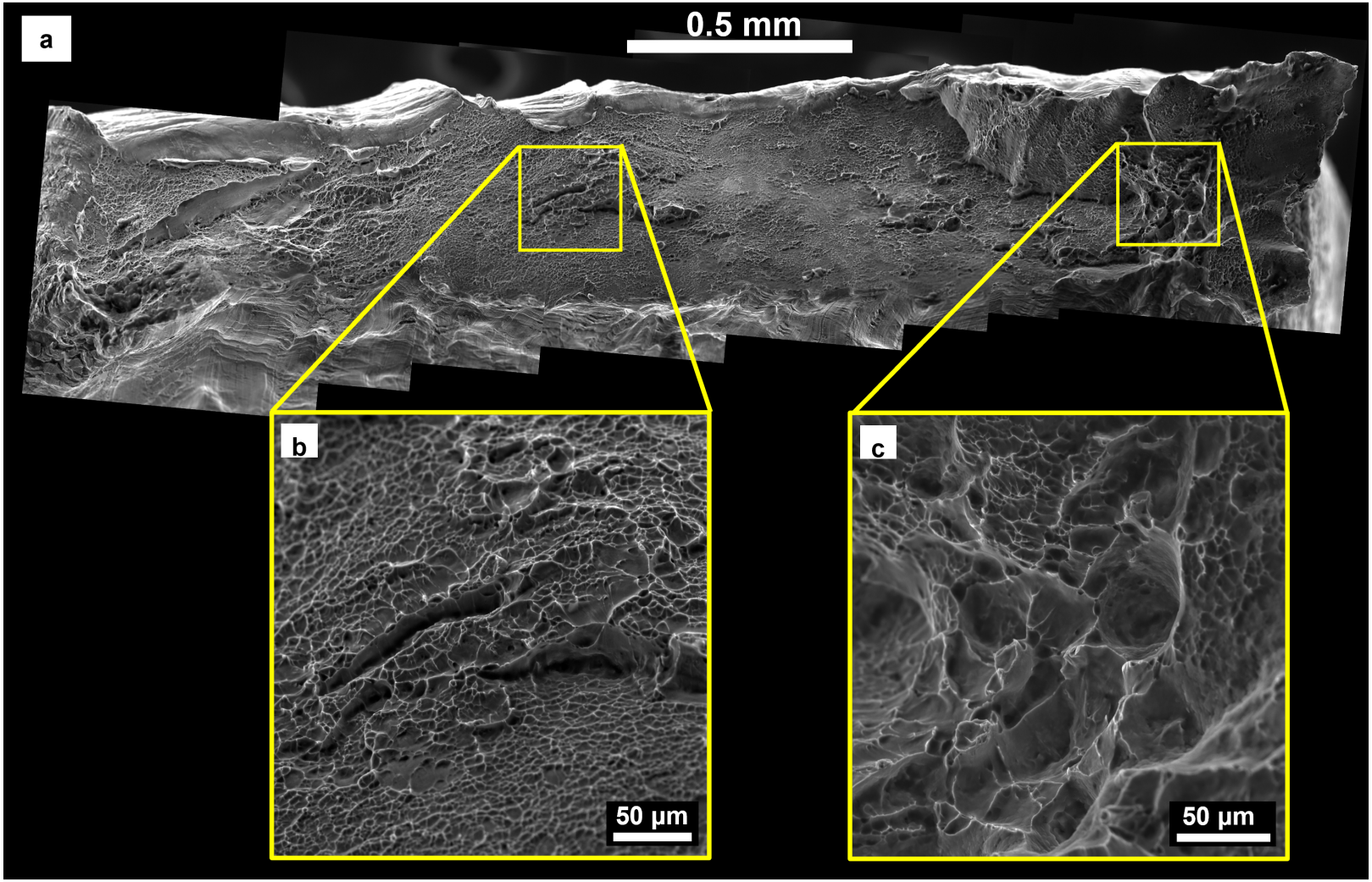

Figure 4.11: (a) SE SEM photomicrographs of the fracture surface from a β-homogenized TCF tensile test sample, stitched together using multiple photomicrographs. (b, c) Higher magnification SE SEM photomicrographs illustrating dimples and tearing.

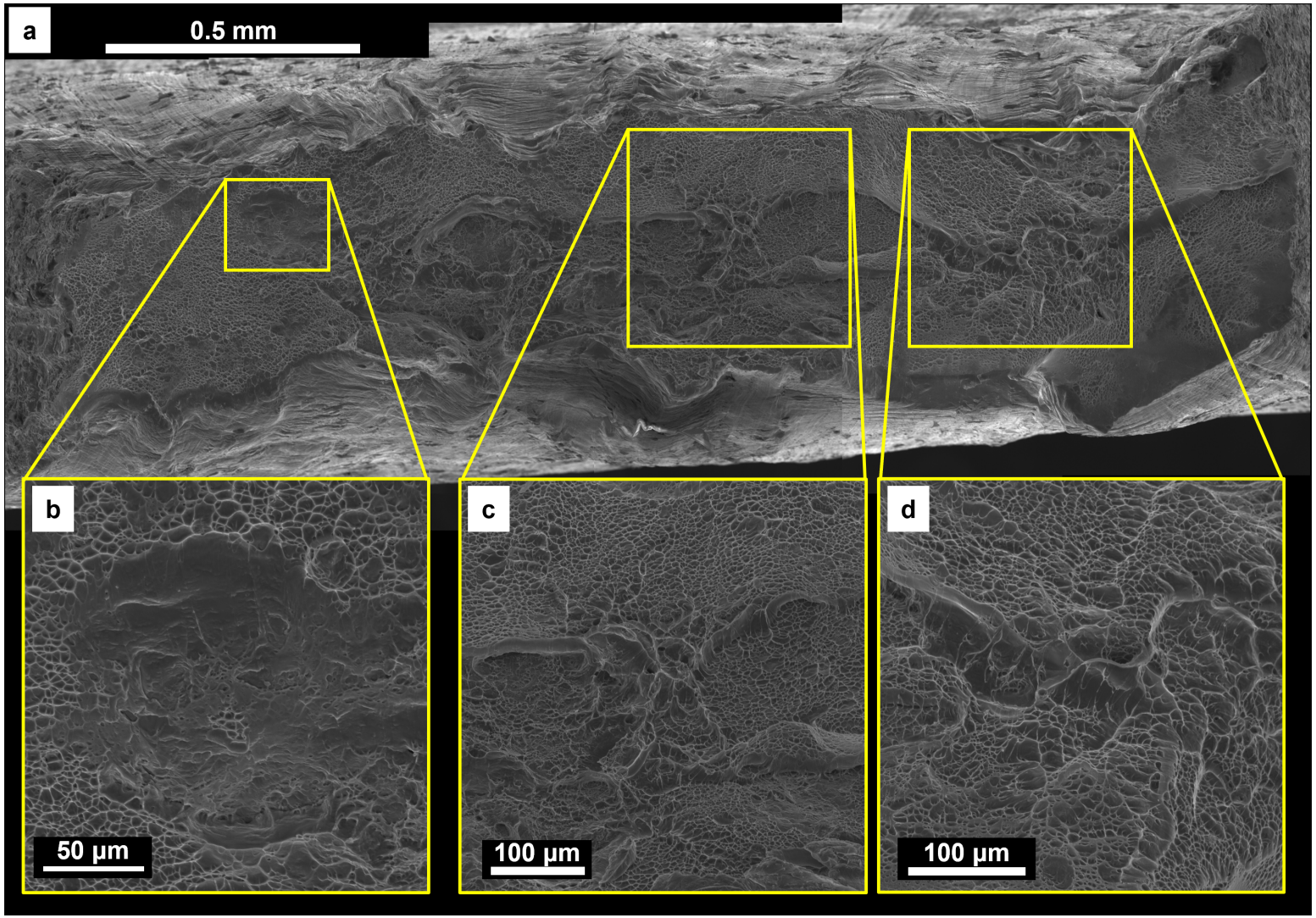

Figure 4.12: (a) SE SEM photomicrographs of the fracture surface from a β-homogenized TCA tensile test sample, stitched together using multiple photomicrographs. Higher magnification SE SEM photomicrograph illustrating (b) a large and smaller dimples and (c, d) dimples and tearing.

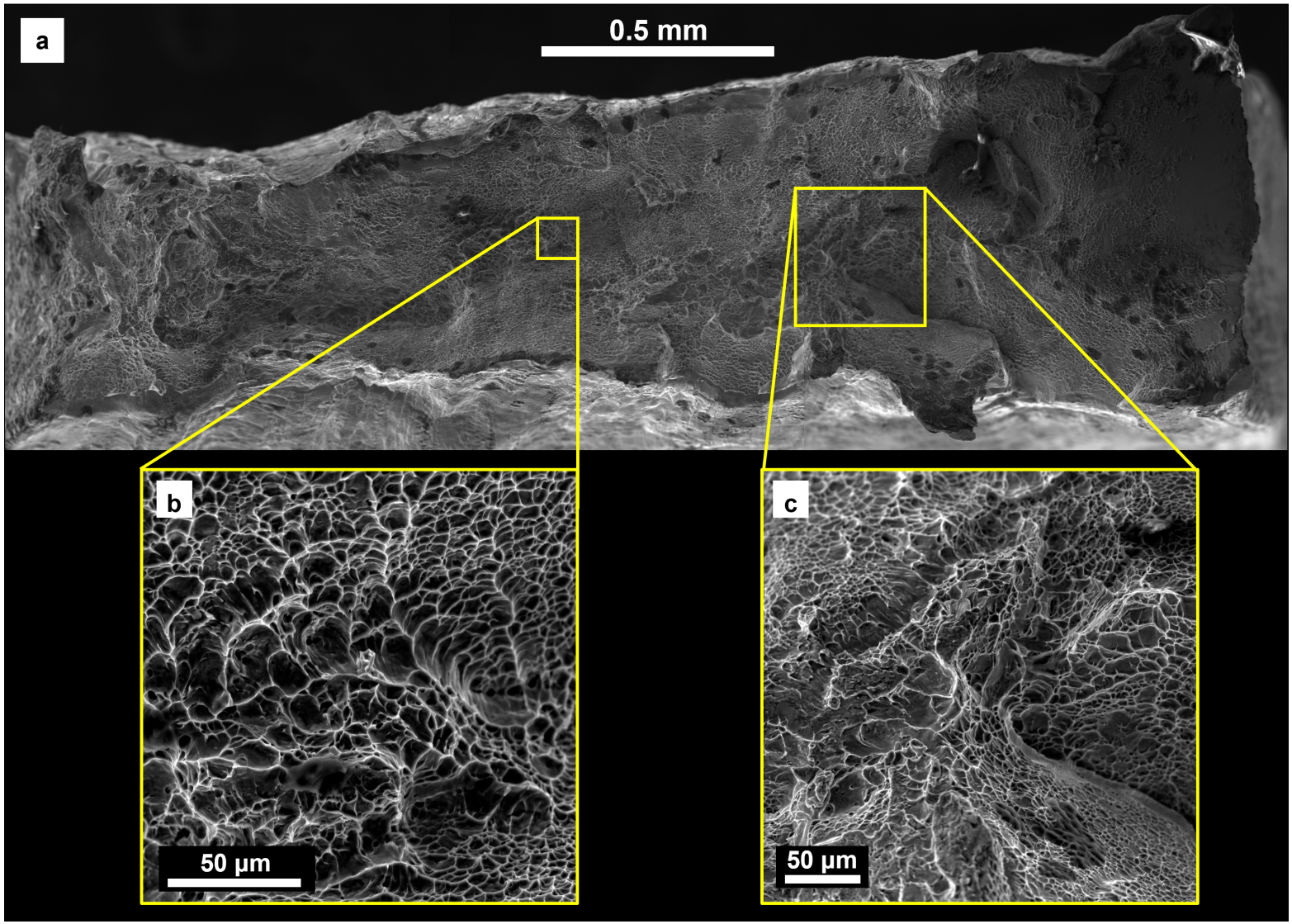

Figure 4.13: (a) SE SEM photomicrographs of the fracture surface from a β-homogenized TCFA tensile test sample, stitched together using multiple photomicrographs. (b, c) Higher magnification SE SEM photomicrographs illustrating dimples and tearing.

CHAPTER 5

DISCUSSION OF β-HOMOGENIZED ALLOYS

In Chapter 4, the results from testing the hypotheses regarding the β-homogenized TC, TCF, TCA, and TCFA were presented. Those results determined whether the hypotheses were correct or incorrect. In this chapter, a discussion of why the hypotheses were correct or incorrect is presented.

In the first section of this chapter, the hypotheses regarding the microstructural characterization are discussed. In the second section of this chapter, the hypotheses regarding the mechanical properties are discussed.

5.1 The effects of Fe and Al on the β-homogenized microstructure

The hypotheses regarding how the Fe and Al additions affected the microstructure of the β-homogenized alloys were as follows:

1. The alloys were fully β-homogenized. If this hypothesis is incorrect and the the α phase was present, it would appear at the grain boundaries due to greater diffusion rates at the boundaries.

2. The alloys would possess similar grain sizes.

3. The alloying elements would be randomly distributed in the microstructure.

4. The alloys' β-phase lattice parameters would be less than that of pure Ti.

5. The small additions of Fe and Al would not affect the β-phase lattice parameters significantly.

The discussions of why each hypothesis was found to be true or false through the XRD, SEM, and APT experiments are presented below.

5.1.1 Microstructural characterization

The hypothesis that the alloys were fully β-homogenized was proven true using XRD and BSE-SEM imaging. The XRD results only found evidence of the β phase in each alloy, and the BSE-SEM imaging of inside the β grains and along the grain boundaries did not find any evidence of the α phase. The α case that was observed along the edges of the forged blocks did not extend into the bulk of the material, and would not have affected any of the other experiments. This hypothesis was true because the β-homogenization treatment and the composition of each alloy were designed to achieve a fully β-phase microstructure.

Each alloy was homogenized at 900 °C, above the β-transus temperature of 882 °C for pure Ti, and well above the 667 °C α-to-β transition temperature for the binary Ti-11Cr alloy [2, 7]. Holding each alloy at 900 °C for one hour and then quenching (according to the β-homogenization process) would allow the β-phase microstructure to be retained at RT.

For 100% of the β-phase microstructure to be retained after quenching from above the β-transus temperature, a Mo-Eq of 10 is required [17]. The Mo-Eq values of TC, TCF, TCA, and TCFA are all greater than 10, see Table 5.1. While the addition of the α-stabilizer Al does reduce the Mo-Eq of TCA and TCFA, the Mo-Eq values are still above 10, so they would still be expected to retain 100% of the β phase upon quenching.

Table 5.1: The Mo-Eq values of TC, TCF, TCA, and TCFA, calculated using the ICP-AES/NDIR bulk concentrations for each alloy.

Alloy	Mo-Eq
TC	19.3
TCF	22.6
TCA	16.7
TCFA	19.6

Although each alloy underwent the same levitation melting, hot forging, and β-homogenization process, and each alloy retained 100% β-phase upon quenching, the hypothesis that the alloys would possess similar grain sizes was false. The alloys possessed a range of grain sizes, with TC

exhibiting the smallest grain size, TCF and TCFA exhibiting intermediate grain sizes, and TCA exhibiting the largest grain size.

It is possible that Fe and Al affected the grain size during the levitation melting, hot forging, and β-homogenization process. However, since grain size increased when Fe was added to TC, and when Al was added to TC, if alloying element was driving the difference in grain size, TCFA would be expected to have the largest grain size. Since TCFA exhibited an intermediate grain size, it is more likely that the processing of the alloys affected grain size instead of Fe or Al addition.

Whereas each alloy underwent the same processing, the heating rates, temperatures, and time spent hot forging each alloy is not known. Alloy grain size at each step of the processing is also not known. If the grain sizes were different before the β-homogenization process, the grain size after the homogenization process would be different, with a finer grain size before the homogenization promoting recrystallization during the homogenization process [197]. Defects in the microstructure can also affect recrystallized grain size. If more defects were present in TC than in the other alloys, a finer recrystallized grain size would occur [197]. Dynamic recrystallization can also occur in β-Ti alloys during hot forging, which could reduce the average grain size of the alloys by introducing smaller β grains at the existing β-grain boundaries [198]. Dynamic recrystallization is sensitive to temperature, so inconsistent temperatures throughout the material during the hot forging could affect the grain size as well [198]. More information is needed on the evolution of the microstructure during the hot forging and β-homogenization process to determine whether inconsistencies in the process or the alloying elements affected the grain size of each alloy.

5.1.2 Alloying element distribution

The results from the APT experiments supported the hypothesis that the alloying elements were randomly distributed in the microstructure, with some local ordering between Ti and Cr, Fe, and Al. This was expected as the levitation melting, hot forging, and β-homogenization process were designed to randomly distribute the alloying elements in a β-phase microstructure.

The local ordering measured using the RDFs has implications for the E and G values of the

alloys, as a shorter distance between atoms implies a stronger bond between those atoms, and bond strength directly affects elastic modulus [199]. According to the bond order (Bo), or the average number of bonds formed by two atoms, Ti atoms should have the strongest bond between them, as Ti-Ti has the highest Bo at 2.790. Cr should have the next strongest bond with a Bo of 2.779, followed by Fe with a Bo of 2.651, followed by Al with a Bo of 2.426 [164].

The RDFs agree with the Bo for Ti and Fe and Ti and Al, with Fe and Al both exhibiting bulk normalized concentrations less than 1 in TCF, TCA, and TCFA. However, Cr exhibited a bulk normalized concentration greater than 1 in each alloy, while Ti exhibited a bulk normalized concentration of 1, suggesting that Cr has a stronger bond with the Ti atoms than other Ti atoms. Factors other than Bo could be affecting the local ordering of the alloying elements.

5.1.3 β-phase lattice parameters

The hypothesis that the alloys' a_β would be less than that of pure Ti and the hypothesis that the small additions of Fe and Al would not affect a_β significantly were both shown to be true. Calculating a_β from the peak positions in the XRD profiles, the a_β of each alloy was 3.22Å, agreeing with Ti-Cr-Nb alloys with similar Cr compositions [162], and which is less than that of pure Ti at 3.282Å [166].

The reduced a_β of the Ti-Cr alloys compared to pure Ti appears to contradict the Bo of Ti, Cr, Fe, and Al; according to Bo, pure Ti should exhibit the smaller a_β as the Bo of Ti and Ti is greater than Ti and Cr, Fe, or Al. a_β may have some relationship with Bo, but has a much stronger relationship with the average d-shell energy (Md) of the alloying elements, average atomic radius of the alloying elements, and overall β stability as described by Mo-Eq, see Figure 5.1.

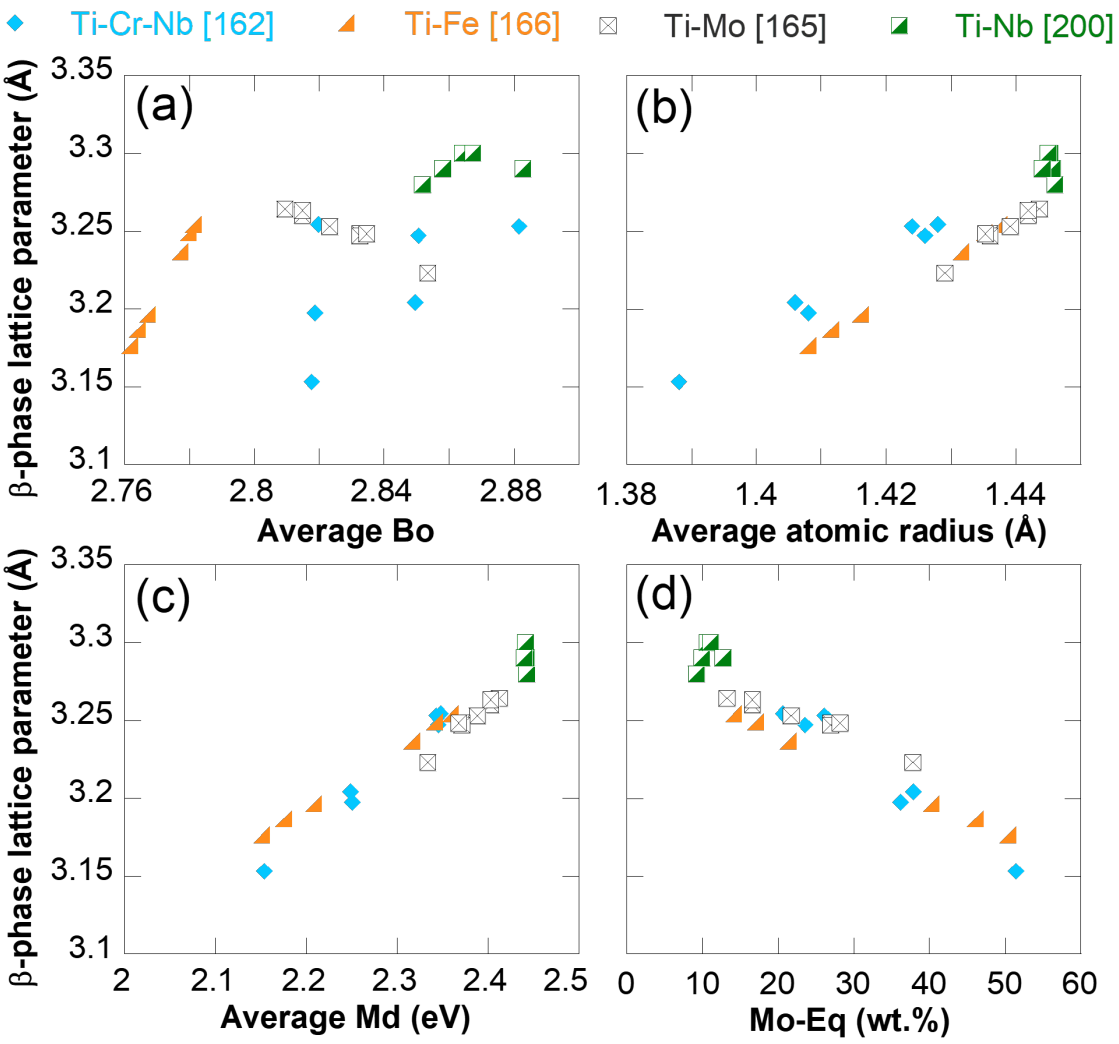

Figure 5.1: The β-phase lattice parameter of Ti-Cr-Nb alloys [162], Ti-Fe alloys [166], Ti-Mo alloys [165], and Ti-Nb alloys [200] as a function of average (a) Bo, (b) average atomic radius, (c) average Md, and (d) Mo-Eq.

a_β decreases with decreased atomic radius and Md and increased Mo-Eq. The decreasing a_β is correlated with higher concentrations of alloying elements. β-stabilizing alloying elements generally have a smaller atomic radius than Ti, see Table 5.2, so higher concentrations of alloying elements should result in a smaller average radius [201]. Md shows a relationship with a_β because atomic radius is directly influenced by the outer electron shell [201]. Mo-Eq also shares the relationship because higher Mo-Eq values correlate with higher alloying element concentrations, which result in lower average atomic radii. β-Ti alloys show a strong relationship between Md,

atomic radius, and Mo-Eq, see Figure 5.2, so further discussions of a_β and alloying element concentration in Section 7.1.2 include all three parameters. The relationship between a_β and alloying element concentration is further discussed in Sections 6.1.1.2 and 7.1.2.

Table 5.2: The atomic radii for Ti and some of its β-stabilizing alloying elements, as reported by Callister [201].

Element	Atomic radius (Å)
Ti	1.45
Cr	1.25
Nb	1.43
Mo	1.36
Fe	1.24

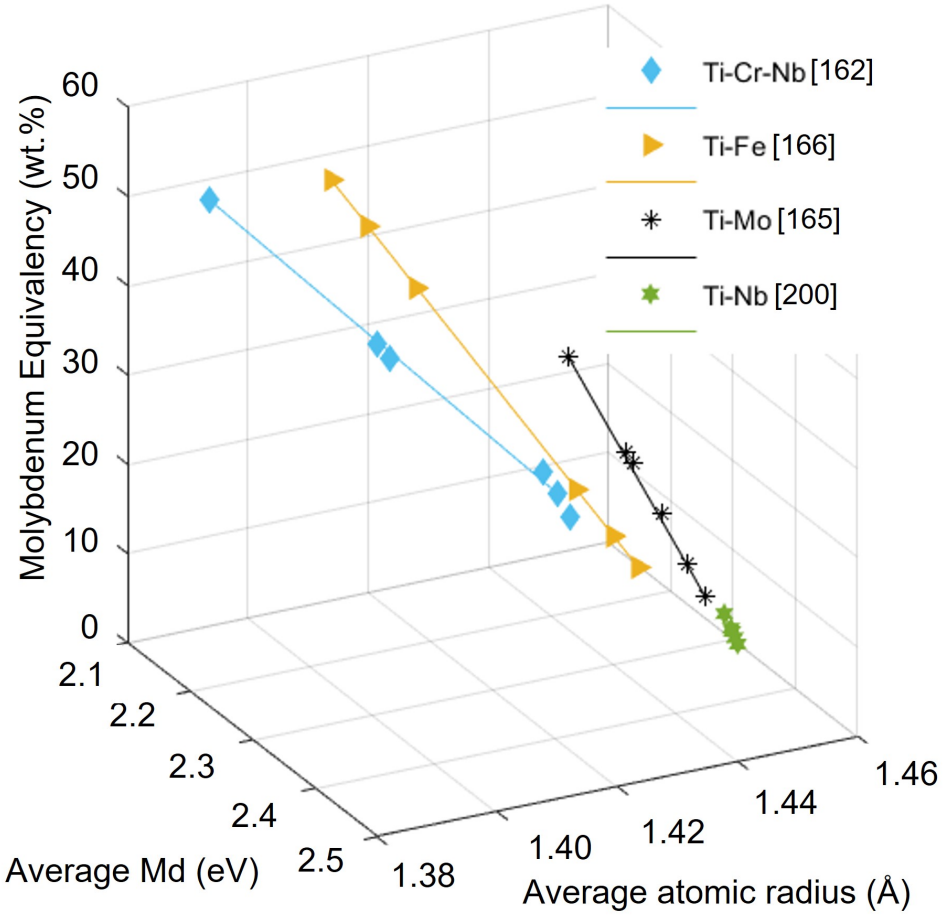

Figure 5.2: The Mo-Eq values of TC, TCF, TCA, TCFA, Ti-Cr-Nb [162], Ti-Fe [166], Ti-Mo [165], and Ti-Nb [200] alloys as a function of average atomic radius (Å) and average Md (eV).

Considering the relationships between a_β and atomic radius, the reduced a_β of the Ti-Cr alloys compared to pure Ti can be attributed to the smaller radius of Cr (1.25 Å) compared to Ti (1.45 Å). The Al addition did not affect the a_β of TCA or TCFA compared to TC because Al has a similar radius to Ti at 1.43 Å. The radius of Fe is smaller than Ti or Cr, at 1.24 Å, but the addition of 0.85% was not large enough to affect the a_β of TCF or TCFA significantly compared to TC.

5.2 The effects of microstructure on the mechanical properties

The hypotheses regarding how the microstructure of the β-homogenized alloys affected their mechanical properties were as follows:

1. As the microstructure of each alloy was hypothesized to be similar, the hardness, σ_y, UTS, ϵ_f values, and fracture mechanisms should also be similar.

2. The 0.85% Fe addition will reduce the bond strengths and moduli in TCF more than in TC.

3. The 5.3% Al addition will reduce the bond strengths in TCA more than the 0.85% Fe addition in TCF, and TCA will exhibit lower moduli than TCF.

4. Adding both Fe and Al will reduce the bond strengths in TCFA the most, and TCFA will exhibit the lowest moduli of TC, TCF, and TCA.

The discussions of why each hypothesis was found to be true or false through the XRD, SEM, APT, Vickers microhardness, Rockwell B hardness, RUS, and tensile experiments are presented below.

5.2.1 Hardness

The hypothesis that each β-homogenized alloy would exhibit similar hardness values was true. Even though each alloy exhibited different grain sizes, each alloy exhibited similar Vickers microhardness and Rockwell B hardness values. The variance in the measurements, while small, could be due to the orientation of the β grains with respect to the tested surface. The Vickers microhardness measurements show more variation between the alloys than the Rockwell B hardness measurements.

The Vickers microhardness indents were approximately 50 µm along the diagonal, which could fall within a single grain in each alloy. Different grain orientations could thus affect the Vickers microhardness measurements more than the Rockqell B hardness measurements, since the Rockwell B indents were approximately 100 µm, and resulted in measurements averaging multiple grains. Since both Vickers microhardness and Rockwell B hardness tests reported similar hardness values for each alloy, grain size did not appear to significantly influence the hardness.

Grain size did not significantly affect the hardness measurements because the primary hardening mechanism of β-Ti alloys is the precipitation of secondary phases, such as the ω or α phases, in the microstructure [7]. Some grain size effects have been explored by Kao et al. [202], who found that β-Ti alloys increased in hardness with increased grain size. The increase in hardness was associated with a higher dislocation density and the formation of martensite in the larger grains rather than grain boundary effects, and which were only observed when the grains were larger than 1000 µm [202]. Since the alloys were fully β-homogenized, and the grain sizes of TC, TCF, TCA, and TCFA were at least 10 times less than the size needed for the grain size effects reported by Kao et al. [202], similar hardness values were expected for each alloy.

5.2.2 σ_y and UTS

The hypothesis that the σ_y and UTS of each alloy would be similar was dependent on the assumption that the microstructure of each β-homogenized alloy would be similar. Because each alloy exhibited different grain sizes, this hypothesis was shown to be false.

A smaller grain size was expected to coincide with a higher strength, as the grain boundaries would prevent the movement of dislocations through the material. σ_y decreased linearly with increasing grain size, see Figure 5.3(a). UTS also decreased with increasing grain size, but did not correlate as strongly as σ_y, see Figure 5.3(b). This decrease in σ_y with increasing grain size does not agree with the results presented by Doraiswamy and Ankem, who reported no change in σ_y for a Ti-9.4Mn(wt.%) alloy with grain sizes between 100 and 500 µm [203]. However, Wang et al. found for a Ti-38Nb-0.2O(wt.%) alloy that σ_y decreased roughly linearly from approximately

620 MPa to 600 MPa when the grain size was increased from 8 to 128 µm.

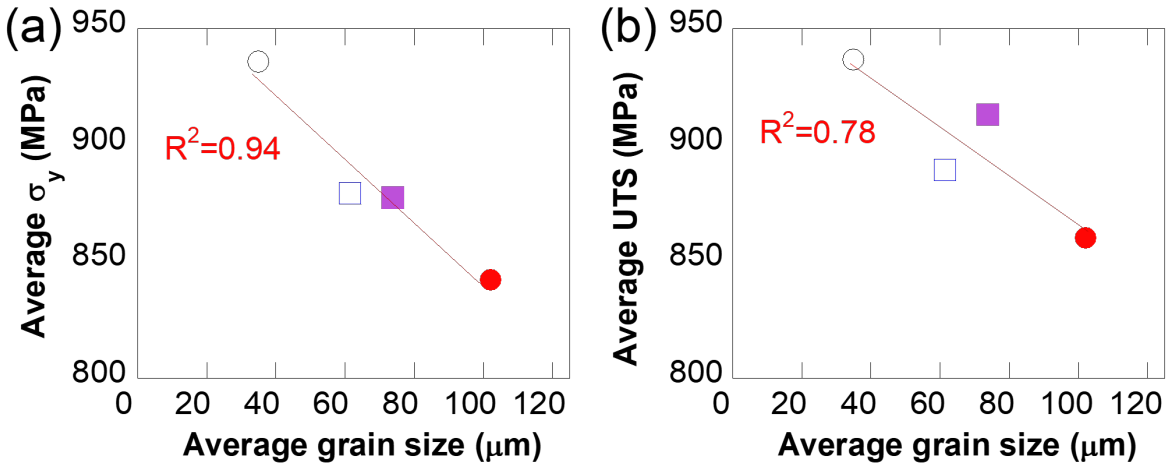

Figure 5.3: The (a) average yield stress and (b) average ultimate tensile strength versus the average grain size of each alloy. Linear curve-fits and the coefficients of determination (R^2) for the datasets are included. An R^2 of 0.95 or greater indicates correlation.

Hardness and strength usually correlate, with higher hardness equating to higher σ_y and UTS values [201]. The discrepancy between the hardness values, which are similar between each alloy, and σ_y and UTS values, which varied between each alloy, is surprising. σ_y and UTS were influenced by grain size, which did not influence the hardness measurements. As discussed in Section 5.2.1, hardness in β-Ti alloys is not significantly influenced by grain size when the grains are smaller than 1000 µm [7, 202]. Thus, with a β-homogenized structure, hardness would not necessarily reflect strength in TC, TCF, TCA, and TCFA.

5.2.3 Elastic moduli

Three hypotheses regarding E and G were proposed. The first hypothesis, that Fe would reduce E and G when added to TC, was true. The second hypothesis, that Al would reduce E and G more than Fe when added to TC, was true. The third hypothesis, that the Fe and Al additions together would reduce E and G more than when added alone was false.

The hypotheses regarding E and G were developed based on the Bo between Ti and Ti, Cr, Fe, and Al. According to the bond order (Bo), adding Fe or Al should reduce the average Bo of the

alloy. Since Bo and bond strength are analogous, a higher average Bo should result in higher E and G values [164, 199]. Considering the Bo for Cr, Fe, and Al in Ti (2.779, 2.651, and 2.426, respectively), TC should have the highest average Bo, TCF should have the next highest average Bo, TCA the next, and TCFA the lowest average Bo [164], and E and G were predicted to reflect that. The RDFs of the APT data also support that TC would exhibit the highest E and G, as Ti and Cr were more associated with each other, suggesting a stronger bond. The RDFs also supported that Fe and/or Al would reduce the E and G, as Fe and Al were less associated with Ti, suggesting a weaker bond.

The reason why TCFA exhibited a higher E and G than TCA is not known at this time. Further investigation into the reason why could explain the synergistic effects of Fe and Al on E and G.

5.2.4 ϵ_f

The hypothesis that the ϵ_f of each alloy would be similar was dependent on the assumption that the microstructure of each β-homogenized alloy would be similar. Since the assumption was incorrect, and each alloy exhibited different grain sizes, each alloy exhibited different ϵ_f values.

One possible way grain size affected ϵ_f is through the critical stress needed for stress-induced martensite (SIM). β-Ti alloys that form SIM are known to have enhanced formability, and so SIM could have a significant effect on ϵ_f [7]. SIM is very sensitive towards alloy composition [7], but Wang et al. [204] found a relationship between the critical stress for SIM and grain size, where the critical stress decreased to a minimum and then increased again as the grain size increased from 8 µm to 128 µm. The grain sizes of TC, TCA, TCF, and TCFA were within that range, and extrapolating from Figure 12(b) of Wang et al., the grain sizes of TCF and TCFA fell close to the minimum critical stress for SIM, see Figure 5.4(a) [204]. Plotting the average ϵ_f of each alloy against the extrapolated critical stress for SIM found that the average ϵ_f decreased linearly with increased critical stress, see Figure 5.4(b). TCF and TCFA have theoretically lower critical stresses for SIM than TC and TCA, and could be activating more martensitic transformations during deformation, which could result in the higher ϵ_f values of TCF and TCFA compared to TC and

TCA.

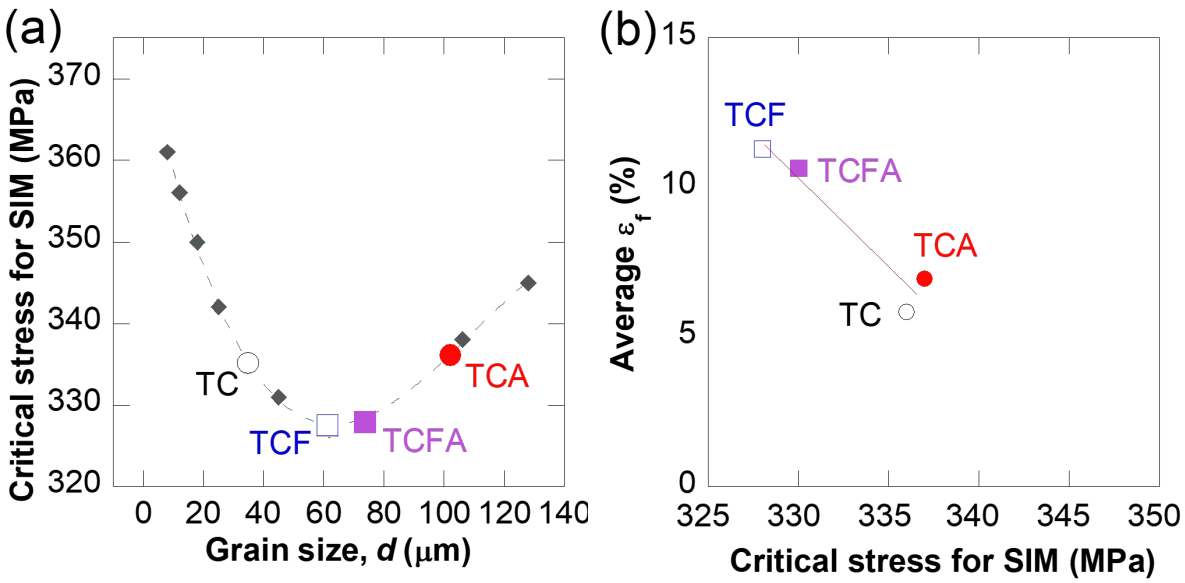

Figure 5.4: The (a) relationship between critical stress for stress induced martensite (SIM) and grain size, recreated from Wang et al. [204], with extrapolated TC, TCF, TCA, and TCFA values included. The (b) average elongation-to-failure (ϵ_f) versus the critical stress for stress-induced martensite (SIM). The critical stress for SIM was extrapolated from data in Wang et al. [204]. A linear curve-fit and the coefficient of determination (R^2) for the dataset are included. An R^2 of 0.95 or greater indicates good correlation.

Although grain size did affect the alloys' ϵ_f, each alloy exhibited dimples and tearing ridges on their fracture surfaces, indicative of ductile fracture typical of the β phase in β-Ti alloys. No features that would explain the different ϵ_f values were observed on the fracture surfacecs.

CHAPTER 6

RESULTS OF AGED ALLOYS

The following questions summarize some of the research gaps outlined in Section 2.6:

1. How do the β- and α-phase stabilizers affect the microstructural evolution during the phase transformations in the Ti-Cr alloy system?

2. Where do such alloying elements (and interstitials) diffuse and how do they affect the phase transformations?

3. How do the microstructural changes affect the mechanical properties of the Ti-Cr alloy system?

In Section 2.6.1, the first question was further broken into two separate questions: *how do the phase volume fractions change?*, and *how do the phase lattice parameters change?*. The first section of this chapter addresses these questions using the 400 °C in-situ XRD data, which was analyzed to identify the phase transformations and lattice parameter changes as a function of time. Once the phases were identified, Rietveld analysis of the XRD data was used to calculate the phase lattice parameters and the phase volume fractions. The overlap of the ω-, α-, and β-phase peaks, along with the broad nature of the peaks, led to difficulty in refining some of the XRD data. To verify the Rietveld phase volume fraction calculations, BSE SEM image threshold analysis was used. Threshold analysis was possible using BSE SEM imaging because of the difference in composition between the β matrix and the precipitated phases, resulting in a difference in contrast. Although threshold analysis had its own challenges, discussed in more detail in Section 6.1.2, it was able to supplement the Rietveld analysis results. The Rietveld analysis and threshold analysis results were used to test the following hypotheses:

Phase volume fraction hypotheses

- Fe would suppress the α- and ω-phase formation, therefore lower α-and ω-phase volume fractions would be expected in the Fe-containing alloys.
- The α-phase stabilizer Al would promote the α-phase formation, and higher α-phase volume fractions would be expected in the Al-containing alloys.

Phase lattice parameter hypotheses

- The diffusion of the β-stabilizers from the α and ω phases into the β phase would increase the stability of the β phase, and the relative β-phase stability of the alloying elements would decrease the β-phase lattice parameter.
- The diffusion of the α-stabilizer Al from the β phase into the α phase would affect the lattice parameter of the α phase in the Al-containing alloys differently than the Al-free alloys.
- The rejection of all alloying elements except Ti from the ω phase would cause the ω-phase lattice parameter to remain constant throughout the transformation. The Fe and Al additions would affect the ω-phase lattice parameter, as different ω-phase lattice parameters have been reported in β-Ti alloys of different compositions.

The XRD phase transformation results are presented first, followed by the Rietveld analysis deconvolution of the phase peaks throughout the 400 °C treatment. The Rietveld-calculated phase lattice parameter results are then presented, followed by the Rietveld-calculated phase volume fraction results and the BSE SEM threshold analysis results.

The hypotheses concerning the second question of where the alloying elements Cr, Fe, and Al diffuse, where the interstitial impurity elements O and H diffuse, and how this diffusion affects the phase transformations were also addressed in the first section of this chapter. The results for the diffusion of the alloying elements Cr, Fe, and Al are presented first, addressing the hypotheses that the β-stabilizers Cr and Fe would diffuse from the α and ω phases into the β phase, the α-stabilizer Al would diffuse from the β phase into the α phase, and the ω-phase would reject

any elements except Ti. The results for the location of the interstitial element O are presented second, addressing the hypothesis that the interstitial O would be present in higher concentrations in the α phase, and would cluster at the ω/β boundary, which could promote the ω-assisted α-phase transformation. The results for the location of the interstitial element H are presented third, addressing the hypothesis that the interstitial H would be present in higher concentrations in the β phase than any other phase, and that if enough H was present in the sample, equilibrium hydrides would form. Also addressed is the hypothesis that a higher electron-beam accelerating voltage during the decomposition of the Pt precursor would cause more gaseous H to be released during the FIB-based lift-out process for APT samples, and would increase the concentration of H in the APT samples.

The discussion related to the microstructural characterization hypotheses is presented in Section 7.1.

The final section of this chapter addresses how the microstructural changes affect the mechanical properties of each alloy. It was hypothesized that a higher volume fraction of the ω and α phases would result in higher moduli, strengths, and hardness values. It was also hypothesized that the β-to-ω transformation would increase the Young's and shear moduli, the strength, and the hardness more than the β-to-α phase transformation. The final hypothesis was that the ω-containing microstructures would fail before yielding, while the ω-free microstructures would yield before failure.

Changes in hardness were measured using Vickers microhardness testing. Changes in E, σ_y, UTS, and ϵ_f were measured using tensile testing. Changes in G were measured during the phase transformations using in-situ 400 °C RUS testing. This section is divided into subsections containing the results from the Vickers microhardness testing, the tensile testing, and the 400 °C RUS testing.

The discussion of why the mechanical property hypotheses were verified or not can be found in Section 7.2.

6.1 Characterization of the microstructural evolution during the β-to-ω and β-to-α phase transformations

In this section, the results and analysis of XRD and BSE-SEM imaging are presented to test the hypotheses regarding the evolution of the phase volume fractions and phase lattice parameters during a 400 °C treatment. The results from those experiments resulted in the conclusions summarized here.

Al appeared to inhibit the β-to-ω transformation as the Al-free TC and TCF formed the ω and α phases, while the Al-containing TCA and TCFA formed only the α phase. Al promoted the β-to-α transformation when added to TC, as TCA exhibited higher α-phase volume fractions than TC. Adding Fe to TCA decreased the α-phase volume fraction compared to both TCA and TC. Adding Fe to TC suppressed the β-to-ω transformation but did not affect the β-to-α transformation: TC and TCF exhibited similar α-phase volume fractions, but TCF exhibited lower ω-phase volume fractions.

During the β-to-ω and β-to-α transformations, the β-stabilizers Cr and Fe diffused from the ω and α phases into the β phase. During the β-to-α transformation, the α-stabilizer Al diffused from the β phase into the α phase.

The a_β of each alloy decreased as the β-to-ω and β-to-α transformations occurred and the β-stabilizers Cr and Fe diffused from the ω and α phases into the β phase. As the β-to-α transformation occurred, the α-phase c/a ratios of TC and TCA approached 1.587, which is the c/a ratio of the α phase in pure Ti, while the c/a ratios of TCF and TCFA approached 1.580. The ω-phase lattice parameters were reduced in TCF compared to TC, but a similar c/a ratio was observed in both alloys. The c/a ratio of TC increased with time at 400 °C while the c/a ratio of TCF remained relatively constant throughout the duration of the 400 °C exposure.

Higher concentrations of the impurity element O were observed in the α and ω phases than in the β phase. Higher concentrations of the impurity element H were observed in the β phase, and some samples formed equilibrium and non-equilibrium hydrides. A lower accelerating voltage during Pt deposition resulted in lower overall H concentrations in the hydride-free APT samples.

The results and a more detailed explanation of each conclusion are provided in the following sections concerning the XRD, electron microscopy, and APT experiments.

6.1.1 XRD results

In the in-situ XRD experiment, samples from the top orientation of each alloy were held at 400 °C for 12 h, with scans being taken every 0.5 h. Particular attention was focused on evidence for the presence of the β, α, ω, and $TiCr_2$ phases. The highest intensity peak for $TiCr_2$ occurs at a 2θ angle of approximately 44° [205]. No peak was observed near 44° in any alloy, so it was assumed that $TiCr_2$ did not form during the 12 h aging treatment. Phase transformations occurred during the first 0.5 h at 400 °C. For TC and TCF, see Figure 6.1(a) and (b), the β-to-ω and β-to-α transformations occurred, and β-, ω-, and α-phase peaks were observed in the 0.5 h XRD profiles. For TCA and TCFA, see Figure 6.1(c) and (d), only the β-to-α transformation occurred during the first 0.5 h, and only β- and α-phase peaks were observed in the 0.5 h XRD profiles.

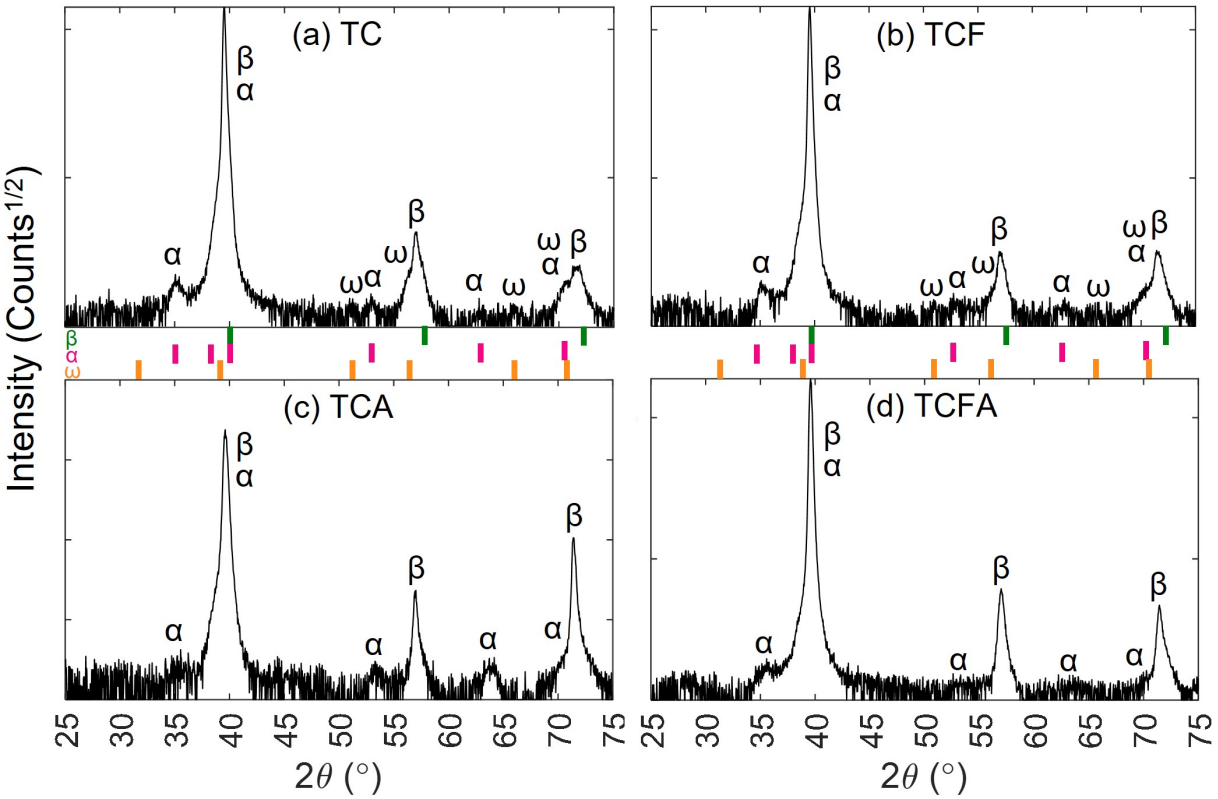

Figure 6.1: HTXRD intensity versus 2θ plots at 0.5 h and 400 °C showing the β-, α-, and ω-phase peaks for (a) TC and (b) TCF, and the β- and α-phase peaks for (c) TCA and (d) TCFA. A square root of the counts on the y-axis was found to suitably distinguish the phase peaks.

After determining the initial phase transformations, all XRD profiles were plotted vertically to show the evolution of the phase peaks with time at 400 °C. Figure 6.2 shows the vertical XRD profile plot for TC. In TC, the β-, α-, and ω-phase peaks were evident in each profile, indicating that the α and ω phase precipitates were present throughout the 12 h treatment.

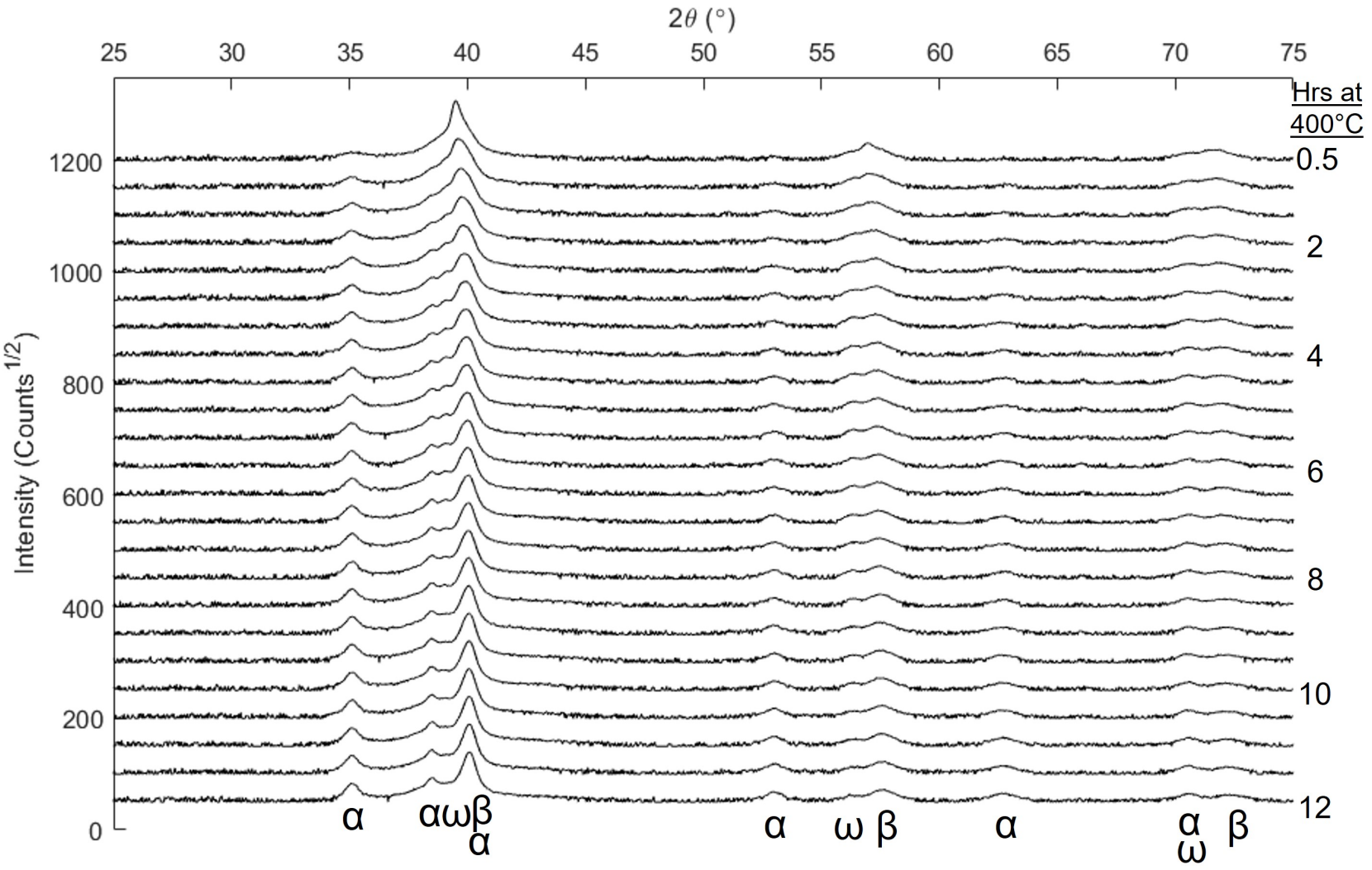

Figure 6.2: HTXRD intensity versus 2θ plots from every 0.5 h during the 400 °C treatment showing the evolution of the β-, α-, and ω-phase peaks for TC. Time spent at 400 °C increases as the plot moves from the top of the page to the bottom. A square root of the counts on the y-axis was found to suitably distinguish the phase peaks.

To determine the volume fractions and lattice parameters of each phase for each profile, a deconvolution of the contributions from the β, ω, and α phases to each XRD profile using Rietveld analysis was performed.

Rietveld analysis summed the β-, α-, and ω-phase peak intensities (from [186], [187], and [188], respectively) to create an initial "theoretical" or "calculated" profile. For more information on the phases, see Table 3.2 and Figure 3.2 in Chapter 3. Beginning with that initial calculated profile, the iterative Rietveld analysis process adjusted different parameters associated with each phase's lattice parameters, peak intensity, and peak shape to match the calculated profile to the experimentally-obtained profile. To determine how well the profiles matched, the difference between the calculated and experimental profiles, also called the residual, was used. A residual of zero indicates a perfect match between the profiles. The iterative Rietveld analysis minimized the residual, and the phase lattice parameters and volume fractions were calculated using the final Rietveld parameter values. Figure 6.3 shows a deconvolution (with residual) of the XRD profile of TC after 1.5 h at 400 °C. While the peak position, shape, and intensity of each phase will differ depending on the experimental profile, this data set is representative of the deconvolution accomplished for each alloy's profiles.

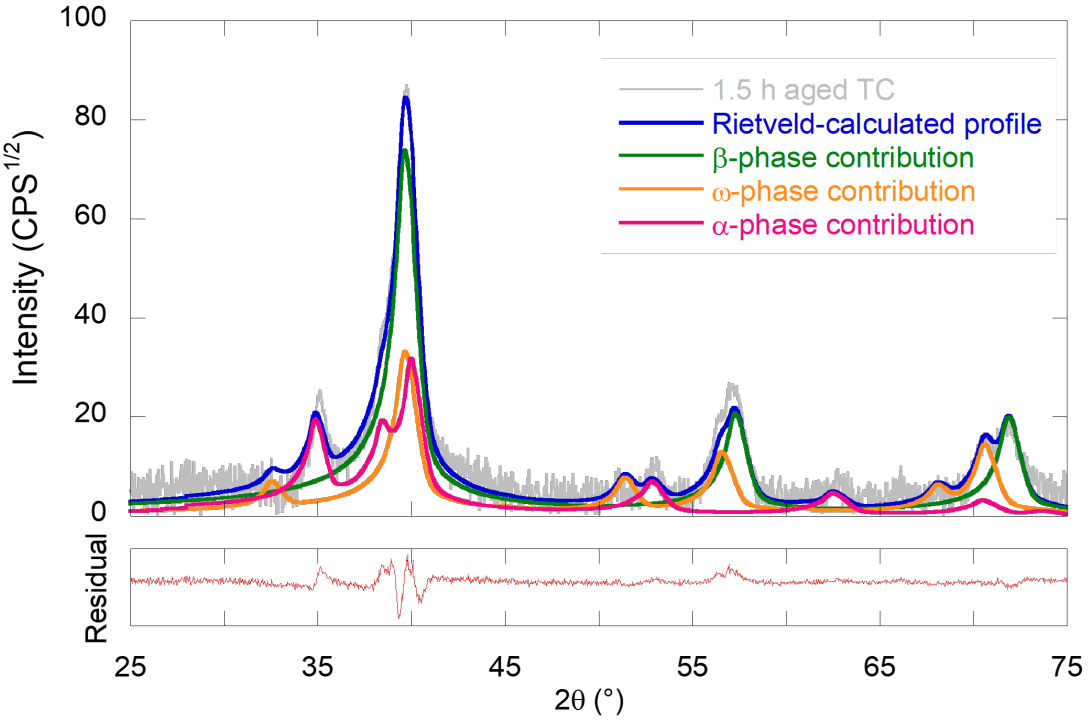

Figure 6.3: The experimental XRD profile of TC at 1.5 h at 400 °C, with the Rietveld-calculated profile. The calculated profile is the sum of the individual contributions from each phase, and the residual shows the difference between the experimental and the calculated profiles.

While the Rietveld analysis was performed for each phase profile shown in Figure 6.2, displaying the deconvolutions like in Figure 6.3 made it difficult to determine the evolution of each phase's peaks. To better reveal the experimental XRD profiles and the deconvolution of the phase profiles, heatmap-style waterfall plots were used, see Figure 6.4. These plots show that the β-phase peaks shifted to a higher angle and the ω- and α-phase peaks appeared to remain relatively constant with respect to their angle with increasing aging time. These peak locations suggest that a_β decreased as the β-to-ω and β-to-α transformations occurred, while the ω- and α-phase lattice parameters stayed relatively constant. The change in intensity of each phase is less evident. The β and ω phases appeared to decrease in intensity and the α phase appeared to increase in intensity with increased aging time. These changes in intensity suggest that the β- and ω-phase volume fractions decreased with increased aging time, while the α-phase volume fraction increased. The lattice parameter and volume fraction changes are covered in more detail in Sections 6.1.1.2 and 6.1.1.1 below.

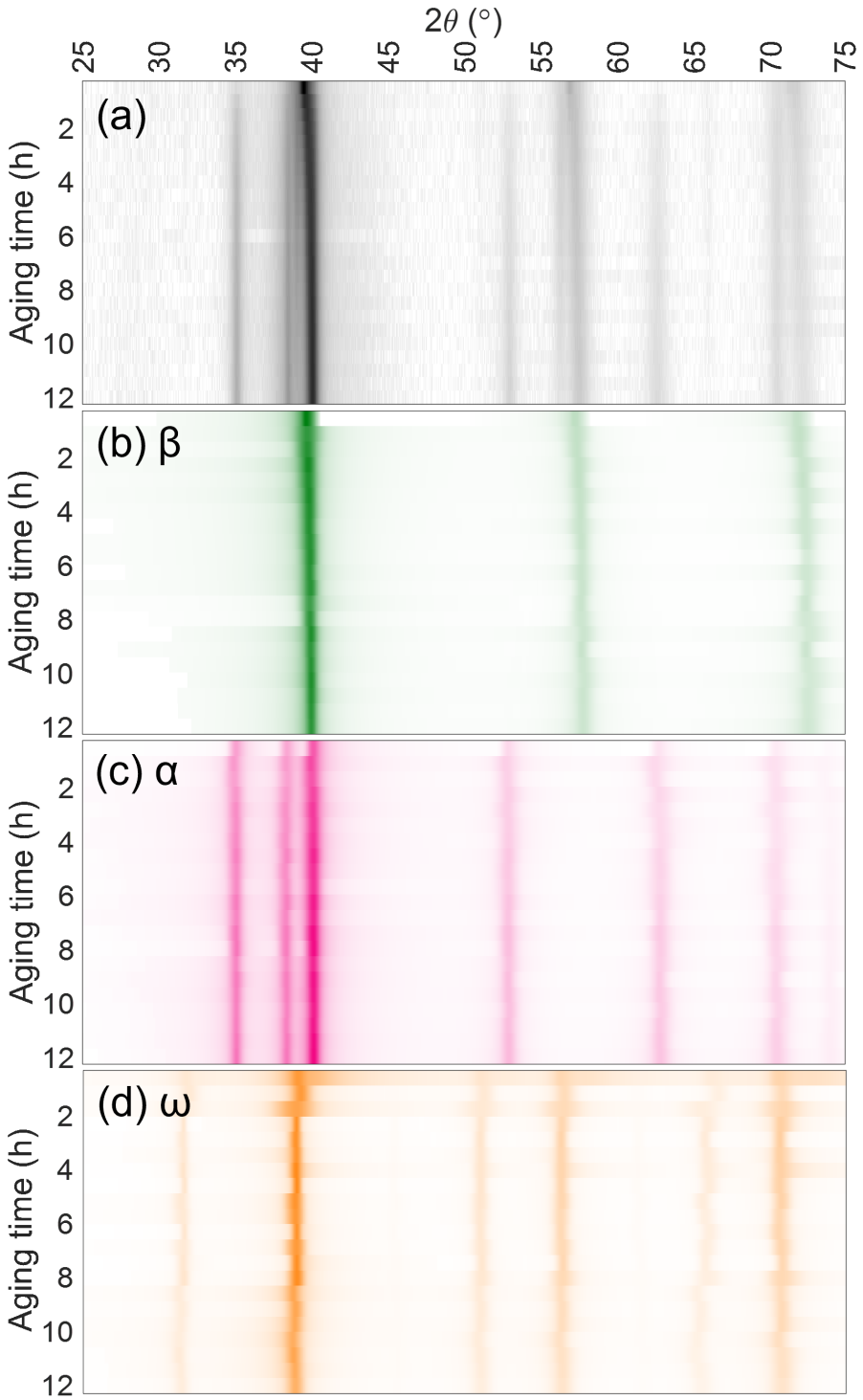

Figure 6.4: The (a) experimental profiles for TC from Figure 6.2 presented as a function of aging time, where darker values indicate higher intensities. The Rietveld-calculated contributions from the (b) β, (c) α, and (d) ω phases are also presented to show the evolution of each phase as a function of aging time.

The deconvolution process was repeated for TCF, see Figure 6.5. The β- , ω-, and α-phase peaks were evident for aging times up to 7.5 h for TCF, after which the ω-phase peaks were not clearly visible in the experimental profiles. This suggested that the ω-phase was only stable up to 7.5 h with the addition of Fe to TC. When the ω phase was included in the Rietveld analysis past 7.5 h, the iterative Rietveld analysis used the ω-phase peaks as a smoothing function to decrease the residual between the calculated and experimental profiles. While this did minimize the residual for the profiles, it also lead to unrealistic lattice parameters and volume fractions for all three phases. Thus, the ω phase was removed from the Rietveld analysis after 7.5 h, see Figure 6.5(d), and only the β and α phases were used for the calculated profiles from 8-12 h. Like in TC, a shift of the β-phase peaks to a higher angle with increased aging time was observed. Also like in TC, the α and ω peaks appeared to remain at a constant angle. The β- and ω-phase peak intensities appeared to decrease and the α-phase peak intensities appeared to increase with increased aging time, consistent with that seen in TC. These results suggest that, like TC, a_β decreased, the β- and ω-phase volume fractions decreased, and the α-phase volume fraction increased with increased aging time.

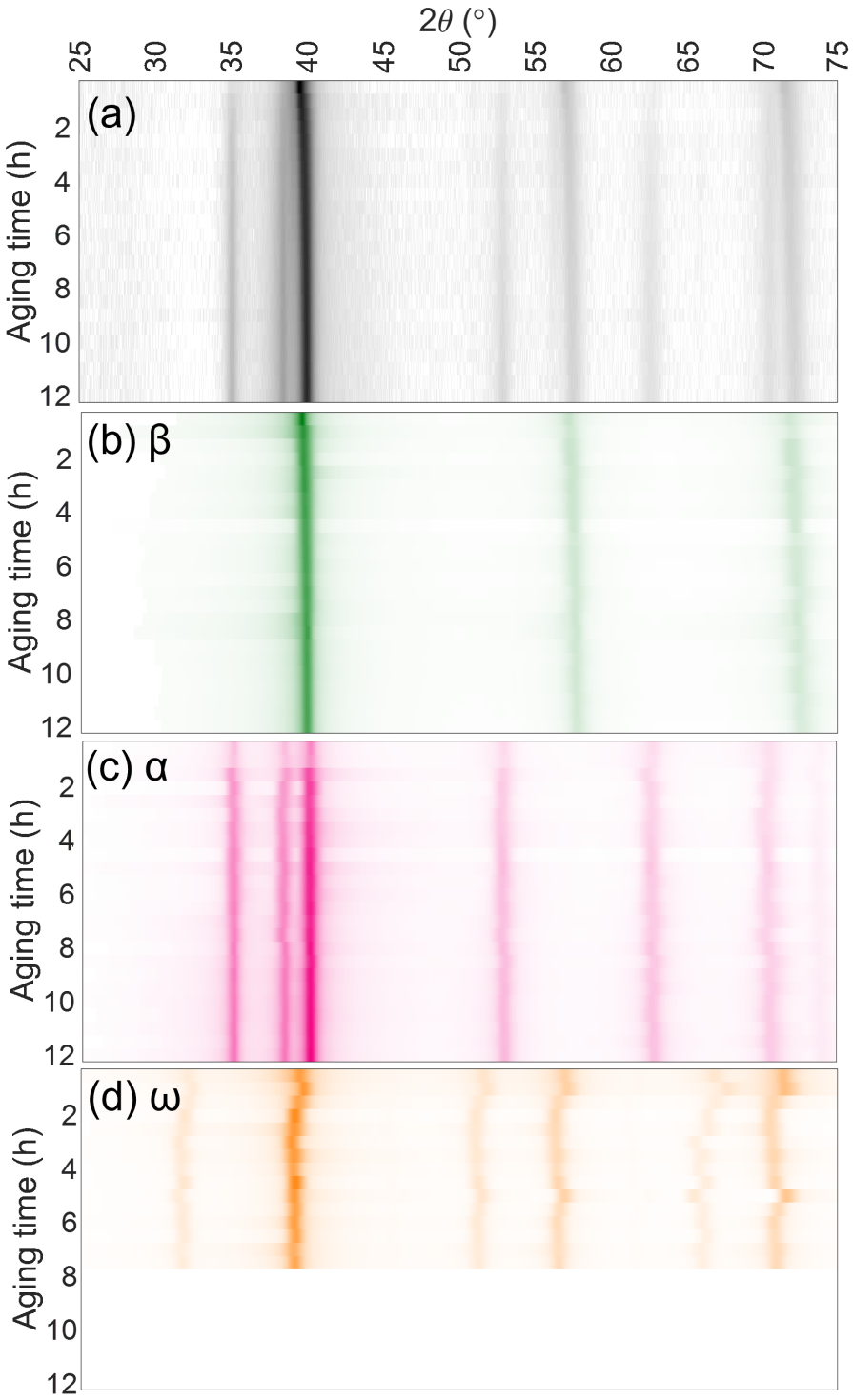

Figure 6.5: The (a) experimental profiles for TCF presented as a function of aging time, where darker values indicate higher intensities. The Rietveld-calculated contributions from the (b) β, (c) α, and (d) ω phases are also presented to show the evolution of each phase as a function of aging time. The ω-phase peaks were not visible after 7.5 h at 400 °C, and so were removed from the Rietveld analysis after that time.

Only the α- and β-phase peaks and intensities were used for the TCA and TCFA Rietveld analysis deconvolution as no ω-phase peaks were observed in any of their XRD profiles. There was less peak overlap between the β and α phases than between the β and ω phases, so the shift in the β peaks to a higher angle and the lack of shift in the α peaks was evident in the experimental profiles, see Figure 6.6(a) and (b) for TCA and TCFA, respectively. The intensity of the α-phase peaks in TCFA was less than that in TCA, indicating that TCFA could exhibit less α-phase volume fraction than TCA. The β-phase peak shift suggested that a_β decreased with increased aging time for TCA and TCFA.

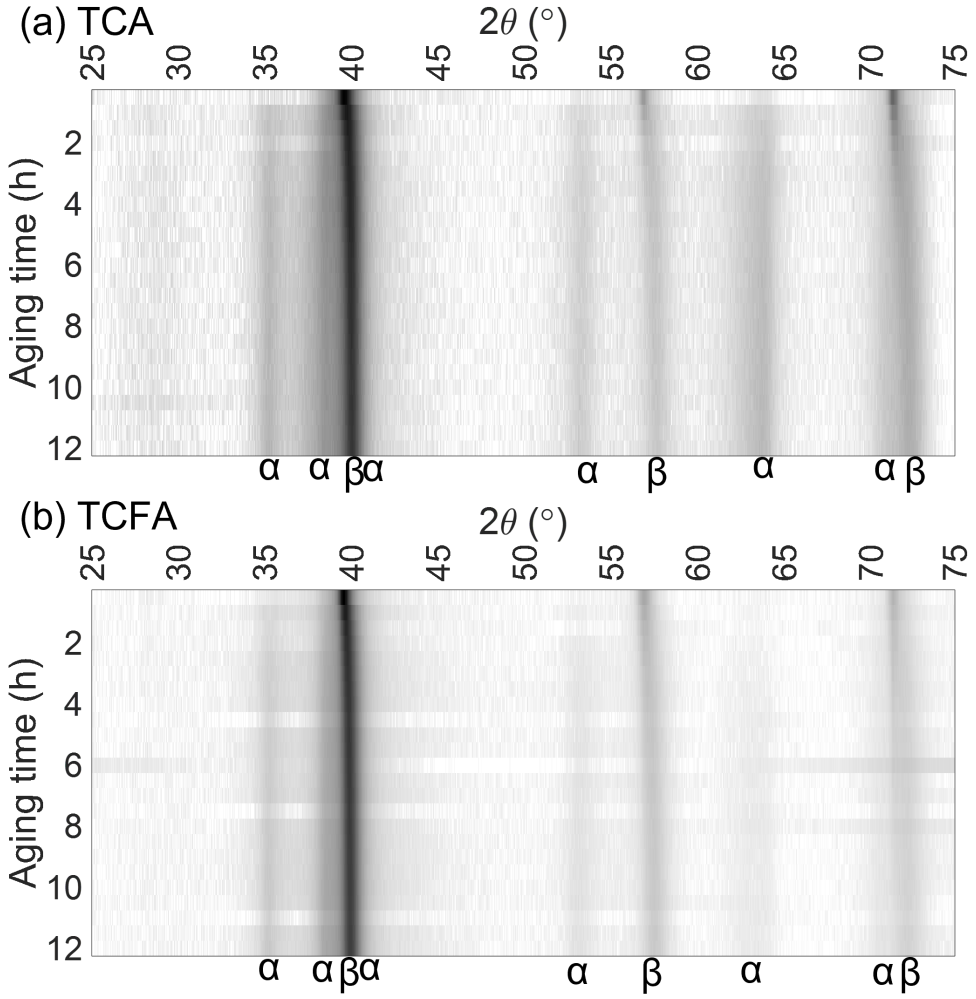

Figure 6.6: The experimental profiles for (a) TCA and (b) TCFA presented as a function of aging time, where darker values indicate higher intensities. Each peak is labeled with its corresponding phase along the bottom axis.

From the Rietveld deconvolutions, the phase volume fractions were determined from the Rietveld parameters associated with the intensities and shapes of the phase peaks. The lattice parameters of each phase were determined from the Rietveld parameters associated with the phase peak locations. In the following sections, the Rietveld-calculated volume fractions are presented first, followed by the lattice parameters.

6.1.1.1 Phase volume fractions

The phase volume fractions were calculated using the height and the shape of the phase peaks. Greater peak intensities indicated higher volume fractions. This is seen when comparing the deconvolutions of TC after 3 and 6 h at 400 °C. The β peaks decreased in intensity from 3 to 6 h, and this is most clearly seen in the $(1\,0\,1)$ peak, see Figure 6.7. This decrease in intensity indicated that the β-phase volume fraction decreased with time at 400 °C, which is consistent with the β phase undergoing the β-to-ω and β-to-α transformations. In contrast, the α-phase peaks increased in intensity from 3 to 6 h, seen when comparing the $(1\,0\,\bar{1}\,1)$ peaks between 3 and 6 h aging in Figure 6.7, which indicated that the α-phase volume fraction increased. The increase is consistent with the β-to-α transformation continuing with time at 400 °C. The ω-phase peaks from 3 to 6 h decrease in intensity, see the $(1\,0\,\bar{1}\,1)$ and $(2\,1\,\bar{3}\,1)$ peaks in Figure 6.7, which indicated a decrease in ω-phase volume fraction from 3 to 6 h.

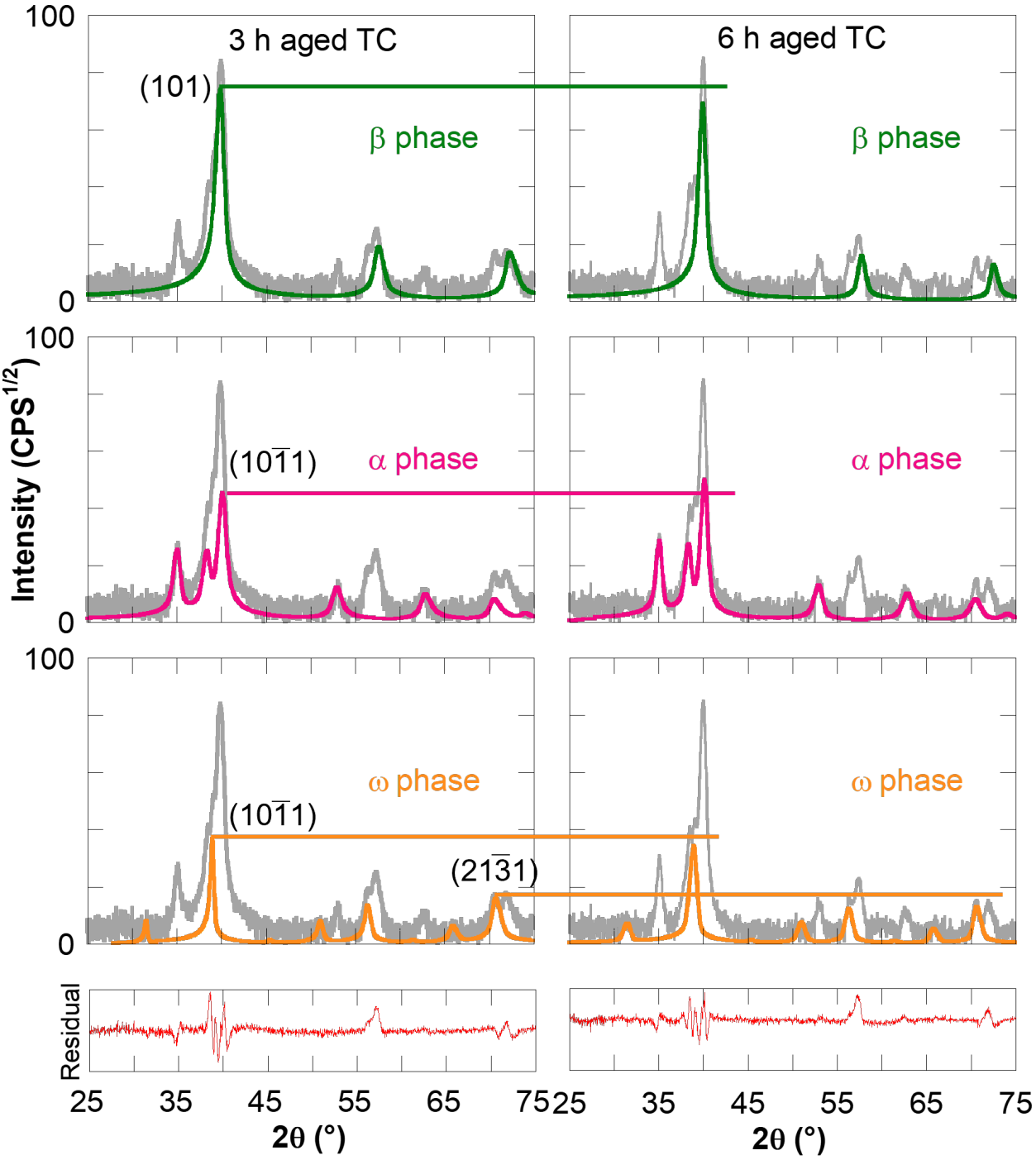

Figure 6.7: The Rietveld refinement phase contributions for the (top) β, (middle) α, and (bottom) ω phases for TC at (left) 3 and (right) 6 h at 400 °C. Guidelines have been added to illustrate the decrease in β and ω peak heights and the increase in α peak height from 3 to 6 h. The residuals are included to show the overall 'goodness-of-fit' of the Rietveld refinement.

Because Rietveld analysis tries to reduce the residuals with each iteration, some parameter adjustments reduced the residuals, but the calculated volume fractions were unrealistic. The analysis tends to favor broader peaks as they tend to produce smoother profiles and smaller residuals, and thereby affect the calculated volume fractions. This was why the ω phase had to be removed from the analysis of TCF after 7.5 h, as the analysis was using the ω phase as a smoothing function, which reduced the residuals but led to unrealistic volume fractions of the three phases in TCF. Thus, some variation in volume fraction was observed, particularly in TCA, where the broad experimental phase peaks were difficult to refine. All calculated volume fraction values are presented here, and the trends are discussed in more detail in Section 7.1.1.

The Rietveld-calculated β-, α-, and ω-phase volume fractions in each alloy were plotted as a function of aging time, see in Figure 6.8. Throughout the 12 h aging, the β-phase volume fraction decreased and the α-phase volume fraction increased for each alloy, see Figure 6.8(a) and (b). TC and TCF both exhibited the highest ω-phase volume fractions after 0.5 h, and the associated ω-phase volume fractions decreased with increased aging time. For TCF, the ω-phase was removed from the Rietveld analysis after 7.5 h, thus a 0% ω-phase volume fraction was reported for 8-12 h of aging.

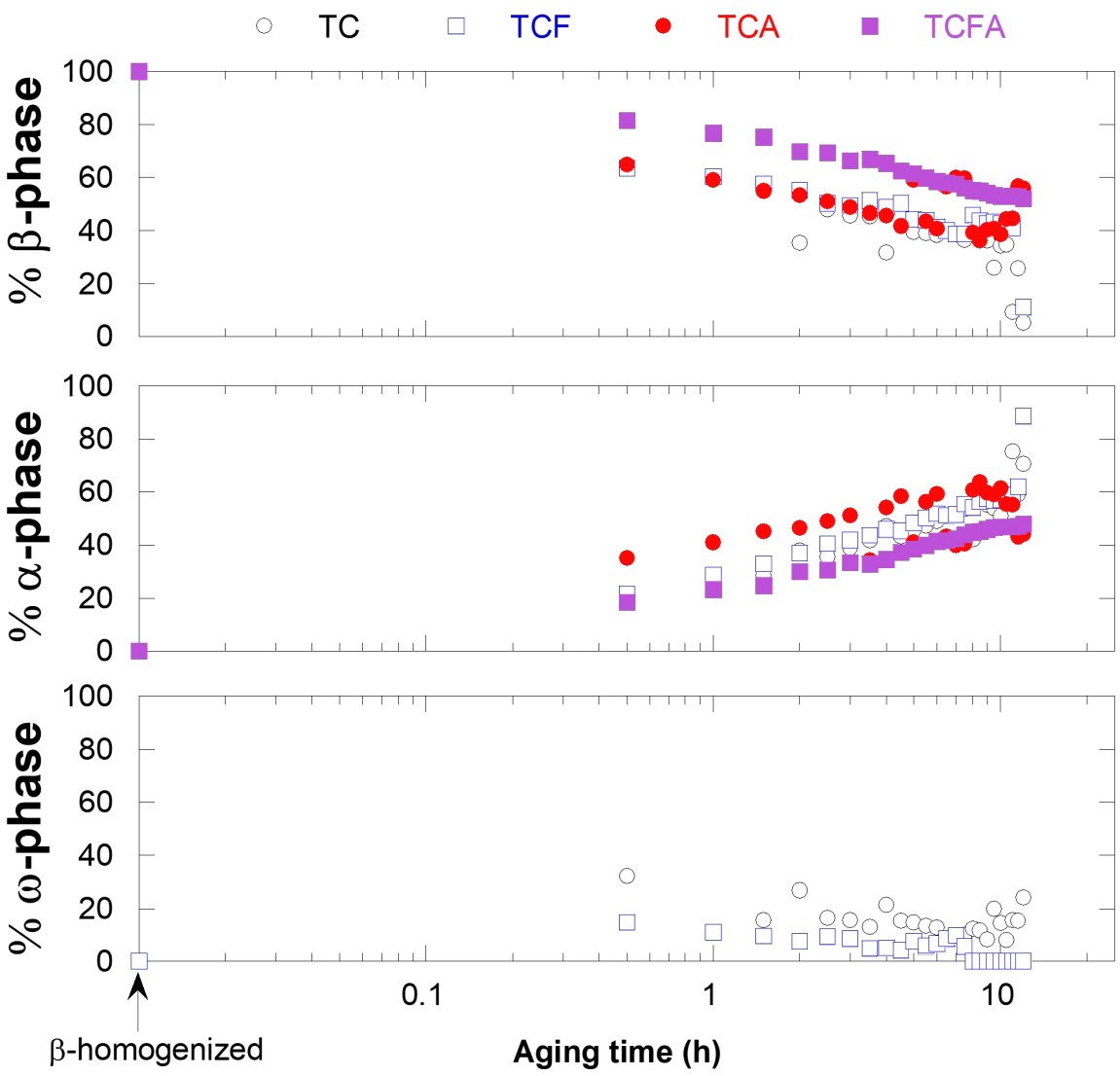

Figure 6.8: The Rietveld refinement calculations of the volume fractions of the (a) β phase, (b) α phase, and (c) ω phase for TC, TCF, TCA, and TCFA as a function of aging time at 400 °C.

The Fe addition to TC appeared to reduce the ω-phase volume fraction in TCF, as TCF exhibited lower ω-phase volume fractions than TC. The Fe addition to TCA appeared to reduce the α-phase volume fraction in TCFA, as TCFA exhibited lower α-phase volume fractions than TCA. The Fe addition did not appear to affect the α-phase volume fraction in TCF, as TC and TCF exhibited similar α-phase volume fractions. The Al addition appeared to promote the β-to-α transformation when Fe was not present, as TCA exhibited higher α-phase volume fractions than TC or TCFA. The effects of the alloying additions are discussed in more detail in Section 7.1.1.

6.1.1.2 Phase lattice parameters

The lattice parameters of each phase were calculated from the Rietveld analyses of the profiles during the 400 °C aging treatment of each alloy. Some scatter existed in the calculated lattice parameters of each phase. This scatter came from certain inaccuracies within the Rietveld refinement technique. Some profiles were more difficult to refine; the TCA profiles were particularly difficult due to the broadness of the peaks, particularly during the later aging times. The peak overlap and peak broadness led to some profiles from each alloy being more difficult to refine. In both TC and TCF, where there was significant overlap between the β, ω, and α peaks, the Rietveld analysis tended to reverse the ω- and α-peak locations. This reversal led to calculated lattice parameters which did not follow the trends of the previous profile results, and which were unrealistic according to the literature values for each phase. When these inaccuracies occurred, the Rietveld analysis was redone, holding peak shape and location parameters constant whenever necessary to prevent the reversals. This generally followed the pattern of holding the ω and α phase constant to refine the β phase, holding the ω and β phases constant to refine the α phase, and holding the β and α phases constant to refine the ω phase. This process was repeated as necessary to complete the analysis. The calculated β-phase lattice parameters are presented first, followed by the α-phase lattice parameters, followed by the ω-phase lattice parameters.

Rietveld analysis was critical to deconvolute each phase's peak locations. This deconvolution allowed the peak shift in the β-phase to be separated from the α and ω phases. To better illustrate the β-phase peak shift, the $(2\,0\,0)_\beta$ peak was isolated from the TC profiles, see Figure 6.9. As the aging time increased, and the β-to-ω and β-to-α transformations occurred, the $(2\,0\,0)_\beta$ peak shifted to a higher angle which indicates that a_β decreased according to Bragg's Law, see Equation 4.1 in Section 4.1.

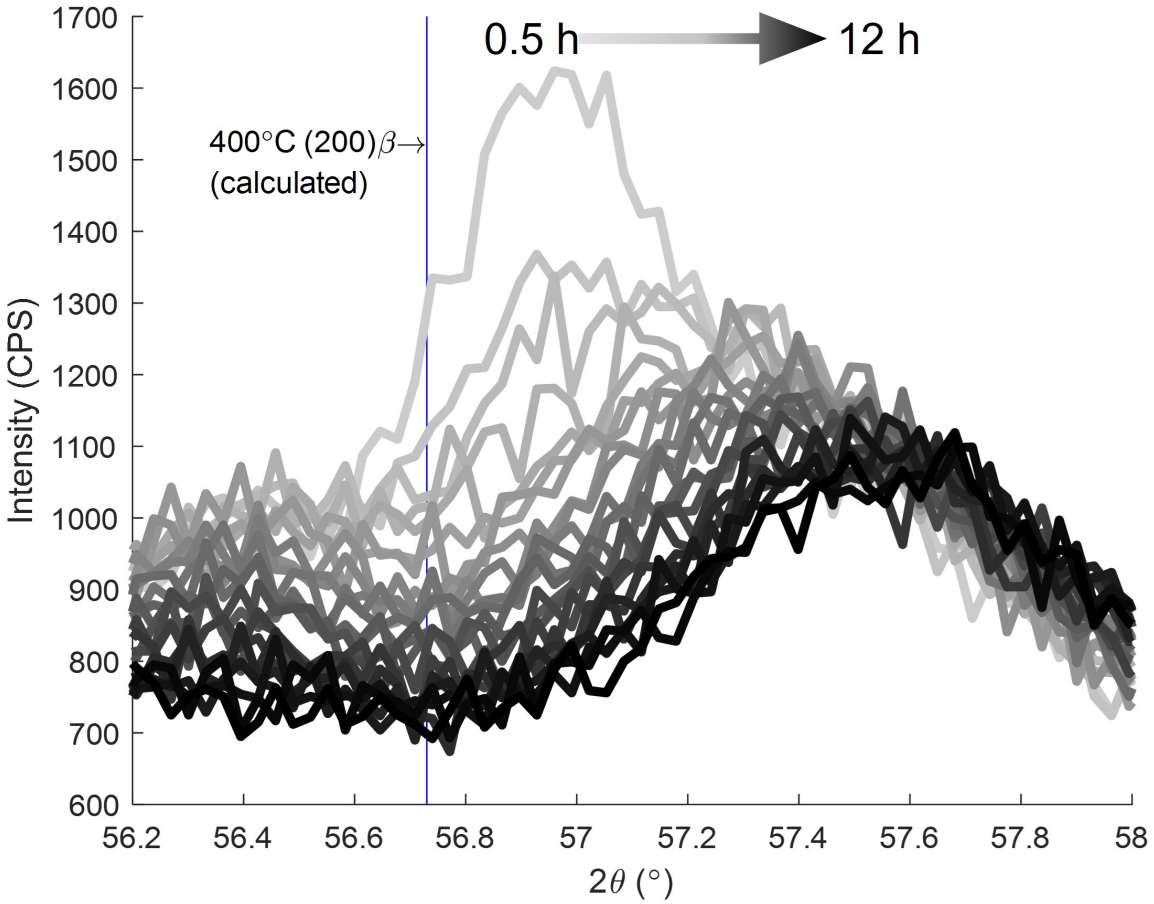

Figure 6.9: Intensity versus 2θ plots of TC highlighting the $(2\,0\,0)_\beta$ peak for 0.5 to 12 h aging times; the peak shifted to a higher angle with increased aging time, i.e. the darker the line, the longer the aging time.

Some shift in the β-phase peaks of all alloys was expected, as going from RT to 400 °C would cause expansion of the crystallographic lattice. To determine how much thermal expansion would affect the β-phase peak position, the 400 °C a_β was calculated using the equation of thermal expansion provided in Equation 6.1. In Equation 6.1, T_1 was the aging temperature of 400 °C, T_0 was RT (i.e. 23 °C), L_0 was the original β-homogenized a_β of 3.22 Å, and δL was the change in lattice parameter. The coefficient of thermal expansion for Ti (8.5×10^{-6}/°C) was taken from Hidnert in [206].

$$\delta L = L_0\,(8.5 * 10^{-6}/°\mathrm{C})\,(T_1 - T_0) \tag{6.1}$$

According to Equation 6.1, the β-phase lattice parameter should increase by 0.01 Å upon increasing

the temperature from RT to 400 °C. Similarly, when the sample is cooled from 400 °C to RT, the lattice should decrease by 0.01 Å. A decrease in a_β of 0.011 Å was measured between the a_β at 400 °C after 12 h aging and the a_β at RT after 12 h aging, confirming that the lattice parameter decreased due to temperature. With the lattice parameter change due to heating and cooling identified, any other lattice parameter changes could be attributed to factors other than temperature.

The increase in β-phase peaks, shown for TC in Figure 6.9, was observed in all alloys, and the a_β of each alloy decreased with increased aging time, see Figure 6.10. The a_β values of the Fe-containing and the Fe-free alloys decreased at different rates; the a_β of TC and TCA were comparable, and the a_β of TCF and TCFA were comparable and greater than those of TC and TCA at all aging times.

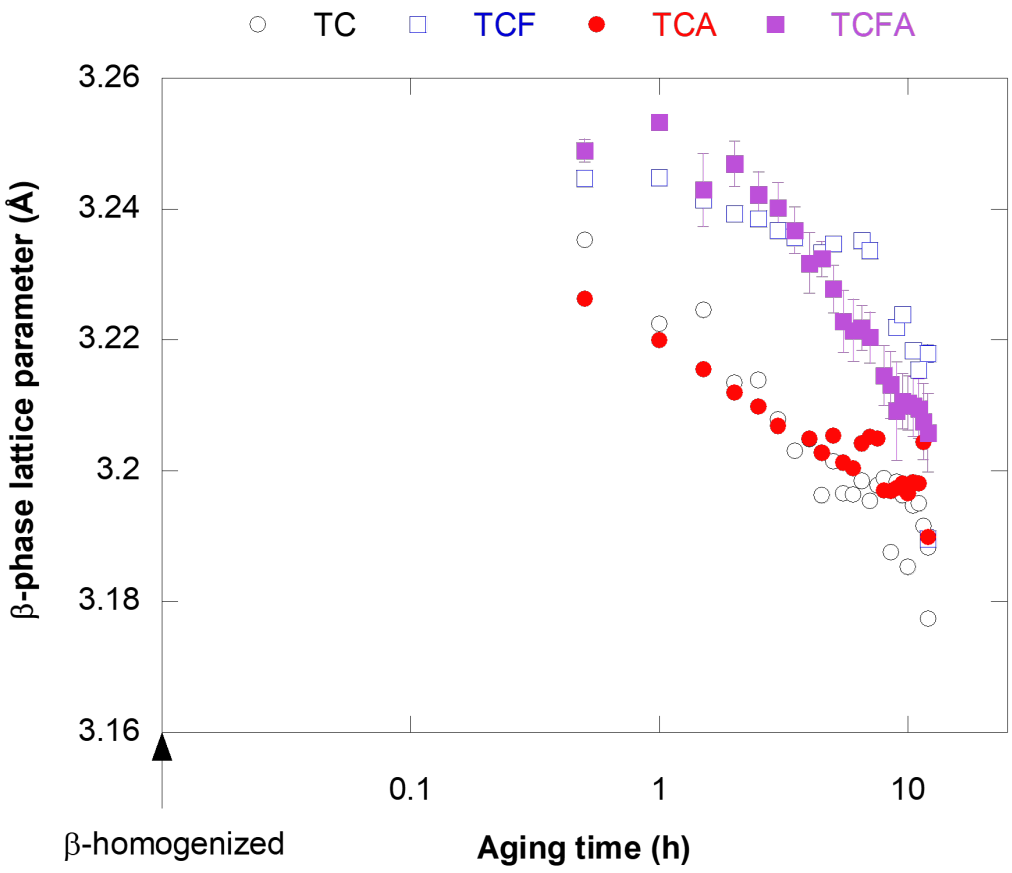

Figure 6.10: The β-phase lattice parameters (a_β) for each alloy, calculated using Rietveld analysis, as a function of aging time at 400 °C.

The ‘a’ (a_α) and ‘c’ (c_α) lattice parameters and the c/a ratio of the α phase were plotted as a function of aging time for each alloy, see Figure 6.11(a), (b), and (c), respectively. The variation of lattice parameters will be discussed, especially that of TCF and TCA, in more detail in Section 7.1.2.

The a_α of TC and TCA and TCFA decreased with increased aging time, while the a_α of TCF remained approximately constant (around 2.99Å). The c_α of TC and TCA remained approximately constant, the c_α of TCF appeared to slightly increase, and the c_α of TCFA decreased with increased aging time. These trends led to the c/a ratio of TC, TCF, and TCA to increase and the c/a ratio of TCFA to decrease with increased aging time, see Figure 6.11(c). While the c/a ratio of TC, TCF, and TCA all increased with increased aging time, TC and TCA exhibited similar α-phase c/a ratios throughout the aging period, with both approaching the value of approximately 1.587 by 12 h aging. It is noted that the c/a ratio of the α phase in pure Ti is 1.587 [7,207]. The c/a ratio of TCF increased by a similar rate as that of TC and TCA, but with a value approximately 0.005 lower at all time steps, approaching 1.582 instead of 1.587. TCFA behaved differently from the other alloys, with the c/a ratio decreasing from approximately 1.590 to approximately 1.580, and plateauing at 1.580 instead of at 1.587.

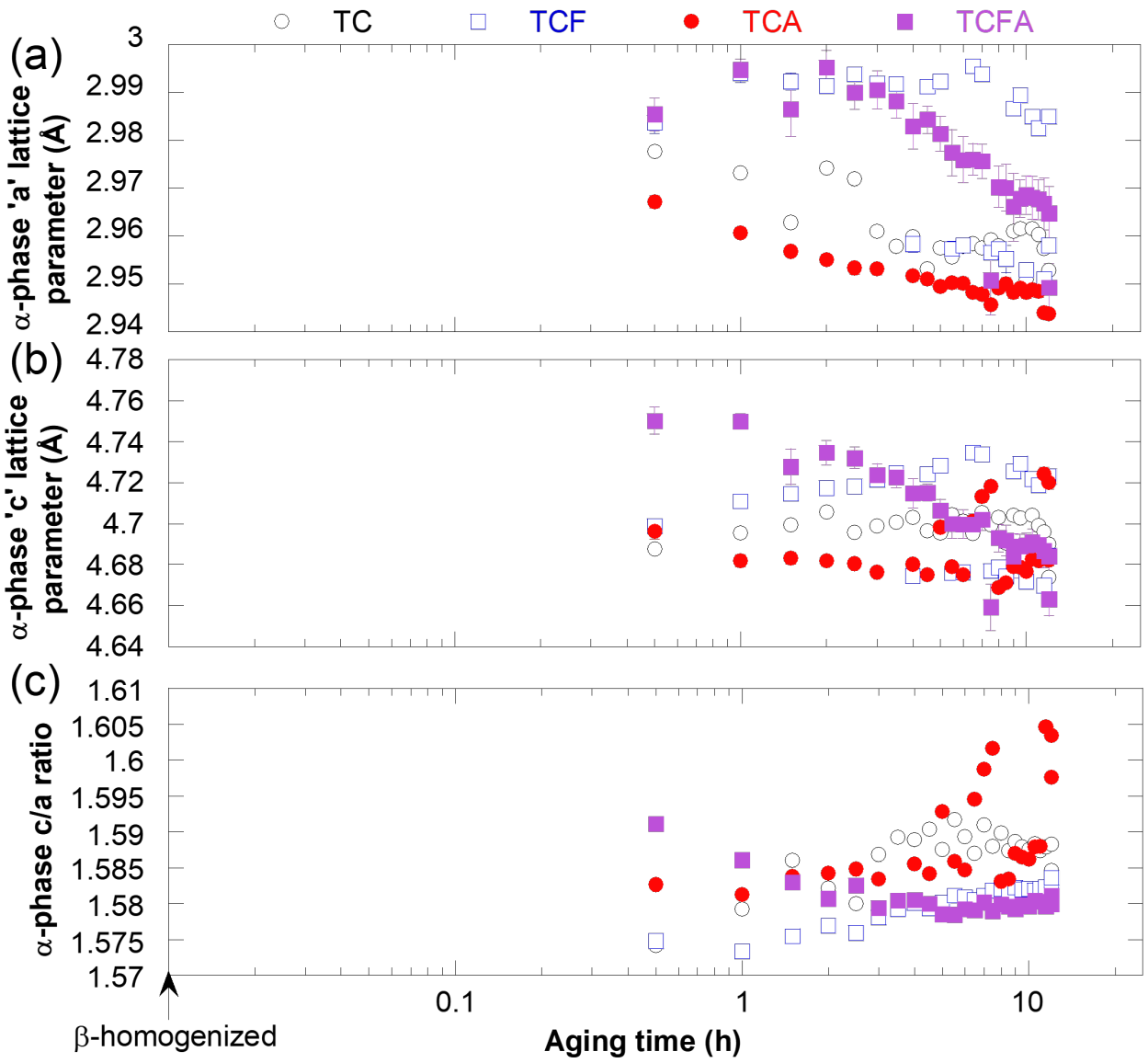

Figure 6.11: The lattice parameters (a) a_α, (b) c_α, and (c) c/a ratio of the α phase as a function of aging time at 400 °C for each alloy.

The 'a' (a_ω) and 'c' (c_ω) lattice parameters and the c/a ratio of the ω phase were plotted as a function of aging time for TC and TCF, see Figure 6.12(a), (b), and (c), respectively. The a_ω of TC before aging (~4.63Å) decreased with increased aging time and approached 4.60Å. The c_ω of TCF (~2.78Å) remained relatively constant throughout the aging treatment, while the c_ω of TC before aging (~2.84Å) increased to 2.86Å during aging. The c/a ratio of TCF was approximately 0.613, and remained relatively constant throughout the aging period. The c/a ratio of TC started at

approximately 0.613 and increased with increased aging time to ~0.622. The a_ω, c_ω, and c/a ratios are within the range of lattice parameters reported for other β-Ti and Zr alloys [33, 35, 51, 55, 56].

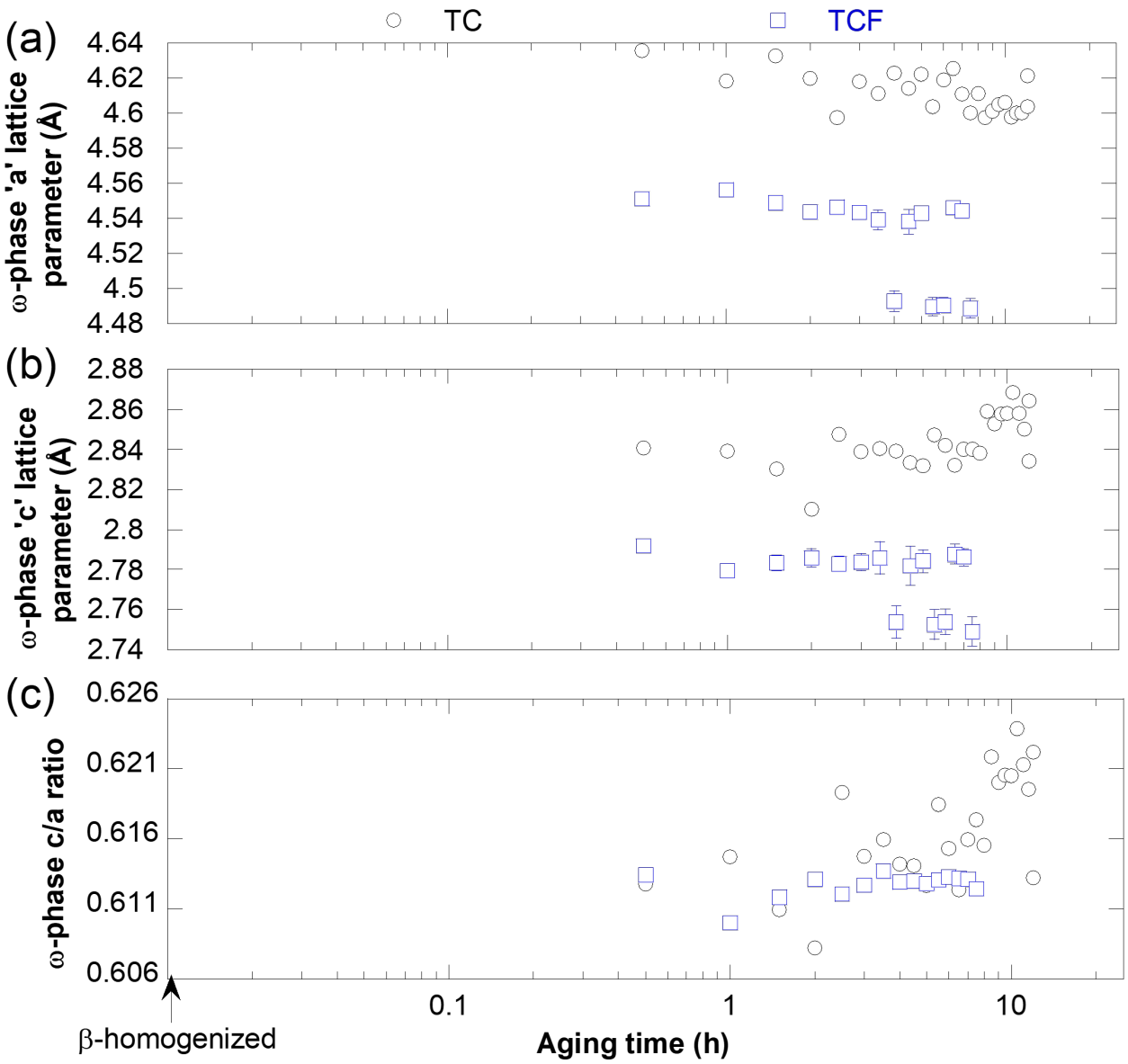

Figure 6.12: The lattice parameters (a) a_ω (b) c_ω and (c) c/a lattice parameter ratio (c) of the ω phase as a function of aging time at 400 °C for each alloy.

6.1.2 Electron microscopy results

High resolution electron microscopy was required to resolve the nanoscale ω and α precipitates. To view these nanoscale precipitates, the aged samples were ion milled prior to imaging in the SEM. Images were acquired at three different magnifications for each alloy. Figures 6.13, 6.14, 6.15, and 6.16 contain the BSE SEM photomicrographs acquired for the 0.75 h aged samples of TC, TCF, TCA, and TCFA, respectively. Representative BSE SEM photomicrographs of the remaining aged samples can be found in Appendix C, Figures C.1 through C.12. For each alloy, the precipitates appeared with darker contrast in the lighter β matrix, indicating a composition difference between the precipitates and the β matrix. The compositional differences between the phases are explored in more detail in Section 6.1.3. These darker precipitates appeared along the β grain boundaries and were also randomly distributed throughout the β grains.

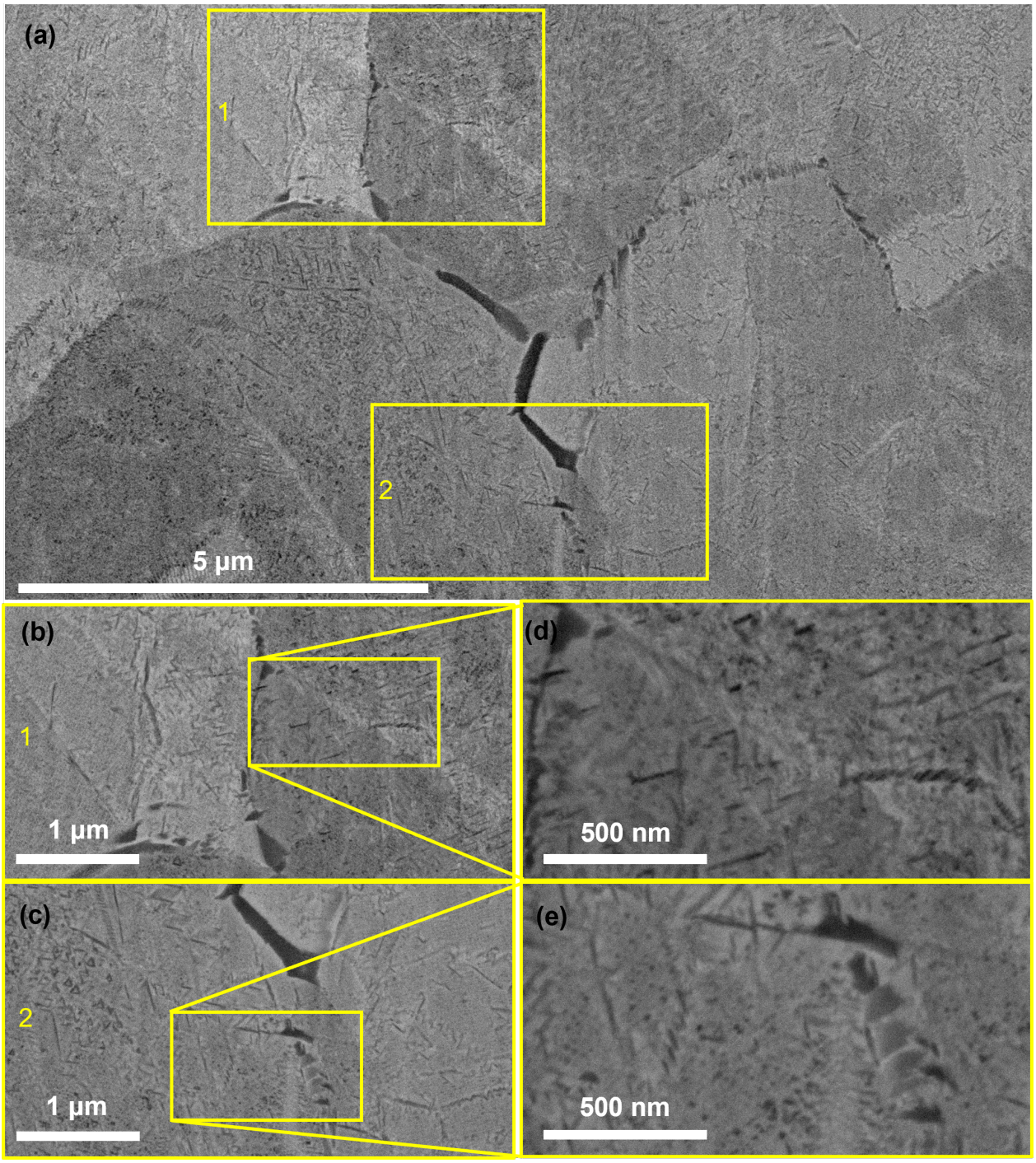

Figure 6.13: BSE SEM photomicrographs of TC aged at 400 °C for 0.75 h at (a) lower magnification, showing darker precipitates in a light β-phase matrix. Higher magnification BSE SEM photomicrographs of areas (b) 1 and (c) 2 (defined in (a)). The highest magnification BSE SEM photomicrographs (d) and (e).

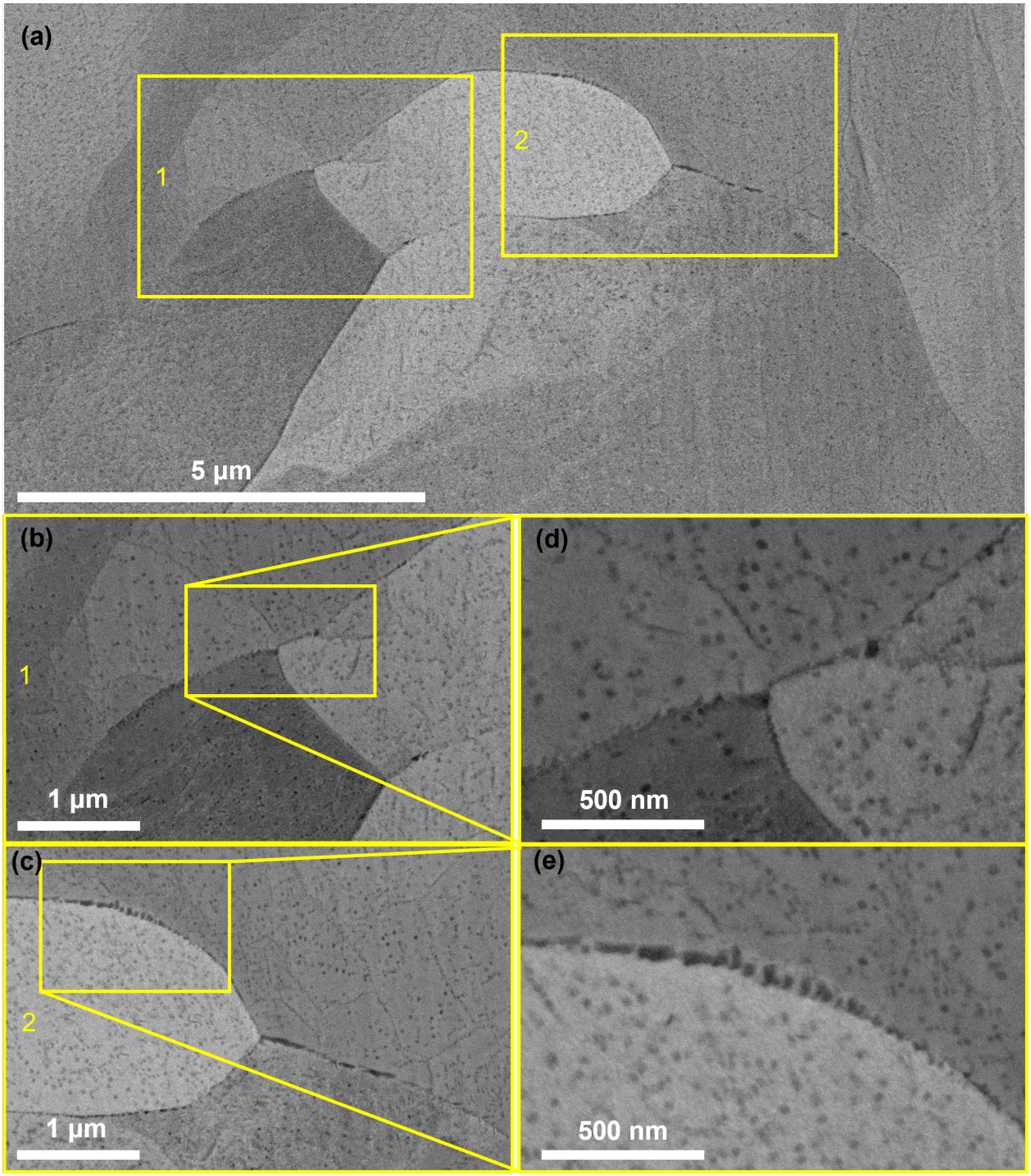

Figure 6.14: BSE SEM photomicrographs of TCF aged at 400 °C for 0.75 h at (a) lower magnification, showing darker precipitates in a light β-phase matrix. Higher magnification BSE SEM photomicrographs of areas (b) 1 and (d) 2 (defined in (a)). The highest magnification BSE SEM photomicrographs (d) and (e).

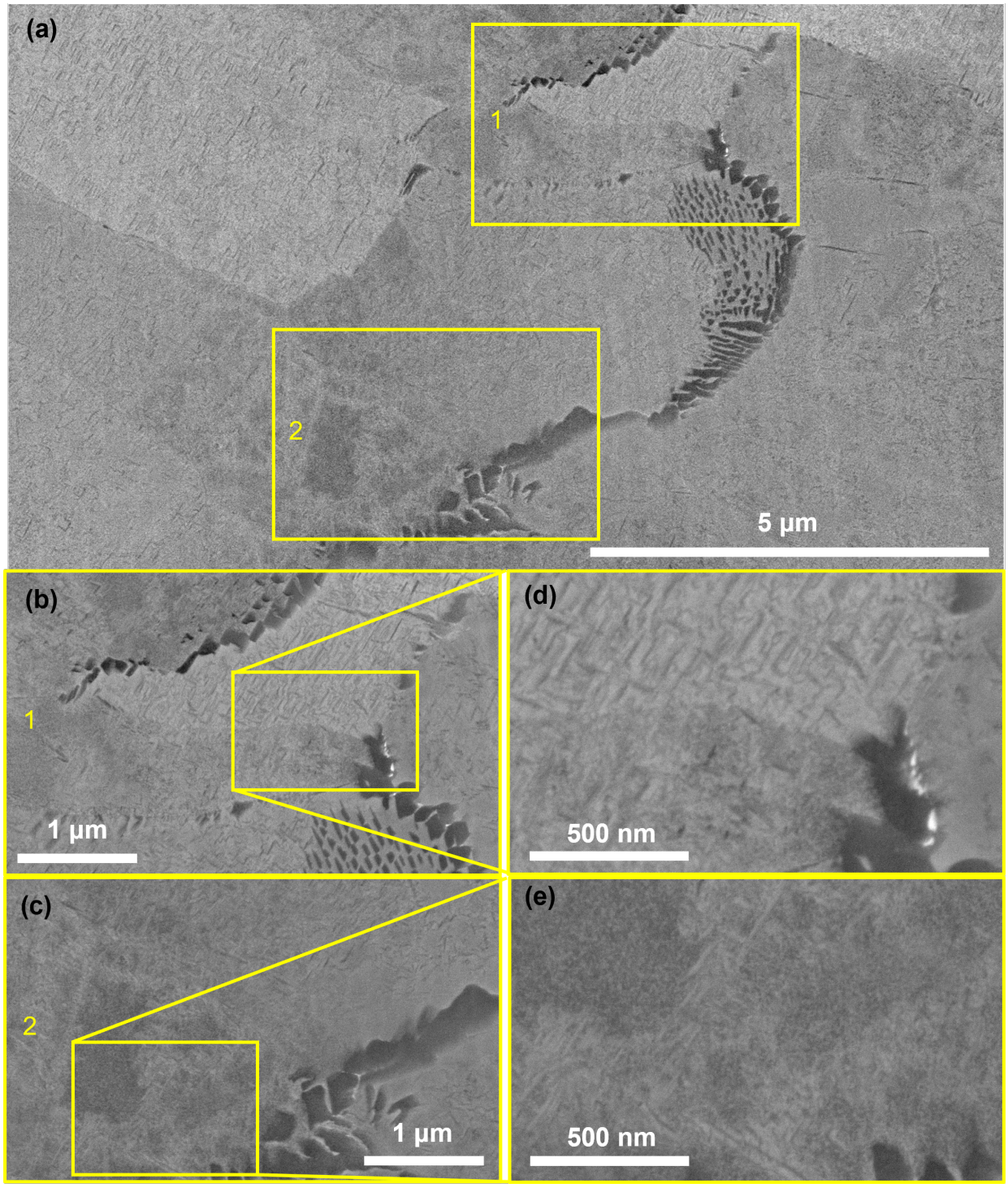

Figure 6.15: BSE SEM photomicrographs of TCA aged at 400 °C for 0.75 h at (a) lower magnification, showing darker precipitates in a light β-phase matrix. Higher magnification BSE SEM photomicrographs of areas (b) 1 and (d) 2 (defined in (a)). The highest magnification BSE SEM photomicrographs (d) and (e).

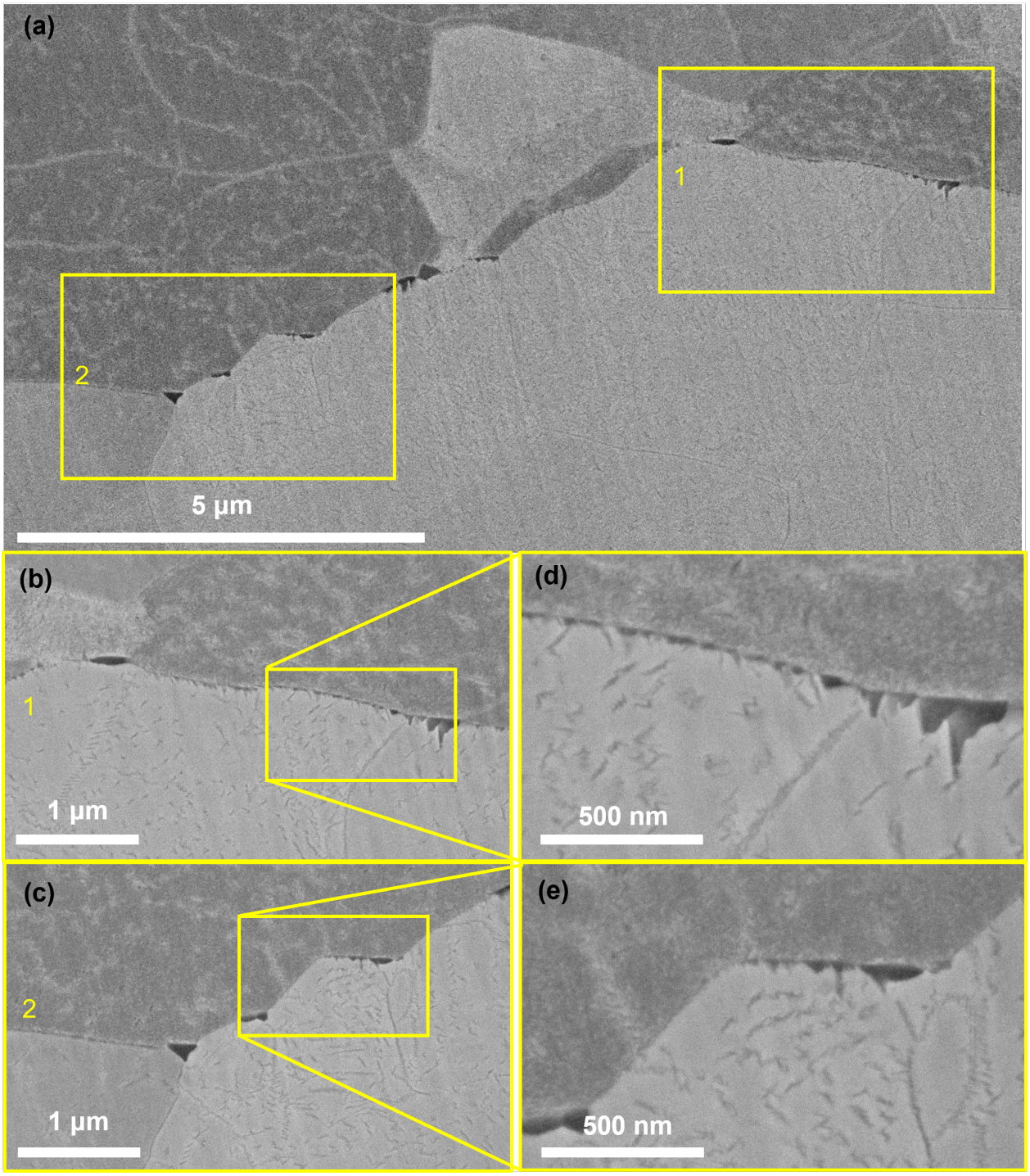

Figure 6.16: BSE SEM photomicrographs of TCFA aged at 400 °C for 0.75 h at (a) lower magnification, showing darker precipitates in a light β-phase matrix. Higher magnification BSE SEM photomicrographs of areas (b) 1 and (d) 2 (defined in (a)). The highest magnification BSE SEM photomicrographs (d) and (e).

From the XRD results, the precipitates in TC and TCF after 0.75 h aging should be the ω and α phases. The precipitates after 0.75 h aging in TCA and TCFA should be α phase precipitates.

The larger and smaller precipitates along the β grain boundaries are consistent with grain boundary α-phase, which tend to exhibit the equiaxed morphology instead of the lamellar morphology, and which can appear larger or smaller depending on the orientation of the α phase and the sectioning plane of the sample [7, 208–211]. The small lenticular precipitates visible in the β grains of each sample are also consistent with intergranular α phase [9,27,208,210,211]. TEM was used to confirm that the lenticular precipitates were α phase. The HAADF STEM photomicrograph of TCFA after 12 h aging, see Figure 6.17(a), illustrated the lenticular α-phase precipitates, which were confirmed to be the α phase by the SAD pattern, see Figure 6.17(b), which indicated only β- and α-phase spots.

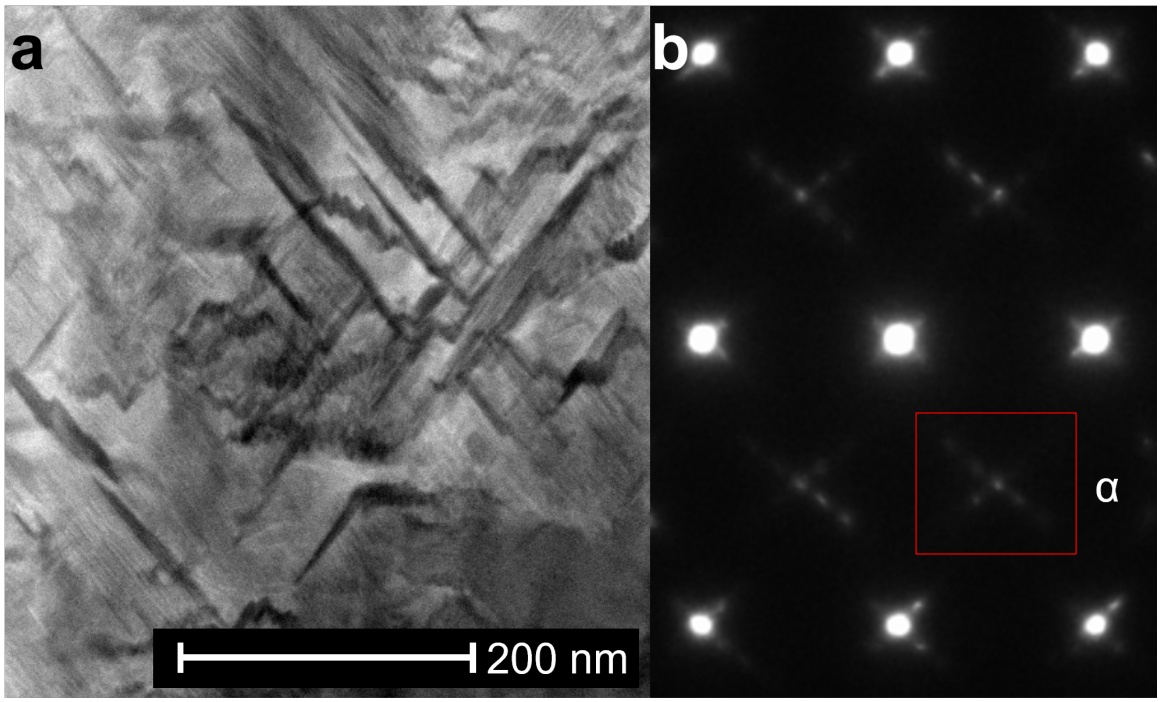

Figure 6.17: (a) HAADF STEM image and (b) representative SAD pattern of the $\langle 1\,1\,0 \rangle_\beta$ zone axis for the TCFA 12 h aged sample. All spots within the red box in (b) are associated with α-phase reflections.

In TC and TCF, small cuboidal or ellipsoidal precipitates were observed at less than 50 nm in size. These precipitates were consistent with the ω-phase precipitates in BSE SEM photomi-

crographs by Bartha et al., who confirmed the ω-phase precipitate size and morphology using TEM [212], see Figure 6.18(a) and (b). In TC, the presumed ω-phase precipitates appear smaller than those in TCF, and appear in greater numbers than those in TCF. The lack of these cuboidal or ellipsoidal precipitates in TCA and TCFA (which exhibited the two-phase β+α microstructure) also supports that they are the ω phase; if they were α-phase precipitates, similar features should be visible in the TCA and TCFA BSE SEM photomicrographs.

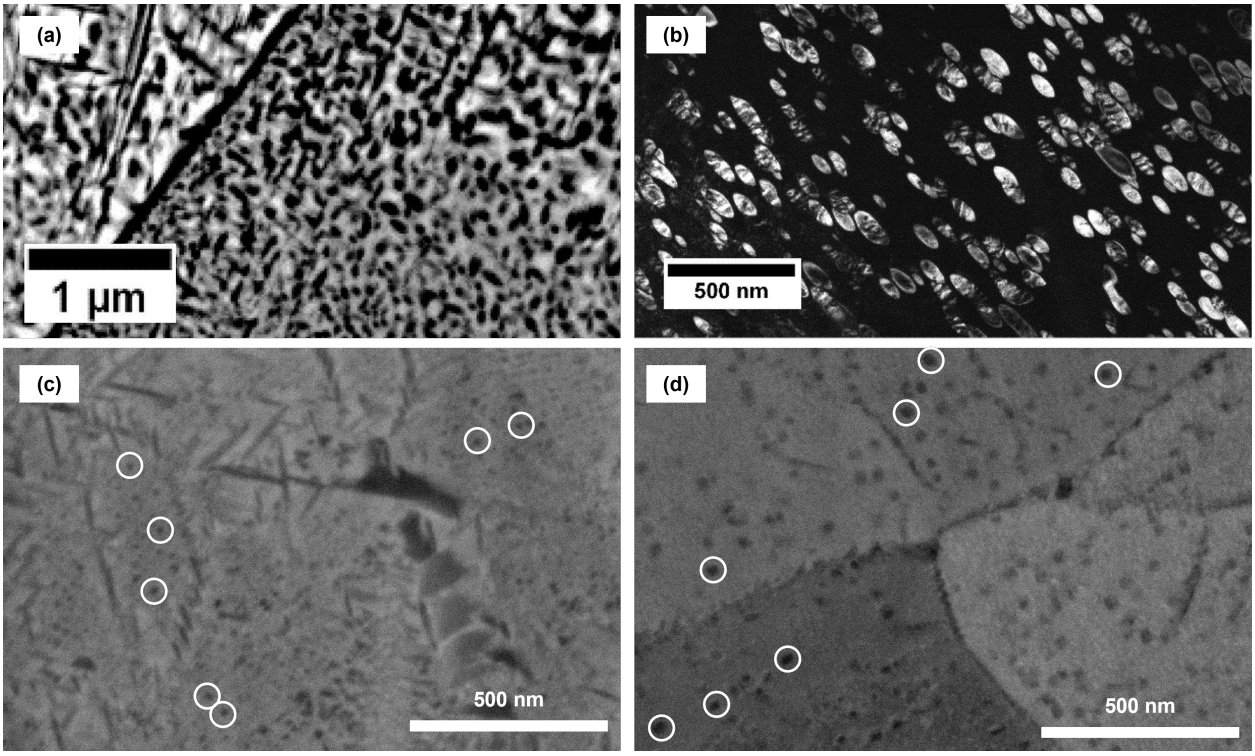

Figure 6.18: (a) BSE-SEM photomicrograph of a β+ω+α microstructure in Ti-15Mo and (b) corresponding dark-field TEM image using a diffraction spot from one variant of the ω phase from the same microstructure. (a) and (b) are reproduced from Bartha et al. [212]. BSE-SEM photomicrographs of (c) TC and (d) TCF with several precipitates consistent with the ω phase circled in white.

6.1.2.1 Threshold analysis

ImageJ software was used to estimate the volume fractions of the precipitating phases in the aged microstructures by taking subsets of each BSE SEM photomicrograph, setting a threshold value, and counting the fraction of pixels that were darker than the set threshold value. Due to their similarly dark contrast, the ω and α phases could not be isolated using this analysis, therefore they were combined in the volume fraction measurements for TC and TCF. A minimum of 9 and a maximum of 31 measurements were made from each set of images. The threshold-calculated volume fractions were lower than the Rietveld-calculated volume fractions, but agreed with the trends in the Rietveld volume fraction results, see Figure 6.19. The difference between the threshold and the Rietveld analysis can be explained by the limitations of the threshold analysis technique. Because the contrast differences between β grains could affect the precipitate volume fraction measurements, the threshold analysis volume fraction measurements were generally taken from the inside of single β grains. While this decreased the measurement inaccuracy due to differing β-grain contrast, it introduced inaccuracy wherein the grain boundary α phase was underrepresented. The exclusion of the grain boundary α-phase precipitates from the volume fraction calculation could lead to significant underestimations of the precipitate volume fractions in each alloy. However, since these inaccuracies were consistent throughout the threshold analysis, the threshold analysis could be used to verify the volume fraction trends from the Rietveld analysis. The threshold analysis confirms that the precipitate volume fraction increased with increased aging time.

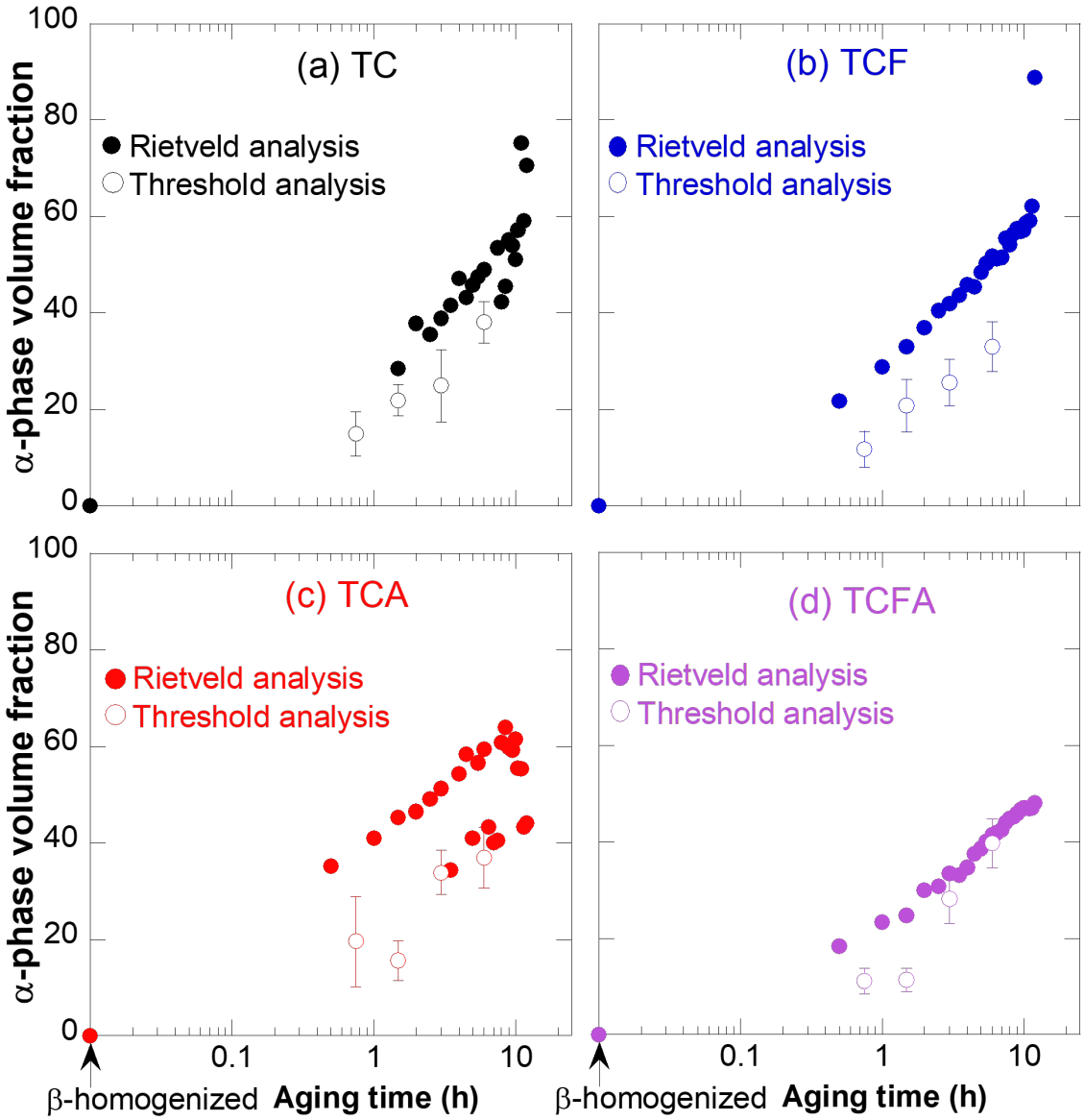

Figure 6.19: The threshold analysis precipitate volume fraction results compared to the Rietveld analysis volume fraction results for (a) TC, (b) TCF, (c) TCA, and (d) TCFA. The Rietveld analysis precipitate volume fraction for TC and TCF was calculated by summing the α- and ω-phase volume fractions. The threshold analysis results are consistent with the Rietveld analysis that the precipitate volume fractions increased with time at 400 °C.

6.1.3 APT

The sub-nanometer resolution of APT was critical to investigate the diffusion of Ti, Cr, Fe, and Al concentrations in the β, α, and ω phases, as well as the locations of the interstitial elements O and H. In this section, the diffusion of the alloying elements, β-stabilizers Cr and Fe and α-stabilizer Al, are presented first. An analysis of the interstitial impurity element O is presented next, followed by an analysis of the interstitial impurity element H.

6.1.3.1 The diffusion of Ti, Cr, Fe, and Al

The phase compositions of each alloy were measured after 0.75, 1.5, 3, 6, and 12 h at 400 °C. Cr isosurfaces were used to illustrate the precipitates in each alloy. The α and ω phases were always rich in Ti and contained almost none of the β-phase stabilizing elements Fe and Cr. The β phase was rich in the β-phase stabilizing elements. Representative reconstructions from the 0.75 h aged condition for TC, TCF, TCA, and TCFA are shown in Figure 6.20(a), (b), (c), and (d), respectively, along with their corresponding proximity histograms.

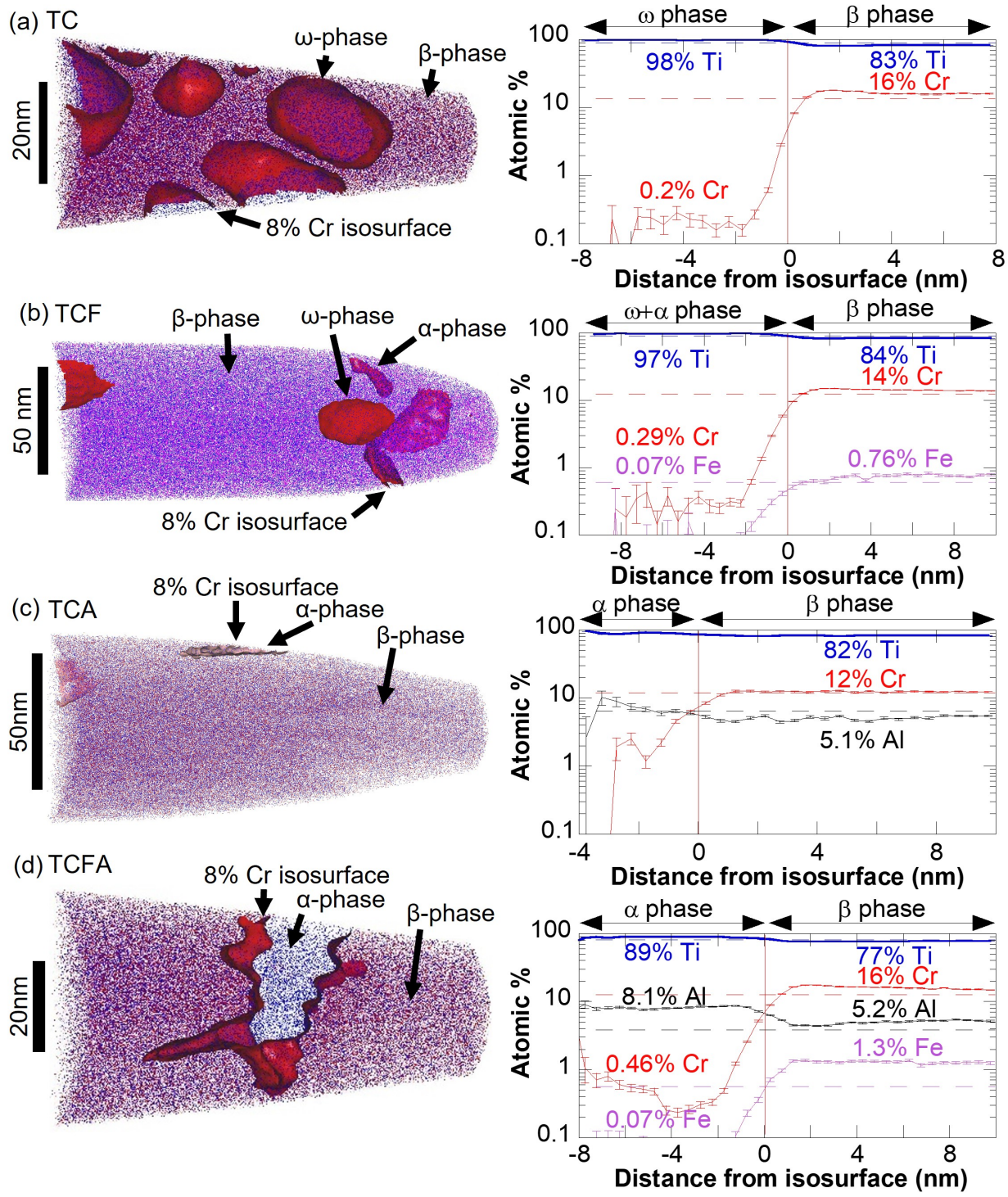

Figure 6.20: APT tip reconstruction of (a) TC with corresponding proximity histogram (b). Tip reconstruction of (c) TCF with corresponding proximity histogram (d). Tip reconstruction of (e) TCA with corresponding proximity histogram (f). Tip reconstruction of (g) TCFA with corresponding proximity histogram (h). All samples were aged at 400 °C for 0.75 h.

The compositions of the phases as a function of 400 °C aging are summarized in Figure 6.21. As the β-to-ω and β-to-α transformations occurred, and the volume fractions of the α phase increased, the β-phase stabilizers Cr and Fe diffused from the precipitated phases into the β matrix. Thus, the β phase increased in β-stabilizer content with time. The β phase in TC increased in Cr content significantly more than TCF (27% Cr in TC after 12 h aging compared to 15.5% Cr in TCF) even with similar α-phase volume fractions. This difference could be explained by the higher ω-phase volume fraction in TC than TCF, as TC contained approximately 10% more ω phase than TCF throughout the 12 h aging. In contrast, the compositions of the α and ω phases remained relatively constant with increased aging time, see Figure 6.21(b). Even when a small amount of the α phase was observed in the 0.75 h aged TCA sample, see Figure 6.20(c), Cr depletion of the α phase was still evident. This suggests that the β-to-ω and β-to-α transformations could be limited by the speed of diffusion of Cr and Fe. The α phase in TCA and TCFA exhibited slightly higher Al contents than the β matrix, and the α-phase precipitates in TCA and TCFA contained approximately 10% less Ti than both the α- and ω-phase precipitates in TC and TCF. This difference was attributed to the increased Al concentrations increasing the stability of the α-phase, as Al is an α-phase stabilizer.

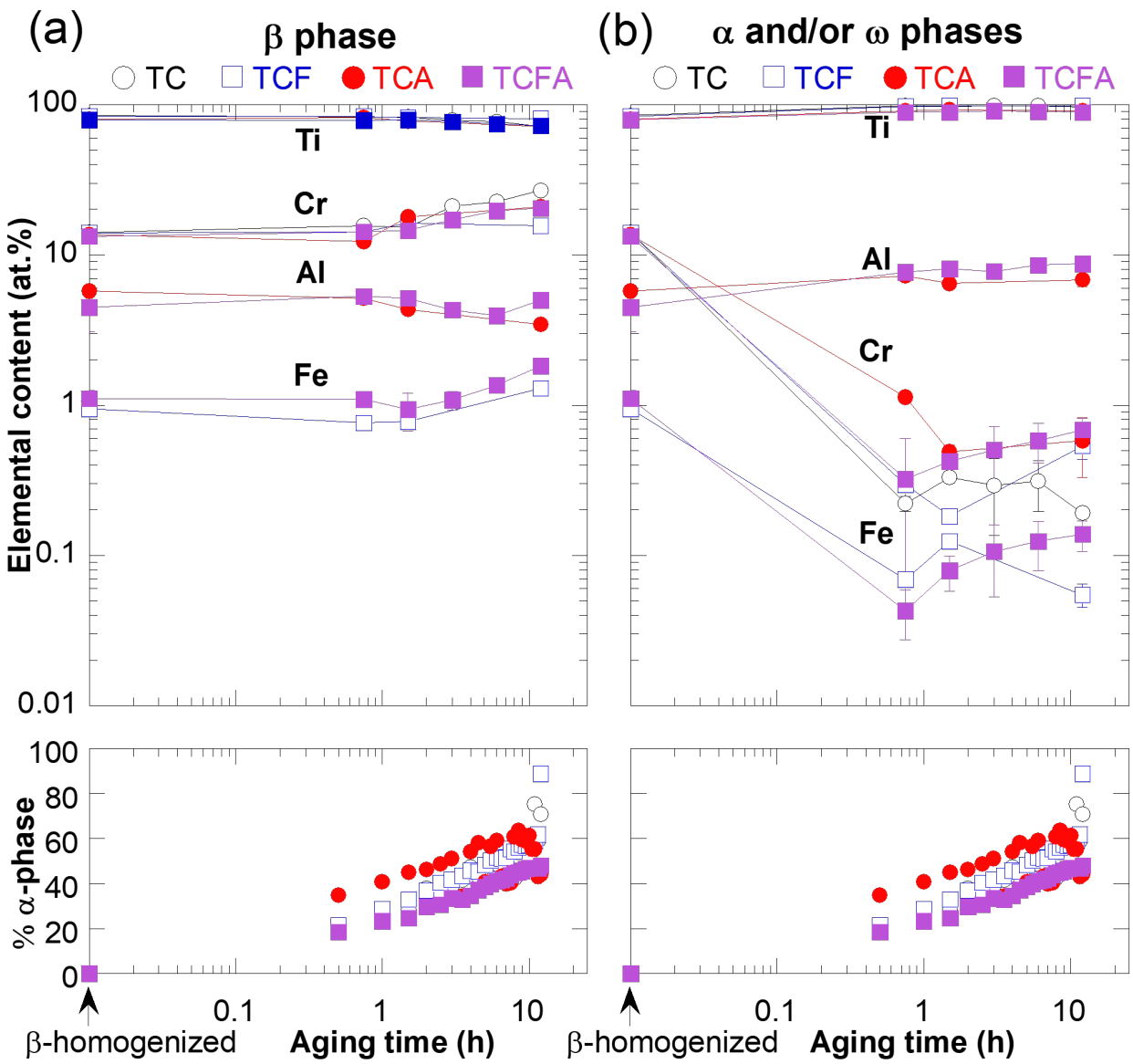

Figure 6.21: The APT measured Ti, Cr, Fe, and Al concentrations of the (a) β phase and (b) α and ω phases as a function of aging time. Error bars indicate ±1 standard deviation; where error bars are lacking, only one measurement was taken.

6.1.3.2 The interstitial O

Evaluating the location of O within β-Ti alloy microstructures is important since O is an α-phase stabilizer and could be related to the ω-assisted α-phase transformation [128]. In each alloy, O was observed in both the β phase and the ω and α phases. More O was observed in the α phase than in the β phase, see a representative sample in Figure 6.22, where the O content in the group of α-phase precipitates was about an order of magnitude higher than the surrounding β matrix. Because O is an impurity element, the average concentrations of O were low in all samples, but the average O content in the α phase was about four times larger than the average O content in the β phase, see Figure 6.23.

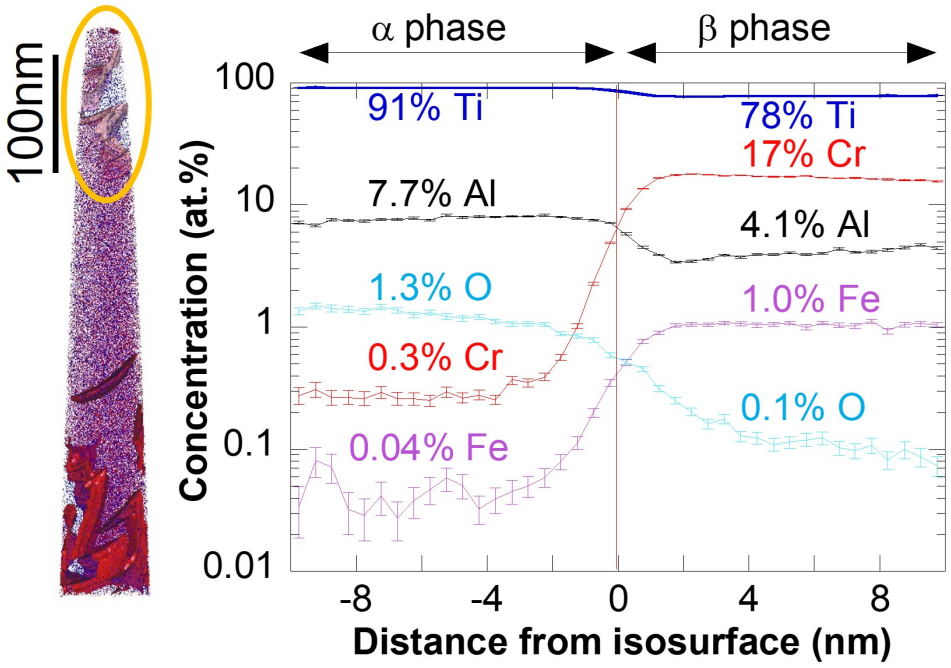

Figure 6.22: The APT tip reconstructions and corresponding proximity histogram for the group of α-phase precipitates highlighted at the thin end of the APT tip.

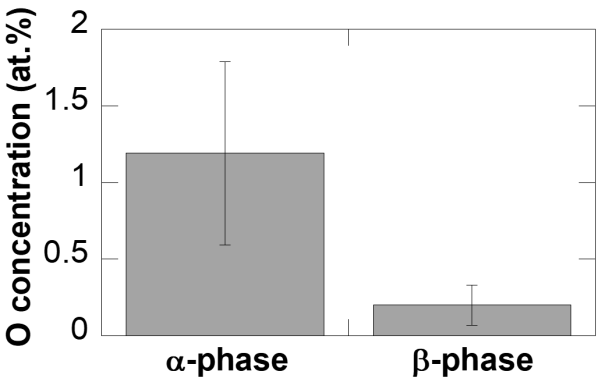

Figure 6.23: The average O concentrations of the α and β phases in all alloys. Error bars indicate 1 standard deviation.

O was also measured across the α/β interface using a 1-D concentration profile across the α precipitate in Figure 6.24. The enrichment of Al and rejection of Cr from the α phase during α-phase precipitation is evident in the 1-D concentration profile. An O content of approximately 0.5at.% both within the α precipitate and near the α/β interface was calculated, compared to the average O content of 0.1at.% in the β matrix.

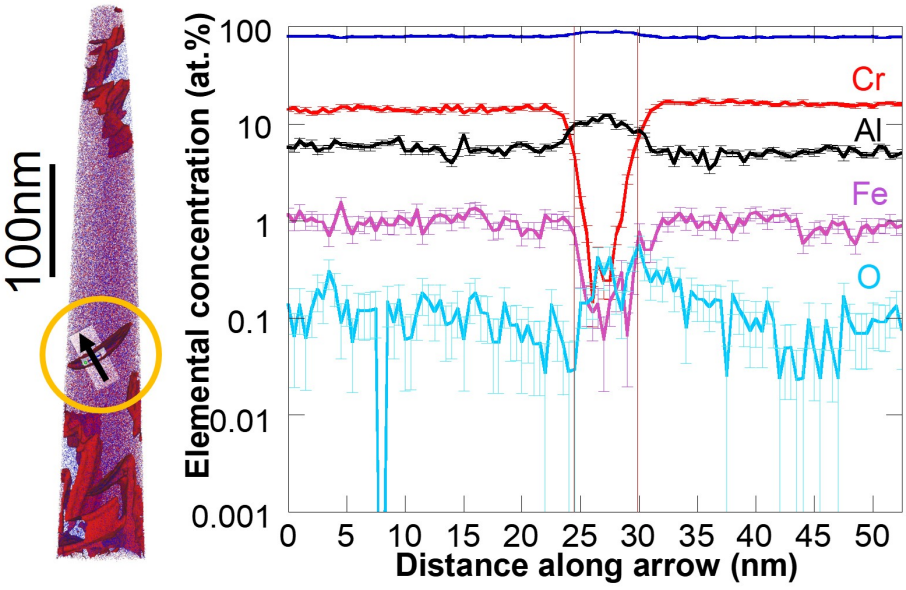

Figure 6.24: The APT tip reconstruction and 1-D concentration profile for the α-phase precipitate highlighted in the middle of the APT tip showing higher O concentrations in the precipitate and along the α/β boundary. The α/β boundary, as delineated by the Cr isosurfaces, are shown with the vertical red lines.

6.1.3.3 The interstitial H

In atom probe mass spectra, elemental H has a peak at 1 Da corresponding to the H^+ ion and a peak at 2 Da corresponding to H_2^+. These peaks do not overlap with any other elements. The concentration of H in each sample was calculated using the background corrected counts of H found at the 1 Da and 2 Da peaks to determine the at.% of H in the samples.

Microstructure, whether fully β-homogenized, β+α, or β+α+ω, did not significantly affect the overall concentration of H measured in the samples, see Figure 6.25. While there was a slight shift between the β-homogenized and 12 h aged samples, the β-homogenized samples were shifted right by less than a factor of 10, and H concentrations in the range of approximately 0.8 to 35 at.% were measured regardless of microstructure.

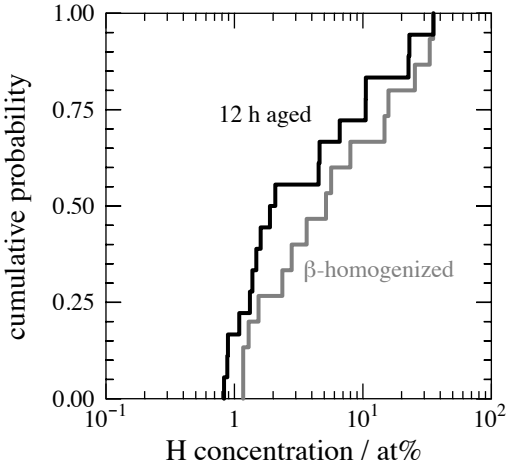

Figure 6.25: A cumulative probability distribution plot of the H concentrations in the β-homogenized (gray) and the 12 h aged (black) samples. H concentrations were calculated using the background corrected counts of H found at the 1 Da and 2 Da peaks to determine the at.% of H in the samples. Data from TC, TCF, TCA, and TCFA are combined in this figure.

In the samples containing multiple phases, the β phase exhibited higher concentrations of H than the α phase, see Figure 6.26(a). These results are consistent with similar APT experiments on β+α microstructures [213]. The ratio of H in the β phase to H in the α phases was dependent on the overall H concentration in the sample, and it was less than the 20:1 solubility ratio of H for the β/α phases, see Figure 6.26(b) and (c) for β/α ratios of approximately 5:1 and 3:1, respectively.

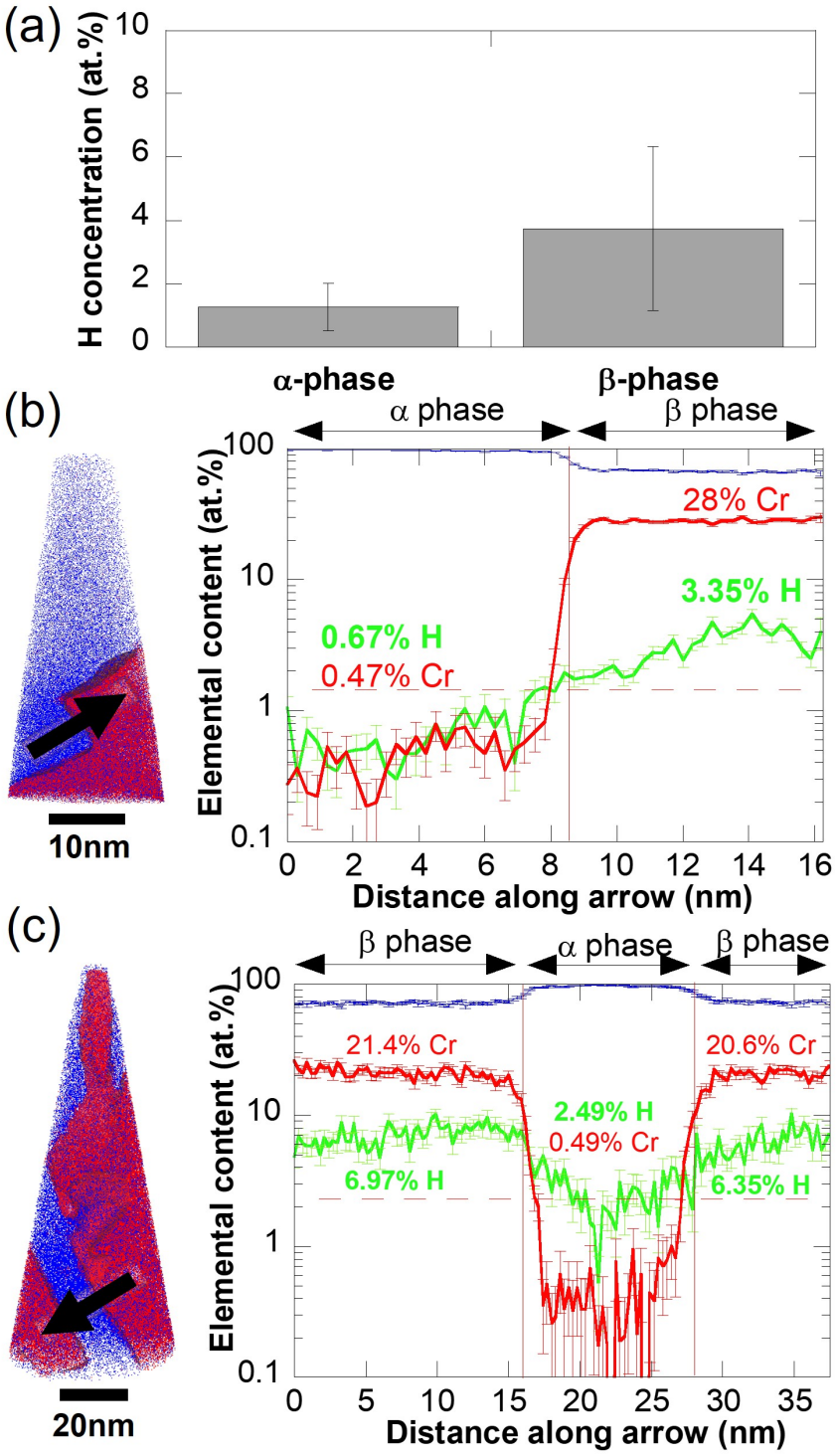

Figure 6.26: The (a) average H concentrations of the α and β phases in all alloys (error bars indicate 1 standard deviation). The element distribution map and 1-D concentration profiles measuring Ti, Cr, and H concentrations through the α and β phases in (b) one TC 12 h aged sample and (c) a second TC 12 h aged sample.

The effect of electron-beam accelerating voltage during the Pt-cap deposition step of the APT sample lift-out process on the H concentration in APT samples was explored. Two accelerating beam voltages, 5 kV and 30 kV, were used. Samples made using a 5 kV accelerating voltage during Pt deposition contained significantly less H than those made using a 30 kV accelerating voltage, with the exception of TC samples, see Figure 6.27. The data in Figure 6.27 showed the same shift between β-homogenized and aged samples as in Figure 6.25.

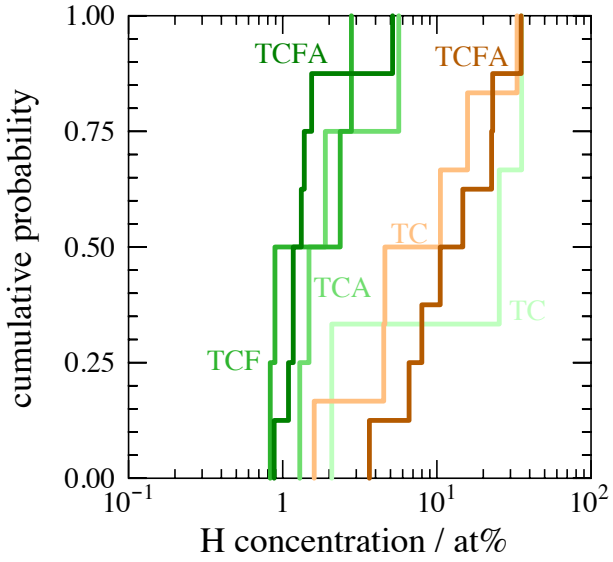

Figure 6.27: A cumulative distribution plot comparing the H concentrations in TC, TCF, TCA, and TCFA samples using a 5 kV (green) or 30 kV (orange) accelerating voltage during Pt deposition.

The higher concentrations of H observed in both the 5 kV and 30 kV TC samples were investigated using 1-D concentration profiles. The profiles taken across the 30% H isosurfaces calculated varying H compositions, from 20% to 50% H or higher, see a representative example in Figure 6.28(a). The volumes containing 50% or higher H were consistent with equilibrium hydrides (i.e. TiH_x where $1 \leq x \leq 2$) [168], while the 20% H volume was consistent with an H-rich β phase.

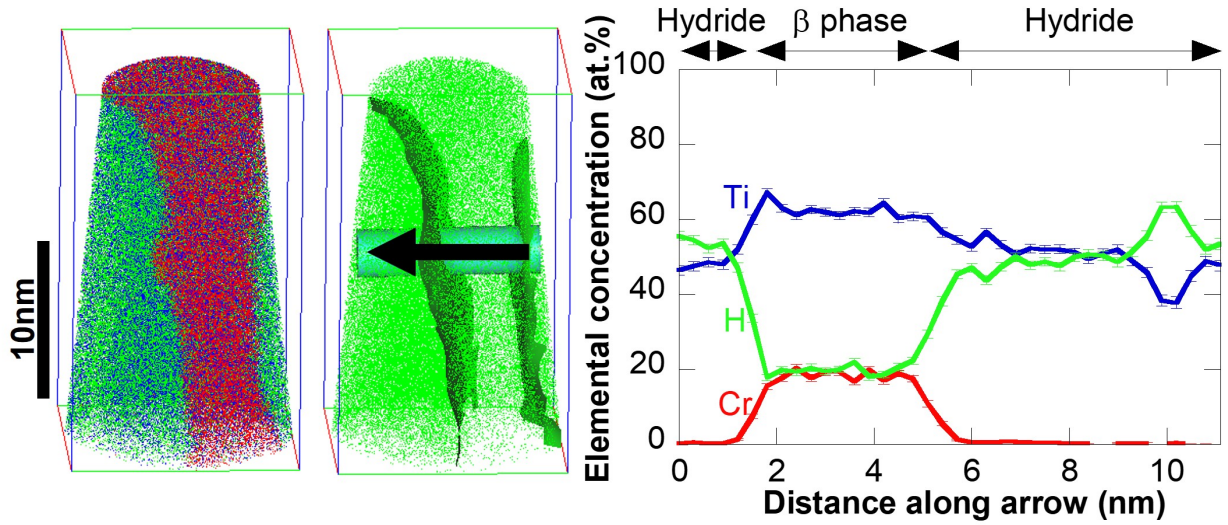

Figure 6.28: The element distribution maps and 1-D concentration profile of a TC sample after 12 h at 400 °C, using a 5kV electron beam accelerating voltage during Pt deposition. An element distribution map showing only the H atoms, a 30% H isosurface, and an arrow indicating the 1-D concentration profile is included.

In TCFA, H-rich volumes consistent with hydrides were only observed when a 30 kV accelerating voltage was used. These hydrides did not reach an equilibrium concentration of at least 50%, and instead contained non-equilibrium concentrations between 20% and 40%, see Figure 6.29. These hydrides are classified as non-equilibrium hydrides because the concentration of H in the hydrides is less than the 50% minimum necessary to form TiH. However, the hydrides are still considered hydrides because they are not the β phase, as they were almost completely Cr-free, and they are not the α phase, as the H concentration is significantly higher than the solubility of H in α-phase Ti.

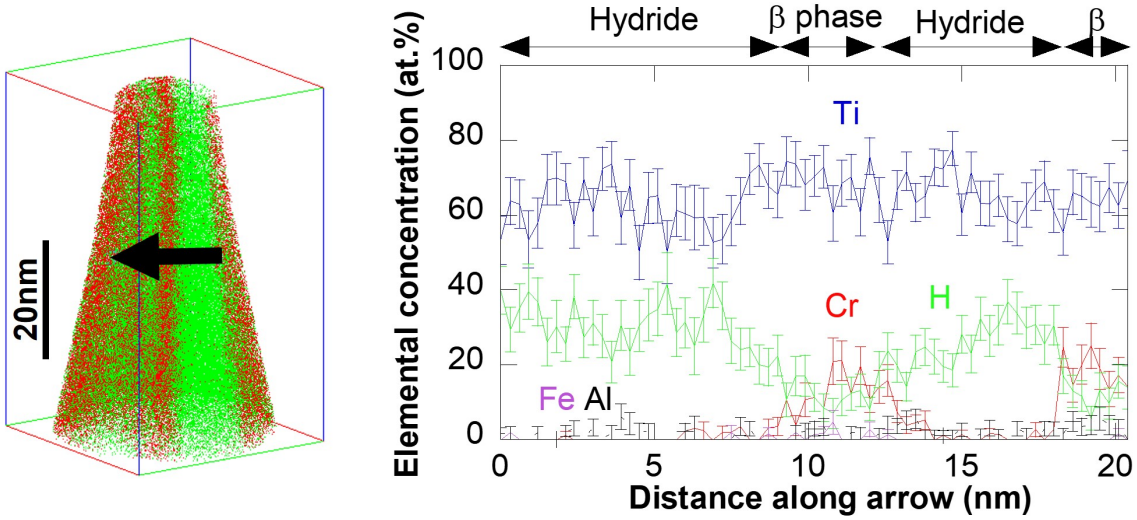

Figure 6.29: The element distribution map and 1-D concentration profile of a TCFA sample after 12 h at 400 °C, using a 30kV electron beam accelerating voltage during Pt deposition, with an arrow indicating the 1-D concentration profile.

6.2 Characterization of the mechanical properties during the β-to-ω and β-to-α phase transformations

The effect of the microstructural changes on the mechanical properties was explored using Vickers microhardness, RUS, and tensile testing. The results of the experiments resulted in the conclusions summarized here.

A higher volume fraction of the ω and α phases resulted in higher Vickers microhardness and higher strengths.

A higher volume fraction of the ω and α phases resulted in higher G values in TC and TCF which followed the rule of mixtures (ROM). While an increased α-phase volume fraction in TCA and TCFA did result in higher G values, they did not follow the ROM. For TCA and TCFA, E also followed the ROM, and increased linearly with increased α-phase volume fraction. For TC and TCF, E did not increase according to the ROM.

The ω-containing TC failed before yielding while the ω-containing TCF did not.

The results and a more detailed explanation of each conclusion are provided in the following sections concerning the Vickers microhardness, RUS, and tensile experiments.

6.2.1 Vickers microhardness

The Vickers hardness was measured after 0.75, 1.5, 3, 6, and 12 h of aging. After 0.75 h aging, the three-phase (β+α+ω) TC exhibited the highest hardness of all the alloys, as well as the highest ω-phase volume fraction, see Figure 6.30. The hardness of TC decreased as the ω-phase volume fraction decreased from 0.75 h to 6 h of aging. Once the α-phase volume fraction was greater than approximately 50%, the hardness increased again with increasing α-phase volume fraction. TCF exhibited a similar hardness evolution as TC, however the ω-phase volume fractions of TCF were less than TC, leading to TCF exhibiting lower hardness than TC. The two-phase (β+α) TCA and TCFA exhibited increased hardness with increased α-phase volume fraction. TCA exhibited higher hardness values and higher α-phase volume fractions than TCFA. After 6 h at 400 °C, TCFA exhibited similar hardness as TCA, even though TCFA exhibited lower α-phase volume fractions than TCA. No further significant increase in Hv was measured up to 300+ h of 400 °C aging for TC, TCF, TCA, or TCFA [214].

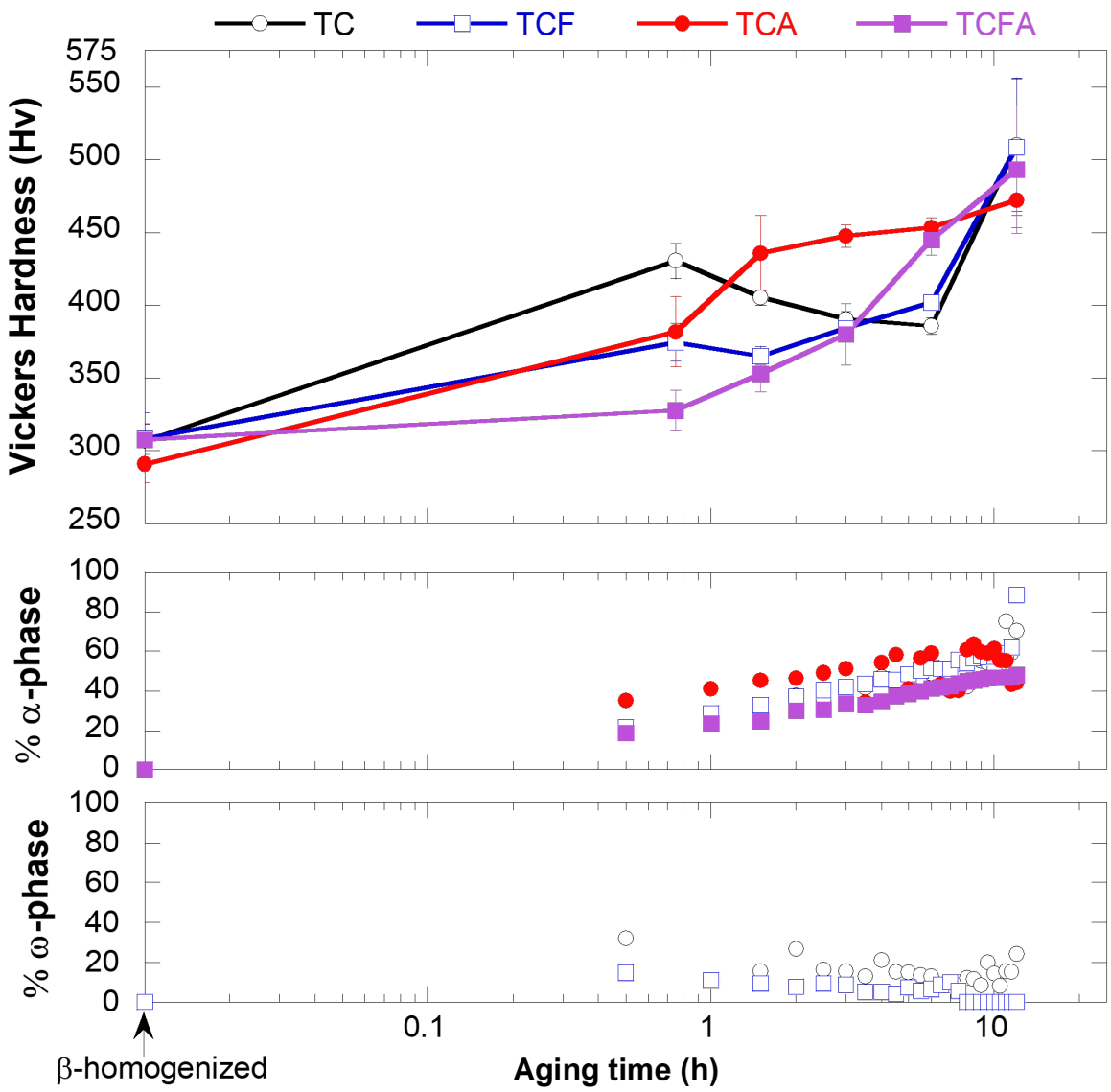

Figure 6.30: Vickers hardness as a function of 400 °C aging time for TC, TCF, TCA, and TCFA. The α- and ω-phase volume fractions are provided for reference.

6.2.2 RUS

The RT RUS measurements of the β-homogenized samples resulted in G values of 37 GPa, 33 GPa, 30 GPa, and 33 GPa for TC, TCF, TCA, and TCFA, respectively. As the sample temperature increased to 400 °C, the G values decreased due to the softening of the lattice, except for the TCA G values, which increased. Each sample reached 400 °C after 15 minutes. The 400 °C G values were 34 GPa, 31.5 GPa, 32 GPa, and 32 GPa for TC, TCF, TCA, and TCFA, respectively. Because

TCA exhibited an increase in G, phase transformations were assumed to have occurred in TCA while the alloys were heating to 400 °C. If transformations were occurring in TCA, it is possible that they occurred in TC, TCF, and TCFA during heating as well.

The three-phase (β+α+ω) TC and TCF exhibited a higher increase in G during the 24 h 400 °C experiment than the two-phase (β+α) TCA and TCFA, see Figure 6.31. With the precipitation of the ω phase during the first 0.5 h at 400 °C, TC exhibited an increase of 9 GPa (or 26%) and TCF exhibited an increase of 2.5 GPa (or 8%). The G values of TC and TCF continue to increase as the ω-phase volume fraction decreases.

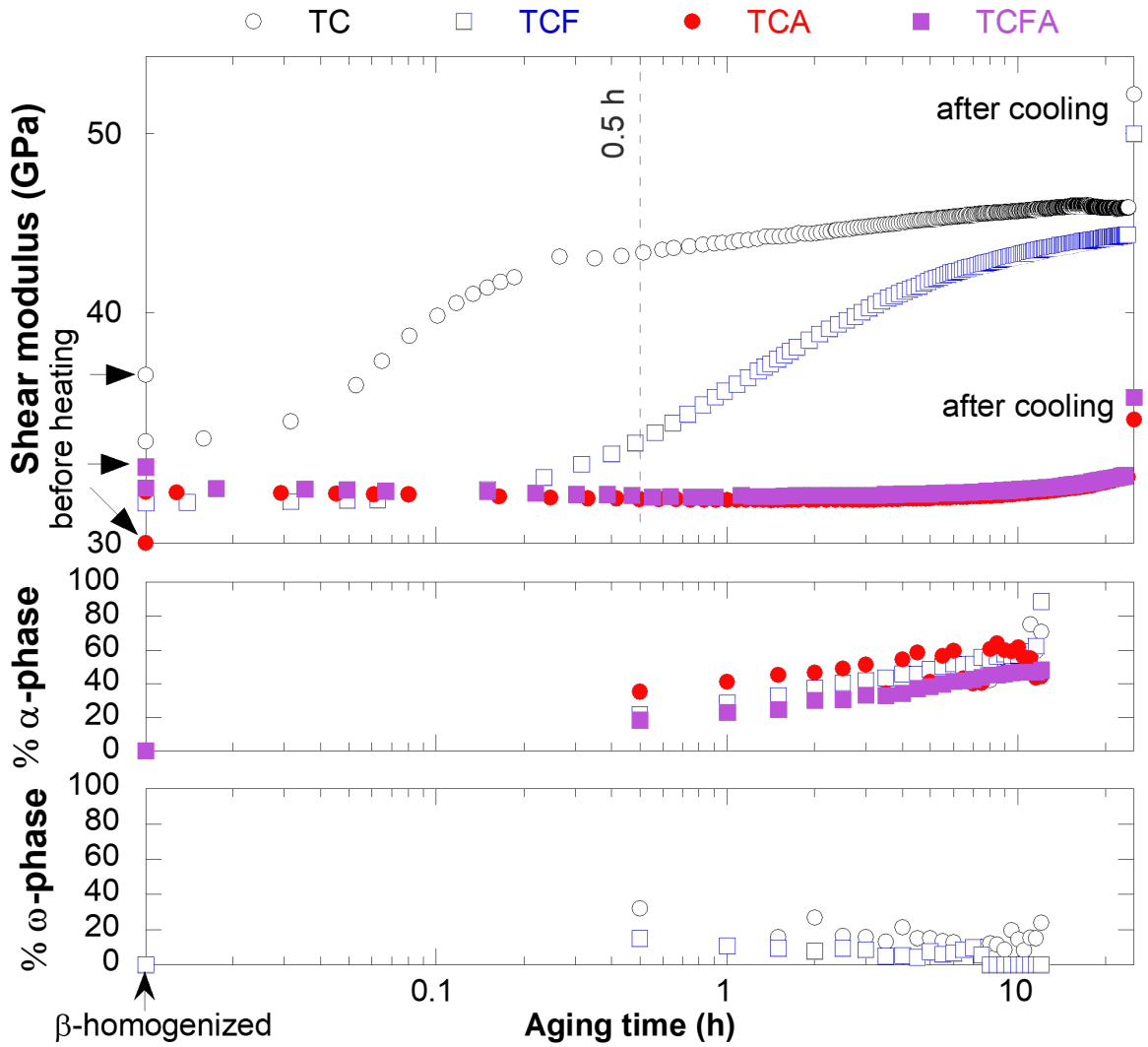

Figure 6.31: The shear modulus of each alloy at 400 °C measured using resonance ultrasound spectroscopy (RUS) as a function of aging time. RT measurements are included for reference.

After the 24 h experiment, the samples were cooled to RT and final measurements were taken. The post-transformation RT G values were 52.5 GPa, 50 GPa, 35 GPa, and 36 GPa for TC, TCF, TCA, and TCFA, respectively. TCF exhibited the largest relative increase in G at 51%, followed by TC with an increase of 42%, while TCA and TCFA exhibited increases of 17% and 9%, respectively.

Since the G values of each alloy were hypothesized to increase according to the ROM, the ROM for a two-phase material was used to calculate the predicted G values for TCA and TCFA, with the upper bound for the ROM calculated using Equation 6.2 and the lower bound for the ROM calculated using Equation 6.3. The RUS-measured 400 °C G values of 32 GPa were used for the G_β of TCA and TCFA (the G values of each alloy after reaching 400 °C). It was assumed that these G values were of the β phase of each alloy at 400 °C, and that the β-to-α transformation had not occurred when the RUS measurement was taken. Because the α phase exhibits different G values along different crystallographic directions, upper and lower bounds for the ROM were calculated using maximum and minimum G values. The maximum G_α occurs along $\langle 1\,1\,\bar{2}\,0 \rangle$, and has a value of approximately 35 GPa at 400 °C, while the minimum G_α occurs along $\langle 0\,0\,0\,1 \rangle$, and has a value of approximately 20 GPa at 400 °C [77, 215]. The Rietveld-measured α-phase volume fraction for each alloy was used for v_α.

$$G_{max} = G_\beta\, v_\beta + G_\alpha\, v_\alpha \tag{6.2}$$

$$G_{min} = \left(\frac{v_\beta}{G_\beta} + \frac{v_\alpha}{G_\alpha}\right)^{-1} \tag{6.3}$$

The RUS-measured G values for both TCA and TCFA fell within the range of values predicted by the ROM, see Figure 6.32.

The ROM for a three-phase material was used to calculated the predicted G values for TC and TCF, with the upper bound for the ROM calculated using Equation 6.4 and the lower bound for the ROM calculated using Equation 6.5. The RUS-measured 400 °C G values of 34 GPa and 31.5 GPa were used for were used for the G_β of TC and TCF, respectively, and the same assumption, that the RUS measurements were taken at 400 °C before the β-to-ω or β-to-α transformations had occurred, was made. Because the ω and α phases exhibit different G values along different crystallographic directions, upper and lower bounds were calculated for each phase. The same 400 °C G_α values

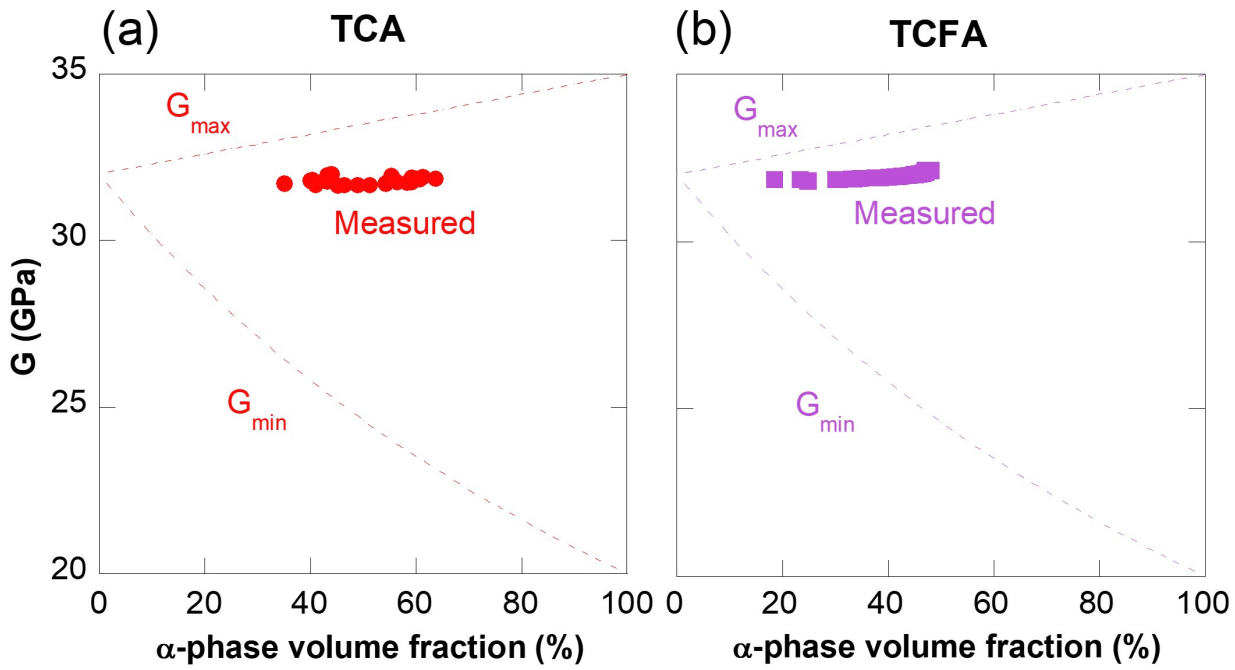

Figure 6.32: The RUS-measured G values for (a) TCA and (b) TCFA compared to the ROM-predicted G values.

as for Equations 6.2 and 6.3 were used. The values of G_ω at 400 °C were not known, so the RT maximum and minimum G_ω values of 70 GPa along $\langle 1\,1\,\bar{2}\,0 \rangle$ and 45 GPa along $\langle 0\,0\,0\,1 \rangle$ were used [77]. The Rietveld-measured α- and ω-phase volume fractions for each alloy were used for v_α and v_ω, respectively.

$$G_{max} = G_\beta\, v_\beta + G_\alpha\, v_\alpha + G_\omega\, v_\omega \tag{6.4}$$

$$G_{min} = \left(\frac{v_\beta}{G_\beta} + \frac{v_\alpha}{G_\alpha} + \frac{v_\omega}{G_\omega}\right)^{-1} \tag{6.5}$$

The RUS-measured G values for both TC and TCF fell within the range of values predicted by the ROM, see Figure 6.33.

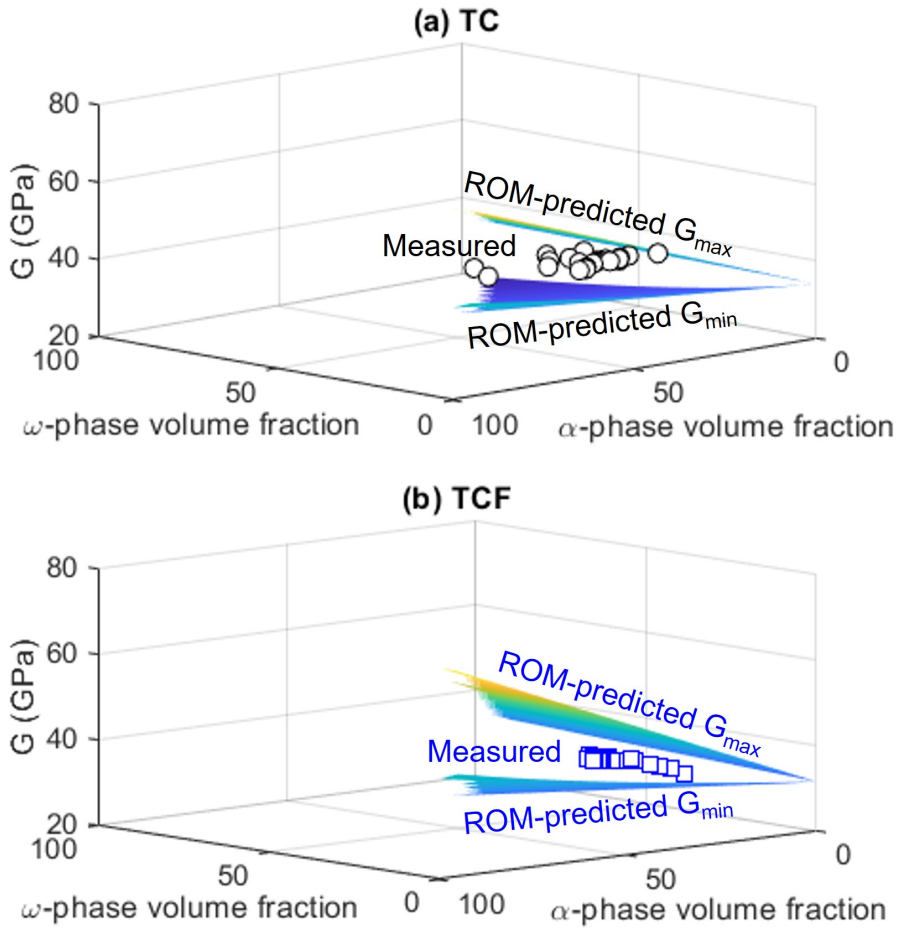

Figure 6.33: The RUS-measured G values (data points) for (a) TC and (b) TCF compared to the ROM-predicted G values (green and blue contours). The G values fell within the range of values predicted by the ROM.

6.2.3 Tensile testing

Dogbone-shaped samples were uniaxially tensile tested after 0.75, 1.5, 3, 6, and 12 h of aging to determine the E, σ_y, UTS, and ϵ_f of each alloy as a function of aging time. Engineering stress versus engineering strain was plotted to determine the differences in tensile properties between each alloy after each aging time. tensile-tested samples of β-homogenized and aged TC, TCF, TCA, and TCFA in Figures 6.34(a-d), respectively. The E, ϵ_f, σ_y, and UTS values were calculated according to sections 7.7.1, 7.10, and 7.11.5 of ASTM standard E8-E8M-13a, and are covered in detail below.

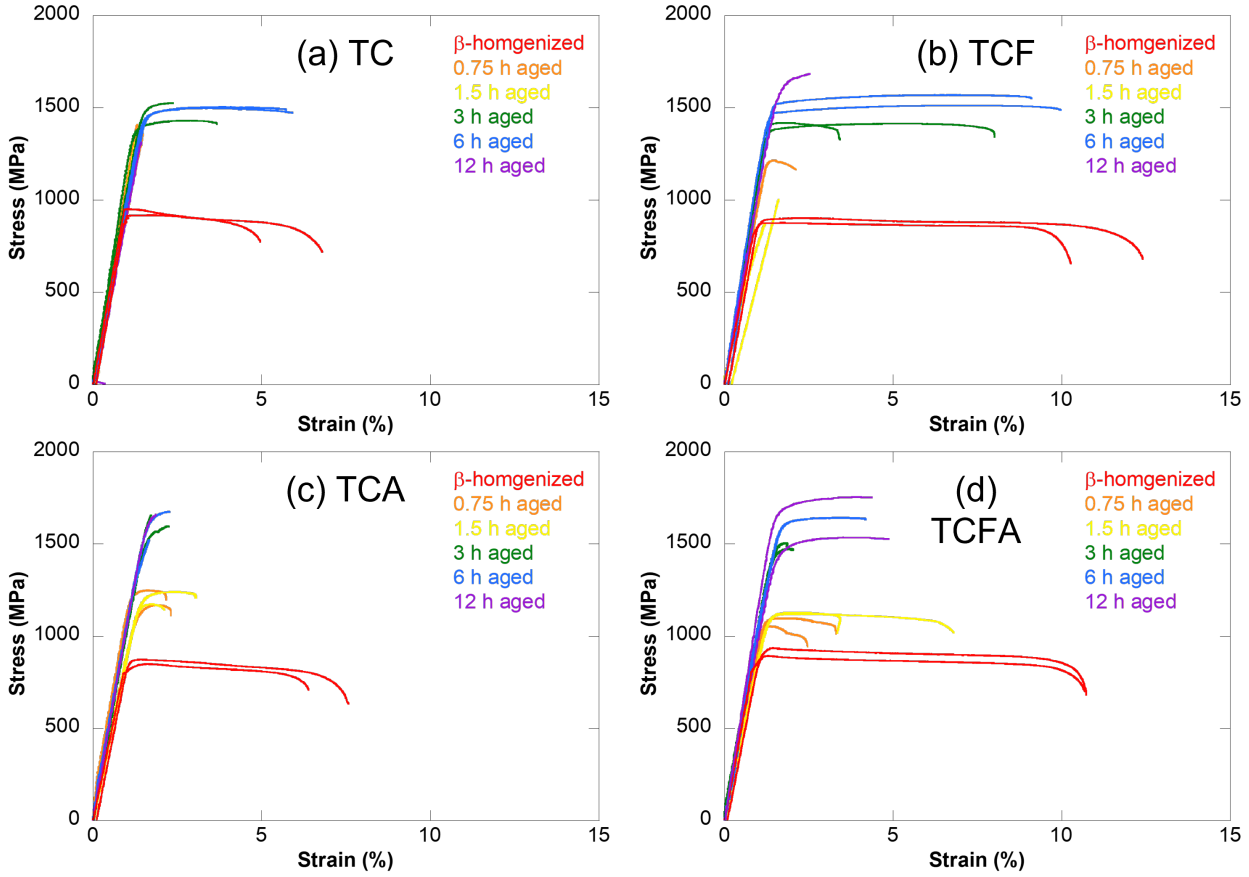

Figure 6.34: Engineering stress versus engineering strain curves for (a) TC, (b) TCF, (c) TCA, and (d) TCFA in the β-homogenized condition, as well as after aging for 0.75, 1.5, 3, 6, and 12 h.

6.2.3.1 Young's Modulus

Unlike the G values calculated from the RUS experiment, TC did not exhibit a clear relationship between either α- or ω-phase volume fractions and E, as E remained approximately constant throughout the 12 h aging, see Figure 6.35. TCF appeared to exhibit a decrease as the ω-phase volume fraction decreased from 0.75-3 h aging, and increased after 6 h aging as the α-phase volume fraction increased past approximately 50%. The E values for TCA and TCFA also exhibited a decrease from 0.75 to 1.5 h aging, and exhibited an increase with increased α-phase volume fraction after 1.5 h aging.

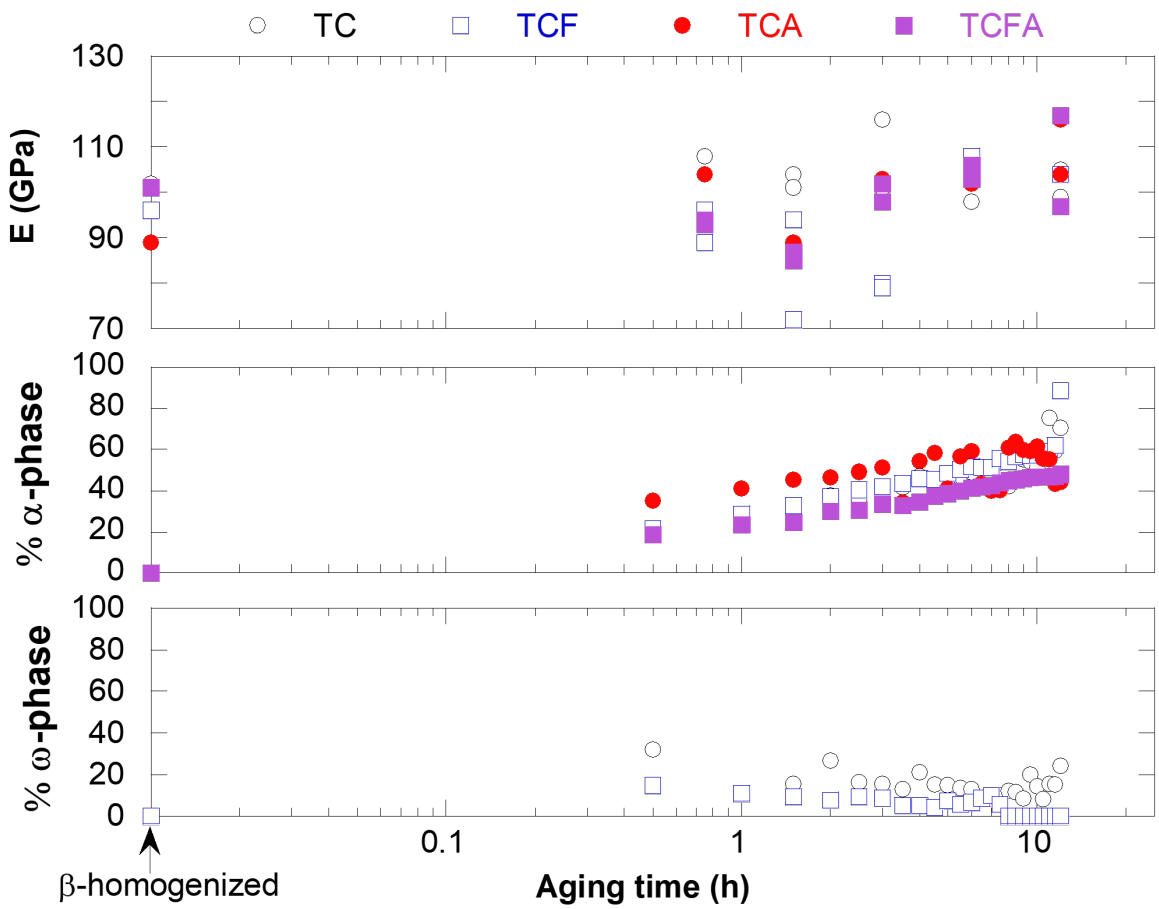

Figure 6.35: The E values calculated from two tensile tests per aging time for each alloy. The phase volume fractions are included for reference.

Because the tensile tests were conducted at RT, RT values for the β, ω, and α phases were used. Equations 6.2 and 6.3 were used for the upper and lower bounds, respectively, of the two-phase alloys TCA and TCFA, and Equations 6.4 and 6.5 were used for the upper and lower bounds, respectively of the three-phase alloys TC and TCF. The β-homogenized E values of 103.5 GPa, 97.5 GPa, 90.5 GPa, and 97 GPa were used for the G_β of TC, TCF, TCA, and TCFA, respectively. The E values in the $\langle 0\,0\,0\,1 \rangle$ direction for the ω and α phases were used for the upper bounds, at 201.0 GPa and 143.3 GPa, respectively, and the E values in the $\langle 1\,1\,\bar{2}\,0 \rangle$ direction for the ω and α phases were used for the lower bounds, at 129.0 GPa and 104.4 GPa, respectively [77].

TCA and TCFA both exhibited some E values within the range of values predicted by the ROM. One E value for TCA fell below the ROM lower bound.

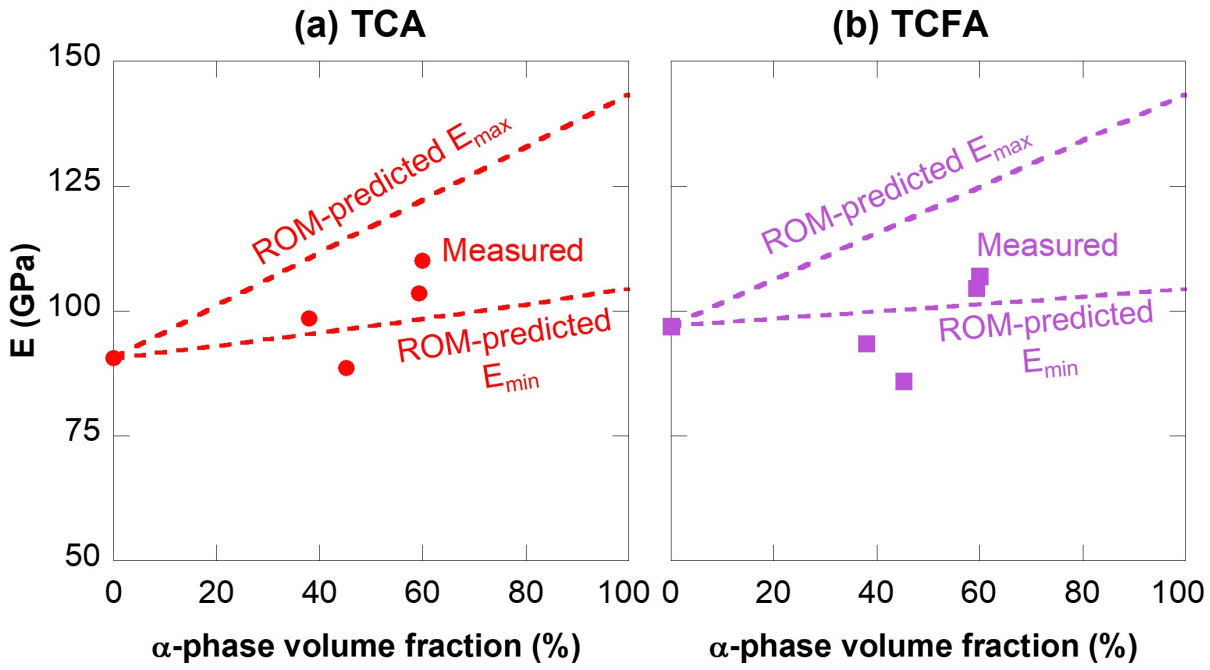

Figure 6.36: The average E values calculated from two tensile tests per aging condition for (a) TCA and (b) TCFA, compared to the ROM-predicted values.

TC and TCF both exhibited E values below the range of values predicted by the ROM. TCF exhibited the closest value to the predicted value when the ω-phase volume fraction was 0% after 12 h aging.

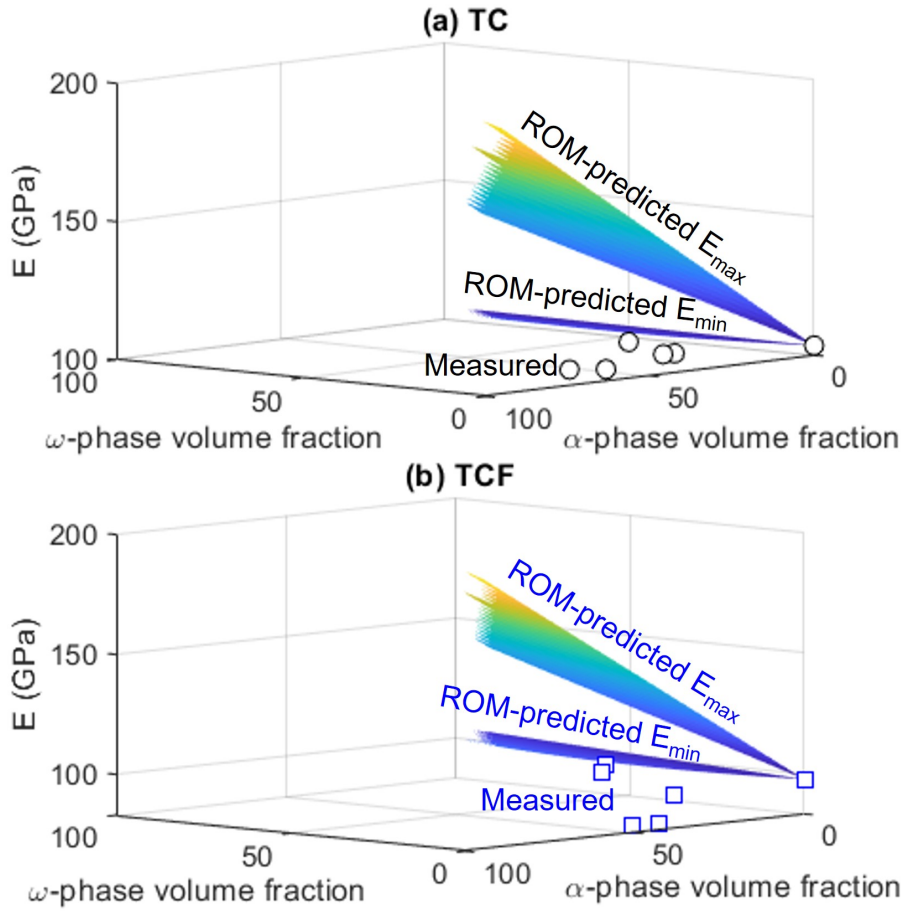

Figure 6.37: The average E values (data points) calculated from two tensile tests per aging condition for (a) TC and (b) TCF compared to the ROM-predicted values (green and blue contours). The E values fell below the minimum ROM-predicted E values for TC and TCF.

6.2.3.2 σ_y and UTS

σ_y and UTS increased with increasing α-phase volume fraction, see Figure 6.38. TC failed before yielding after 0.75, 1.5, and 12 h aging, so σ_y could not be calculated for those times. TC exhibited a higher UTS than TCF, TCA, or TCFA after 0.75 and 1.5 h aging. The higher UTS values of TC after 0.75 and 1.5 h aging could be attributed to the higher ω-phase volume fractions at those times. However, TCF did not exhibit significantly different σ_y or UTS values than TCA or TCFA even though TCF contained the ω-phase microstructure. This suggests that there is a critical volume fraction of ω phase that is necessary to achieve a higher UTS than what can be achieved with the α phase microstructure alone.

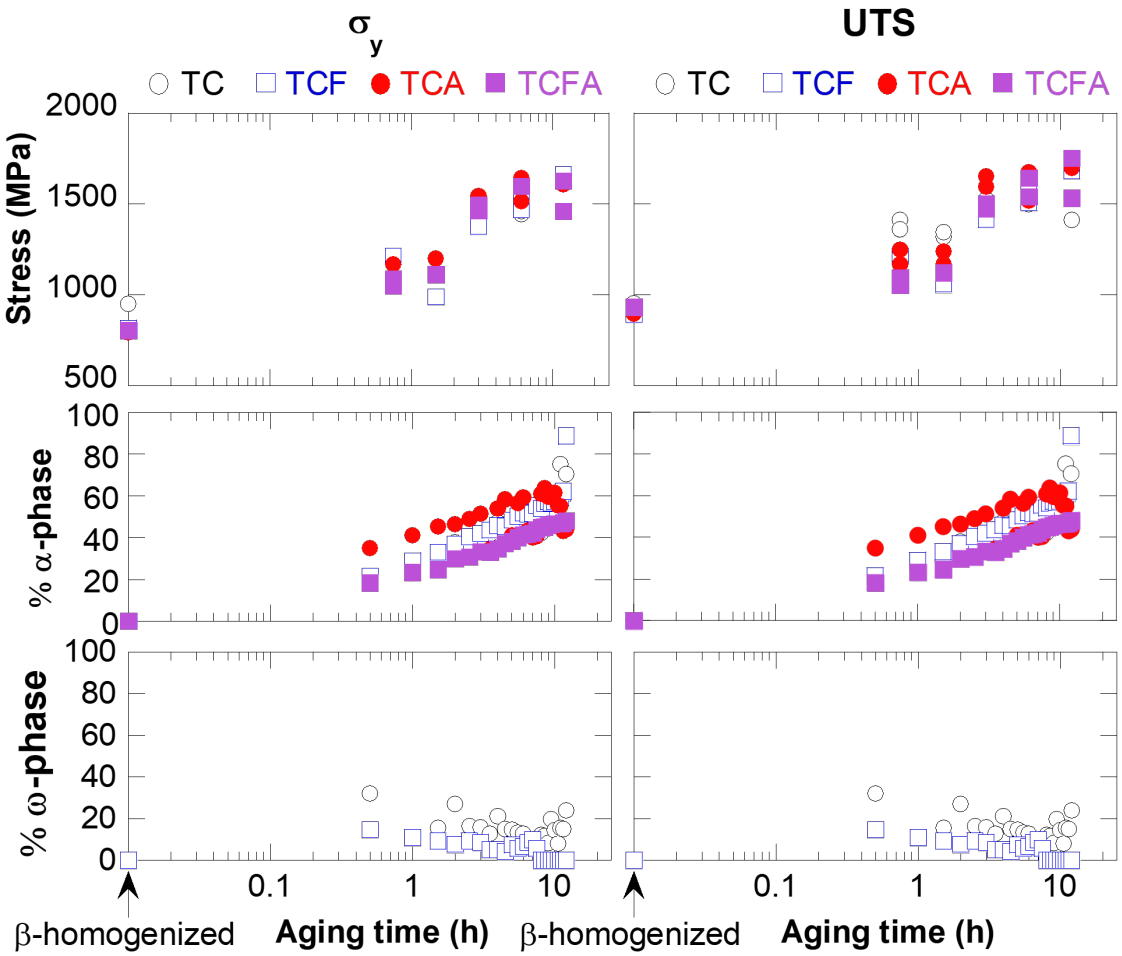

Figure 6.38: The σ_y (left) and UTS (right) values calculated from each tensile test shown in Figure 6.34, with the α- and ω-phase volume fractions for reference.

6.2.3.3 ϵ_f and fracture surfaces

ϵ_f decreased with the precipitation of the ω and/or the α phases in each alloy, see Figure 6.39. No other relationship between microstructure and ϵ_f was evident. TC failed before yielding after 0.75, 1.5, and 12 h aging. The failure before yielding could be attributed to the ω phase, as it is known to cause embrittlement in β-Ti alloys [48, 119, 149, 150]. However, TC yielded after 3 and 6 h aging, even though the ω-phase microstructure was present. TCF, which also contained the ω-phase microstructure, did not fail before yielding in any of the tensile tests. The grain boundary α-phase microstructures could be affecting the ϵ_f of the alloys more than the volume fractions of the phases.

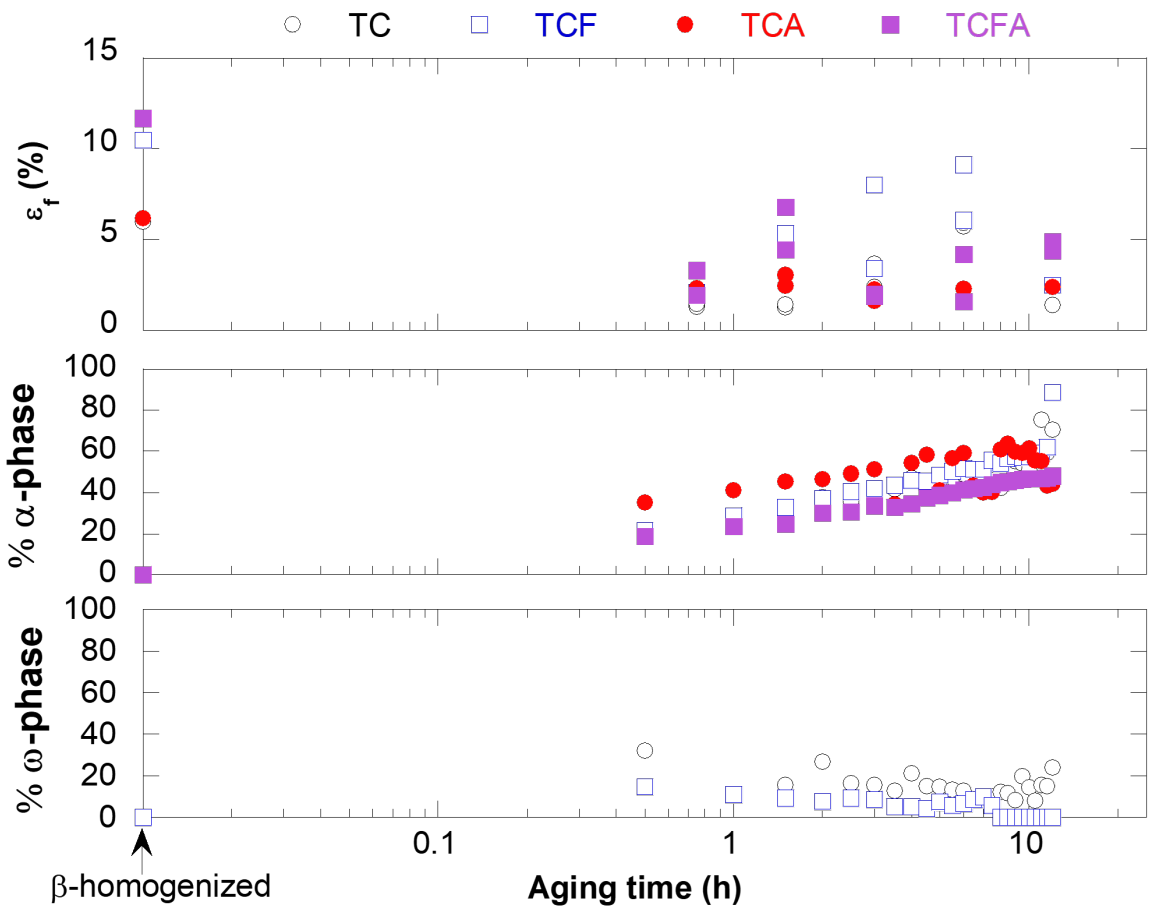

Figure 6.39: The ϵ_f values calculated from each tensile test shown in Figure 6.34, with the α- and ω-phase volume fractions for reference.

The fracture surfaces of the tensile tests were viewed using SE-SEM imaging to investigate the failure modes of each alloy. Evidence of mixed-mode failure was visible on all of the fracture surfaces evaluated. Representative fracture surfaces from the aged conditions of TC, TCF, TCA, and TCFA are provided in Figures 6.40, 6.41, 6.42, and 6.43, respectively. SE-SEM photomicrographs of the fracture surfaces of the remaining aged tensile-tested samples of each alloy are provided in Appendix D, in Figures 6.40 through D.16.

Dimples indicative of ductile fracture are present on all of the aged fracture surfaces. The dimples were formed when the more ductile β phase pulled around the less ductile ω and α phase precipitates. The smaller dimples on each fracture surface could be associated with the smaller α or ω precipitates, while larger features are most likely associated with larger α-phase precipitates

that form along the β-grain boundaries.

River patterns, secondary cracks, and intergranular failure were observed on the fracture surfaces as well, indicative of brittle fracture. Flat surfaces, also associated with brittle fracture rather than ductile fracture, were observed on all fracture surfaces. The dimples appear alongside these features, and in the case of the flat surfaces and grains associated with the intergranular fracture, often appear on the features.

Lamellar-like structures were observed on some of the fracture surfaces, see Figure 6.41(b) and (c). These structures could be colonies of α phase, separated by the β phase containing ω precipitates. The presence of the lamellar structures on the fracture surface are influenced by the orientation of the α-phase plates towards the fracture surface. If the plates intersect with the fracture surface in an edge-on orientation, the features could appear to be lenticular or lamellar in structure. If the plates intersect with the fracture surface face-on, the features could appear to be flat planes with no dimples. The orientation of the β grains and the α-phase plates could cause some of the large disparities in features between different regions of the same fracture surface, see Figure 6.40(b) and (c). The ω-phase, in contrast, should appear the same at any orientation with the fracture surface, as the ω phase morphology in Ti-Cr alloys is cuboidal and thus would look similar regardless of orientation.

No clear differences in failure were observed between the alloys to explain the differences in exhibited ϵ_f. Each alloy exhibited the mixed-mode failure features typical of multi-phase Ti alloys.

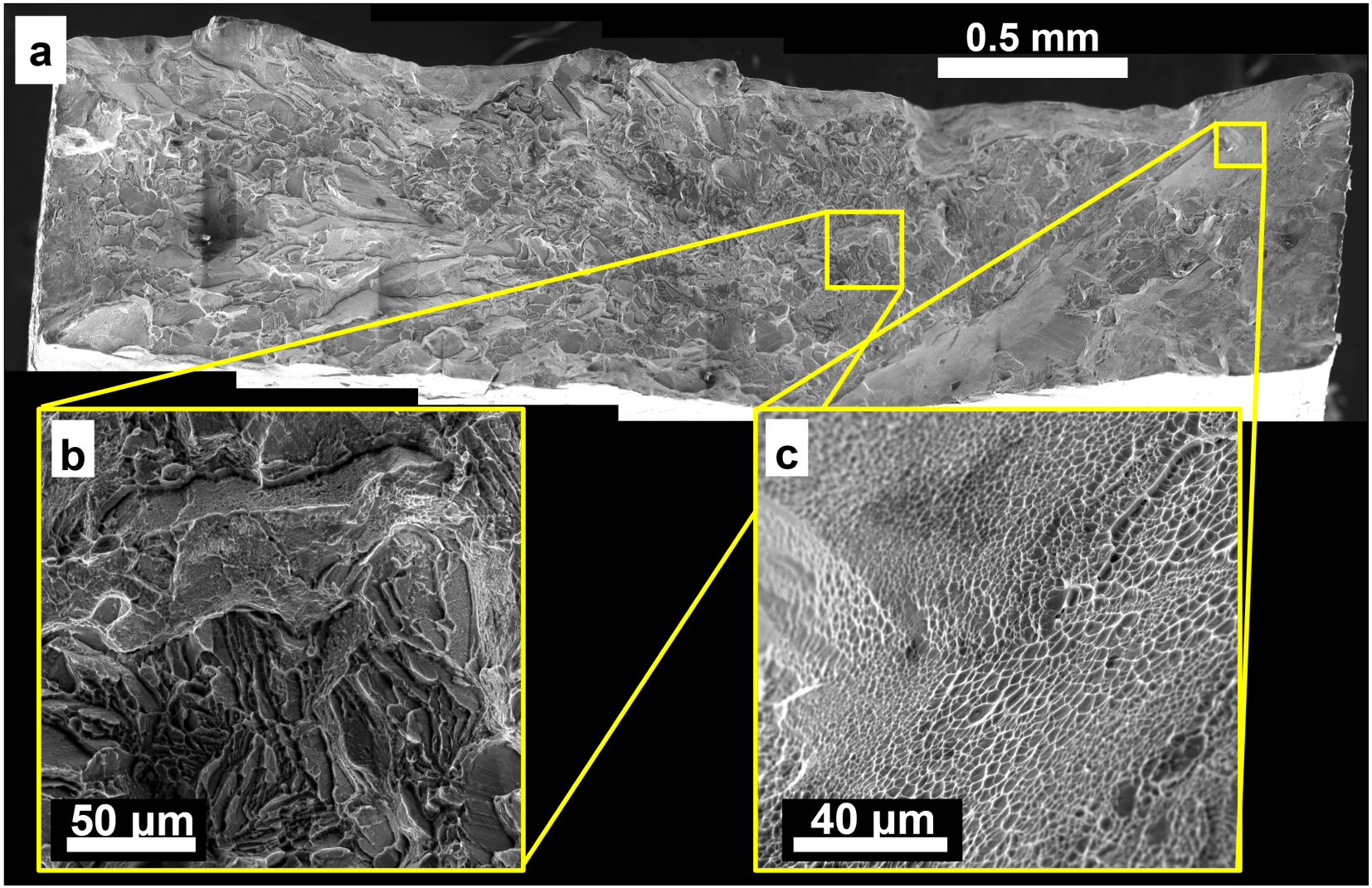

Figure 6.40: (a) SE SEM photomicrographs of the fracture surface from a TC tensile test sample aged for 0.75 h, stitched together using multiple photomicrographs. Higher magnification SE SEM photomicrograph illustrating (b) possible intergranular fracture or fracture of larger α-phase precipitates and (c) dimples on the fracture surface.

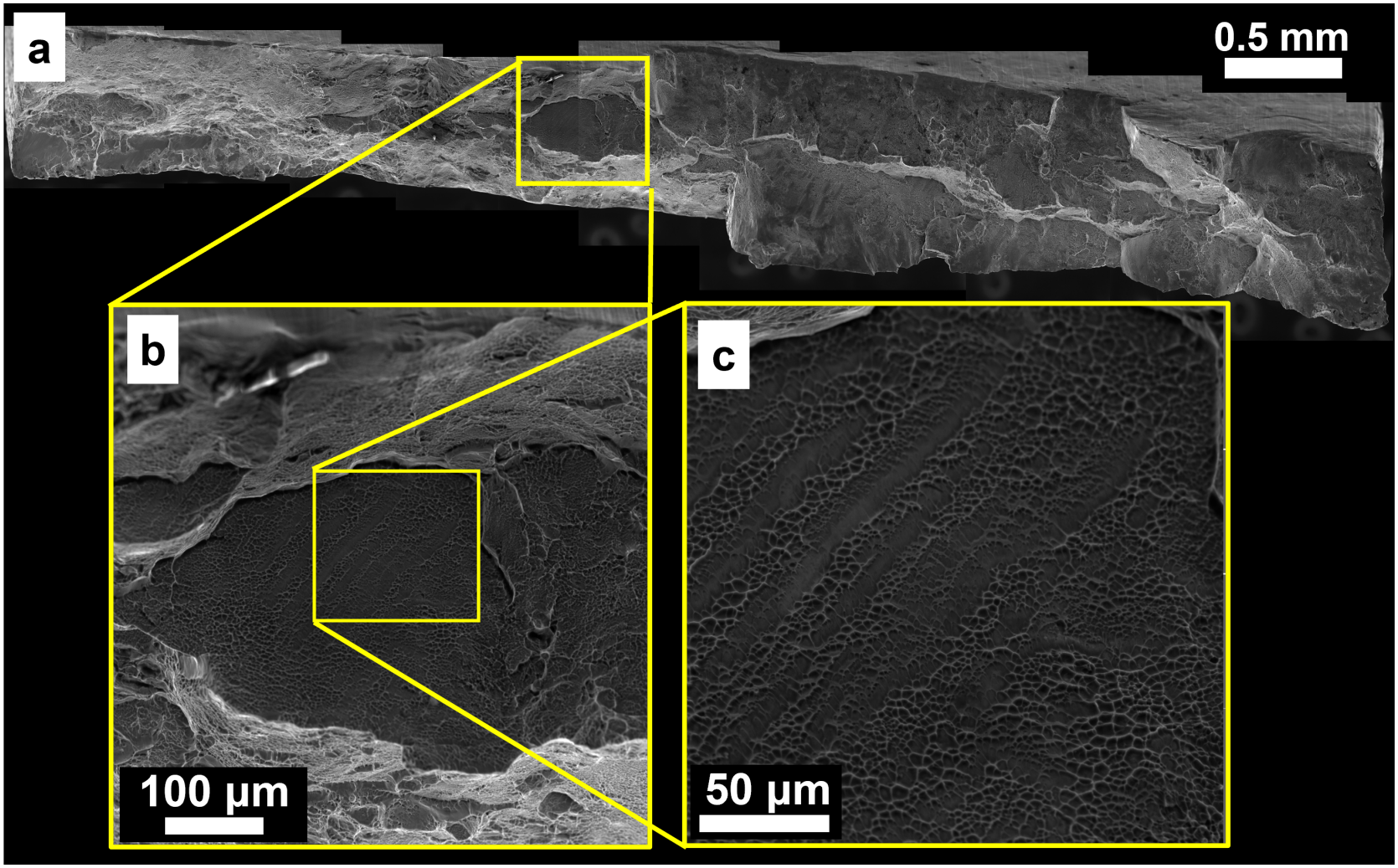

Figure 6.41: (a) SE SEM photomicrographs of the fracture surface from a TCF tensile test sample aged for 0.75 h, stitched together using multiple photomicrographs. Higher magnification SE SEM photomicrograph illustrating (b) a large flat plane containing dimples, possible tearing ridges, and lamellar structures, and (c) a higher magnification of the lamellar structure with dimples.

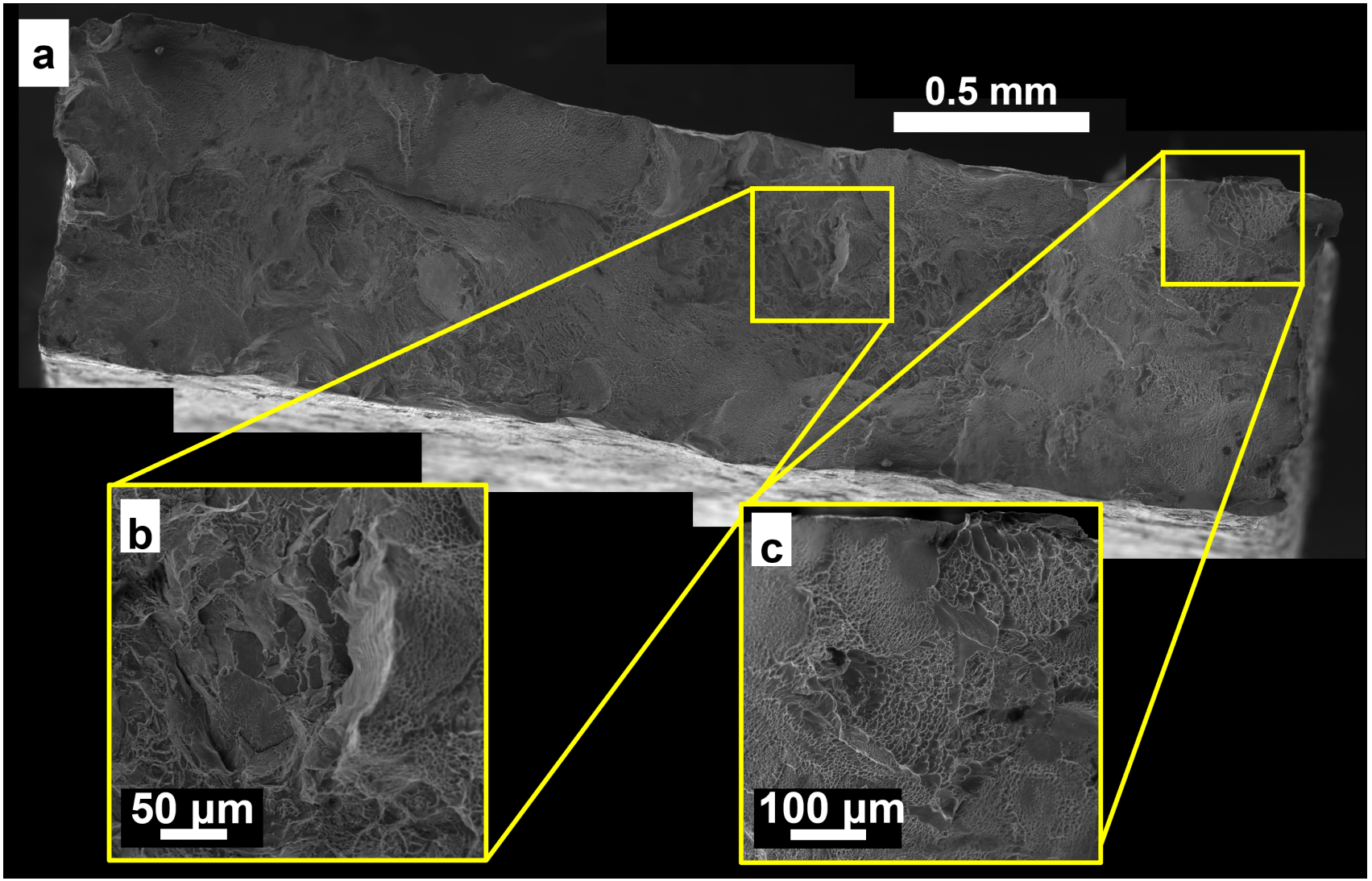

Figure 6.42: (a) SE SEM photomicrographs of the fracture surface from a TCA tensile test sample aged for 1.5 h, stitched together using multiple photomicrographs. Higher magnification SE SEM photomicrograph illustrating (b) intergranular fracture with dimples and (c) dimples and larger features where larger α phase precipitates could have separated from the β matrix.

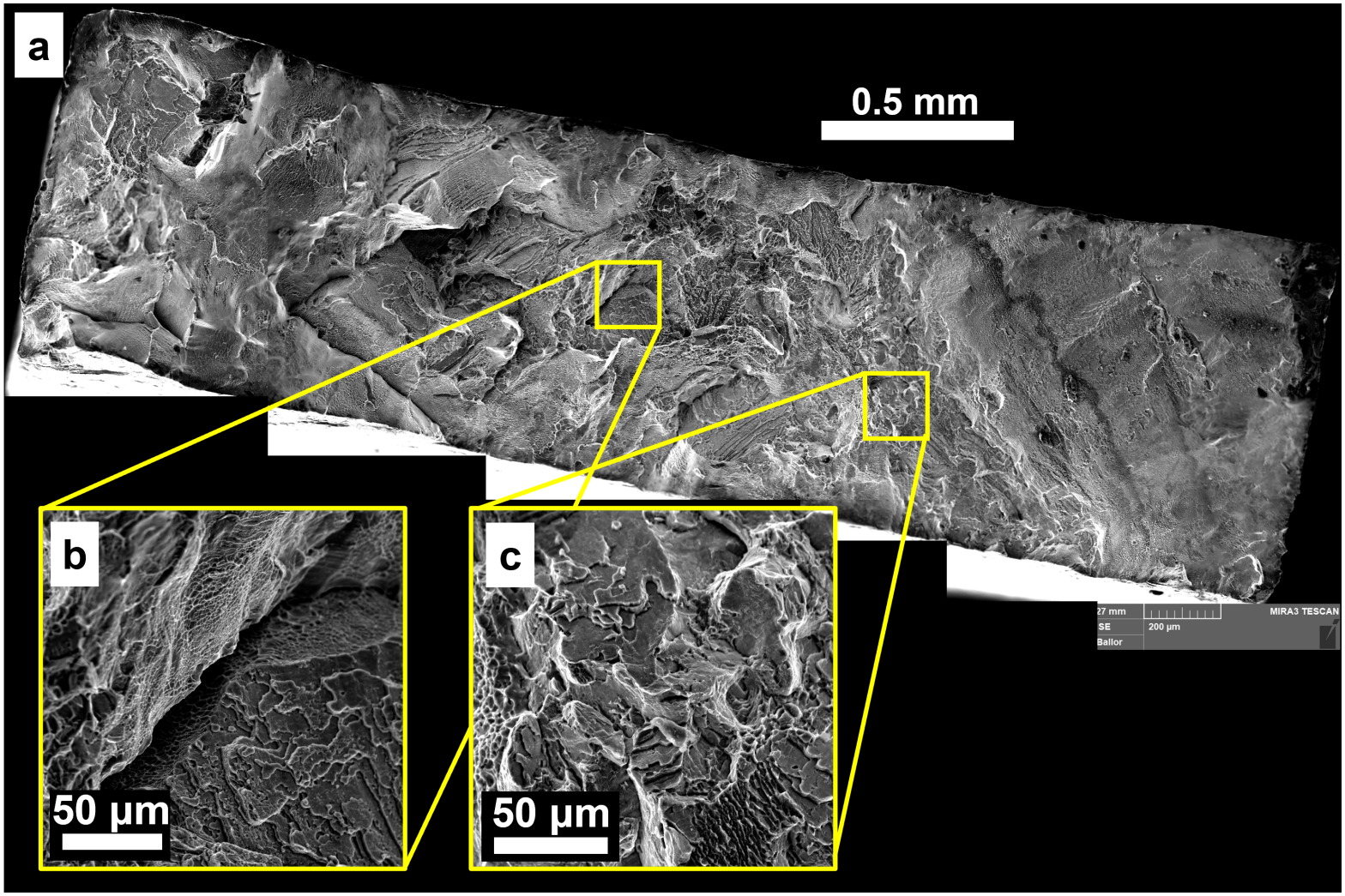

Figure 6.43: (a) SE SEM photomicrographs of the fracture surface from a TCFA tensile test sample aged for 3 h, stitched together using multiple photomicrographs. Higher magnification SE SEM photomicrograph illustrating (b) dimples along a crack and (c) dimples and faceted fracture.

CHAPTER 7

DISCUSSION OF AGED ALLOYS

In Chapter 6, the results from testing the hypotheses regarding the microstructural and mechanical property evolutions of TC, TCF, TCA, and TCFA during a 400 °C treatment were presented. In this chapter, the discussions of why the hypotheses were correct or incorrect are presented.

The discussions of the microstructural characterization hypotheses are presented first, separated into the discussions regarding the phase volume fraction, phase lattice parameter, and phase composition hypotheses. The discussions of mechanical property hypotheses are presented second, separated into the discussions regarding the hardness, elastic moduli, strength, and ϵ_f hypotheses.

Finally, a comparison between the mechanical properties of TC, TCF, TCA, TCFA, and the commonly used aerospace α+β alloy Ti-6Al-4V(wt.%) is presented.

7.1 Microstructural characterization

Hypotheses regarding the microstructural characterization fell into one of three categories: phase volume fraction, phase lattice parameter, and phase composition. The hypotheses were as follows:
Phase volume fraction hypotheses

- Fe would suppress α- and ω-phase formation, therefore lower α-and ω-phase volume fractions would be expected in the Fe-containing alloys.
- The α-phase stabilizer Al would promote the α-phase formation, and higher α-phase volume fractions would be expected in the Al-containing alloys.

Phase lattice parameter hypotheses

- The diffusion of the β-stabilizers from the α and ω phases into the β phase would increase the stability of the β phase, and the relative β-phase stability of the alloying elements would affect the β-phase lattice parameter differently.

- The diffusion of the α-stabilizer Al from the β phase into the α phase would affect the lattice parameter of the α phase in the Al-containing alloys differently than the Al-free alloys.
- The rejection of all alloying elements except Ti from the ω phase would cause the ω-phase lattice parameter to remain constant throughout the transformation. The Fe and Al additions could affect the ω-phase lattice parameter, as different ω-phase lattice parameters have been reported in different compositions of β-Ti alloys.

Phase composition hypotheses

- The β-stabilizers Cr and Fe would diffuse from the α and ω phases into the β phase.
- The α-stabilizer Al would diffuse from the β phase into the α phase.
- The ω-phase would reject any elements except Ti.
- The interstitial O would be present in higher concentrations in the α phase than the other phases.
- The interstitial O would be rejected from the ω phase and cluster at the ω/β boundaries, which would promote the ω-assisted α-phase transformation.
- The interstitial H would be present in higher concentrations in the β phase than in any other phase. If enough H was present in the sample, equilibrium hydrides would form.
- During the FIB-based lift-out process for APT samples, a higher electron-beam accelerating voltage during the decomposition of the Pt precursor would cause more gaseous H to be released, and this would result in an increase in the H concentration in the APT samples.

The discussions of why each hypothesis was found to be true or false through the XRD, SEM, TEM, and APT experiments are presented below.

7.1.1 Phase volume fraction hypotheses

The phase volume fraction hypotheses addressed how the alloying element additions Fe and Al would affect the volume fractions of the β, α, and ω phases. The Rietveld and threshold analyses were able to calculate the phase volume fractions as the β-to-ω and β-to-α transformations occurred, allowing the volume fraction hypotheses to be tested.

7.1.1.1 The effect of Al on α-phase volume fraction

The first hypothesis, that Al would promote the α-phase formation, and that higher α-phase volume fractions would be expected in the Al-containing alloys, was partially true. The addition of the α-phase stabilizer Al into the Ti-Cr alloy system made the β-to-α transformation more favorable than the β-to-ω transformation (promoting α-phase formation), thus the ω phase was not formed in TCA or TCFA. However, even though Al promoted the β-to-α transformation over the β-to-ω transformation, the Al-containing TCFA exhibited lower α-phase volume fractions than the Al-free TC and TCF. The limiting effect of Fe on the α-phase volume fraction in TCFA was stronger than the promotional effect of Al.

Fe could prevent the longer-range diffusion needed for α-phase formation [160], which would limit the α-phase volume fraction of TCFA compared to TCA. Fe could also affect α-phase volume fraction more than Al due to its diffusion speed at 400 °C. Diffusion coefficients for Cr, Fe, and Al at temperatures between 900 °C and 1350 °C were taken from diffusion data of a Ti-18Cr [216], a Ti-1Fe alloy [217], and a Ti-2.1Al alloy [218], see Figure 7.1. Extrapolating the trends of D from the 900 °C and 1350 °C temperature range to 400 °C, D for Cr, Fe, and Al at 400 °C were calculated, see Table 7.1. The D for Al is 100x lower than the D of Fe, thus Al should diffuse significantly slower than Fe during the β-to-α transformations. In TCFA, Fe could diffuse into the β-phase faster than Al could diffuse to the α phase in TCFA, and the strong β-stabilizing effect of Fe could limit the precipitation and growth of the α phase in TCFA compared to the Fe-free β matrix of TCA.

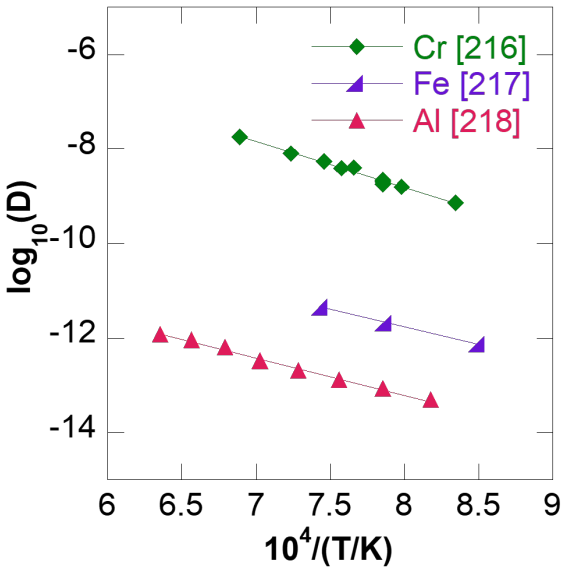

Figure 7.1: The diffusion data used to calculated the diffusion coefficients for Cr, Fe, and Al in Ti at 400 °C.

Table 7.1: The calculated diffusion coefficients (D) for Cr, Fe, and Al in Ti at 400 °C.

Element	**Calculated D at** 400 °C	**Using data from**
Cr	2.98×10^{-16} m^2 s^{-1}	[216]
Fe	1.49×10^{-17} m^2 s^{-1}	[217]
Al	2.48×10^{-19} m^2 s^{-1}	[218]

7.1.1.2 The effect of Fe on α- and ω-phase volume fraction

Similarly, the hypothesis that Fe would suppress α- and ω-phase formation, resulting in lower α-and ω-phase volume fractions in the Fe-containing alloys, was partially correct.

The Fe addition in TCF resulted in lower ω-phase volume fractions than TC. Since the β-to-ω transformation is diffusion controlled [7], and Cr has a D approximately 10x larger than Fe, see Table 7.1, the slower diffusion of Fe could have limited the β-to-ω transformation in TCF. The higher β-stability from the Fe addition in TCF could have also reduced the free energy of the β phase compared to the ω phase, thereby preventing the β-to-ω transformation in TCF [158].

As described above, Fe limited the β-to-α transformation in TCFA, reducing the α-phase volume fraction of TCFA compared to TCA. However, the addition of Fe in TCF did not reduce the α-phase volume fraction, and similar α-phase volume fractions were exhibited by TC and TCF. Fe

could still be limiting the β-to-α transformation in TCF, like in TCFA, but the ω phase could have increased the α-phase volume fraction in TCF through the ω-assisted α-phase transformation. The ledges and interfacial energy at the ω/β boundary would act as a favorable nucleation site for the α phase [9, 10, 40, 49, 128]. The lack of β-stabilizers in the ω phase could also promote the formation and growth of the α phase [42, 59], and could be promoting a higher α-phase volume fraction in TCF compared to TCFA.

BSE-SEM photomicrographs of TCF contain features that could provide evidence for the occurrence of the ω-assisted α-phase transformation. Some spheroidal or cuboidal precipitates, presumed to be the ω phase, appeared near clusters or lines of small precipitates, presumed to be the α phase. Figure 7.2 identifies some of these presumed ω and α phases in TCF. These features are not conclusive, as the precipitates are nano-scale and the morphology of the ω and the α phases are difficult to resolve, but are worth further investigation.

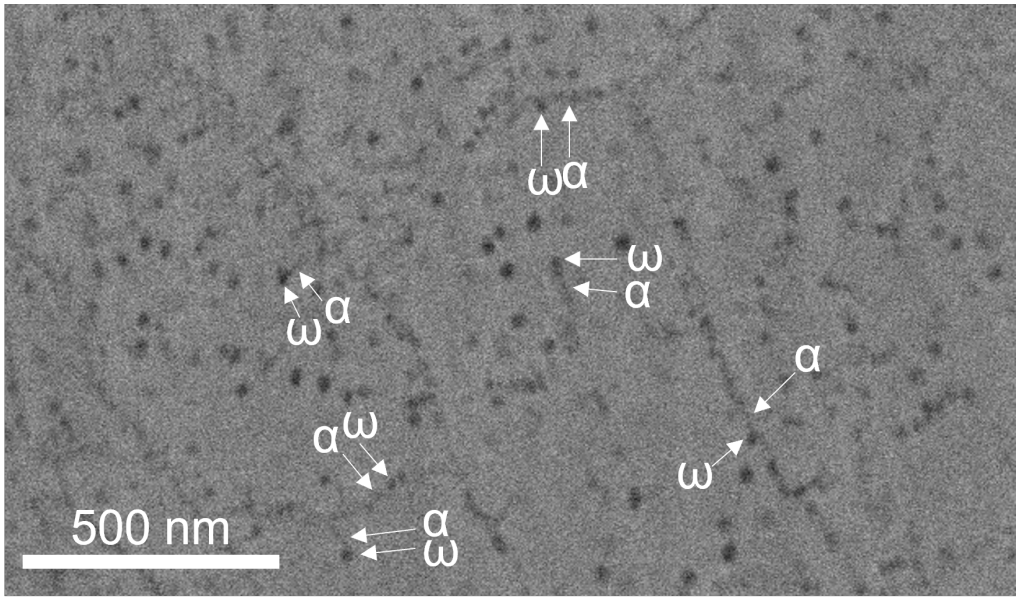

Figure 7.2: BSE-SEM photomicrographs indicating possible ω-assisted α-phase precipitates in TCF aged at 400 °C for 0.75 h. The identified ω and α phases are assumed to be those precipitates by their morphology, and are not confirmed as ω or α precipitates.

7.1.1.3 Proposed TTT diagrams

The previous hypotheses addressed how Fe and Al affected the phase stability and the phase transformations in the Ti-Cr-Fe-Al alloy system. Combining the data from this work with a similar study by Chakravarty [214] allowed TTT diagrams for TC, TCF, TCA, and TCFA to be proposed.

Chakravarty investigated the phase transformations of TC, TCF, TCA, and TCFA after aging at 210 °C, 300 °C, and 350 °C for 12 h [214]. In TCA and TCFA, the Al addition promoted the β-to-α transformation over the β-to-ω transformation at all aging temperatures, resulting in only β+α microstructures for TCA and TCFA at aging temperatures where β+ω+α microstructures were observed for TC and TCF, see Figure 7.3 [214].

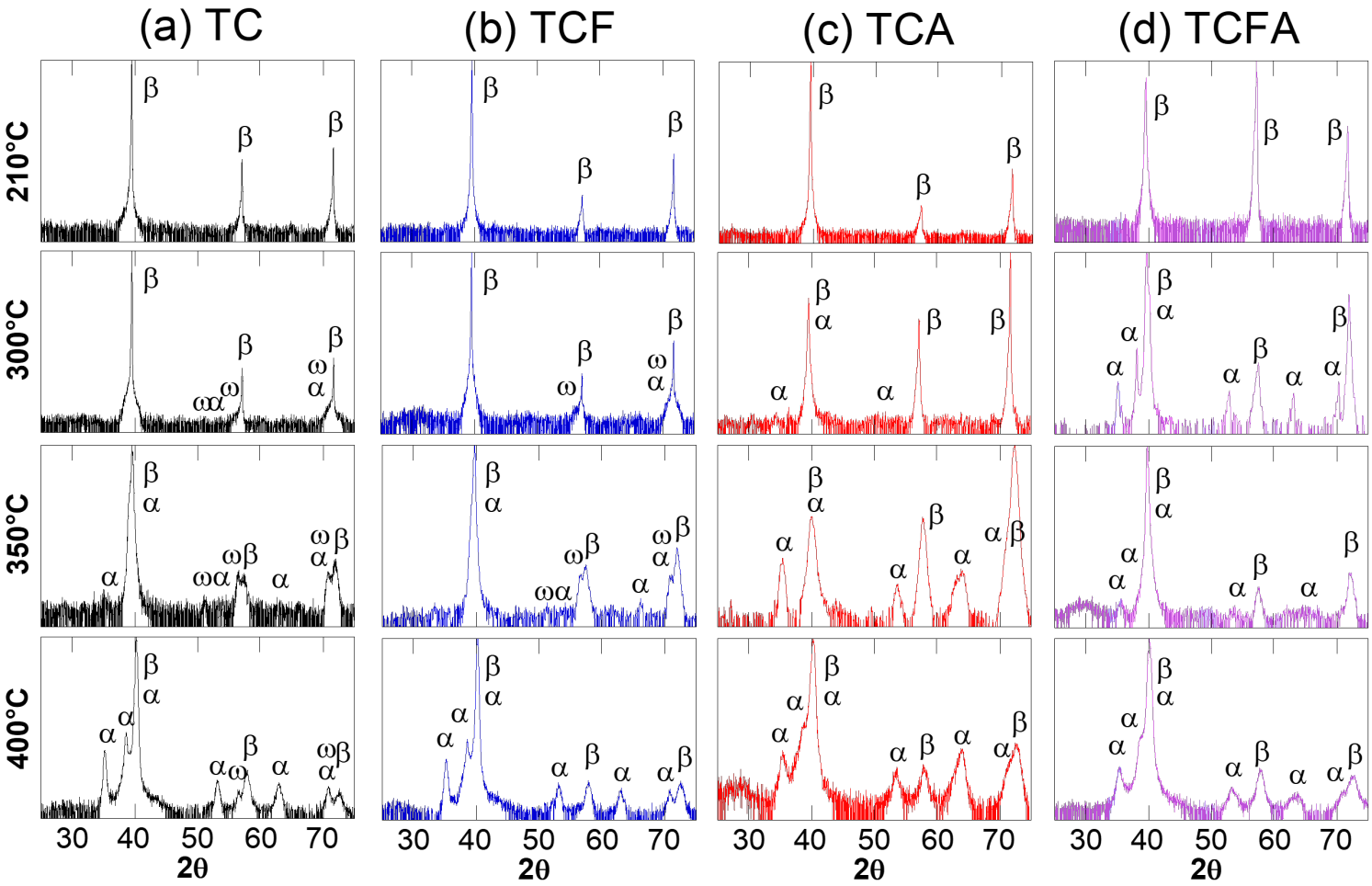

Figure 7.3: Intensity versus 2θ plots for (a) TC, (b) TCF, (c) TCA, and (d) TCFA after 12 h aging at 210 °C, 300 °C, 350 °C, and 400 °C. All intensities are in arbitrary units. The 210 °C, 300 °C, and 350 °C plots were recreated using data from Chakravarty [214].

Using the identified phase transformations in the XRD data in Figure 7.3, TTT diagrams for each alloy were proposed, assuming that the overall behavior of the TTT diagram is similar to that of Figure 2 of Hickman [33], see Figure 7.4. It is possible that the peaks identified in TCF at 300 °C were only ω-phase peaks, since the α- and ω-phase peaks overlap at approximately 71° 2θ, and no purely α-phase peaks were observed in that profile. It is also possible that the ω phase formed in TCA and TCFA before 12 h aging was reached at the lower aging temperatures, as those temperature ranges are within the range of ω-phase stability [10, 41, 42, 42, 43, 47, 49, 50, 58, 93, 98, 98–100]. More data is needed to create more reliable TTT diagrams of each alloy.

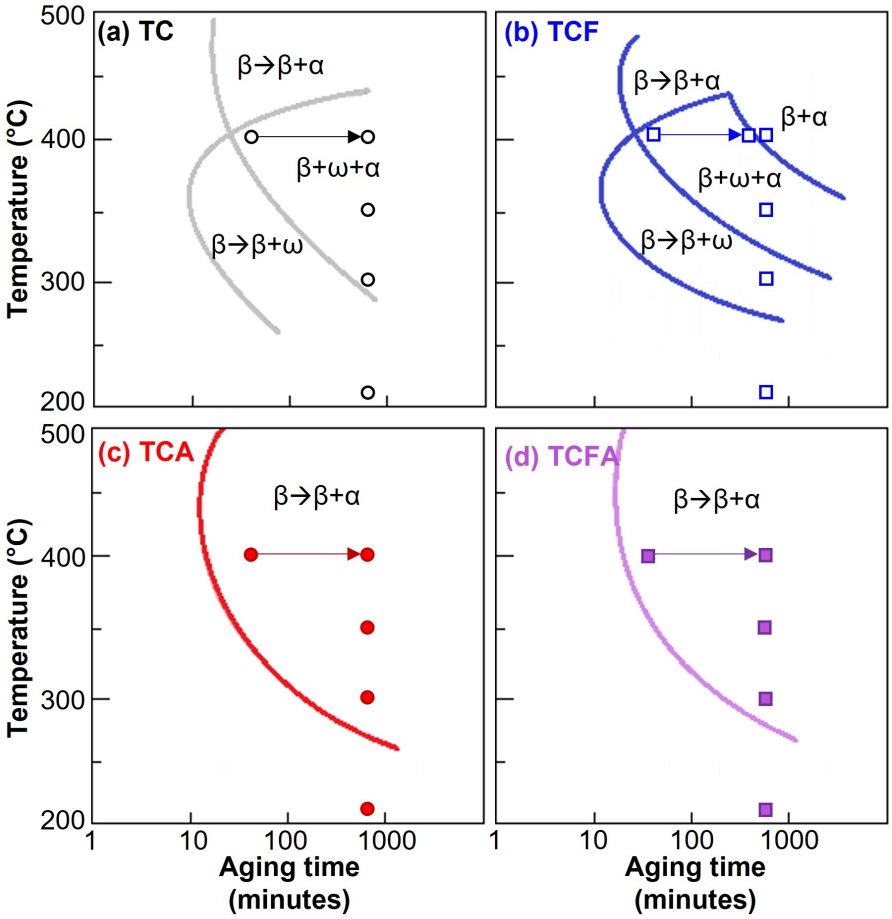

Figure 7.4: Proposed TTT diagrams for (a) TC, (b) TCF, (c) TCA, and (d) TCFA. Phases were indentified using XRD and data is included from this work at 400 °C and from Chakravarty at all other temperatures [214]. Data points indicate completed characterization experiments, and the location of demarcation lines is inspired by Hickman [33] and not violated by any of the observations. Proposed boundaries would need confirmation through further experiments and characterization.

7.1.2 Phase lattice parameter hypotheses

The hypotheses about the phase lattice parameter concerned the β-phase, the α phase, and the ω phase, and are presented in that order below.

7.1.2.1 The β phase

The hypothesis that the diffusion of the β-stabilizers from the α and ω phases into the β phase would increase the stability of the β phase, and the relative β-phase stability of the alloying elements would decrease the β-phase lattice parameter was true. The Rietveld analysis of the XRD data showed the decrease in a_β with increased aging time, and the APT results confirmed that the β-stabilizers Cr and Fe diffused from the precipitated α and ω phases into the β phase during the β-to-α and β-to-ω transformations. Phase compositions were calculated from the APT data by averaging the compositions of each phase from the proximity histograms generated for each sample. The relationship between elemental concentration, β-stability, and a_β is explored below.

Comparing a_β to the Ti, Cr, Fe, and Al contents illustrated the relationships between elemental content and a_β, see Figure 7.5. Each alloy exhibited similar relationships between Cr and a_β, see Figure 7.5(b), but different relationships between Ti and a_β, see Figure 7.5(a). Importantly, the Fe-containing TCF and TCFA exhibited different linear trends with Ti content than the Fe-free TC and TCA, suggesting a synergistic effect of Cr and Fe on the a_β of TCF and TCFA. Al did not appear to affect a_β, see Figure 7.5(d).

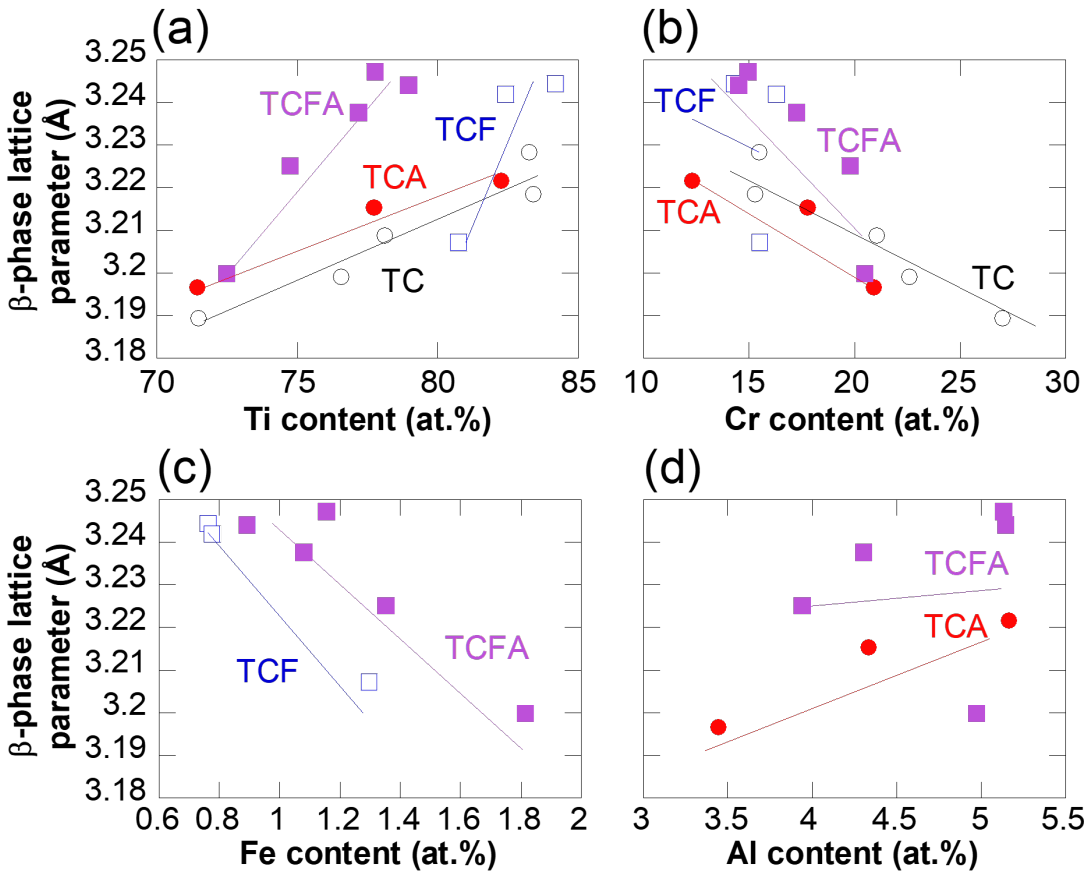

Figure 7.5: The Rietveld analysis β-phase lattice parameters as a function of APT-measured (a) Ti content, (b) Cr content, (c) Fe content, and (d) Al content. The data was taken along the aging evolution from 0.75 h to 12 h.

Because Mo-Eq, average atomic radius, and average Md are all related to a_β, as described in Section 5.1.3, a_β exhibited a linear relationship with each, see Figure 7.6. a_β decreased with increased Mo-Eq, and increased with increased average atomic radius or Md. As discussed in Section 5.1.3, the β-stabilizing elements have smaller radii than Ti, so higher concentrations of the alloying elements correspond to smaller average radii. Similarly, higher alloying element concentrations correspond to higher Mo-Eq values, i.e., higher β-phase stability.

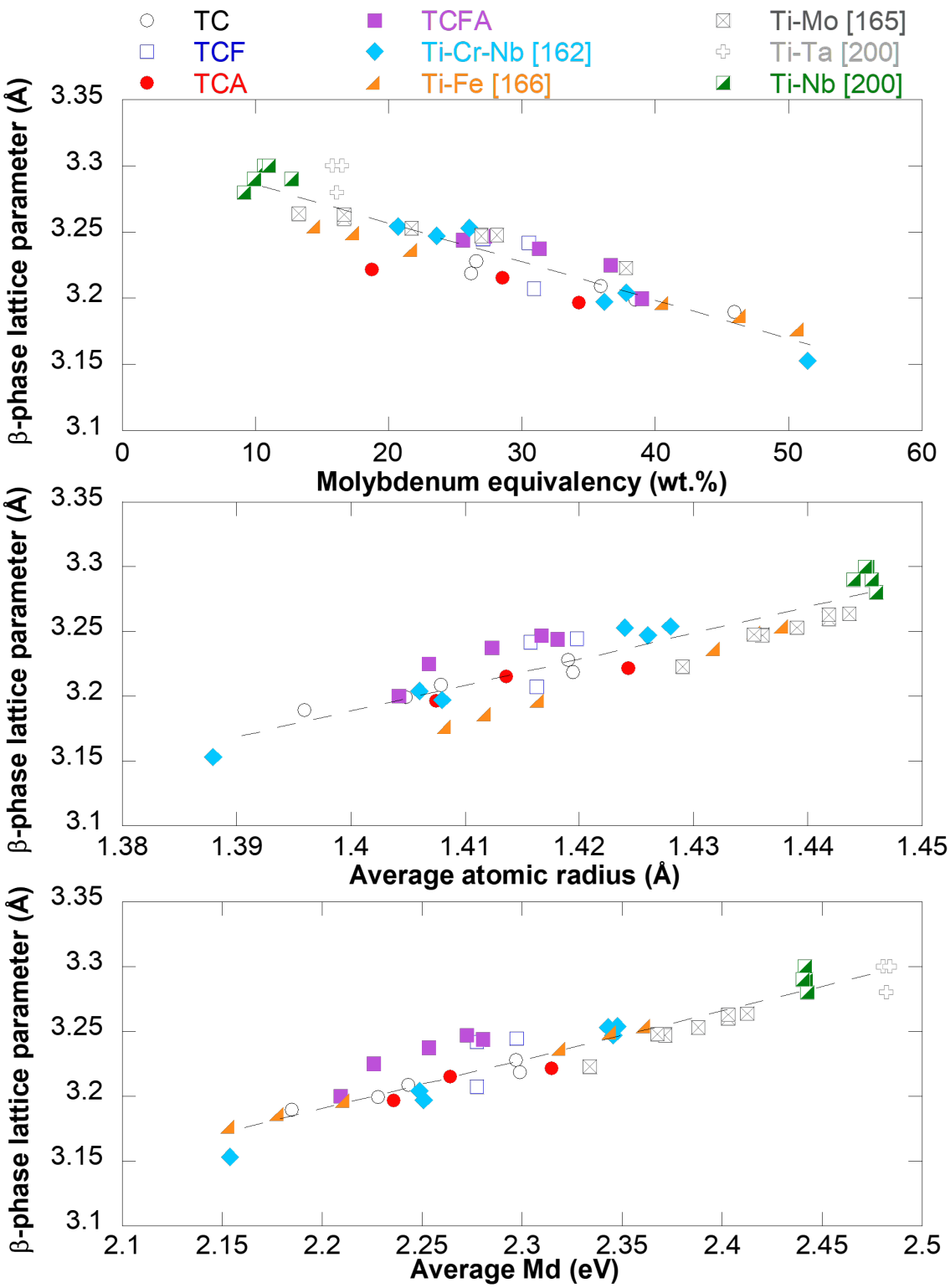

Figure 7.6: The β-phase lattice parameters as a function of Mo equivalency (top), average atomic radius (middle), and average Md (bottom). Data was taken from this work and work involving Ti-Cr-Nb alloys [162], Ti-Fe alloys [166], Ti-Mo alloys [165], Ti-Ta alloys [200], and Ti-Nb alloys [200].

7.1.2.2 The α phase

The hypothesis that the diffusion of the α-stabilizer Al from the β phase into the α phase would affect the lattice parameter of the α phase in the Al-containing alloys differently than the Al-free alloys was false. Fe appeared to have a larger influence on the α-phase lattice parameters and c/a ratio than Al.

TCA did not exhibit any clear relationships between the α-phase c/a ratio and Ti, Cr, or Al, while TCF and TCFA exhibited relationships with both Cr and Fe, see Figure 7.7. a_α and c_α of any alloy did not show correlation with the elemental content, and therefore such plots are not presented here.

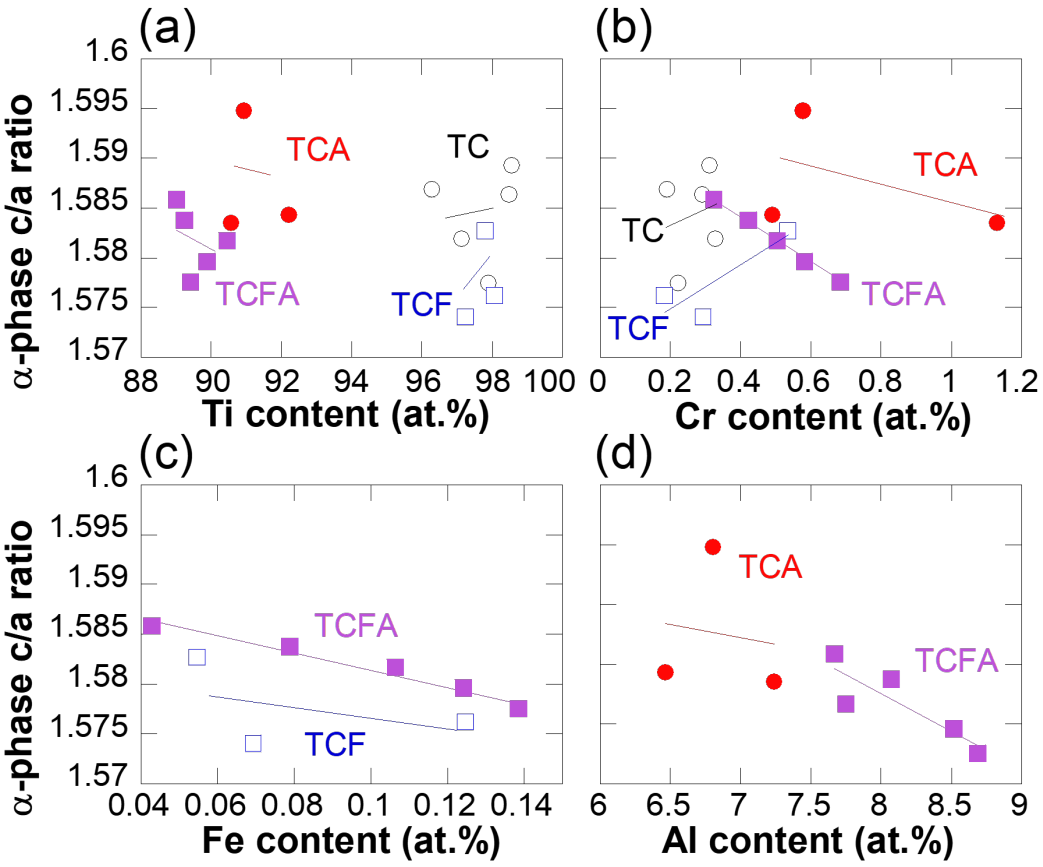

Figure 7.7: The Rietveld analysis α-phase c/a ratios of TC, TCF, TCA, and TCFA as a function of the APT-measured (a) Ti, (b) Cr, (c) Fe, and (d) Al contents. The data was taken along the aging evolution from 0.75 h to 12 h.

Considering that a_β for TCF and TCFA was dependent on both Fe and Cr content, the relationship between a_β and α-phase c/a ratio for each alloy was explored. The α-phase c/a ratio appeared to have a stronger relationship with the β-phase lattice parameter than elemental content, see Figure 7.8. The relationship appears consistent for TC, TCA, and TCF, where an increased a_β resulted in a decreased α-phase c/a ratio. TCFA, which exhibited a c/a ratio that increased with aging time (unlike that of TC, TCA, or TCF) similarly exhibited an increased α-phase c/a ratio with an increased a_β.

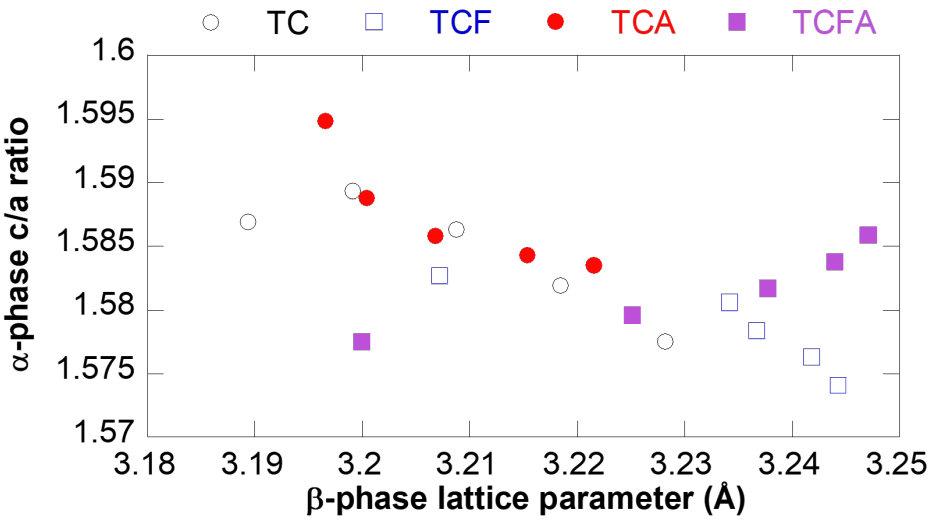

Figure 7.8: The α-phase c/a ratio as a function of a_β for each alloy.

The α-phase c/a ratio could be affected by a_β through stresses or strains at the α/β boundary. As a_β changes as the alloying elements diffuse during the β-to-α transformation, the misfit between the α and β phases could be affected [219]. The changing a_β could also affect the coherency strains along the $(\bar{1}\,1\,0\,0)_\alpha$ and $(\bar{1}\,1\,\bar{2})_\beta$ planes, where the misfit between the α and β phases is minimized [219]. If the changing a_β and c/a ratio affect the misfit between the two phases, the ledges that transition the crystal from the α to the β phase could be affected.

Further investigation into how misfit and coherency strain between the α and β phases are affected as a_β, a_α, c_α, and the c/a ratio change would be valuable.

7.1.2.3 The ω phase

The hypothesis that the Fe and Al additions could affect the ω-phase lattice parameter was true, as TCF exhibited a smaller a_ω and c_ω than TC. The effect of Al on the ω-phase lattice parameters could not be explored, as the β-to-ω transformation did not occur in the Al-containing alloys.

The hypothesis that the rejection of all alloying elements except Ti from the ω phase would cause the ω-phase lattice parameter to remain constant throughout the transformation was true for TCF but false for TC. The c/a ratio of TCF increased slightly from approximately 0.612 to 0.613 during the 7.5 h that the ω phase was present, but was close to 0.613 for the majority of that time, and 0.613 is the ω-phase c/a ratio reported in several studies of β-Ti alloys [33,55,56]. In contrast, the c/a ratio of TC was approximately 0.613 at the start of the 12 h aging, and increased linearly with increased aging time to approximately 0.622. A c/a ratio of 0.622 has been reported in a Zr alloy by Hatt and Roberts [51], but has not been reported in Ti alloys.

Because the morphology of the ω phase is determined by the elastic strain energy in the crystal introduced by the difference between the radii of alloying elements and Ti [40, 105], and because a_β was shown to change with changing composition, the ω-phase c/a ratio was plotted against a_β. Like the α phase, the ω-phase c/a ratio showed a relationship with a_β. Unlike the α phase, the relationship was consistent for both TC and TCF, approaching a ratio of 0.612 as a_β increased.

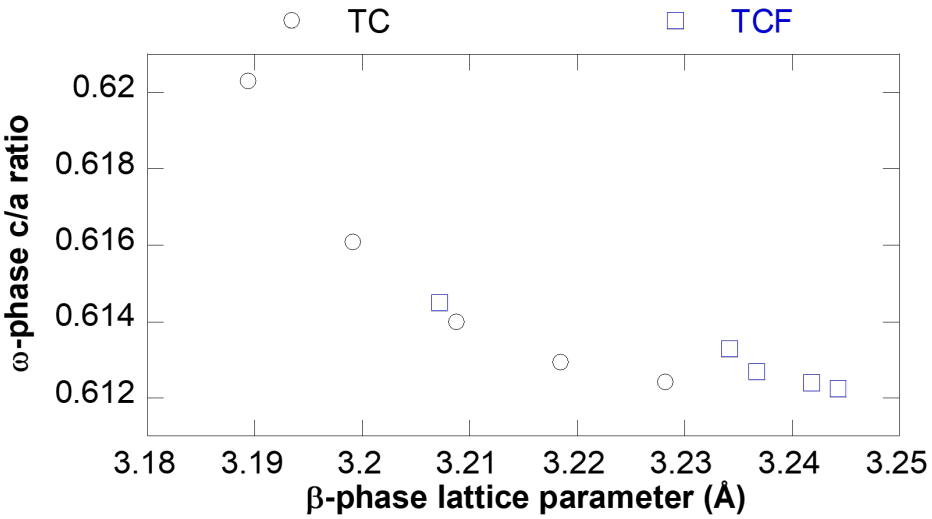

Figure 7.9: The ω-phase c/a ratio as a function of a_β for TC and TCF.

The changing a_β and ω-phase c/a ratio could also affect the interfacial energy at the ω/β boundary, which is known to be important for the ω-assisted α-phase transformation [10, 128]. Coherency strains at the ω/β interface have also been noted to affect the ω-assisted α-phase transformation [123], and the changing a_β and ω-phase c/a ratio could affect those strains as well.

Further exploration into the effect of the changing a_β and the changing ω-phase c/a ratio on the interfacial energy and coherency strains and the ω-assisted α-phase transformation could shed light on the ω-assisted α-phase transformation.

7.1.3 Phase composition hypotheses

The hypotheses concerning the diffusion during the β-to-ω and β-to-α transformations involved the alloying elements (Cr, Fe, and Al), the impurity element O, and the impurity element H. The following sections address these hypotheses in the same order.

7.1.3.1 Diffusion of Cr, Fe, and Al during the β-to-ω and β-to-α transformations

The hypothesis that the β-stabilizers Cr and Fe would diffuse from the α and ω phases into the β phase was correct. The β-phase of each alloy increased in β-stabilizer content with time as the β-to-ω and β-to-α transformations occurred, as the β-to-ω_{iso} and β-to-α transformations are diffusion controlled displacive/diffusive transformations [7, 83, 111].

The hypothesis that the α-stabilizer Al would diffuse from the β phase into the α phase was true, as the α phase in TCA and TCFA increased in Al content with time. Unlike the α and ω phases, which completely rejected the β-stabilizers Cr and Fe, the β phase did not completely reject Al. This could be due to the slower diffusion rate of Al than Cr or Fe, see Table 7.1, where Al may not have had enough time to completely diffuse out of the β phase.

The hypothesis that the ω-phase would reject any elements except Ti was partially correct. The ω-phase rejected all β-stabilizing alloying elements, but higher O concentrations in the ω phase than the surrounding β matrix were observed. This is discussed in more detail below.

7.1.3.2 The impurity element O in the microstructure

The hypothesis that the interstitial O would be present in higher concentrations in the α phase than the other phases was true, as the average O content in the α phase was higher than the average O contents in the β or ω phases. O is an α-phase stabilizer [7], and so diffused towards the α phase during the β-to-α transformation.

O also appeared in higher concentrations near the α/β boundary. The O at the α/β interface and in the surrounding β matrix could promote the growth of the α-phase, or promote the precipitation of new α precipitates near the existing precipitate. This could create "strings" or "clusters" of α phase stacked next to each other in the microstructure. Since the α phase rejects Cr, it appears as a darker precipitate in the lighter Cr-rich β matrix in BSE-SEM imaging, or as Cr-poor volumes in APT samples. The clusters would appear as several small precipitates seemingly attached to create a larger cluster or string inside the β grains. These clusters were observed in the APT reconstructions as several plate-like precipitates attached along the flat surfaces, see Figure 7.10(a), and in the BSE-SEM photomicrographs as a series of darker precipitates in the lighter β matrix, see Figure 7.10(b).

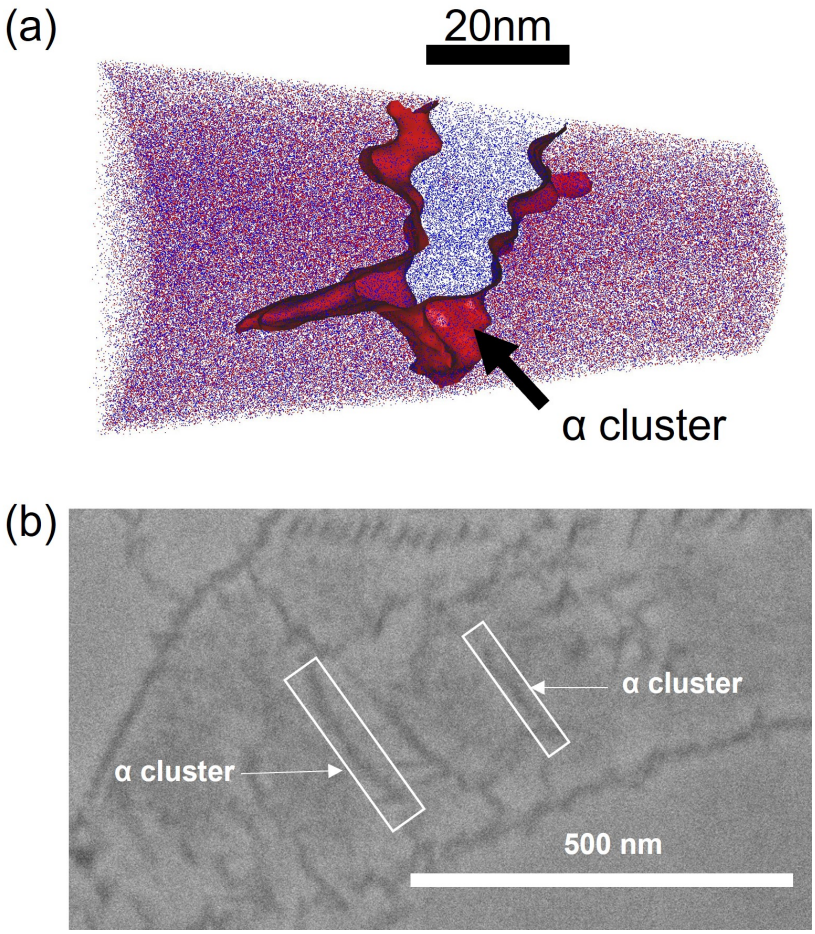

Figure 7.10: The APT tip reconstruction of TCFA after 1.5 h aging showing an α-precipitate cluster, and (b) BSE SEM photomicrograph of TCFA after 0.75 h aging showing α precipitate clusters which could form due to the higher O concentrations at or near the α/β boundaries.

While O was found at the α/β boundary, the hypothesis that the interstitial O would be rejected from the ω phase and cluster at the ω/β boundary was false. While it is possible that O did cluster at the ω/β boundary, those clusters were not observed in the APT samples studied. Instead, higher O contents were observed in the ω precipitates than in the surrounding β matrix. O in the ω phase has not been widely reported in the literature, but O has been found to stabilize the ω phase in certain Ti-Nb alloys [106, 220].

Although ledges, compositional differences, and the strain at the β/ω interface appear to contribute more towards the ω-assisted α transformation than O concentration [9, 10, 123, 128], the higher O content within the ω phase could support the ω-assisted α-phase transformation.

7.1.3.3 The impurity element H in the microstructure

The hypothesis that the interstitial H would be present in higher concentrations in the β phase than in any other phase was true. The β phase is known to exhibit higher H concentrations than other phases typically found in Ti alloys (e.g. α, α") [167, 174] because H has a 20 times higher solubility limit in the β-phase of Ti than in the α-phase [221]. The higher solubility limit is due to the higher number of interstitial sites in the BCC β-phase lattice compared to the HCP α-phase lattice [168, 172].

Samples that contained hydrides also had higher H contents in the overall sample, supporting the hypothesis that if enough H was present in the sample, equilibrium hydrides would form. These hydrides usually obscured the original microstructures in the samples, creating a β+hydride microstructure instead of the possible β+α or ω microstructures. In one sample, the original microstructures were not completely obscured. In this sample, shown in Figure 7.11, 25% H isosurfaces were used to define the hydrides and Cr isosurfaces were used to define the β-phase. A profile, taken through the volume of the material that did not contain hydrides, measured compositions of the β and α phases. The compositions were consistent with those measured in hydride free-tips. The consistent compositions indicated that, as long as hydride formation does not completely obscure the original microstructure, compositional information may still be obtained from Ti samples containing hydrides.

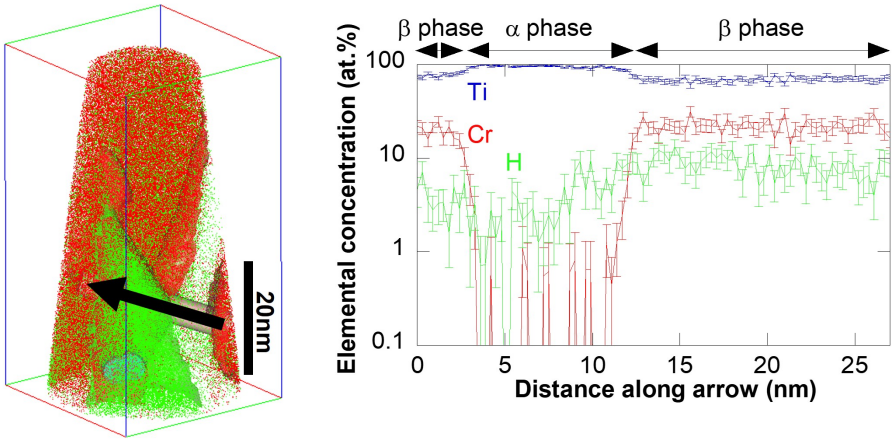

Figure 7.11: A reconstructed 12 h aged TC sample with 25% H isosurfaces delineating the hydrides and 9% Cr isosurfaces delineating the β phase. The 1-D concentration profile was taken along the arrow passing through the β and α phases and missing all hydrides.

The hypothesis that during the FIB-based lift-out process for APT samples, a higher electron-beam accelerating voltage during the decomposition of the Pt precursor would cause more gaseous H to be released, resulting in an increased H concentration in the APT samples appeared to be true for TCF, TCA, and TCFA. The hypothesis was not true for TC, which reported higher hydrogen after both accelerating voltages, due to the formation of hydrides in the TC samples at both accelerating voltages.

When the Pt precursor, composed of the molecule Trimethyl(methylcyclopentadienyl) platinum(IV), abbreviated as $MeCpPtMe_3$, in an amorphous carbonaceous matrix [178], decomposes, it is accompanied by the evaporation of methane and gaseous H [179]. The higher energy of the 30kV accelerating voltage could cause more gaseous H to be released from the amorphous carbonaceous matrix, leading to more H available that could diffuse into the APT samples. A 30kV accelerating voltage beam also induces more secondary electrons than a 5kV accelerating voltage beam. Secondary electrons can decompose transiently adsorbed precursor molecules [179], so more secondary electrons could lead to more H diffusing into the samples. After Pt deposition, the ion beam could also decompose hydrocarbons and moisture from the sample surface [222]. If the H source was from the decomposition of these surface hydrocarbons and moisture instead of from the decomposition of the Pt precursor, the 5kV-deposited Pt layer could have protected the sample

more than the 30kV-deposited Pt layer. Further investigation is needed to conclusively determine how accelerating voltage during Pt deposition could affect the H concentration in the APT samples.

7.2 Mechanical property characterization

The hypotheses regarding the mechanical property evolution during the β-to-α and β-to-ω transformations were as follows:

- The elastic moduli would increase with increasing volume fractions of the ω and α phases according to the rule of mixtures.
- The σ_y and UTS values would increase with increasing volume fractions of the ω and α phases.
- The hardness values would increase with increasing volume fractions of the ω and α phases.
- Increasing the ω-phase volume fraction would increase E, G, σ_y, UTS, and the hardness more than increasing the α-phase volume fraction.
- Alloys containing any amount of the ω-phase microstructure would fail before yielding.

The discussions of why each hypothesis was found to be true or false through the Vickers microhardness, RUS, tensile testing, and SE-SEM imaging of the fracture surfaces are presented below.

7.2.1 Hardness evolution during the β-to-ω and β-to-α transformations

The hypothesis that the hardness values would increase with increasing volume fractions of the ω and α phases was true.

For the two-phase (β+α) microstructures of TCA and TCFA, hardness increased linearly with increased α-phase volume fraction, see Figure 7.12.

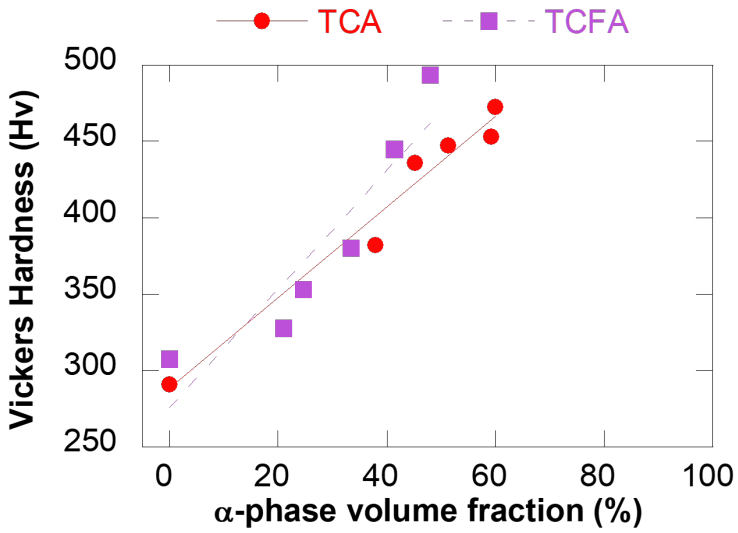

Figure 7.12: Vickers hardness as a function of α-phase volume fraction for TCA and TCFA.

For the three-phase (β+α+ω) microstructures of TC and TCF, an apparent increase in hardness was observed when the ω- and α-phases precipitated, followed by an apparent decrease in hardness as the aging time increased from 0.75 to 1.5 h. While this decrease appears to contradict the hypothesis that hardness would increase with ω- and α-phase volume fractions, the decreased hardness from 0.75 to 1.5 h was associated with a decrease in ω-phase volume fraction in both TC and TCF, see Figure 7.13.

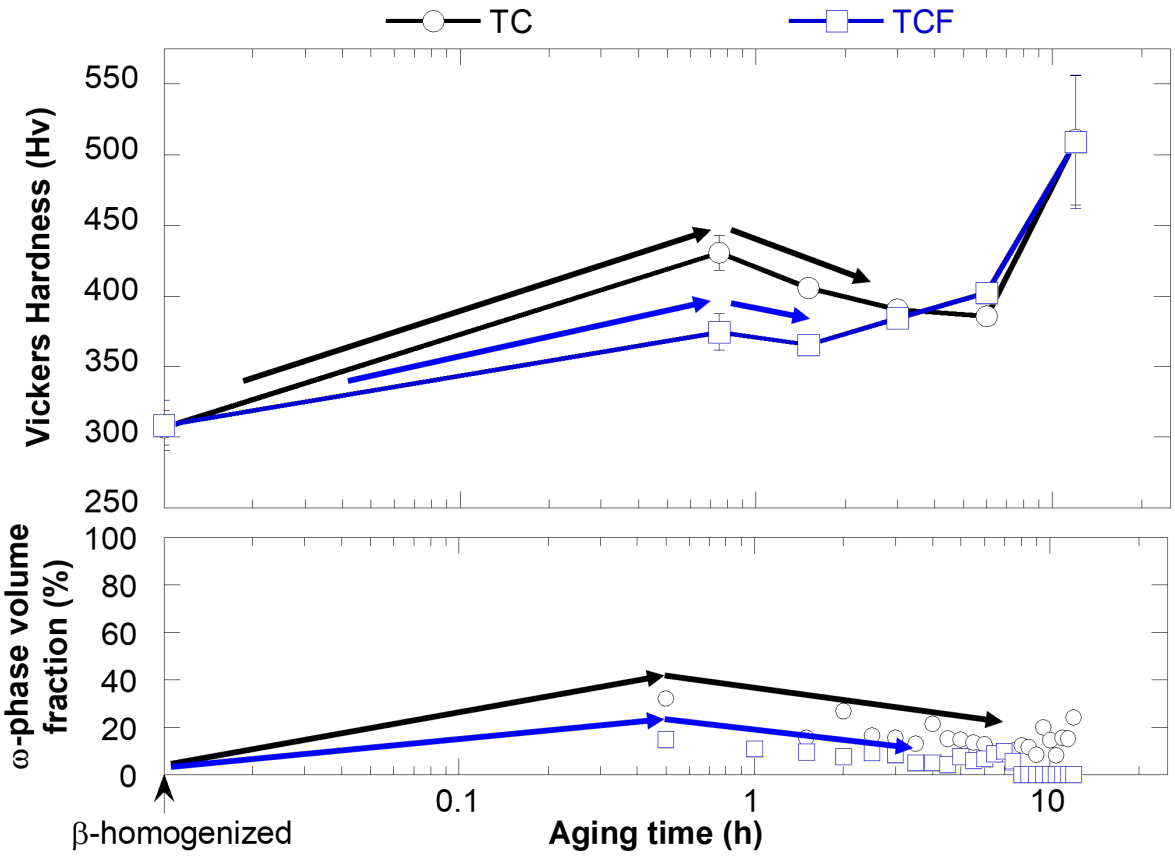

Figure 7.13: The Vickers hardness and ω-phase volume fraction evolutions with increased aging time for TC and TCF. The arrows highlight the similar increases and decreases in hardness and ω-phase volume fraction.

The decrease in hardness with decreased ω-phase volume fraction also provides evidence for the hypothesis that the hardness values would increase more with increased ω-phase volume fraction than with increased α-phase volume fraction. This hypothesis appears to be true when the ratio of the ω phase to the α phase is greater than 0.25. Once the ω/α ratio falls below 0.25, the α-phase volume fraction becomes the dominant hardening phase, and TC and TCF exhibited increased hardness with increased α-phase volume fraction even as the ω-phase volume fraction decreased, see Figure 7.14.

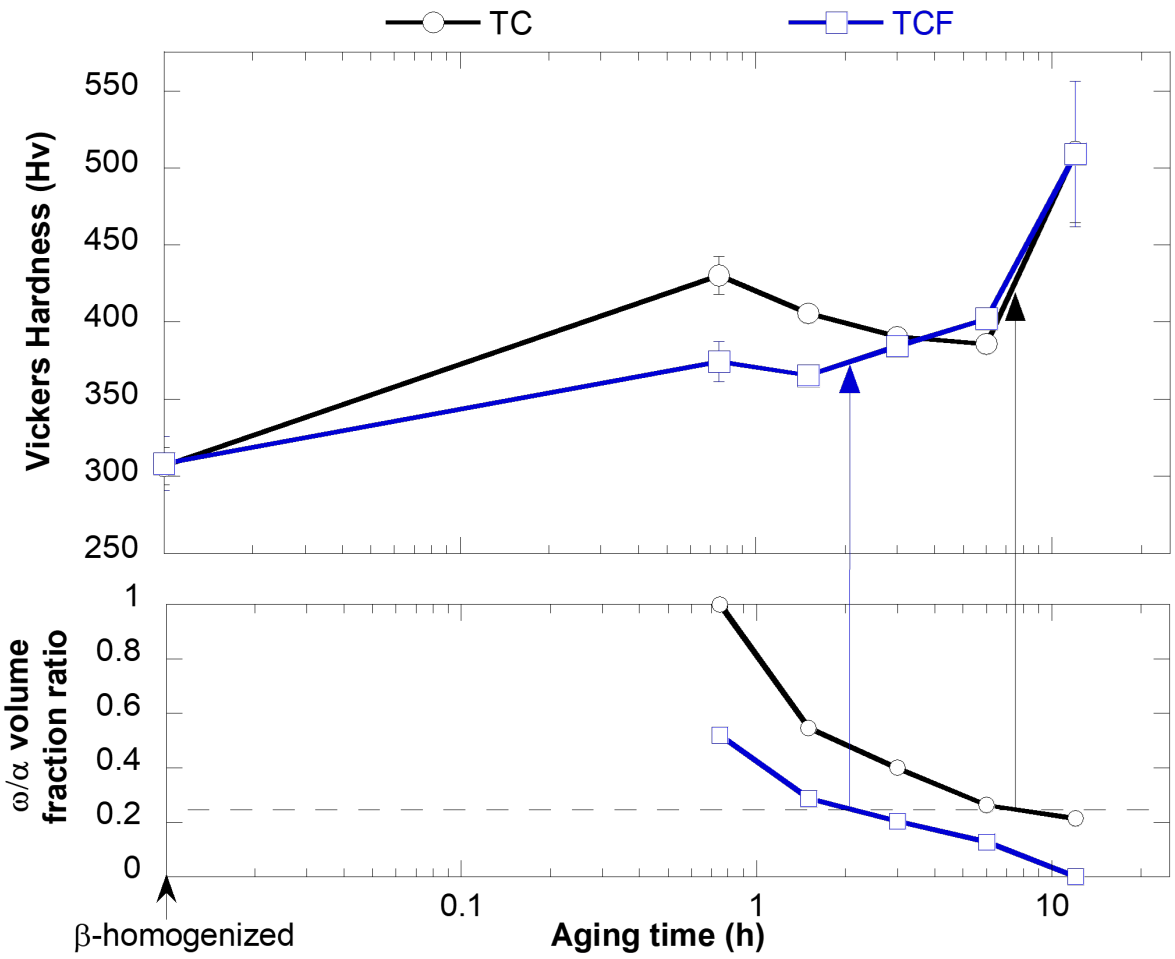

Figure 7.14: The Vickers hardness and ω/α volume fraction ratio evolutions with increased aging time for TC and TCF. The arrows highlight the increased hardness when the ω/α ratios fell below 0.25.

7.2.2 Elastic moduli evolution during the β-to-ω and β-to-α transformations

The hypothesis that G would increase with increasing volume fractions of the ω and α phases according to the ROM, and that the ω-phase volume fraction would increase G more than the α-phase volume fraction, was partially true. Although the G values of TCA and TCFA did not appear to increase significantly with an increase in α-phase volume fraction, the change in G was within the range predicted by the ROM. The G values of TC and TCF were also within the range of values predicted by the ROM. The ω-phase microstructure resulted in a significant G increase in TC and TCF compared to the ω-free TCA and TCFA, with TC and TCF exhibiting final G

values 42% and 51% greater than their initial values, respectively, while TCA and TCFA exhibited increases of 17% and 9%, respectively.

While none of the alloys violated the ROM, the smooth increase in G for TC and TCF was not entirely expected. Similar to the hardness evolution, the evolution of G was expected to follow the evolution of the ω-phase volume fraction: an initial increase with ω-phase precipitation, followed by a decrease as the ω-phase volume fraction decreased, followed by an increase when the ω/α ratio fell below 0.25. Currently, there is no reasonable explanation for the smooth increase of G as ω-phase volume fraction decreased for TC and TCF. Further investigation into the mechanisms by which the α and ω phases increase G is necessary to explain these changes.

The hypothesis that E would increase with increasing volume fractions of the ω and α phases according to the ROM, and that the ω-phase volume fraction would increase E more than the α-phase volume fraction, was partially true. TCA and TCFA both exhibited E values within the range predicted by the ROM, but TC and TCF exhibited E values below the range predicted by the ROM. The ω-phase microstructure appears to be the reason for the lower E values, as TCF exhibited values closest to the ROM after 6 and 12 h aging, when the ω-phase was almost or completely gone from the microstructure. The low E values exhibited by TC and TCF are not consistent with E and G values for the α and ω phases [77], see Table 7.2, or with the increased G values calculated from the RUS data. These results are also not consistent with those reported in literature, where the ω phase has been shown to significantly increase E [99, 109, 142]. The reason for this inconsistency between the predicted E values for the ω-containing TC and TCF, the RUS-calculated G values, and the literature is not known at this time, and should be a topic of further study.

Table 7.2: The RT ω- and α-phase E and G values, all in GPa, from Tane et al. [77].

Phase	$E_{\langle 0\,0\,0\,1\rangle}$ (GPa)	$E_{\langle 1\,1\,\bar{2}\,0\rangle}$ (GPa)	E_{iso} (GPa)	G_{iso} (GPa)
ω	201.0±7.4	129.0±3.9	152.8±0.6	60.1±0.3
α	143.3	104.4	114.6	43.4

7.2.3 σ_y and UTS evolution during the β-to-ω and β-to-α transformations

The hypothesis that the σ_y and UTS values would increase with increasing volume fractions of the ω and α phases was true.

The two-phase (β+α) TCA and TCFA exhibited a linear increase in both σ_y and UTS with increased α-phase volume fraction, see Figure 7.15. In each alloy, the increase in σ_y was similar to the increase in UTS.

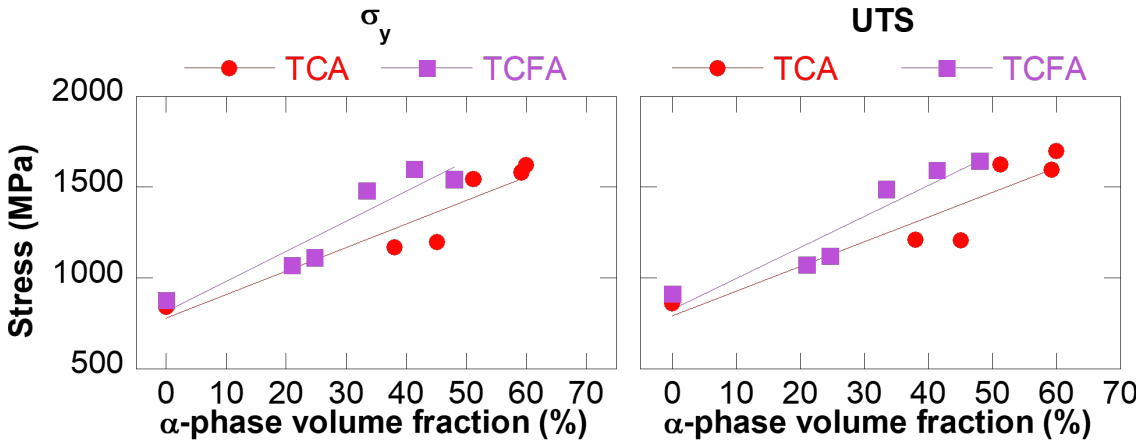

Figure 7.15: The relationship between α-phase volume fraction and (a) σ_y and (b) UTS for TCA and TCFA.

The three-phase (β+ω+α) TC and TCF also exhibited increased σ_y and UTS with increased ω and α volume fractions. TCF exhibited similar σ_y and UTS evolutions as its hardness evolution: an increased σ_y and UTS with increased ω-phase volume fraction, followed by a decrease in σ_y and UTS as the ω-phase decreased. After the ω/α volume fraction ratio dropped below 0.25, the σ_y and UTS of TCF increased with the increased α-phase volume fraction, see Figure 7.16. TC did not exhibit such an evolution due to the brittle failure of TC samples after 0.75, 1.5, and 12 h aging, indicated with a red circle in Figure 7.16. The brittle fractures resulted in no σ_y values for TC after 0.75, 1.5, and 12 h aging, and could have prevented higher strengths from being exhibited for those aging times.

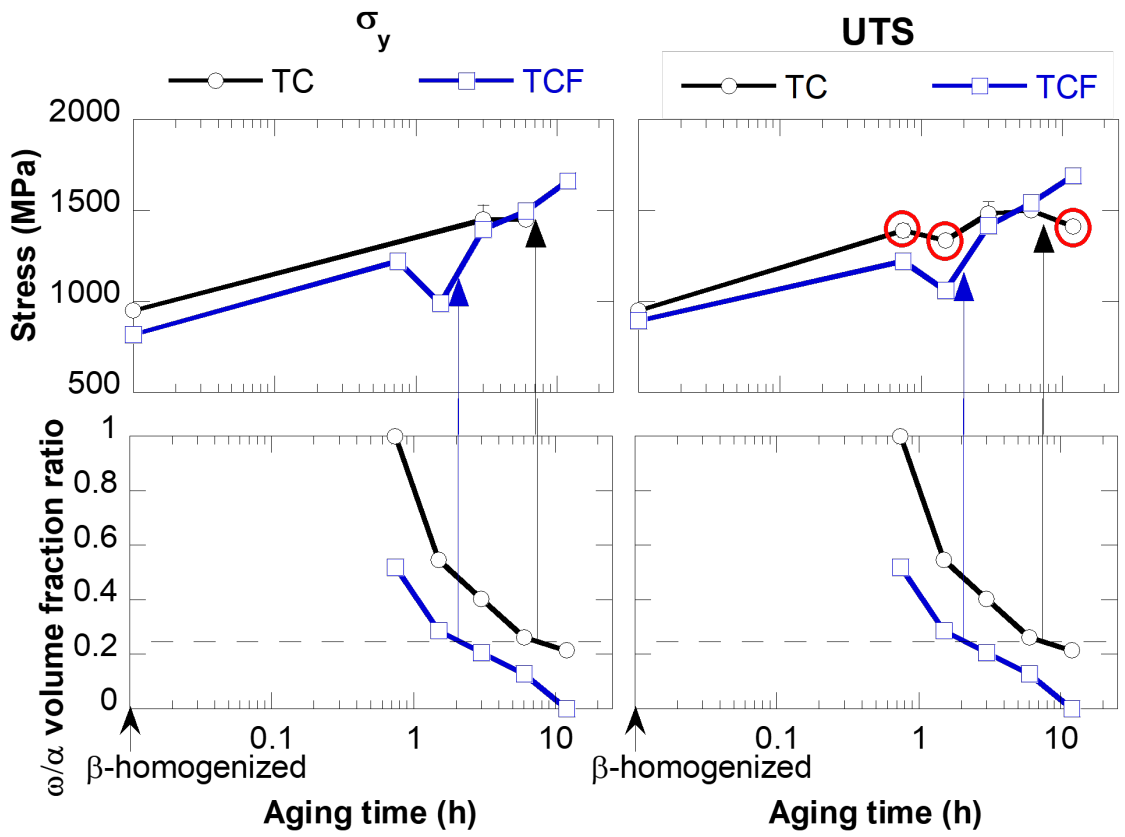

Figure 7.16: The relationship between ω/α volume fraction ratio and σ_y (left) and UTS (right) evolution for TC and TCF. The red circles indicate that the samples failed before yielding.

The hypothesis that increasing the ω-phase volume fraction would increase σ_y and UTS more than increasing the α-phase volume fraction was false; the ω-containing TC and TCF exhibited similar average σ_y and UTS values to the ω-free TCA and TCFA, see Figure 7.17. TC did exhibit higher average UTS values than the other three alloys after 0.75 and 1.5 h, but could not exhibit higher σ_y values due to brittle fracture before yielding. TC also exhibited similar UTS and σ_y values for all other aging times. The hardness evolution of TC suggests that the strength exhibited by TC should have been higher at 0.75 h, decreased from 0.75 to 6 h, then increased again at 12 h if the brittle fractures did not occur.

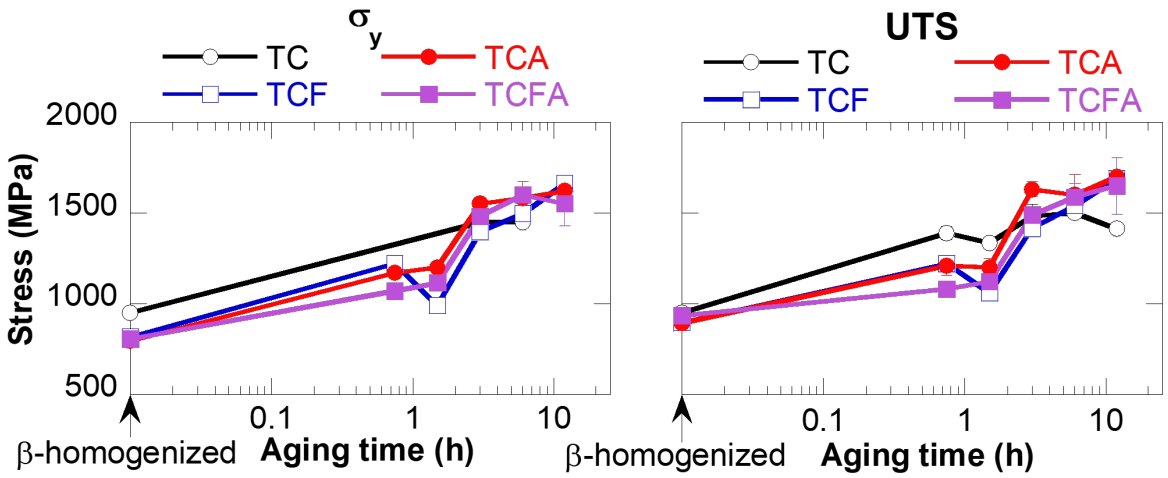

Figure 7.17: The σ_y (left) and UTS (right) values of TC, TCF, TCA, and TCFA.

TCF exhibited similar, but not exact, hardness and strength evolutions, see Figure 7.18. σ_y is compared to hardness in Figure 7.18 because σ_y and UTS were not significantly different in TCF. The differences between the evolutions of hardness and strength could be due to the effects of grain boundary α phase, which could affect dislocation motion in tension but which might not affect the Vickers microhardness measurements.

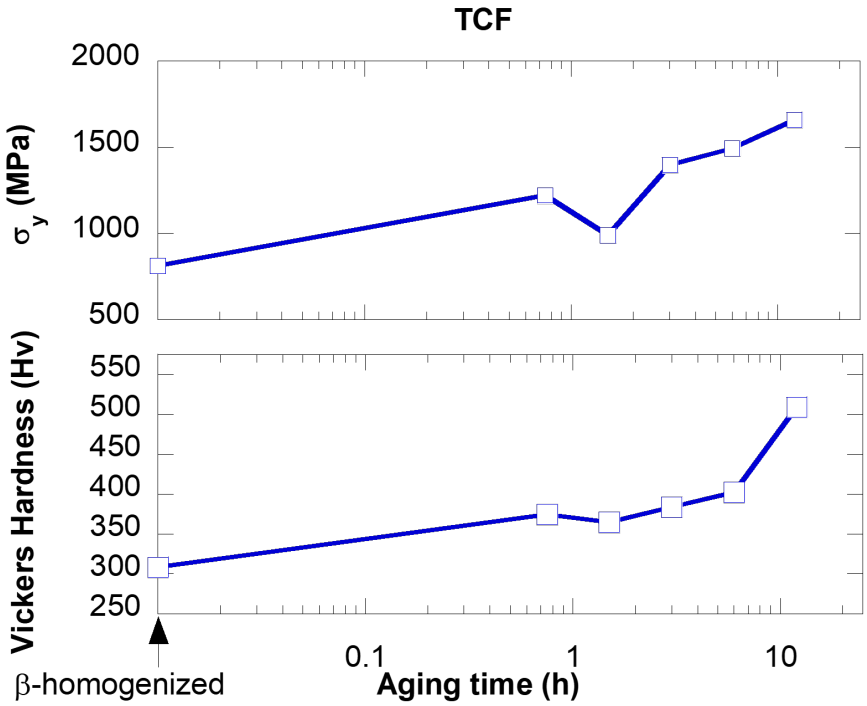

Figure 7.18: The σ_y (top) and hardness (bottom) evolutions of TCF.

7.2.4 The dependence of ϵ_f on microstructure

The hypothesis that alloys containing any amount of the ω-phase microstructure would fail before yielding was false. While TC did fail before yielding after aging for 0.75, 1.5, and 12 h, TC failed after yielding after aging for 3 and 6 h. TC contained the ω-phase microstructure for all aging times. Also, the ω-containing TCF samples failed after yielding for all tensile tests.

Each alloy exhibited a drop in ϵ_f with precipitation of the ω or α phases. After ϵ_f decreased with the precipitation of the ω or α phases, TC, TCF, and TCFA exhibited an increased ϵ_f after different aging times, although the ϵ_f values were always lower than the β-homogenized ϵ_f values. No clear reason for the observed increase was determined, as the changes in ϵ_f do not appear to correspond to changes in phase volume fraction.

The fracture surfaces of the alloys were observed using SE-SEM imaging to determine if any clear features could explain the changing ϵ_f values. Each fracture surface exhibited evidence of mixed-mode fracture. Mixed-mode failure is often seen for Ti alloys containing strong precipitates in a ductile β matrix [223]. No clear differences between the fracture surfaces explain why the alloys exhibited different ϵ_f values. If the β-grain size effects on ϵ_f seen in the β-homogenized alloys hold true after the precipitation of the α and ω phases, the lower critical stress for SIM believed to allow TCF and TCFA to exhibit higher ϵ_f values in the β-homogenized condition could be allowing TCF and TCFA to reach higher ϵ_f values in the aged conditions as well. Further investigation into the deformation modes could provide more insight into why some samples reached higher ϵ_f values than others.

7.2.5 Comparison to α+β alloy Ti-6Al-4V

Having explored the effects of the β-to-ω and β-to-α transformations on the mechanical properties of TC, TCF, TCA, and TCFA, the alloys were compared to Ti-6Al-4V, the most commonly used Ti alloy in the aerospace industry [8]. Reported σ_y values of the two-phase α+β Ti-6Al-4V fall between 760 and 1140 MPa, depending on the processing conditions, with annealed and aged Ti-6Al-4V typically exhibiting σ_y values in the 900 to 1100 MPa range [8]. Reported UTS values of

Ti-6Al-4V fall between 960 and 1170 MPa, and reported ϵ_f values of Ti-6Al-4V fall between 12% and 17% strain, with annealed Ti-6Al-4V exhibiting higher ϵ_f values than aged Ti-6Al-4V [8].

The β-homogenized TC, TCF, TCA, and TCFA exhibited lower E values than the two-phase (α+β) Ti-6Al-4V, see Figure 7.19(a). The average β-homogenized σ_y and UTS values exhibited by TC, TCF, TCA, and TCFA were within or near the lower range of strengths reported for Ti-6Al-4V, see Figure 7.19(b) and (c). The β-homogenized TCF and TCFA exhibited ϵ_f values close to the lower range of ϵ_f values exhibited by Ti-6Al-4V, while TC and TCA exhibited ϵ_f values approximately half that of the Ti-6Al-4V values, see Figure 7.19(d).

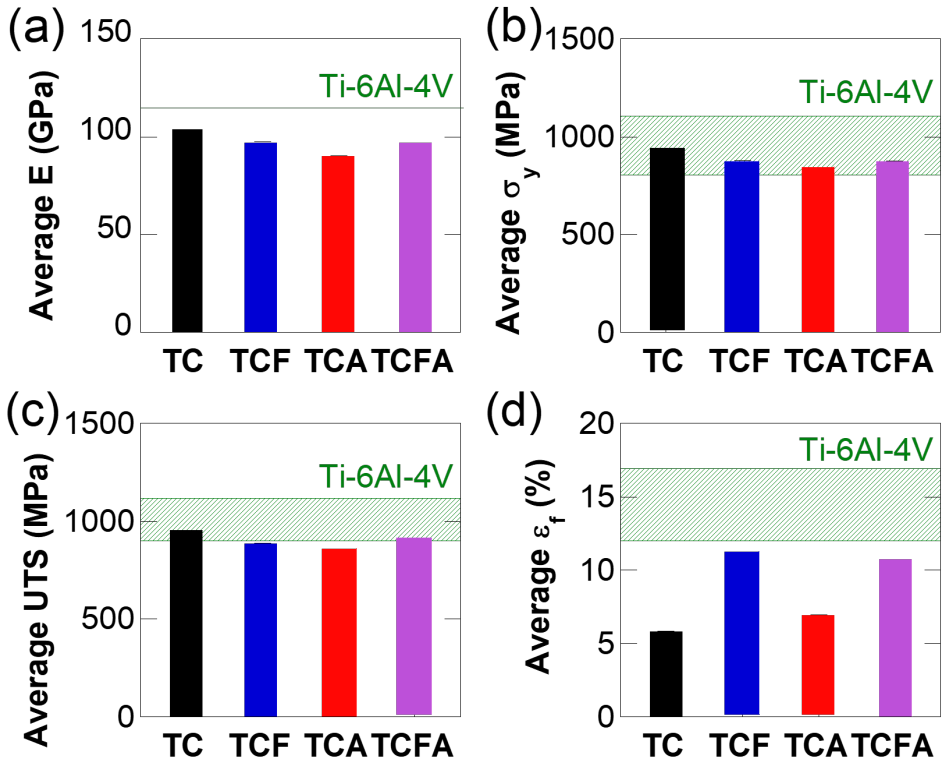

Figure 7.19: The average (a) E, (b) σ_y, (c) UTS, and (d) ϵ_f values of β-homogenized TC, TCF, TCA, and TCFA, compared with the E, σ_y, UTS, and ϵ_f values for Ti-6Al-4V [8].

The two-phase (β+α) TCA and TCFA and the three-phase (β+α+ω) TC and TCF exhibited strengths within or greater than the range of strengths reported for Ti-6Al-4V, see Figure 7.20(a) and (b). Each alloy exhibited E values close to but generally less than the reported E value of Ti-6Al-4V, see Figure 7.20(c). Each aged alloy exhibited lower ϵ_f values than Ti-6Al-4V, see Figure 7.20(d).

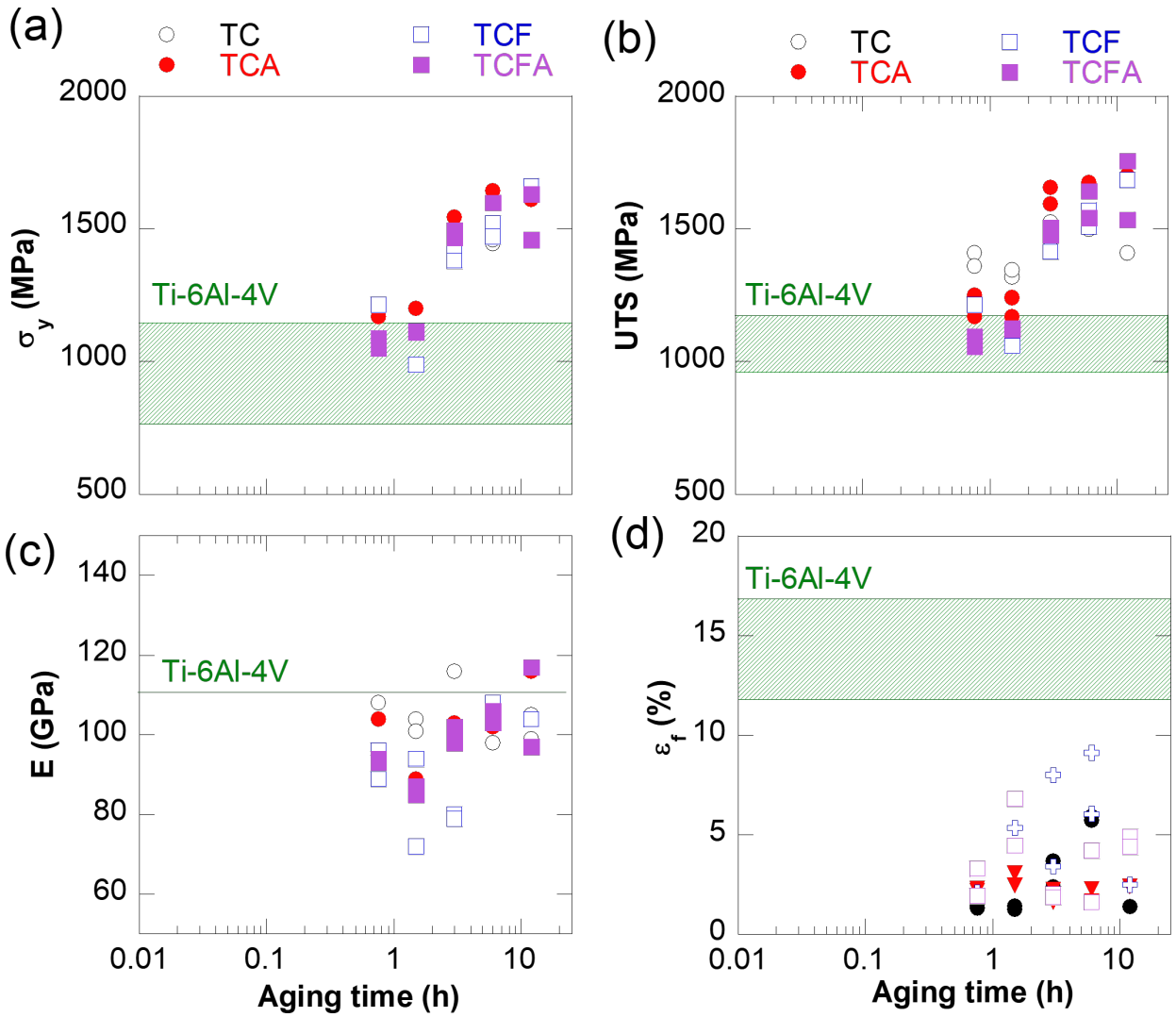

Figure 7.20: The average (a) E, (b) σ_y, (c) UTS, and (d) ϵ_f values of TC, TCF, TCA, and TCFA as a function of 400 °C aging time, compared to the reported E, σ_y, UTS, and ϵ_f values for Ti-6Al-4V [8].

The β-homogenized TC, TCF, TCA, and TCFA all exhibited G values lower than the G of Ti-6Al-4V (42 GPa) [8]. During 400 °C aging, TC exhibited a G of 42 GPa after approximately 0.25 h aging, and TCF exhibited a G of 42 GPa after approximately 5.5 h aging, see Figure 7.21. TCA and TCFA exhibited G values less than Ti-6Al-4V during the entire 24 h aging treatment. After aging for 24 h, TC and TCF exhibited G values greater than Ti-6Al-4V by 125% and 119% respectively.

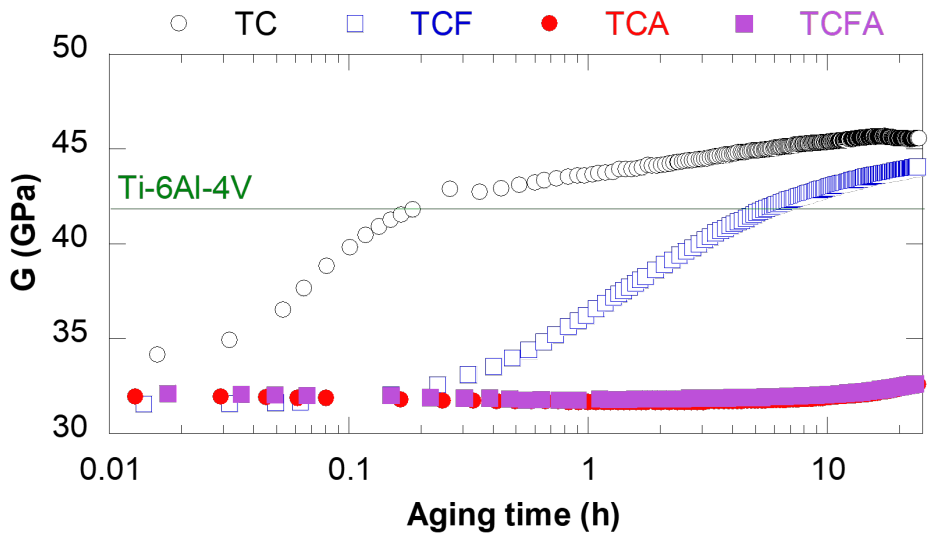

Figure 7.21: The RT G values exhibited by TC, TCF, TCA, and TCFA in the (a) β-homogenized condition and after (b) 24 h 400 °C aging, compared to the G reported for Ti-6Al-4V [8].

While the aged TC, TCF, TCA, and TCFA cannot compete with the ϵ_f values of Ti-6Al-4V, the achievable strengths of each aged alloy, plateauing at approximately 1.5 times greater than that reported for Ti-6Al-4V, might make these alloys more attractive than Ti-6Al-4V for high-strength applications. TCF aged for 6 h at 400 °C appears to be the most competitive option when compared to Ti-6Al-4V, achieving a similar E value as Ti-6Al-4V, the highest ϵ_f of all the aged alloys, and higher G, σ_y, and UTS values than Ti-6Al-4V.

CHAPTER 8

CONCLUSIONS

An investigation into the composition-processing-microstructure-property relationships of Fe- and Al- modified Ti-11at.%Cr was conducted. The β-homogenized alloys were investigated to determine the original microstructure and mechanical properties before aging. The phase transformations, microstructural evolution, and evolution of mechanical properties were investigated as a function of 400 °C aging.

The β-homogenized alloys only contained β-phase microstructures due to the β-homogenization treatment, with alloying elements randomly distributed in the microstructure. Some local ordering at the nanoscale was observed using APT.

Although each alloy underwent the same levitation melting, hot forging, and β-homogenization process, they exhibited different grain sizes. TC exhibited the smallest grain size, TCF and TCFA exhibited intermediate grain sizes, and TCA exhibited the largest grain size.

The alloys' a_β was less than that of pure Ti, since Cr, Fe, and Al all have smaller radii than Ti. The small additions of Fe and Al did not affect a_β significantly, and the measured a_β of each alloy was 3.22 Å.

Each alloy exhibited similar hardness since each alloy was fully β-homogenized, and hardening in β-Ti alloys is primarily due to precipitation of the α or ω phases. Higher σ_y and UTS values were measured in alloys with smaller β-grains. The grain sizes of TCF and TCFA corresponded to lower critical stresses for stress induced martensite, allowing them to exhibit higher ϵ_f values than TC and TCA.

The Fe and Al additions reduced E and G, with Al reducing E and G more than Fe. Fe and Al were predicted to reduce E and G in TCFA the most by lowering the average Bo of the alloy, but TCFA exhibited similar E and G values to TCF. The reductions of E and G were consistent with the nanoscale ordering of Ti, Cr, Fe, and Al observed in the APT data.

During a 400 °C treatment, the β-to-ω and β-to-α transformations occurred in TC and TCF,

and the β-to-α transformation occurred in TCA and TCFA. The Fe addition suppressed α formation in TCFA and ω formation in TCF. The suppressed β-to-ω transformation in TCF resulted in the ω-phase microstructure disappearing between 7.5 and 8 h at 400 °C. Fe may have suppressed the β-to-α transformation in TCF compared to TC, but the ω-assisted α-phase transformation increased α-phase volume fraction in TCF to equivalent amounts as in TC. The Al addition promoted the β-to-α transformation over the β-to-ω transformation, and no ω-phase was observed in the Al-containing TCA and TCFA. Al promoted α-phase formation in TCA compared to TC, resulting in higher α-phase volume fractions. TCFA exhibited the lowest α-phase volume fractions of the alloys, due to the effect of Fe on the β-to-α transformation.

The β-stabilizers Cr and Fe diffused from the α and ω phases into the β phase during the β-to-α and β-to-ω transformations, leaving the α and ω phases almost 100% Cr and Fe free. The α-stabilizer Al diffused from the β phase into the α phase. Some Al remained in the β matrix.

The diffusion of the β-stabilizers from the α and ω phases into the β phase increased the stability of the β phase and decreased a_β in each alloy. A relationship between β-phase stability and a_β was proposed for all β-Ti alloys, and the changing a_β affected the c/a ratios of the α and the ω phases. TCF exhibited smaller ω-phase lattice parameters than TC, but a similar relationship between a_β and ω-phase c/a ratio was observed for both TC and TCF.

Higher contents of the interstitial O were measured in the α and ω phases than in the β phase. O was also measured in higher concentrations at the α/β boundary, which could promote the formation of α-phase clusters in the microstructure.

Higher contents of the interstitial H were measured in the β phase than in any other phase. Due to H ingress, equilibrium and non-equilibrium hydrides formed in some APT samples. During the FIB-based lift-out process for APT samples, a higher electron-beam accelerating voltage during the decomposition of the Pt precursor caused more gaseous H to be released, and resulted in increased H ingress in the APT samples.

G increased with increasing ω- and α-phase volume fractions according to the ROM for two- and three-phase microstructures. E increased with increasing α-phase volume fractions according

to the ROM, but did not increase according to the ROM when the ω phase was present, resulting in lower E values than predicted.

The hardness of each alloy increased as the ω- and α-phase volume fractions increased. The ω phase increased hardness more than the α phase until the ω/α ratio dropped below 0.25, after which the α-phase volume fraction increased hardness more than the ω phase.

The σ_y and UTS values would increase with increasing volume fractions of the ω and α phases. σ_y and UTS evolved similarly to the hardness values, with the ω phase increasing the strength more at ω/α ratios above 0.25.

Alloys containing the ω-phase microstructure did not necessarily fail before yielding. TC containing higher ω-phase volume fractions failed before yielding, but all TCF samples containing ω-phase microstructures failed after yielding.

The aged alloys exhibited strengths up to 1.5x greater than the highest strengths exhibited by the common commercial α+β alloy, Ti-6Al-4V. The G values of TC and TCF could be tuned to meet or exceed the G of Ti-6Al-4V using varying 400 °C aging times. Even though the ϵ_f values of each alloy were less than those of Ti-6Al-4V, the strength and G increases make these alloys a competitive option for high-strength applications.

CHAPTER 9

FUTURE WORK

Through the results and analyses of the results presented in Chapters 4 through 7, many of the unanswered questions pertaining to the composition-processing-microstructure-property relationships of the Fe- and Al-modified Ti-11Cr alloys were addressed. Further areas of interest that were identified during this work are presented here. This chapter is divided into two sections: microstructure and mechanical properties.

9.1 Microstructure

While precipitates consistent with the ω and α phase sizes and morphologies were observed in the BSE-SEM photomicrographs, diffraction data is necessary to conclusively determine the crystal structure of the precipitates. This could be accomplished through TEM SAD or EBSD. TEM SAD or EBSD could provide more information on the relative spacing of the α and ω phases with respect to each other, which is critical to determine how the ω phase in TC and TCF influenced the α phase transformation.

Combining APT with TEM would be beneficial to more accurately determine the relationship between phase composition, a_β, strain at the ω/β and α/β boundaries, and the ω and α phase c/a ratios. TEM or simulations of the crystal interfaces would be helpful to investigate how misfit and coherency strain between the ω or α phases and the β phase change as a_β changes. These investigations could also provide insight into how the changing strain at the ω/β boundary could affect the ω-assisted α-phase transformation.

A preliminary analysis, not presented in this work, of d-orbital energy (Md), Mo-Eq, and a_β suggests a relationship between the three. Further analysis of the relationships between Md, Mo-Eq, and a_β could provide insight into the fundamental relationship between alloying element, β-phase stability, and a_β.

An investigation into the effect of Fe and Al additions on the β-to-ω and β-to-α transformation

energies could help the understanding of how Fe and Al affect the phase transformations and phase volume fractions in each alloy.

Further work could be targeted at improving the threshold analysis technique used to measure the volume fractions from the BSE SEM photomicrographs. The threshold analysis was found to have several weaknesses related to contrast. In the volume fraction measurements, the grain boundary α phase tended to be underrepresented, as contrast differences between β grains skewed the measurements. A more in depth image analysis, possibly adjusting the contrast of individual β grains to a uniform level to make threshold analysis of the ω- and α-phase fractions across multiple grains more feasible, could more accurately represent the phase volume fractions in the BSE-SEM photomicrographs. While this type of image analysis is possible using current image-analysis methods, it is not trivial. The threshold analysis also could not distinguish between the α and ω phases, as both phases exhibited similar contrasts. Machine learning could be used to help distinguish between the cuboidal ω, lenticular α, and globular grain boundary α phases using their distinct morphologies.

The TC samples formed hydrides and resulted in higher H concentrations than the other alloys, suggesting that TC may be more susceptible to H ingress and hydride formation than the Fe- and Al-modified alloys. If TC is more susceptible, this alloy could be used to study hydride formation in β-Ti alloys at the atomic level. Further work to understand the relationships between accelerating voltage during Pt deposition and H concentration would be helpful to reducing H in APT samples.

Further investigation into the relationship of alloy composition and grain size in β-homogenized β-Ti alloys would be valuable since the effect of composition on grain size in β-Ti alloys is less known than the effects of processing on grain size.

Further characterization of the phase transformations in each alloy at temperatures in the 210 °C to 500 °C range, and the 0 to 24 h aging time range, could lead to a better understanding of the phase transformation evolution in these alloys. Further phase characterization at any aging time and temperature could be used to improve the proposed TTT diagrams for these alloys.

9.2 Mechanical properties

First principles calculations of the elastic moduli of β-phase Ti with varying amounts of Cr, Fe, and Al could help determine why the additions of Fe and Al did not result in a lower E and G for TCFA than any other alloy.

Continued RUS studies, targeting the vibrational range associated with E instead of G, could determine how E evolves during the β-to-ω and β-to-α transformations. These studies could help verify whether the E values calculated for TC and TCF are truly lower than predicted, or whether the tensile tests misrepresented the E values for TC and TCF.

An investigation into the deformation mechanisms in each alloy could help determine whether the grain size of TCF and TCFA affected the deformation mode (i.e., TRIP, TWIP, or slip) compared to TC and TCA. Higher amounts of SIM in TCF and TCFA could verify that the critical stress for SIM can influence ϵ_f significantly.

APPENDICES

APPENDIX A

FIB-BASED LIFT-OUT STANDARD OPERATING PROCEDURE

A general standard operating procedure for the FIB-based lift-out and annular milling process is provided here. The FIB-based lift-out process can be accomplished with a dual-beam FIB/SEM equipped with a Pt source and an Omniprobe nanomanipulator. A silicon microtip array and microtip array holder compatible with the CAMERCA LEAP system are necessary. The procedure is divided into three sections. The first section describes a general lift-out process that can be adapted to differing FIB/SEM microscopes. The second section describes how to attach APT samples to the silicon microtip array from the lift-out. The third array describes the annular milling process. Images to supplement each procedure are located at the end of each section.

General instructions for milling a lift-out sample from the bulk material are provided here. If possible, the bulk material and the silicon microtip array should be loaded into the microscope at the same time.

1. Find the site on the bulk material to be lifted out for APT testing. Move that site to the eucentric height.

2. Deposit a Pt cap on the surface of the bulk material to protect the area of interest from Ga implantation during ion milling, see Figure A.1(a) and (b) for an example of the bulk material surface before and after Pt cap deposition, respectively. For the work in this dissertation, a Pt cap of approximately 10 μm long by 1.5 μm wide by 1 μm tall were deposited, and four samples per lift-out were generally obtained. To obtain more samples from a single lift-out, add 2μm per sample to the length dimension. To obtain fewer samples from a single lift-out, subtract 2μm per sample from the length dimension.

3. Tilt the sample to 22°to create a trench at 30°. Make the trench longer than the Pt cap, see Figure A.1(b). Use the focused ion beam to mill the trench, see Figure A.1(c). Once the trench has been cut, tilt the sample back to 0°, rotate the sample, tilt it to 22°, and repeat the

milling process to create a second trench, see Figure A.1(d). The trenches have created a wedge-shaped lift-out.

4. Cut the side of the lift-out that you want to attach the Omniprobe nanomanipulator to so that it is no longer connected to the bulk material, see Figure A.1(e).

5. Tilt the sample back to 0°.

6. Insert the Omniprobe nanomanipulator and lower it towards the sample, see Figure A.1(e).

    - Note: Once the Omniprobe connects with the sample, it is putting pressure on the sample and may drift, putting stress and strain on the sample. To reduce the effects of the Omniprobe on the sample, the next steps should be done quickly.

7. Lightly contact the Omniprobe with the lift-out.

8. Attach the sample to the Omniprobe using Pt deposition, see Figure A.1(f).

9. Using the ion beam, cut the remaining side of the lift-out so that it is no longer connected to the bulk material, and instead is attached only to the Omniprobe nanomanipulator, see Figure A.1(f).

10. Quickly lift the Omniprobe nanomanipulator so that the lift-out cannot crash into the bulk material.

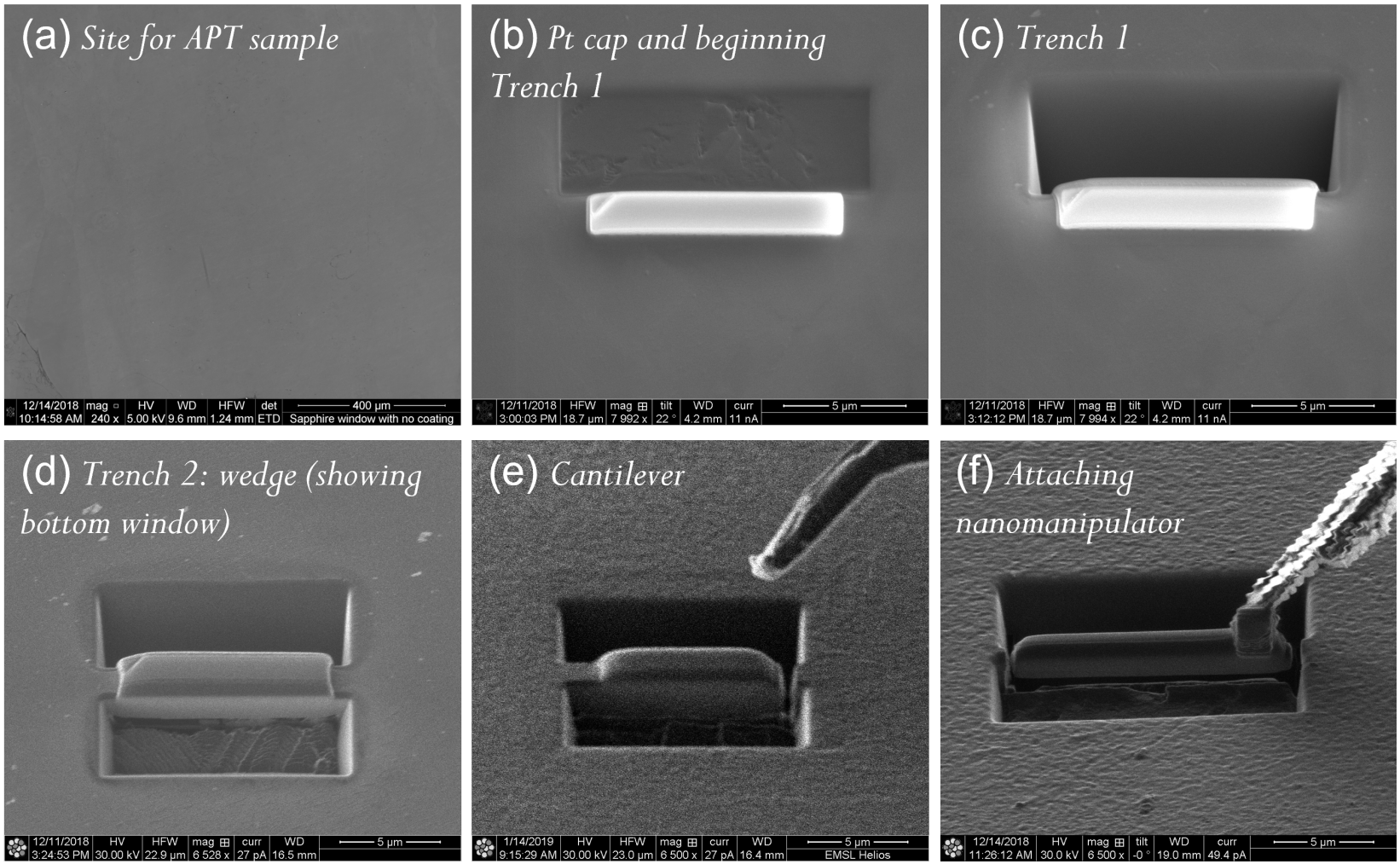

Figure A.1: Photomicrographs of the FIB-based lift-out process detailing (a) a site of interest for APT, (b) a Pt cap protecting the surface of the bulk material with a trench beginning to be milled, (c) the first trench fully milled, (d) the second trench fully milled with the lift-out attached to the bulk material on both sides, (e) the liftout with the right side of the sample milled through in preparation of attachment to the Omniprobe nanomanipulator, and (f) the lift-out separated from the bulk material and attached to the Omniprobe nanomanipulator with a Pt weld.

Once the lift-out has been milled from the bulk material, it must be attached to the microtip array and shaped into an APT tip. A general procedure for attaching samples from the bulk lift-out to the microtip array.

1. Find the eucentric height of the microtip array using the end of a microtip as the focal point. Note: once the eucentric height of the array has been found, do not tilt or rotate the stage until the lift-out samples have been attached to the array.

2. Find a microtip to attach a sample to, see Figure A.2(a) and (b).

3. Move the lift-out towards the microtip, and lower the lift-out until it touches the microtip, see Figure A.2(c). While moving the sample, check its alignment to confirm that the nanomanipulator is not drifting.

4. Using Pt, weld the free end of the lift-out to the microtip, see Figure A.2(d).

5. Use the ion beam to cut the end of the lift-out attached to the microtip free of the rest of the lift-out, see Figure A.2(e).

6. Raise the nanomanipulator so that the lift-out will not crash into the microtip array while moving. Move to the next tip and repeat the lowering and welding process. The final sample will have to be cut free of the nanomanipulator.

7. Once all the samples are placed on microtips, remove the nanomanipulator from the chamber.

8. Rotate the microtip array by 180°. Weld the back side of each sample to the microtip in a similar way to the front of the microtip.

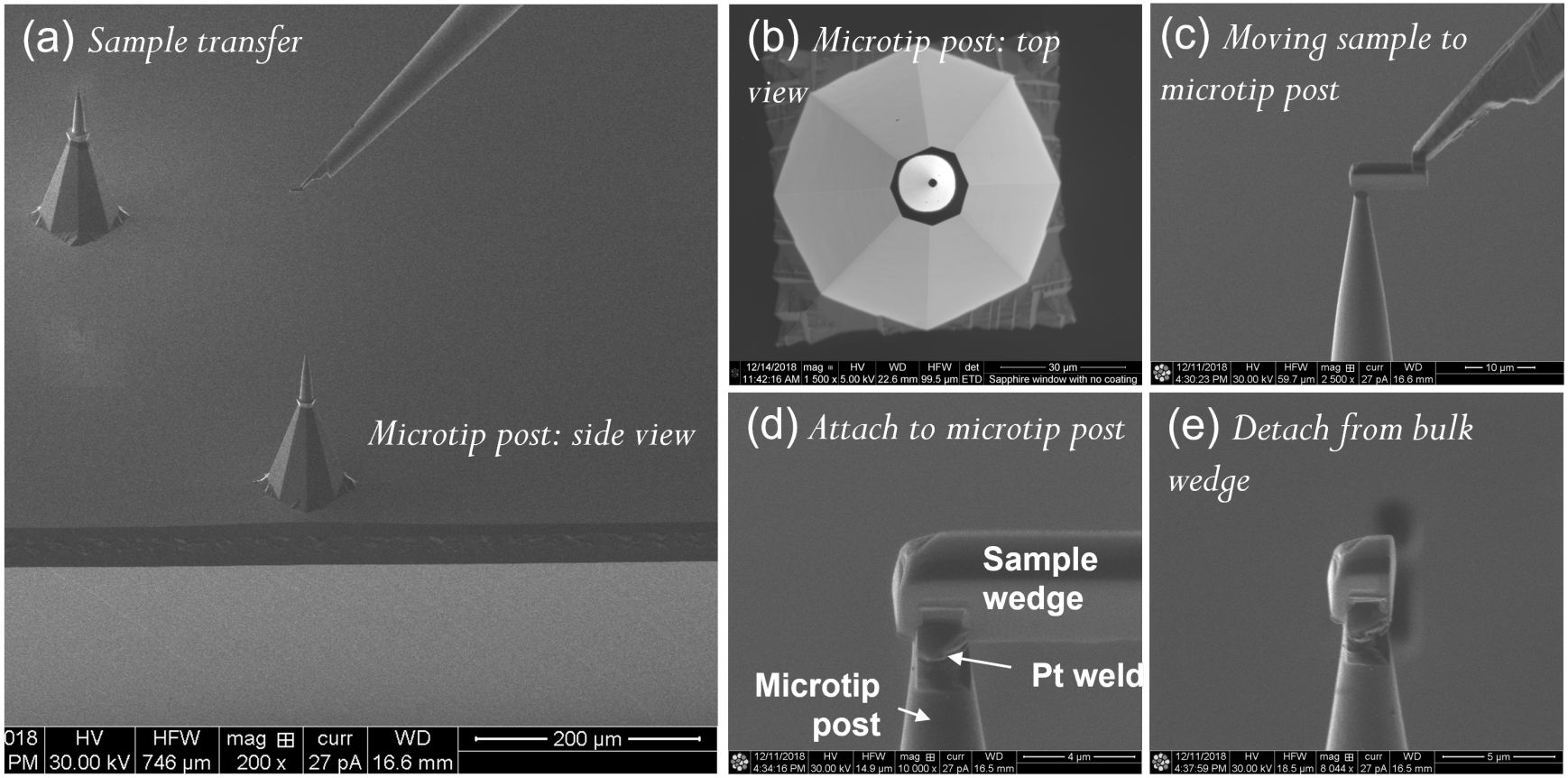

Figure A.2: Photomicrographs of the FIB-based lift-out process detailing (a) a side view of a microtip post on a silicon microtip array and the movement of the lift-out towards the post, (b) a top view of a microtip post, (c) placement of the lift-out onto the microtip post before the sample is welded to the post with Pt, (d) the lift-out attached to a microtip post with a Pt weld, and (e) the sample welded to the microtip post after being cut free form the bulk of the lift-out.

This process is used to shape the sample into a tip shape. A sharper APT tip shape is less likely to fracture during ion evaporation.

1. Rotate the microtip array by 90° so the sample and both Pt welds are visible, see Figure A.3(a).

2. Tilt the stage so that the sample is perpendicular to the ion beam (52°). The ion beam will be used to mill the sample and the electron beam will be used to monitor the sample shape and to measure the size of the sample tip.

3. Slice the side of the sample viewed in the electron beam so that a flat portion is visible. This will help with aligning the annular milling pattern on the sample.

4. Place a circular milling pattern on the sample so that the center 1 μm of the sample is not milled, but the outer edge of the sample is.

5. Mill the sample, taking short images of the sample using the electron beam to check the shape and dimensions of the sample, see Figure A.3(b). When the tip of the sample is approximately 1 μm, stop milling.

6. Adjust the milling pattern so that the center 0.8 μm of the sample is not milled. Repeat the milling process. When the tip of the sample is approximately 0.8 μm, stop milling.

7. Repeat the process for sample diameters of 0.6, 0.4, and 0.2 μm, see Figure A.3(c).

    - Note: during this process, if the tip is not sharp enough at the top (200 μm or less), the final polishing step will not sharpen the tip. A smaller diameter of milling can be used to fix a blunt tip.

    - Note: The final polishing step will remove the Pt cap from the surface of the sample. The ion beam is used to shower the sample with ions and mill the surface of the material directly. The top 0.1 μm of the sample material is milled to remove any possible damage accrued during the mechanical polishing or FIB-based lift-out process.

8. In a lower-magnification view, use lower-energy ions (5 kV and 48 pA was used) to raster over the sample. While this is occurring, use the electron beam to take images of the sample. When the Pt cap and 0.1 μm of the sample material have been removed, stop the ion beam.

9. Using the electron beam, take a picture of the finished tip to record the final tip shape, see Figure A.3. A magnification where the scale bar indicates 200 nm is recommended.

10. Tilt the stage back to 0°, remove the microtip array from the FIB/SEM, and transfer immediately to the CAMECA LEAP.

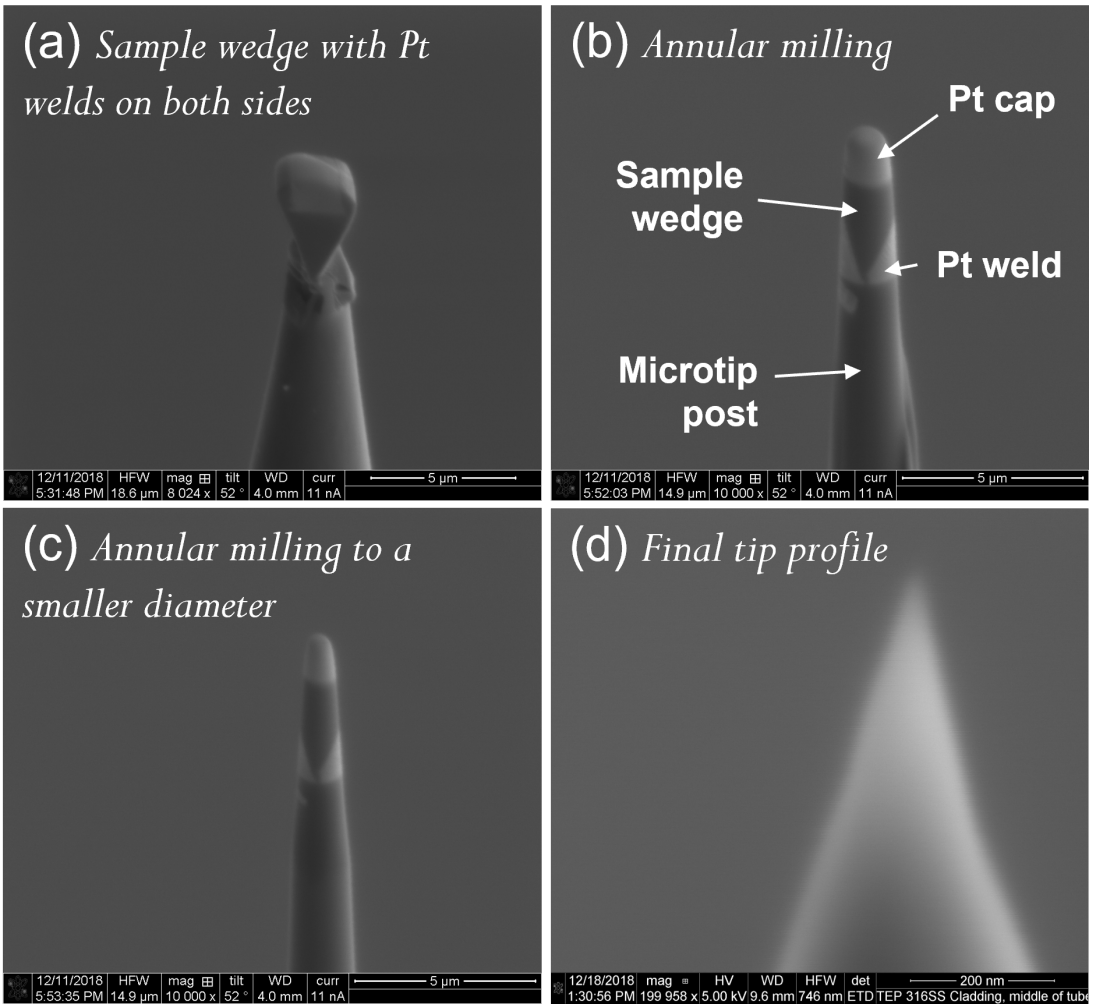

Figure A.3: Photomicrographs of the FIB-based lift-out process detailing (a) the side view of a sample welded to a microtip, (b) the sample after annular milling showing the Pt welds, sample, and microtip post, (c) the sample milled to a smaller diameter, and (d) final tip profile of the sample.

APPENDIX B

400°C XRD INTENSITY VERSUS 2θ PLOTS

The 400°C XRD intensity versus 2θ curves for each alloy are presented here.

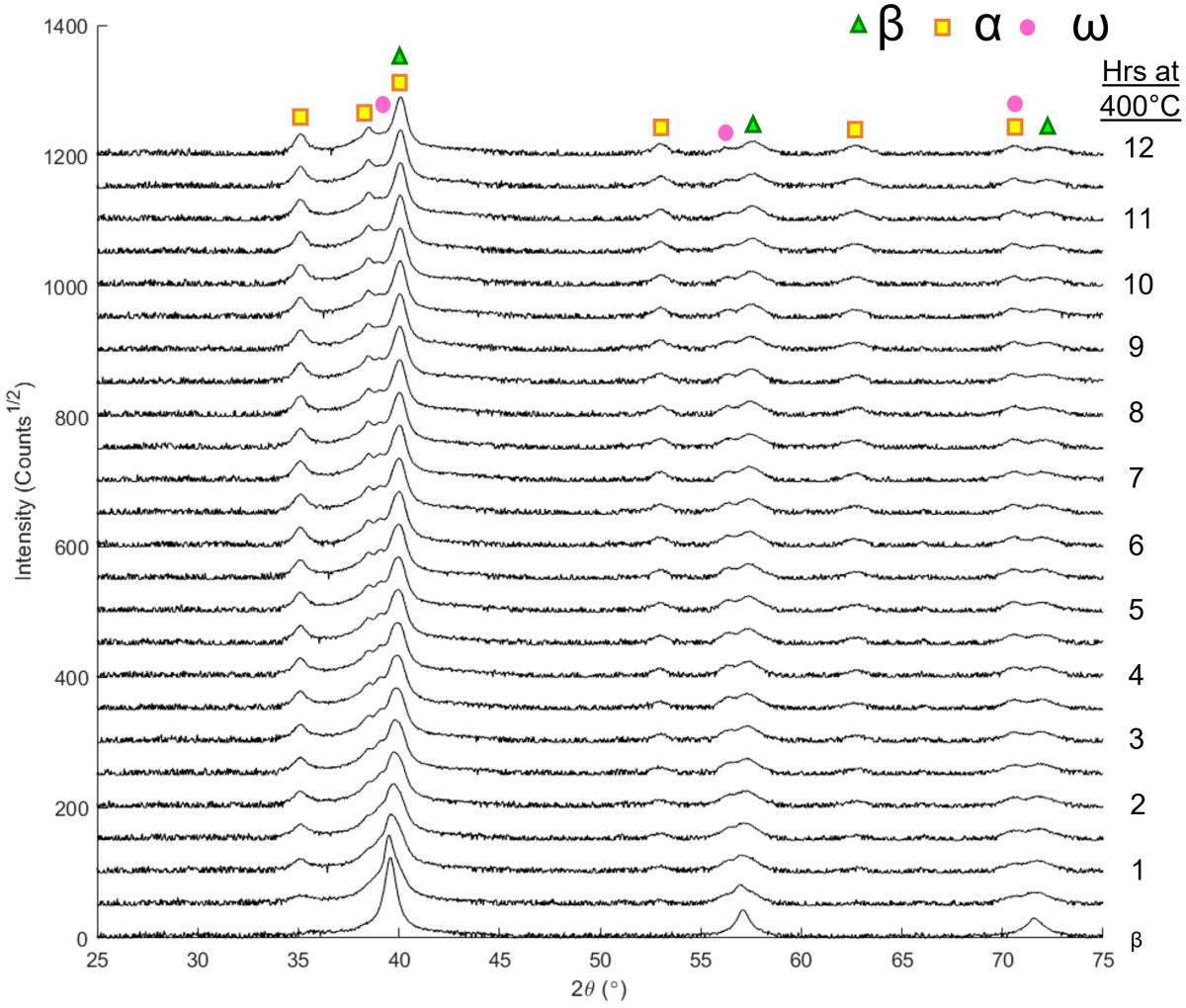

Figure B.1: HTXRD intensity versus 2θ plots showing the evolution of the β-, α, and ω-phase peaks for TC with increasing 400°C aging time.

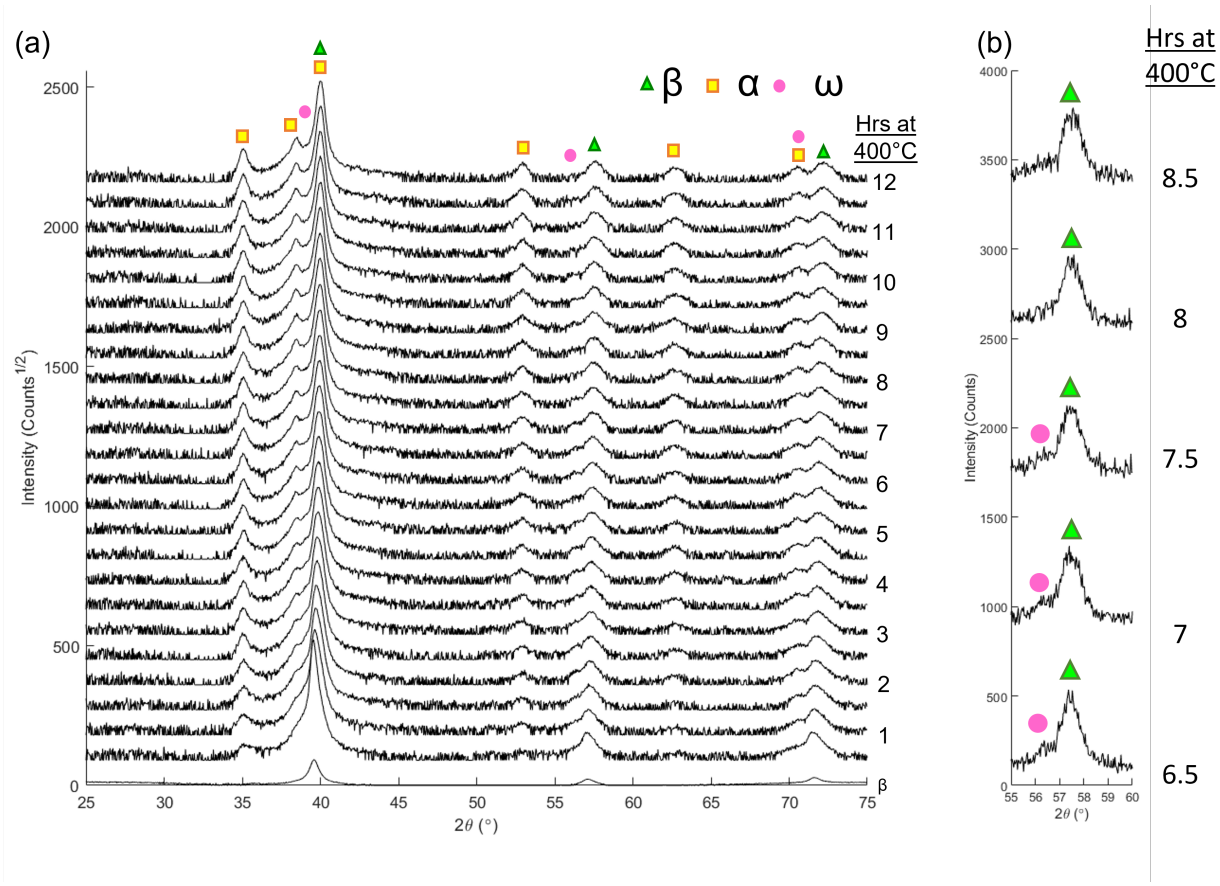

Figure B.2: (a) HTXRD intensity versus 2θ plots showing the evolution of the β-, α, and ω-phase peaks for TCF with increasing 400°C aging time. In (b), the $(201)_{\omega}$ and $(200)_{\beta}$ peaks after 6.5, 7, 7.5, 8, and 8.5 h aging are provided in more detail to show the disappearance of the ω phase.

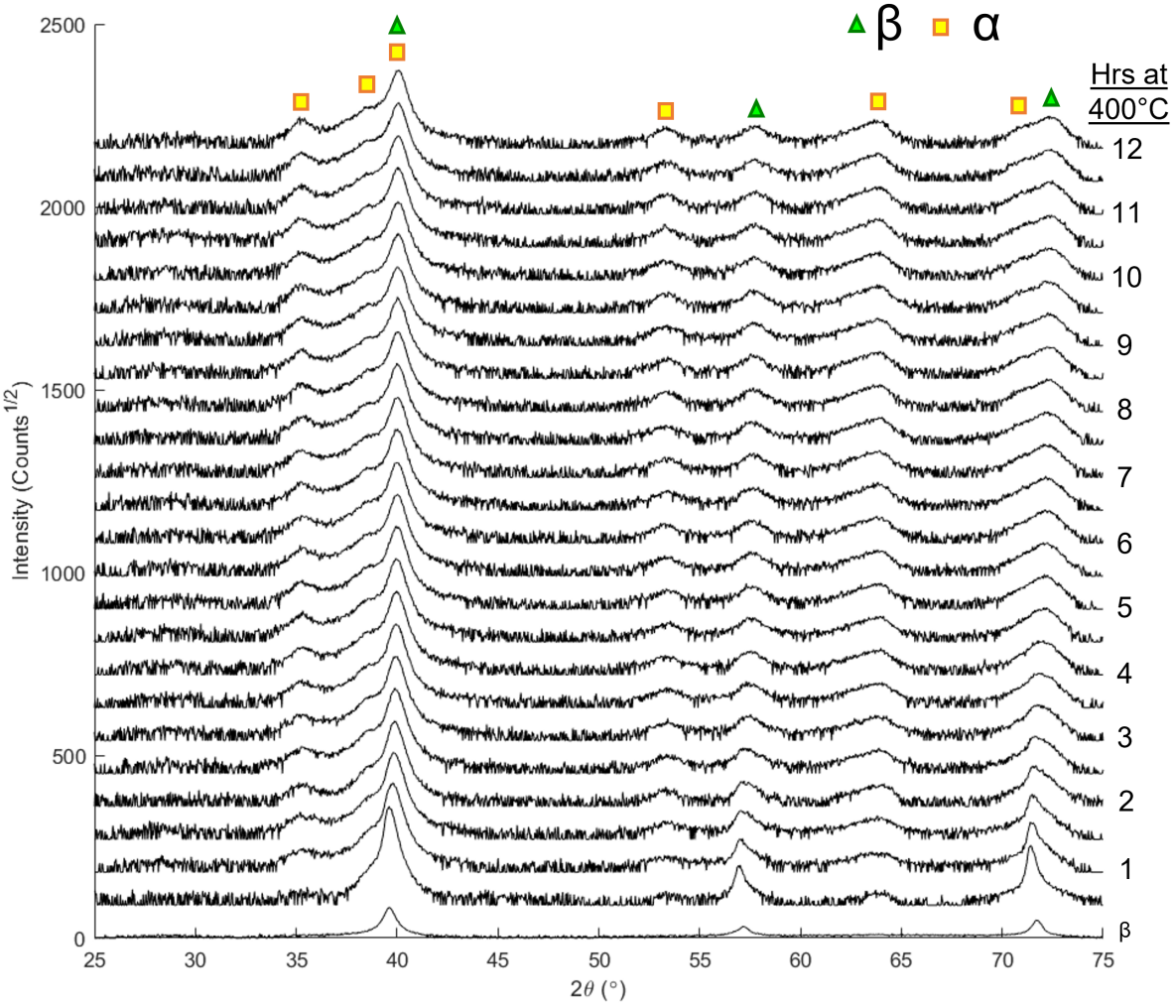

Figure B.3: HTXRD intensity versus 2θ plots showing the evolution of the β- and α-phase peaks for TCA with increasing 400°C aging time.

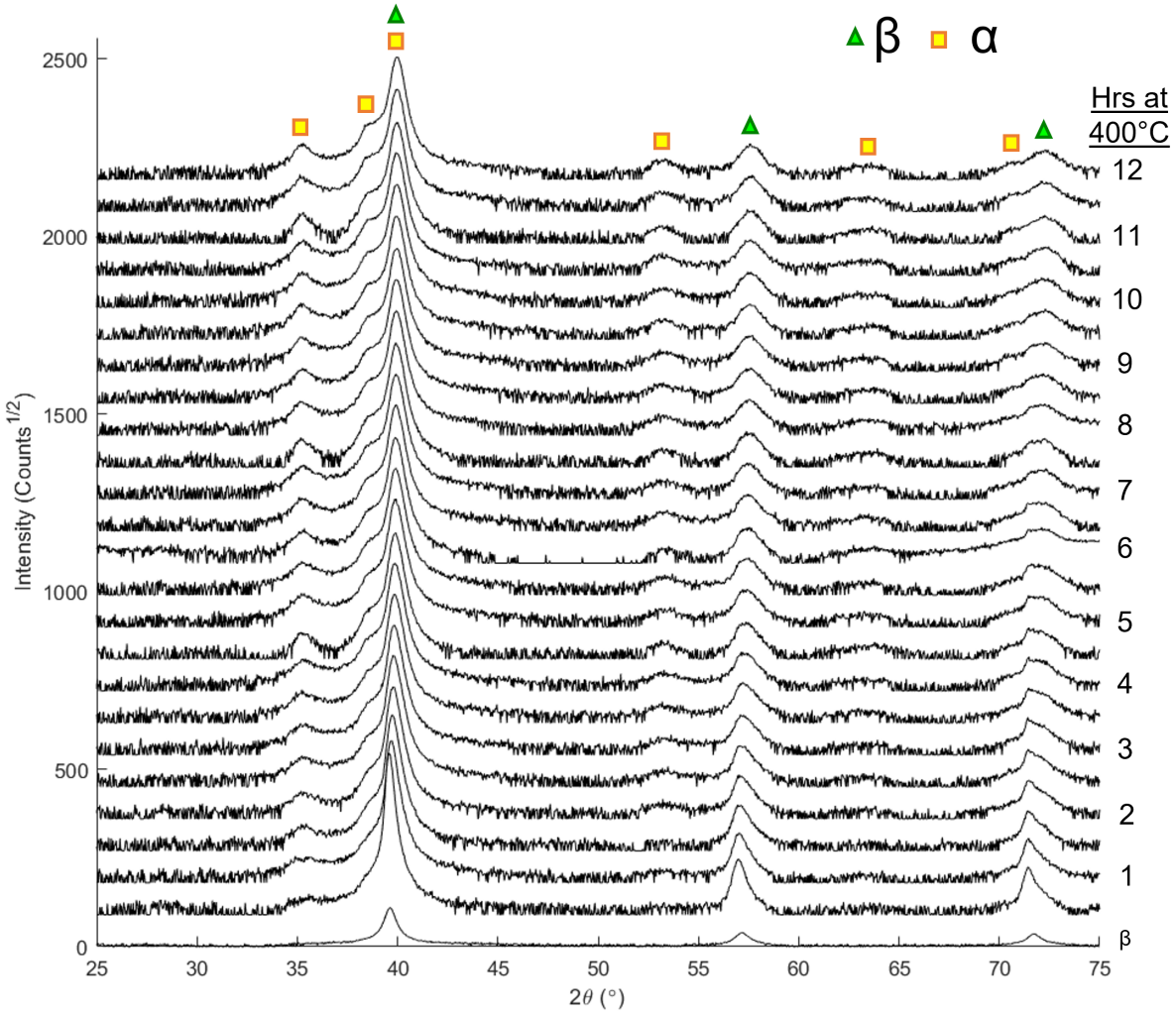

Figure B.4: HTXRD intensity versus 2θ plots showing the evolution of the β- and α-phase peaks for TCA with increasing 400°C aging time.

APPENDIX C

BSE-SEM IMAGES OF THE AGED ALLOYS

BSE-SEM images used to evaluate the size, morphology, and volume fractions of the ω and α phases in TC and TCF and the α phase in TCA and TCFA are provided here.

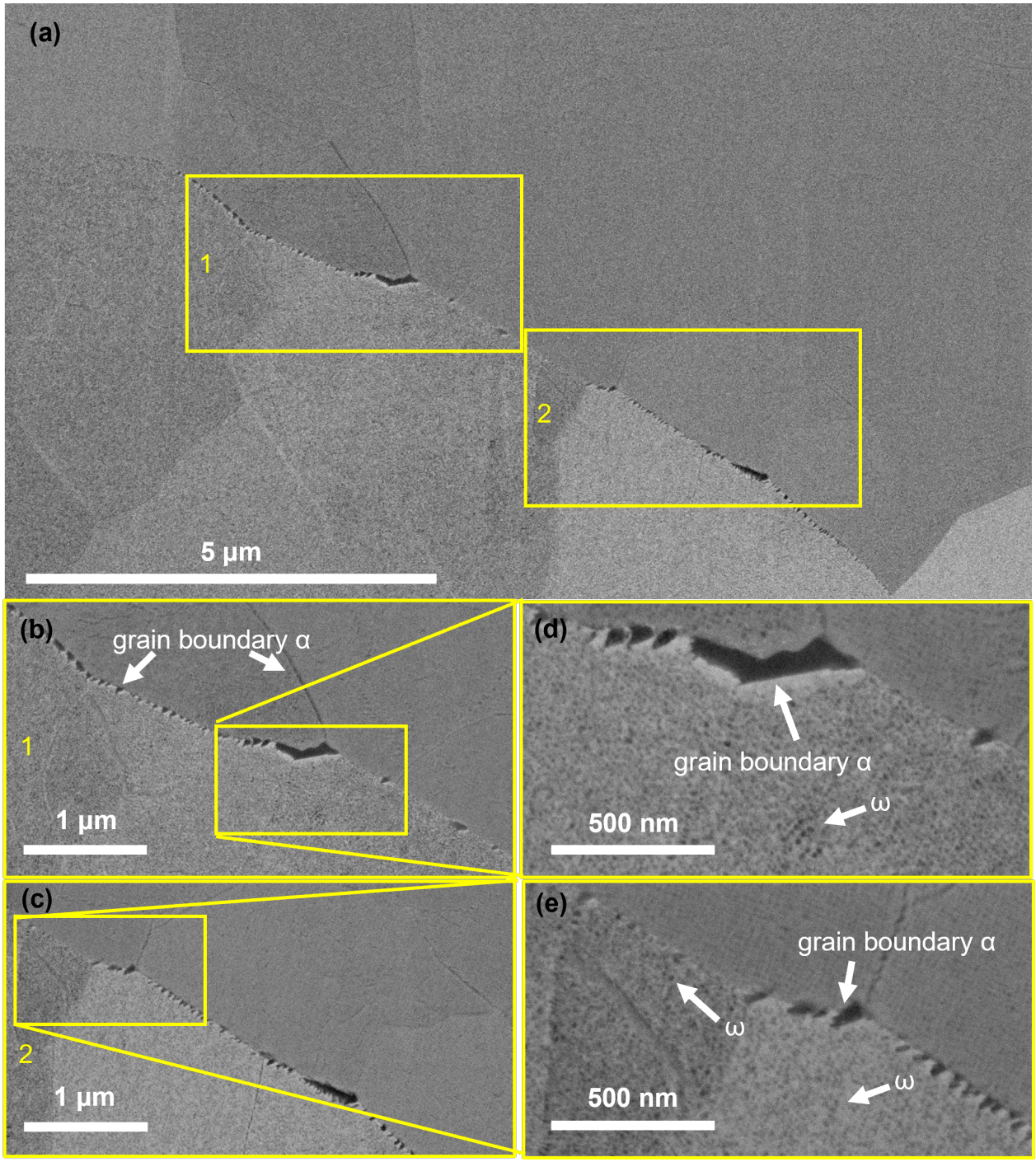

Figure C.1: BSE-SEM photomicrographs of TC aged at 400 °C for 1.5 h at (a) lower magnification, showing darker precipitates in a light β-phase matrix. Higher magnification BSE-SEM photomicrographs of areas (b) 1 and (c) 2 (defined in (a)), illustrating the larger grain boundary α precipitates as well as the smaller precipitates. The highest magnification BSE-SEM photomicrographs (d) and (e), with the ω and α precipitates labeled.

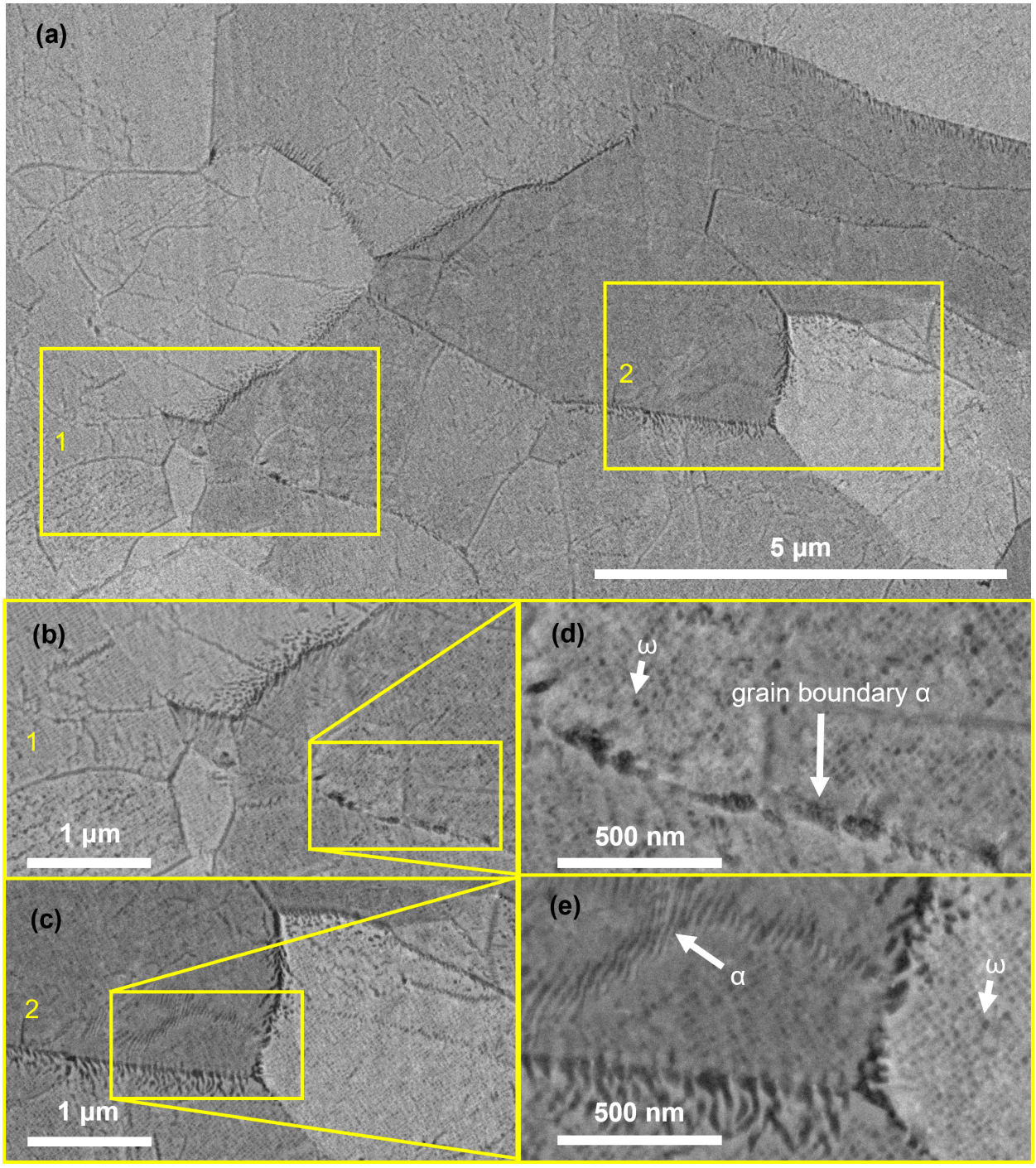

Figure C.2: BSE-SEM photomicrographs of TC aged at 400°C for 3 h at (a) lower magnification, showing darker precipitates in a light β-phase matrix. Higher magnification BSE-SEM photomicrographs of areas (b) 1 and (c) 2 (defined in (a)), illustrating the larger grain boundary α precipitates as well as the smaller precipitates. The highest magnification BSE-SEM photomicrographs (d) and (e), with the ω and α precipitates labeled.

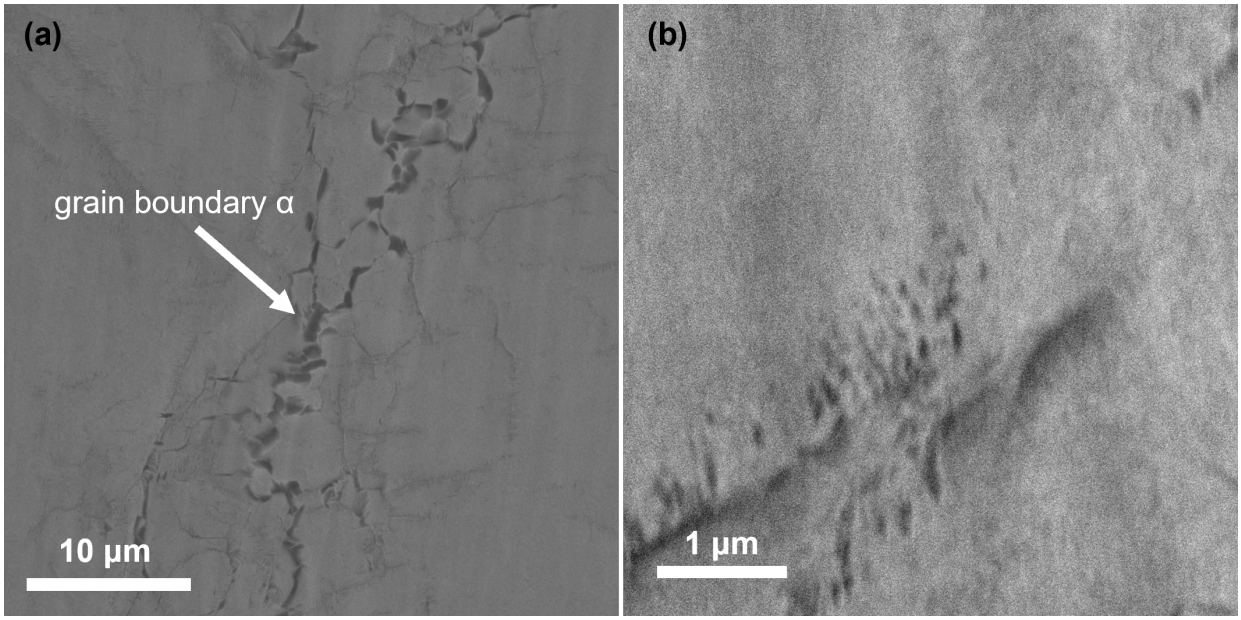

Figure C.3: BSE-SEM photomicrographs of 6 h aged TC at (a) lower magnification, (b) medium magnification, and (c) higher magnification, where darker precipitates are visible in a lighter β-phase matrix.

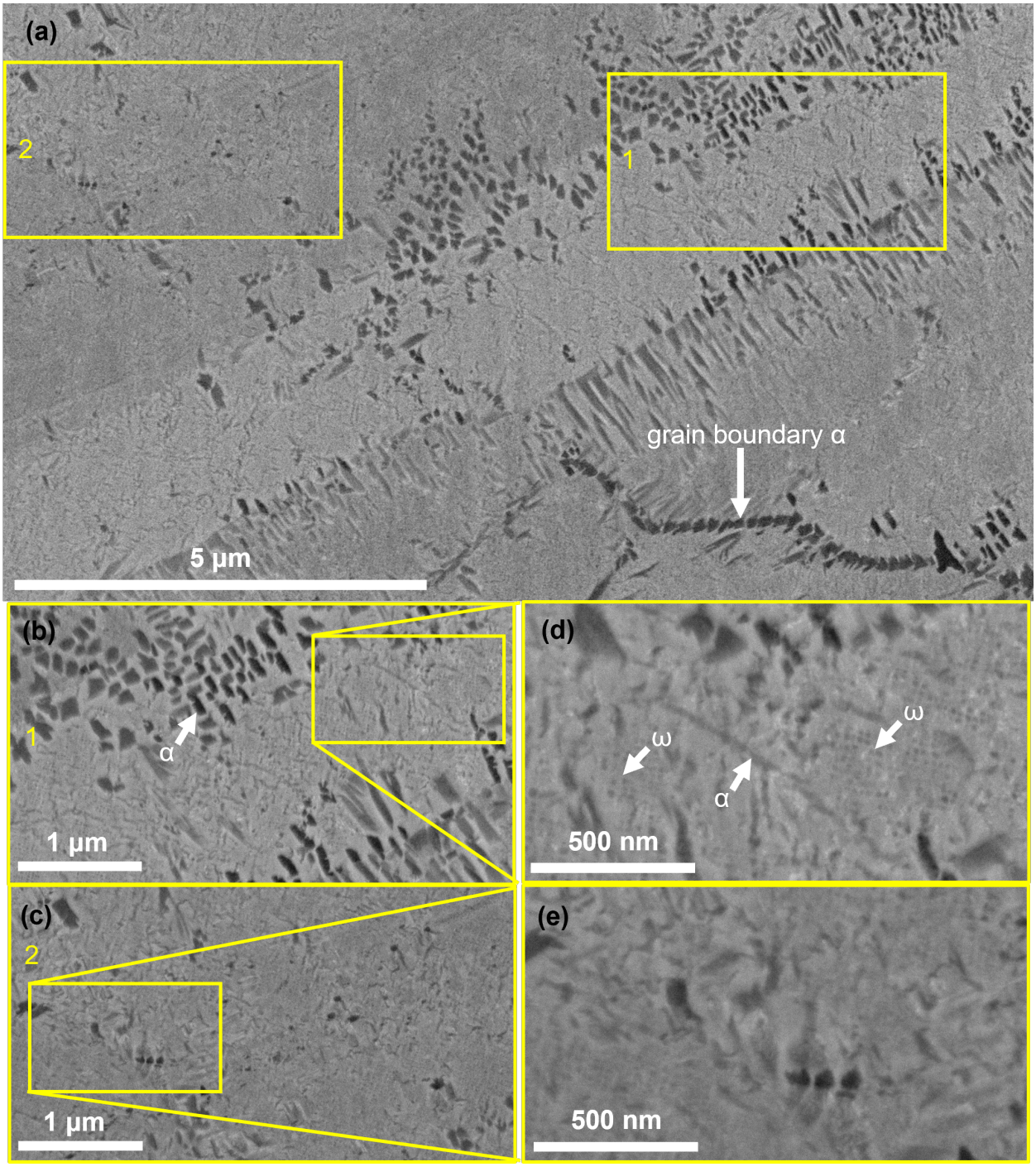

Figure C.4: BSE-SEM photomicrographs of TCF aged at 400°C for 1.5 h at (a) lower magnification, showing darker precipitates in a light β-phase matrix. Higher magnification BSE-SEM photomicrographs of areas (b) 1 and (c) 2 (defined in (a)), illustrating the larger α precipitates as well as the smaller precipitates. The highest magnification BSE-SEM photomicrographs (d) and (e), with the ω and α precipitates labeled.

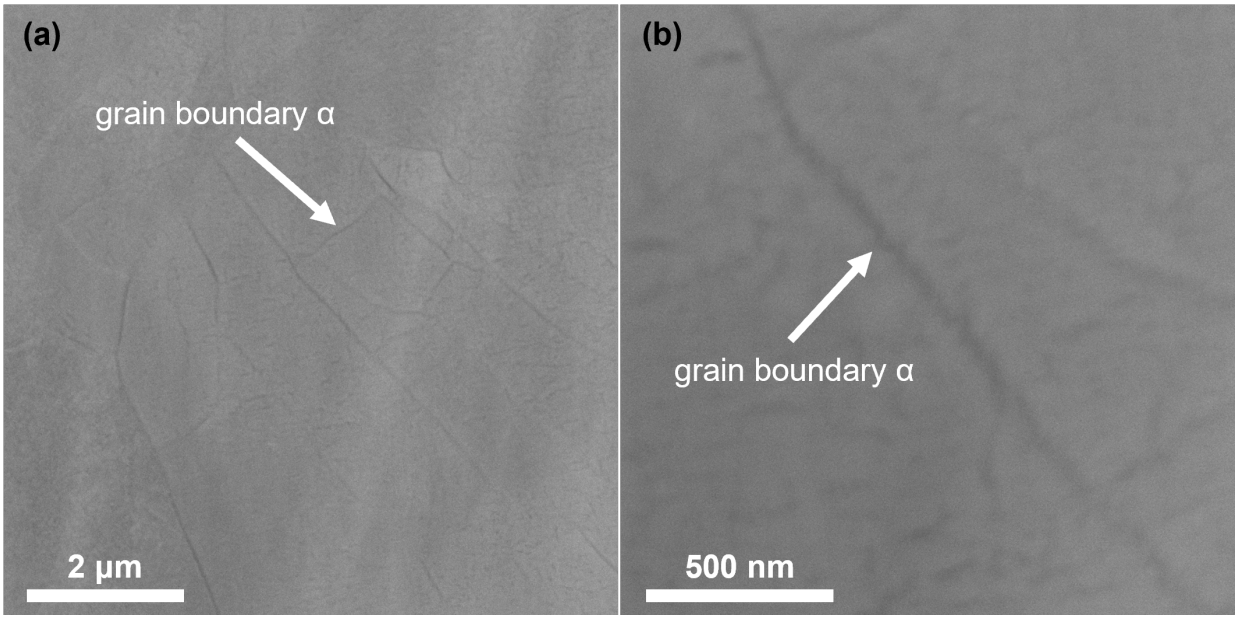

Figure C.5: BSE-SEM photomicrographs of 3 h aged TCF at (a) lower magnification, (b) medium magnification, and (c) higher magnification, where darker precipitates are visible in a lighter β-phase matrix. Curtaining from the ion-milling process is visible in the lower magnification image.

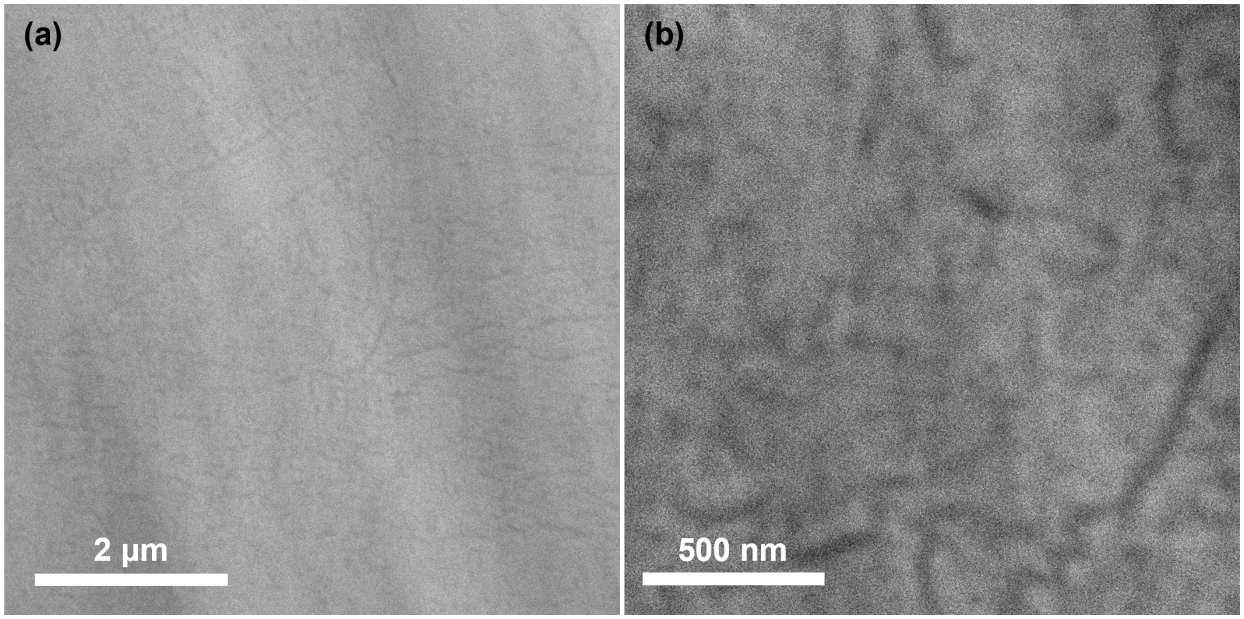

Figure C.6: BSE-SEM photomicrographs of 6 h aged TCF at (a) lower magnification, (b) medium magnification, and (c) higher magnification, where darker precipitates are visible in a lighter β-phase matrix. Curtaining from the ion-milling process is visible in the lower magnification image.

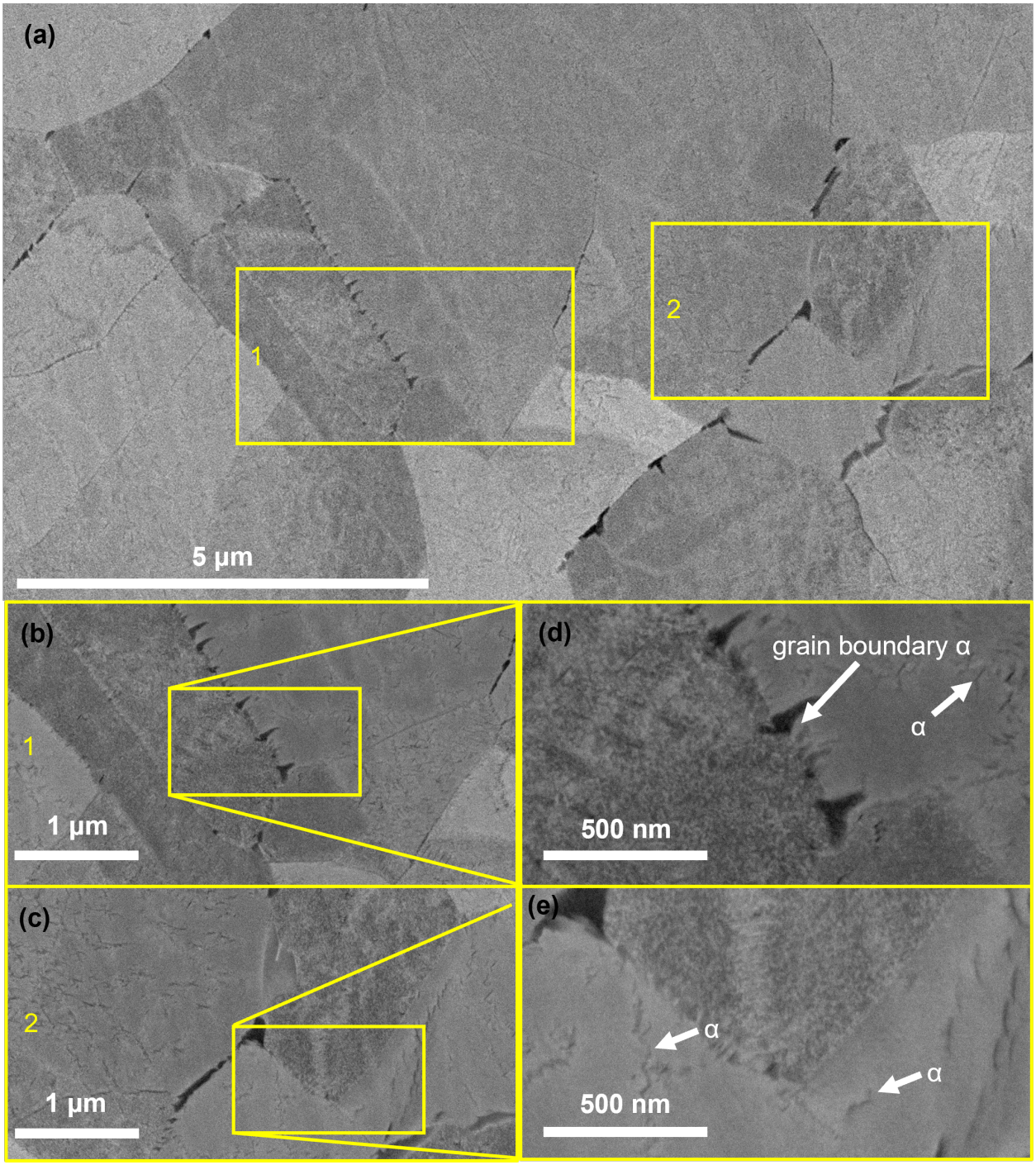

Figure C.7: BSE-SEM photomicrographs of TCA aged at 400°C for 1.5 h at (a) lower magnification, showing darker precipitates in a light β-phase matrix. Higher magnification BSE SEM photomicrographs of areas (b) 1 and (c) 2 (defined in (a)), illustrating the larger and smaller α precipitates. The highest magnification BSE SEM photomicrographs (d) and (e), with the α precipitates labeled.

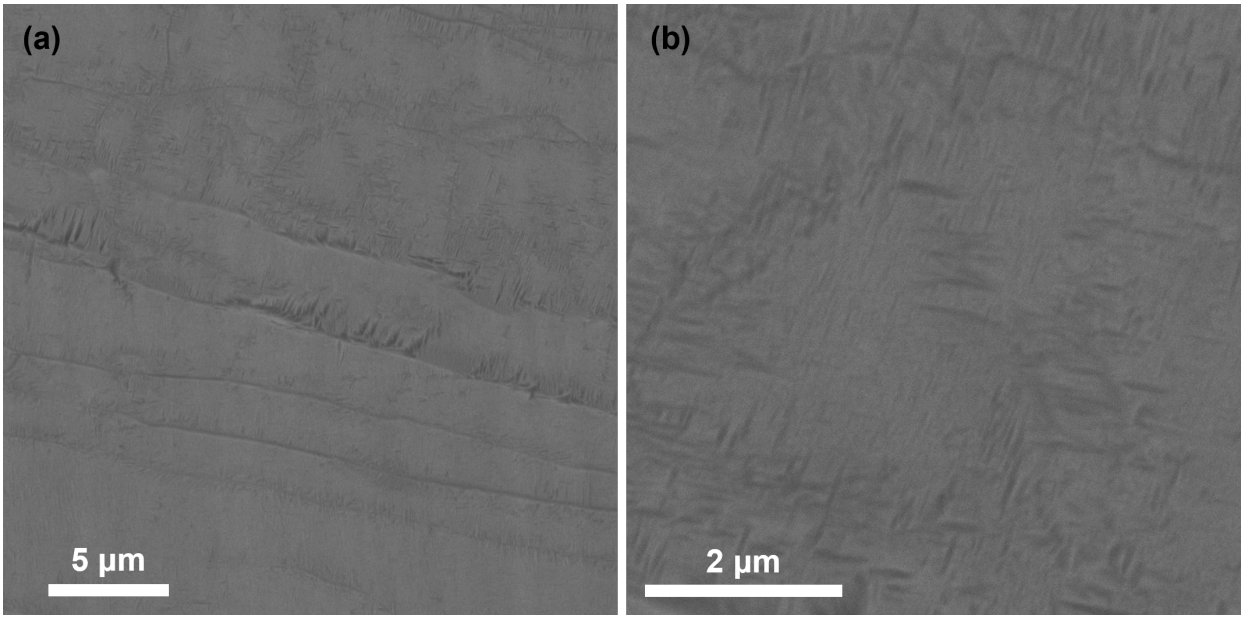

Figure C.8: BSE-SEM photomicrographs of 3 h aged TCA at (a) lower magnification and (b) higher magnification, where darker α-phase precipitates are visible in a lighter β-phase matrix.

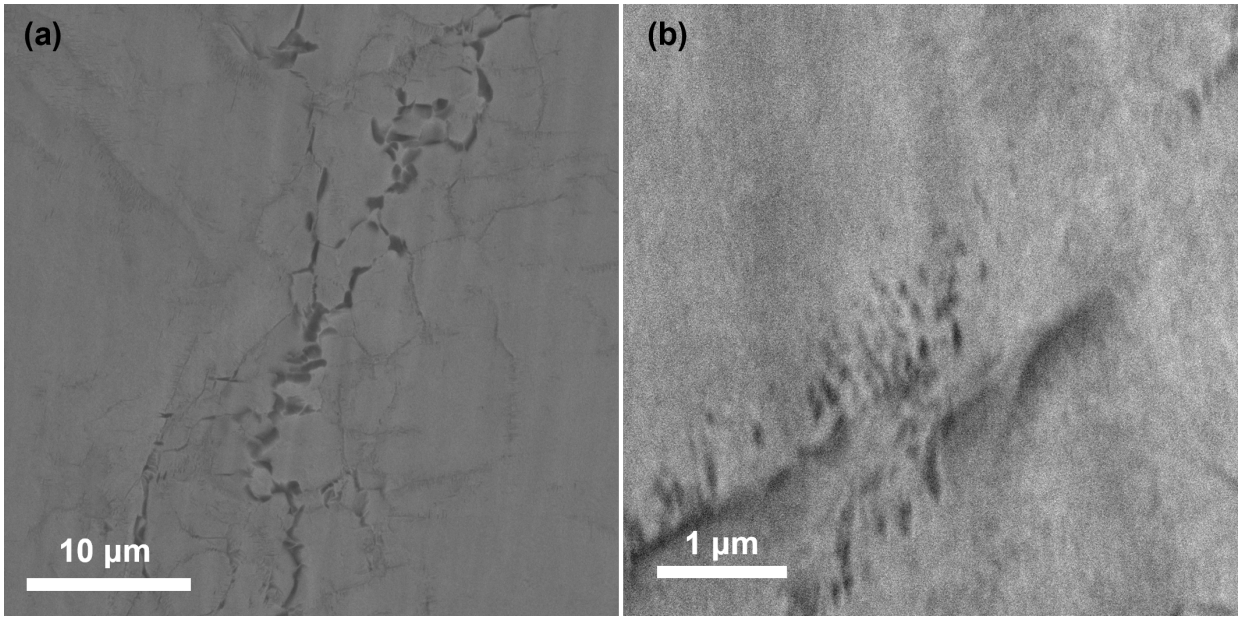

Figure C.9: BSE-SEM photomicrographs of 6 h aged TCA at (a) lower magnification and (b) higher magnification, where darker α-phase precipitates are visible in a lighter β-phase matrix. Curtaining from the ion-milling process is visible in both images.

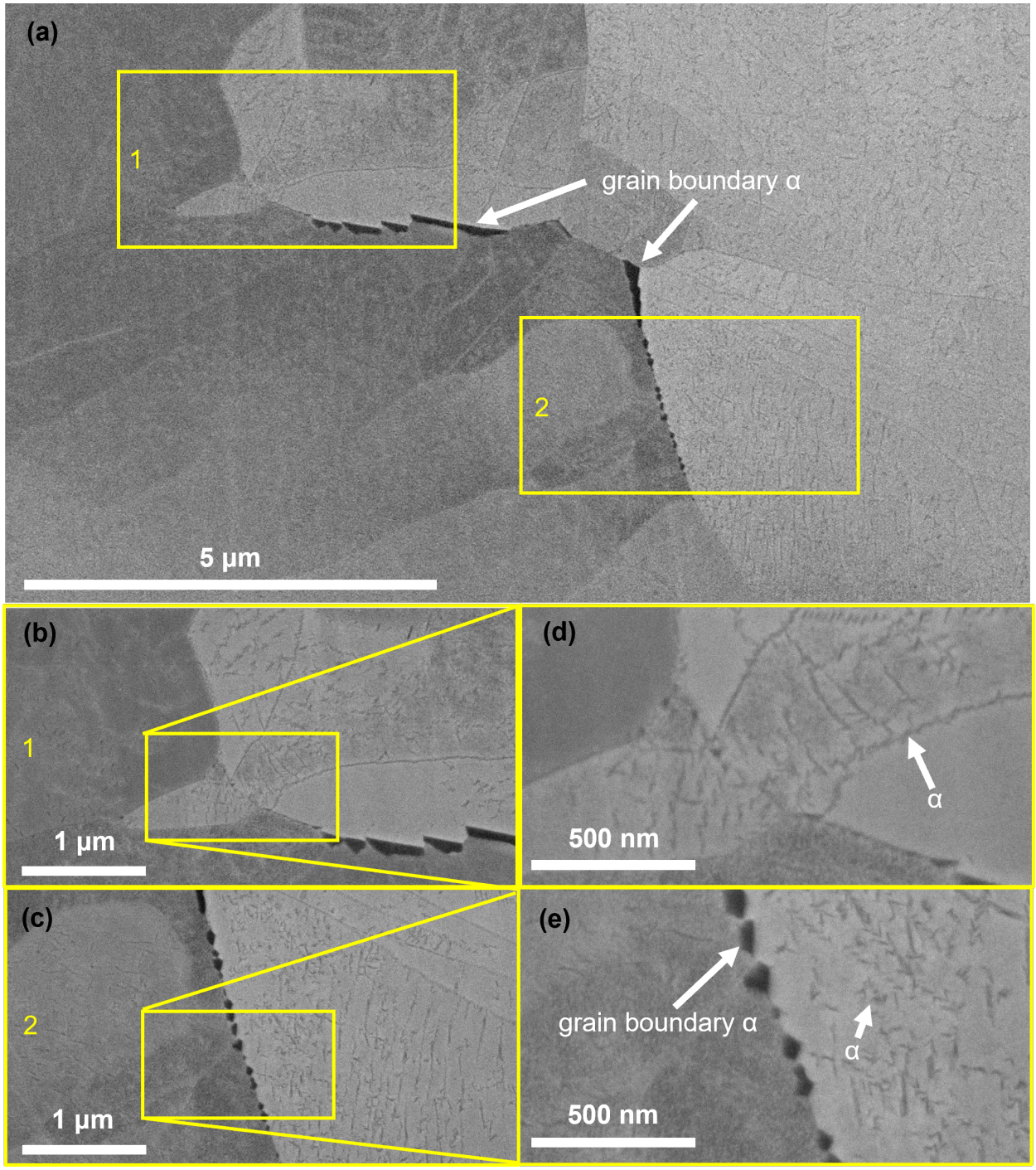

Figure C.10: BSE-SEM photomicrographs of TCFA aged at 400°C for 1.5 h at (a) lower magnification, showing darker precipitates in a light β-phase matrix. Higher magnification BSE-SEM photomicrographs of areas (b) 1 and (c) 2 (defined in (a)), illustrating the larger and smaller α precipitates. The highest magnification BSE-SEM photomicrographs (d) and (e), with the α precipitates labeled.

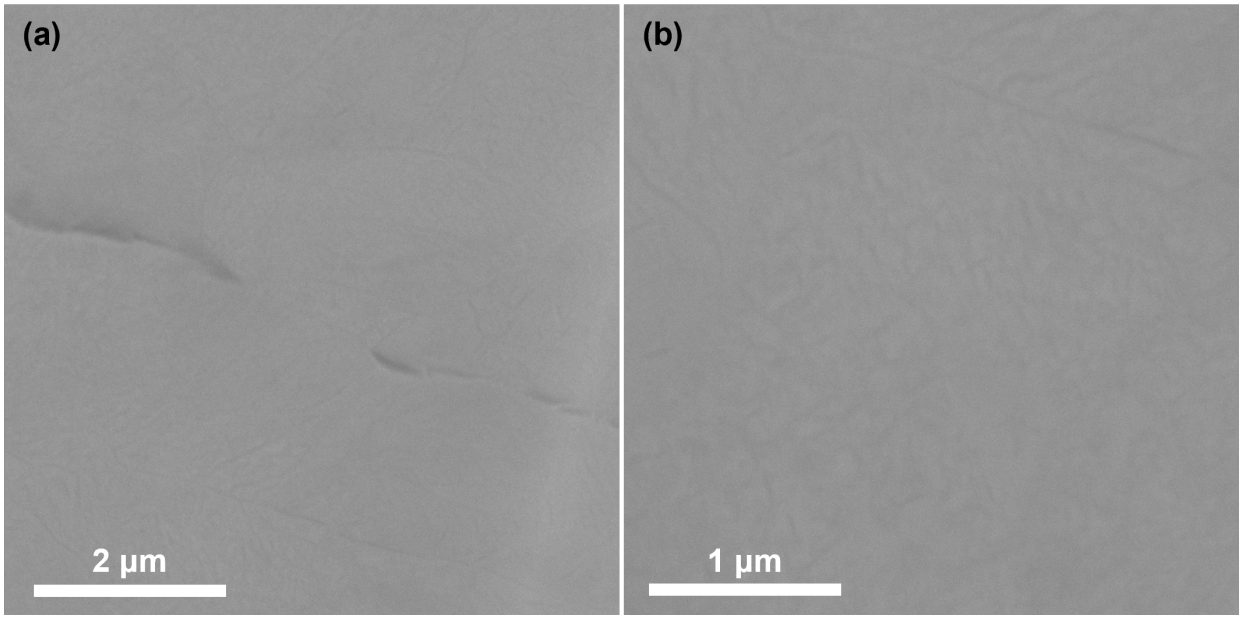

Figure C.11: BSE-SEM photomicrographs of 3 h aged TCFA at (a) lower magnification and (b) higher magnification, where darker α-phase precipitates are visible in a lighter β-phase matrix.

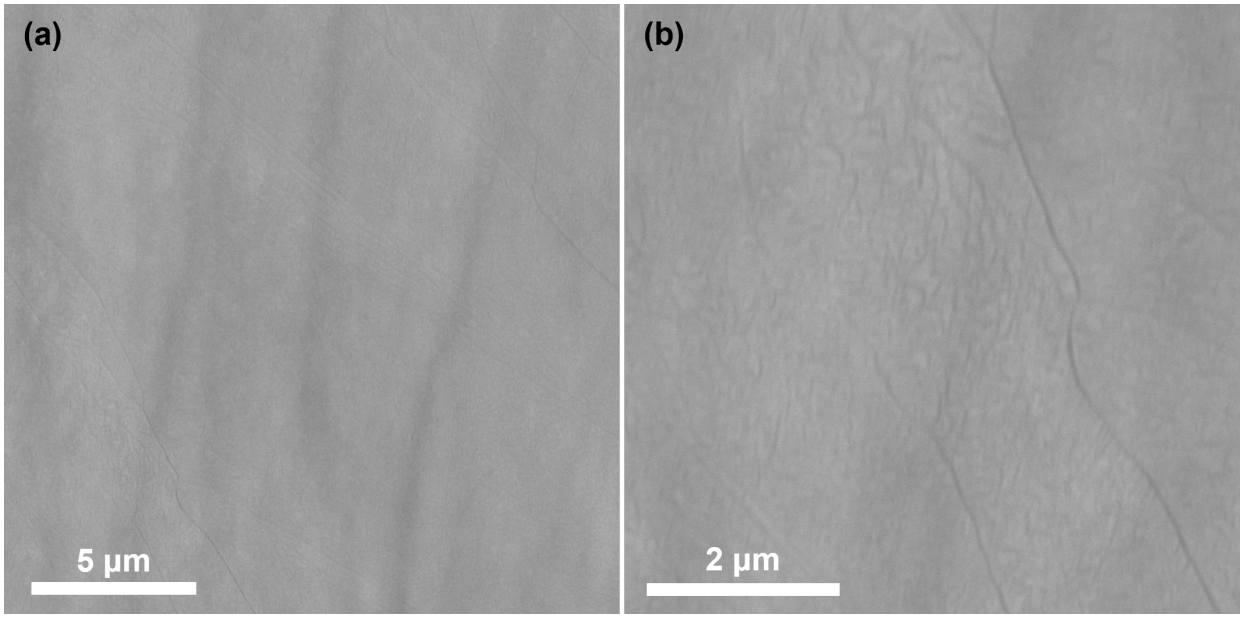

Figure C.12: BSE-SEM photomicrographs of 6 h aged TCFA at (a) lower magnification and (b) higher magnification, where darker α-phase precipitates are visible in a lighter β-phase matrix. Curtaining from the ion-milling process is visible in the lower magnification image.

APPENDIX D

FRACTURE SURFACES OF TENSILE-TESTED ALLOYS

Fracture surfaces of tensile-tested samples of TC, TCF, TCA, and TCFA. SE SEM photomicrographs of tensile-tested samples of TC after 1.5, 3, 6, and 12 h of 400 °C aging are provided in Figures D.1 through D.4. SE-SEM photomicrographs of tensile-tested samples of TCF after 1.5, 3, 6, and 12 h of 400 °C aging are provided in Figures D.5 through D.8. SE-SEM photomicrographs of tensile-tested samples of TCA after 1.5, 3, 6, and 12 h of 400 °C aging are provided in Figures D.9 through D.12. SE SEM photomicrographs of tensile-tested samples of TCFA after 0.75, 1.5, 6, and 12 h of 400 °C aging are provided in Figures D.13 through D.16.

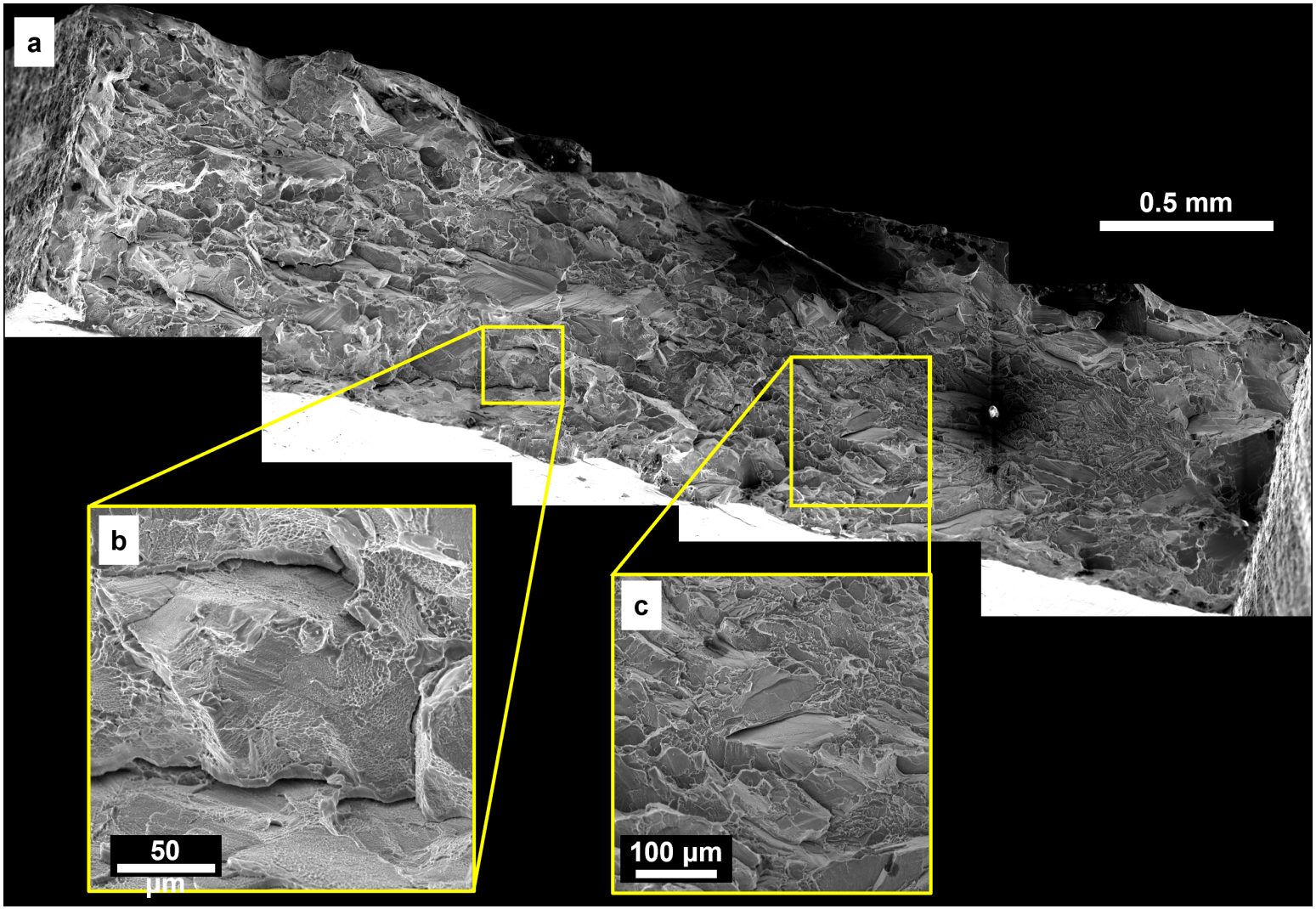

Figure D.1: (a) SE-SEM photomicrograph of the fracture surface from a TC tensile test sample aged 400 °C for 1.5 h, stitched together using multiple photomicrographs. (b, c) Higher magnification SE SEM photomicrographs illustrating mixed-mode failure including intergranular cracks and dimples.

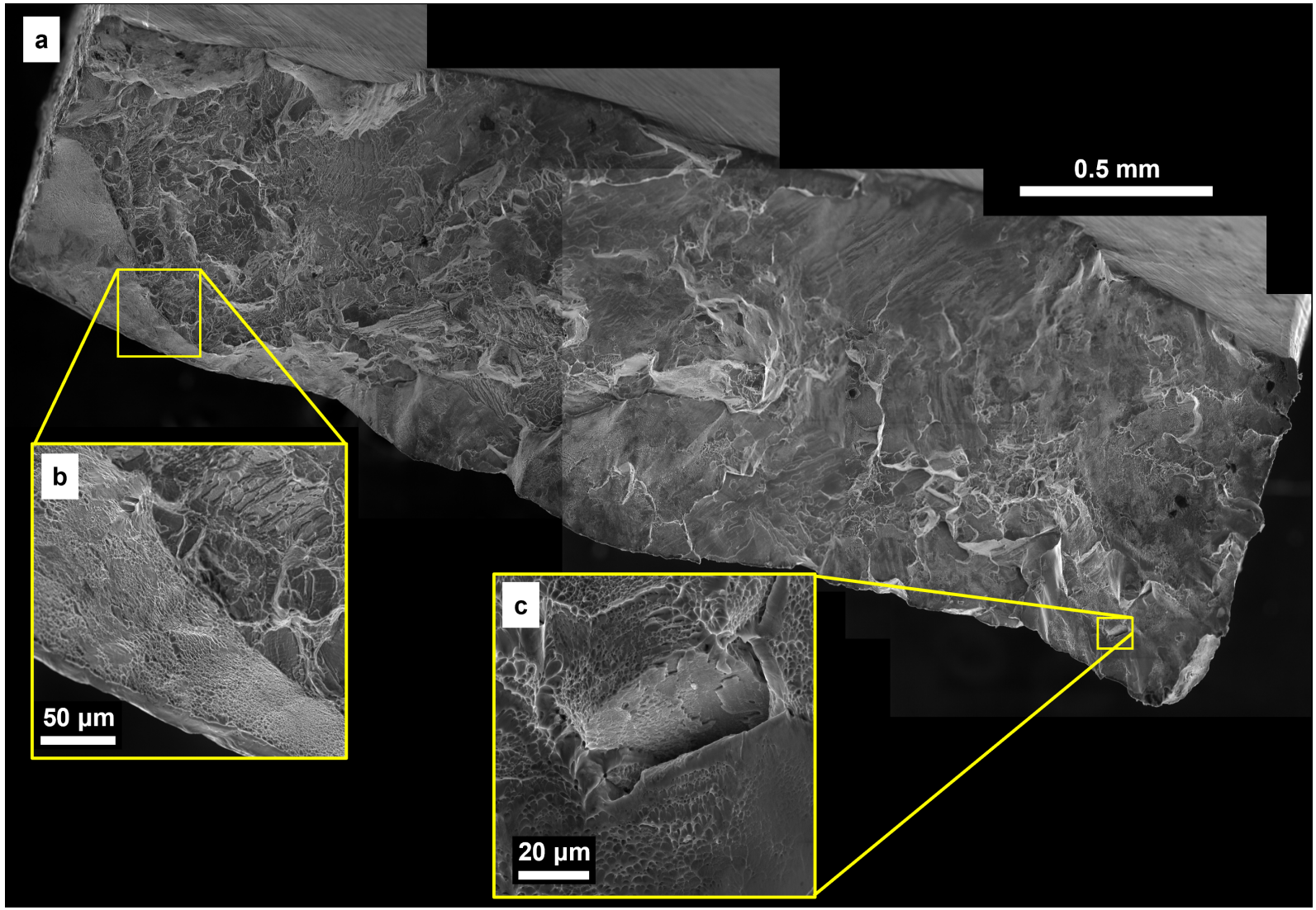

Figure D.2: (a) SE-SEM photomicrograph of the fracture surface from a TC tensile test sample aged 400 °C for 3 h, stitched together using multiple photomicrographs. (b, c) Higher magnification SE SEM photomicrographs illustrating mixed-mode failure including intergranular cracks and dimples.

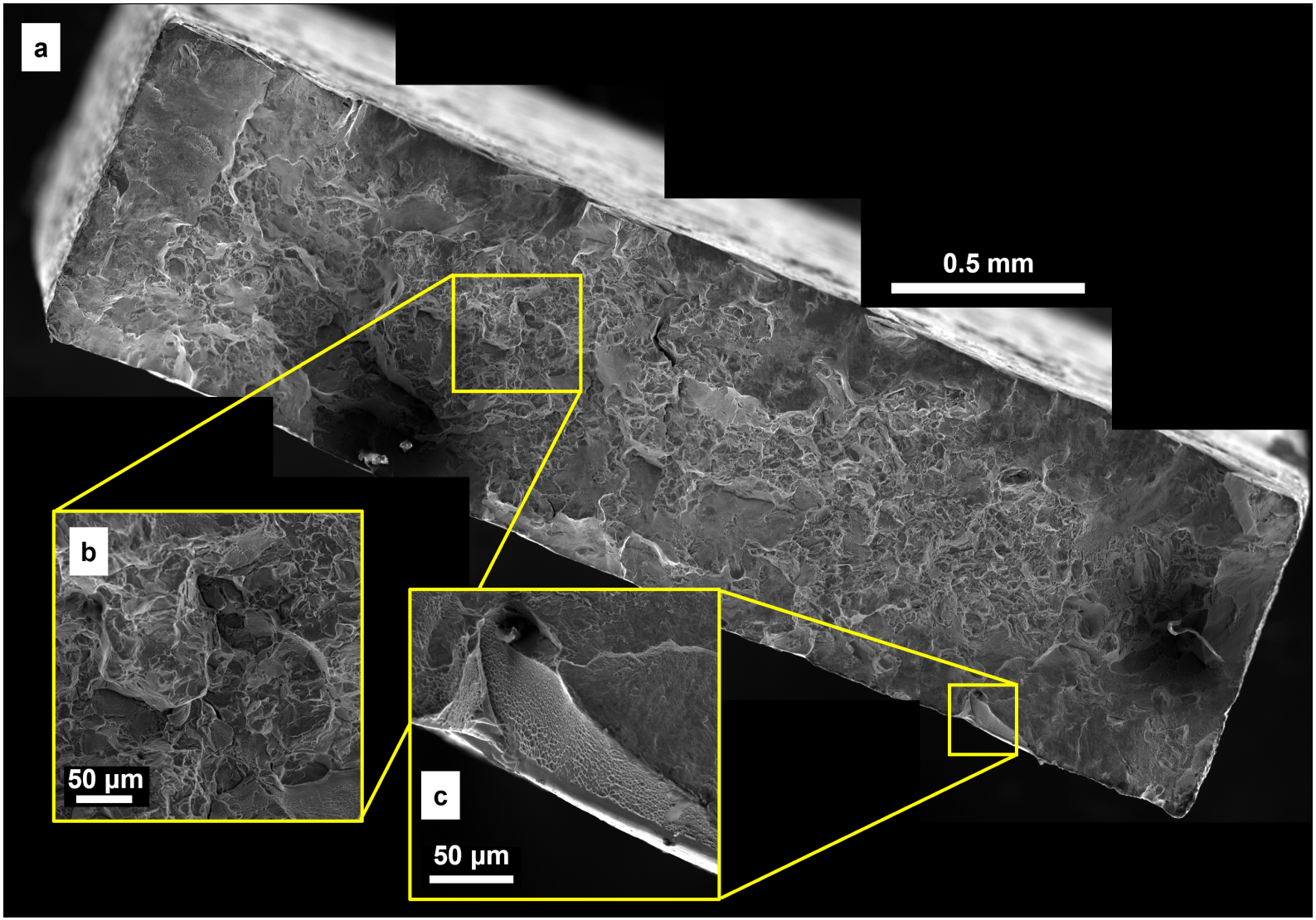

Figure D.3: (a) SE-SEM photomicrograph of the fracture surface from a TC tensile test sample aged 400 °C for 6 h, stitched together using multiple photomicrographs. (b, c) Higher magnification SE SEM photomicrographs illustrating mixed-mode failure including intergranular cracks and dimples.

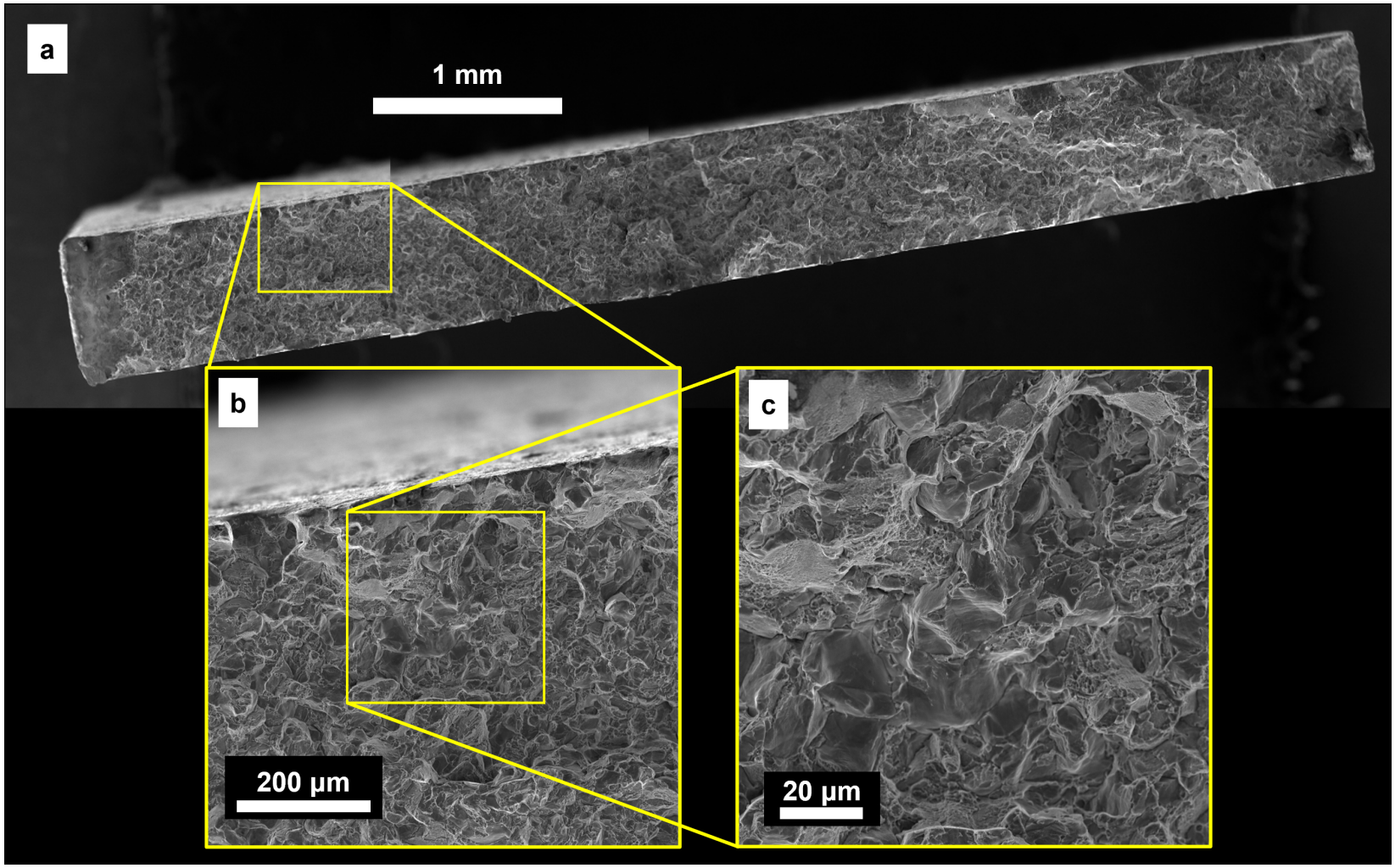

Figure D.4: (a) SE-SEM photomicrograph of the fracture surface from a TC tensile test sample aged 400 °C for 12 h, stitched together using multiple photomicrographs. (b, c) Higher magnification SE SEM photomicrographs illustrating mixed-mode failure including intergranular cracks and dimples.

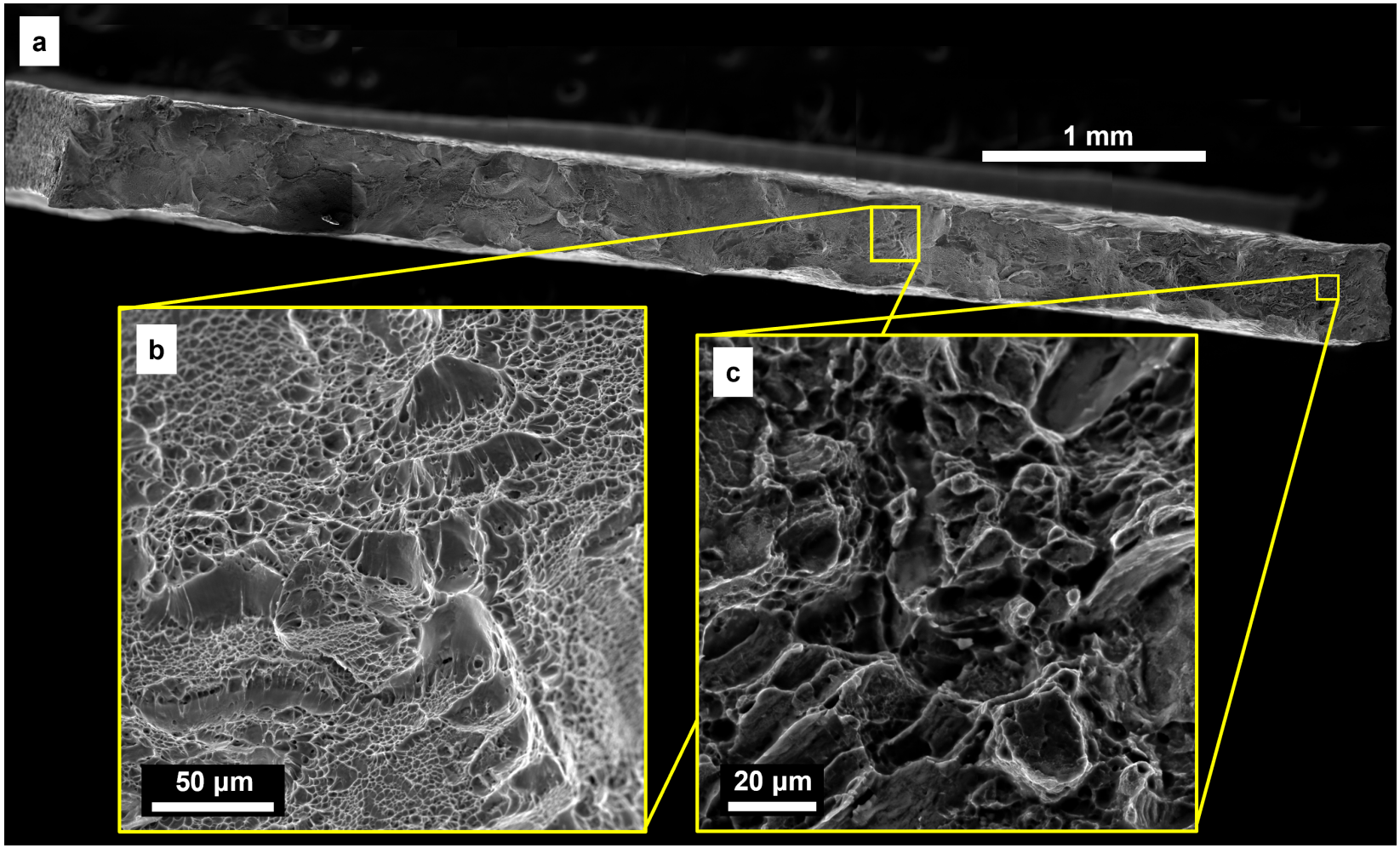

Figure D.5: (a) SE-SEM photomicrograph of the fracture surface from a TCF tensile test sample aged 400 °C for 1.5 h, stitched together using multiple photomicrographs. (b, c) Higher magnification SE SEM photomicrographs illustrating mixed-mode failure including dimples and precipitates.

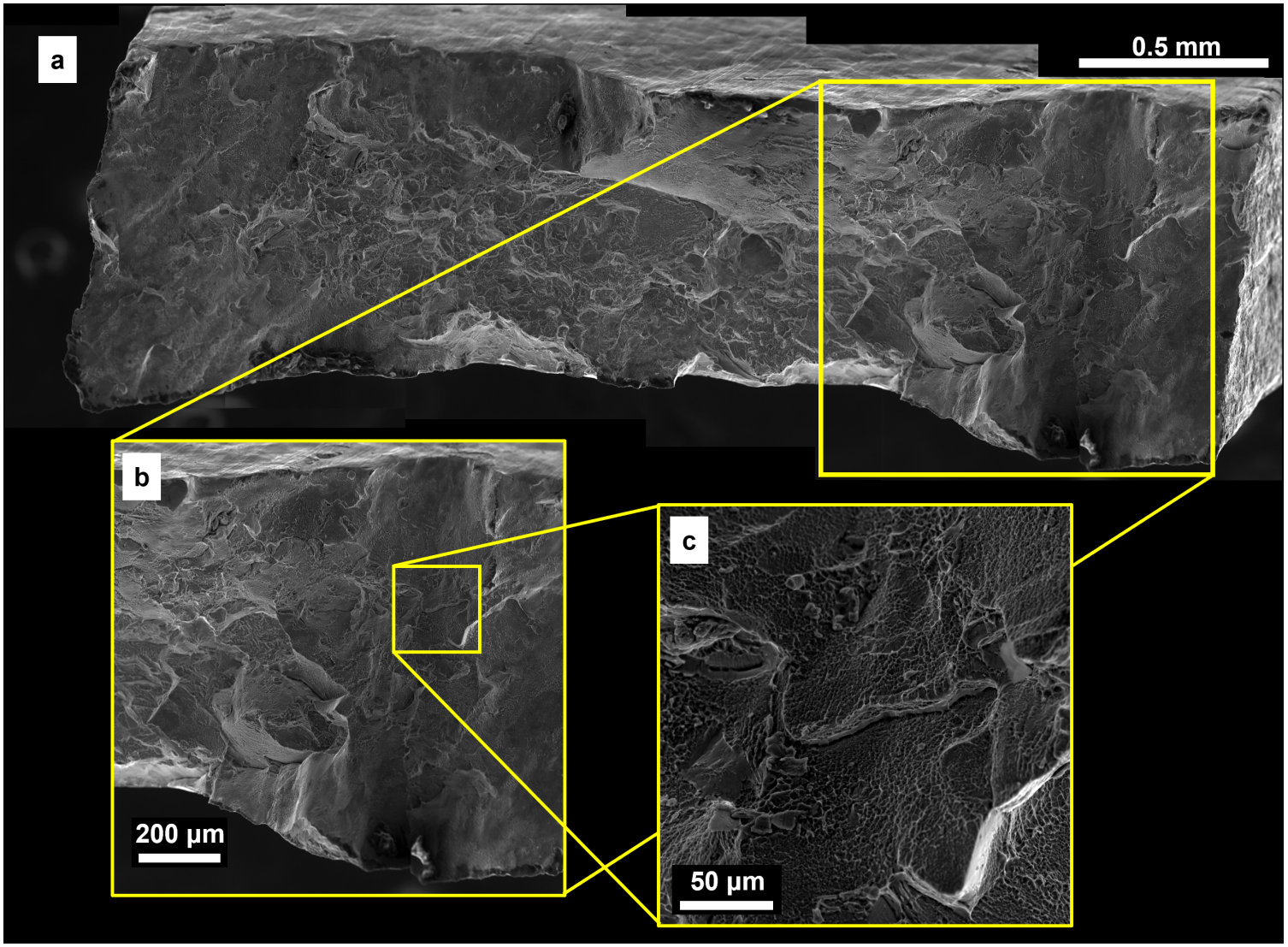

Figure D.6: (a) SE-SEM photomicrograph of the fracture surface from a TCF tensile test sample aged 400 °C for 3 h, stitched together using multiple photomicrographs. (b, c) Higher magnification SE SEM photomicrographs illustrating mixed-mode failure including intergranular cracks and dimples.

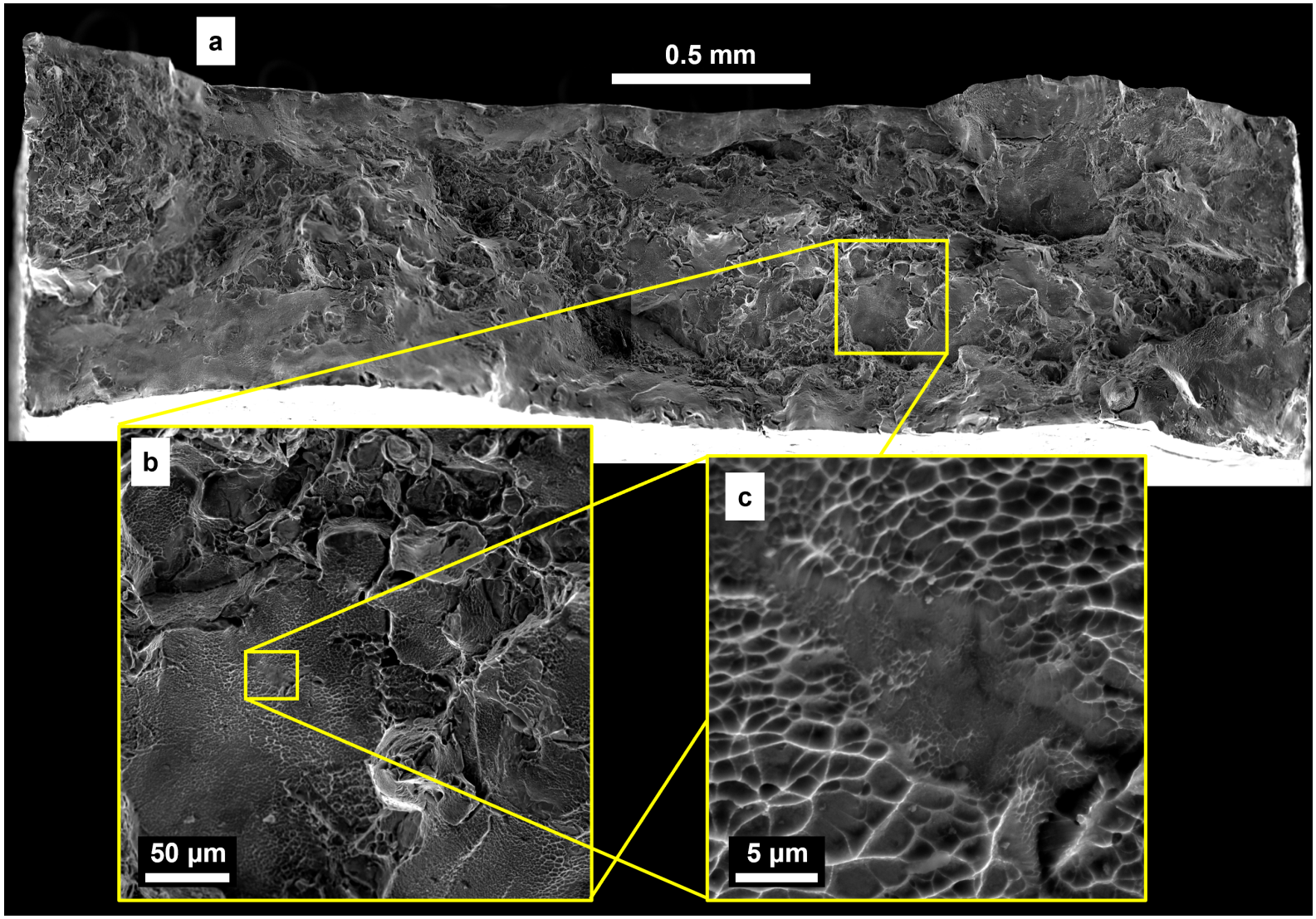

Figure D.7: (a) SE-SEM photomicrograph of the fracture surface from a TCF tensile test sample aged 400 °C for 6 h, stitched together using multiple photomicrographs. (b, c) Higher magnification SE SEM photomicrographs illustrating mixed-mode failure including intergranular cracks, dimples, and a possible α-phase feature.

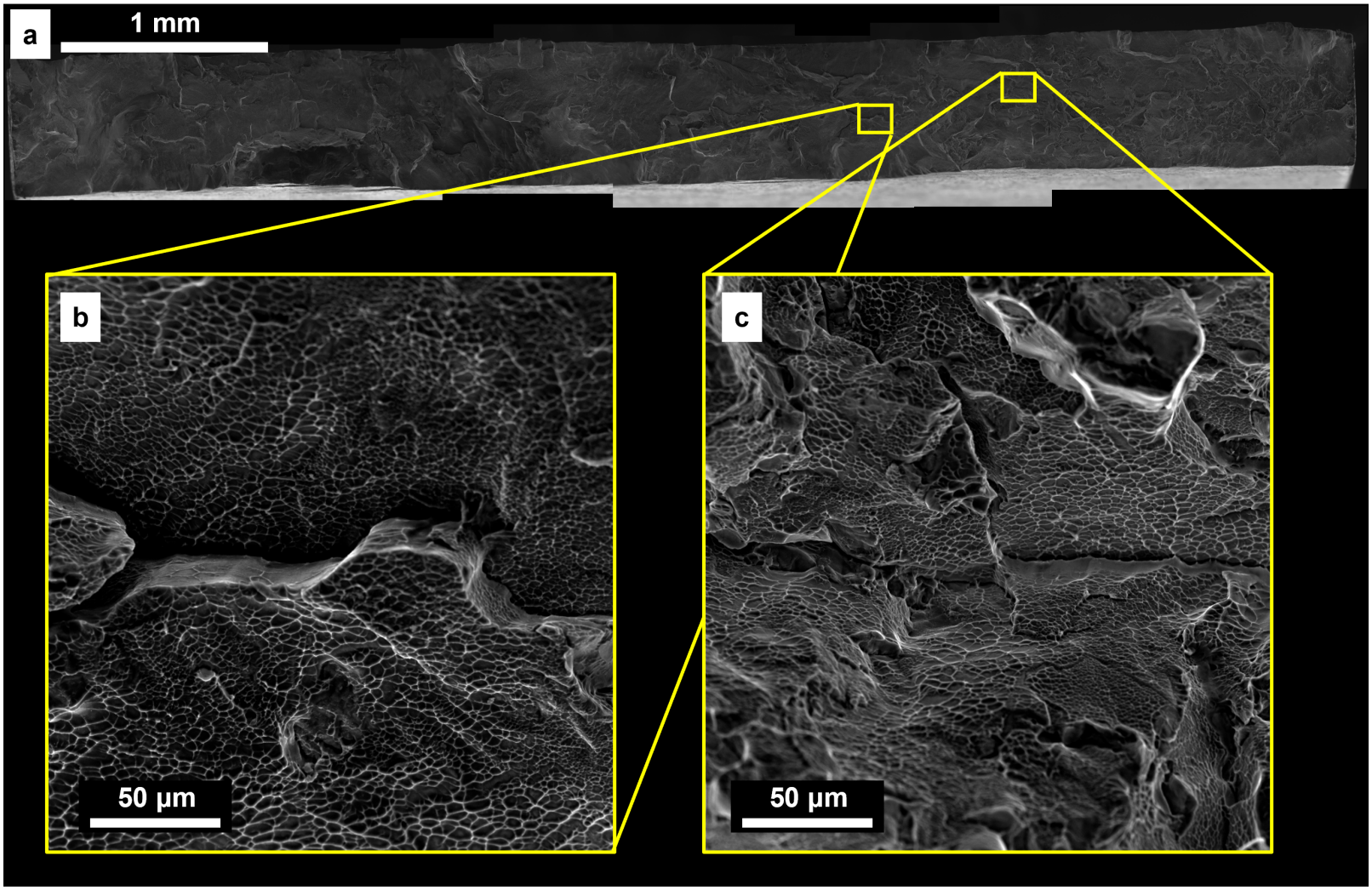

Figure D.8: (a) SE-SEM photomicrograph of the fracture surface from a TCF tensile test sample aged at 400 °C for 12 h, stitched together using multiple photomicrographs. (b, c) Higher magnification SE SEM photomicrographs illustrating mixed-mode failure including intergranular cracks and dimples.

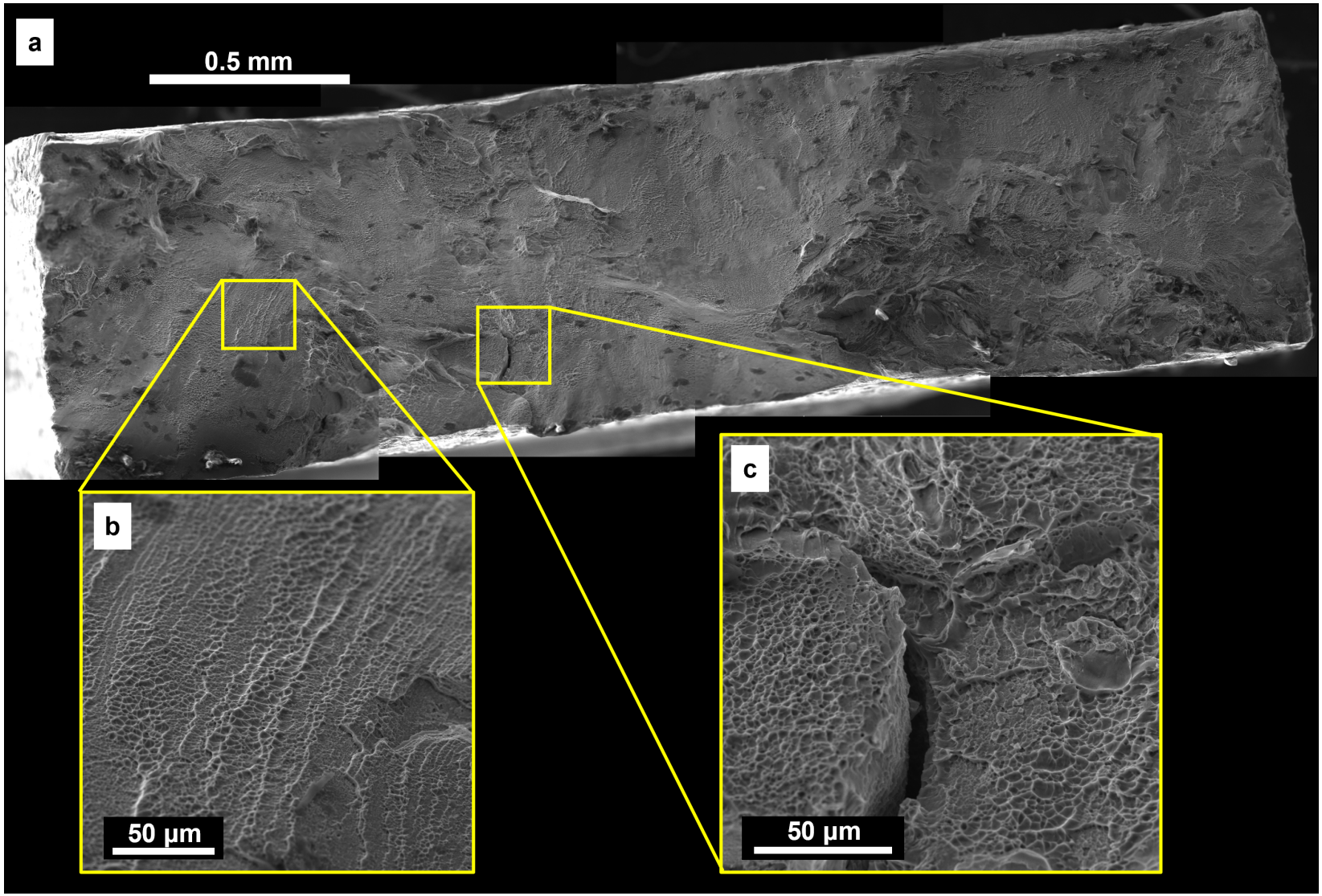

Figure D.9: (a) SE-SEM photomicrograph of the fracture surface from a TCA tensile test sample aged at 400 °C for 0.75 h, stitched together using multiple photomicrographs. Higher magnification SE SEM photomicrographs illustrating (b) dimples on a cleavage facet and (c) a crack and dimples.

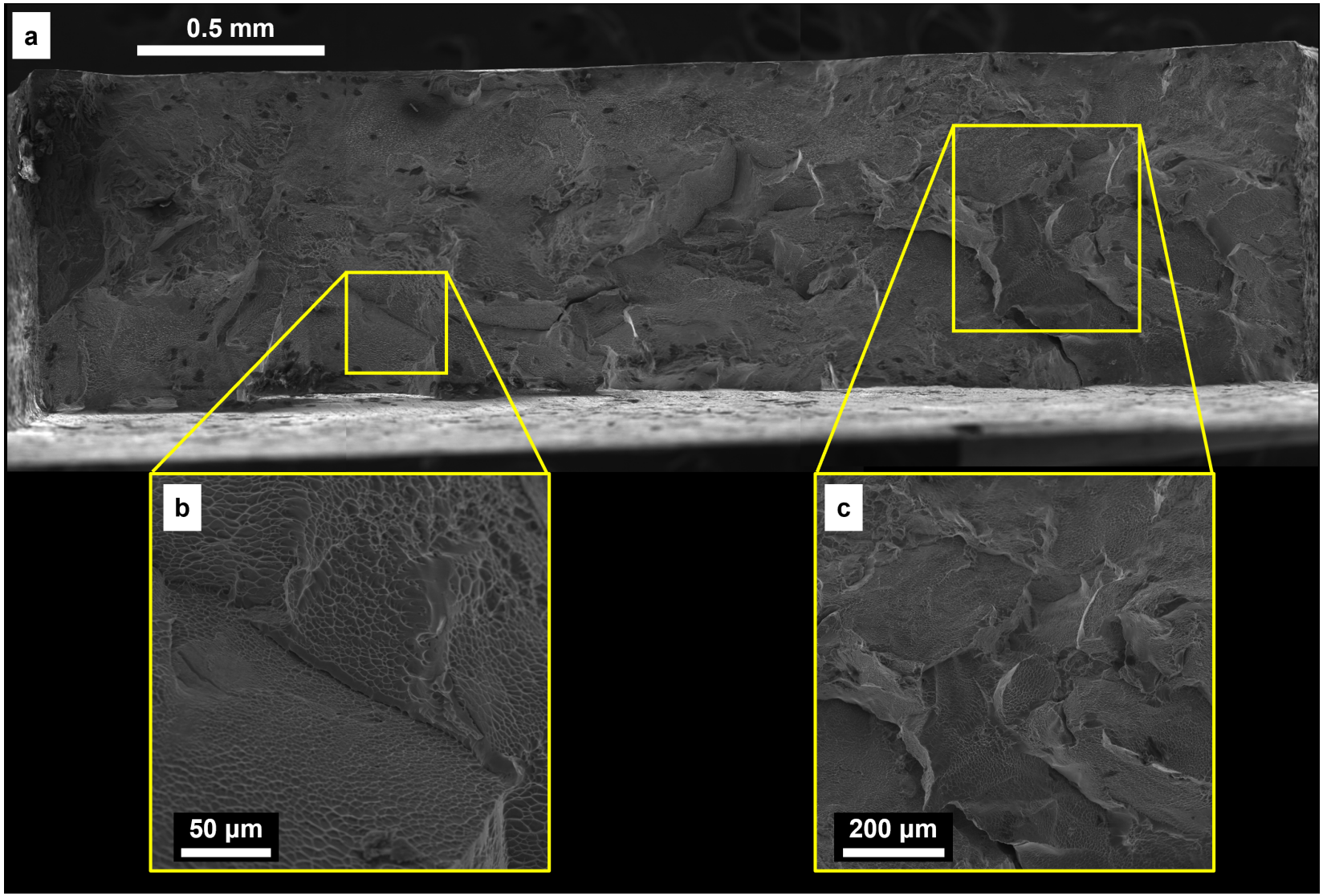

Figure D.10: (a) SE-SEM photomicrograph of the fracture surface from a TCA tensile test sample aged at 400 °C for 3 h, stitched together using multiple photomicrographs. (b, c) Higher magnification SE SEM photomicrographs illustrating mixed-mode failure including a lamellar-like feature, intergranular cracks, and dimples.

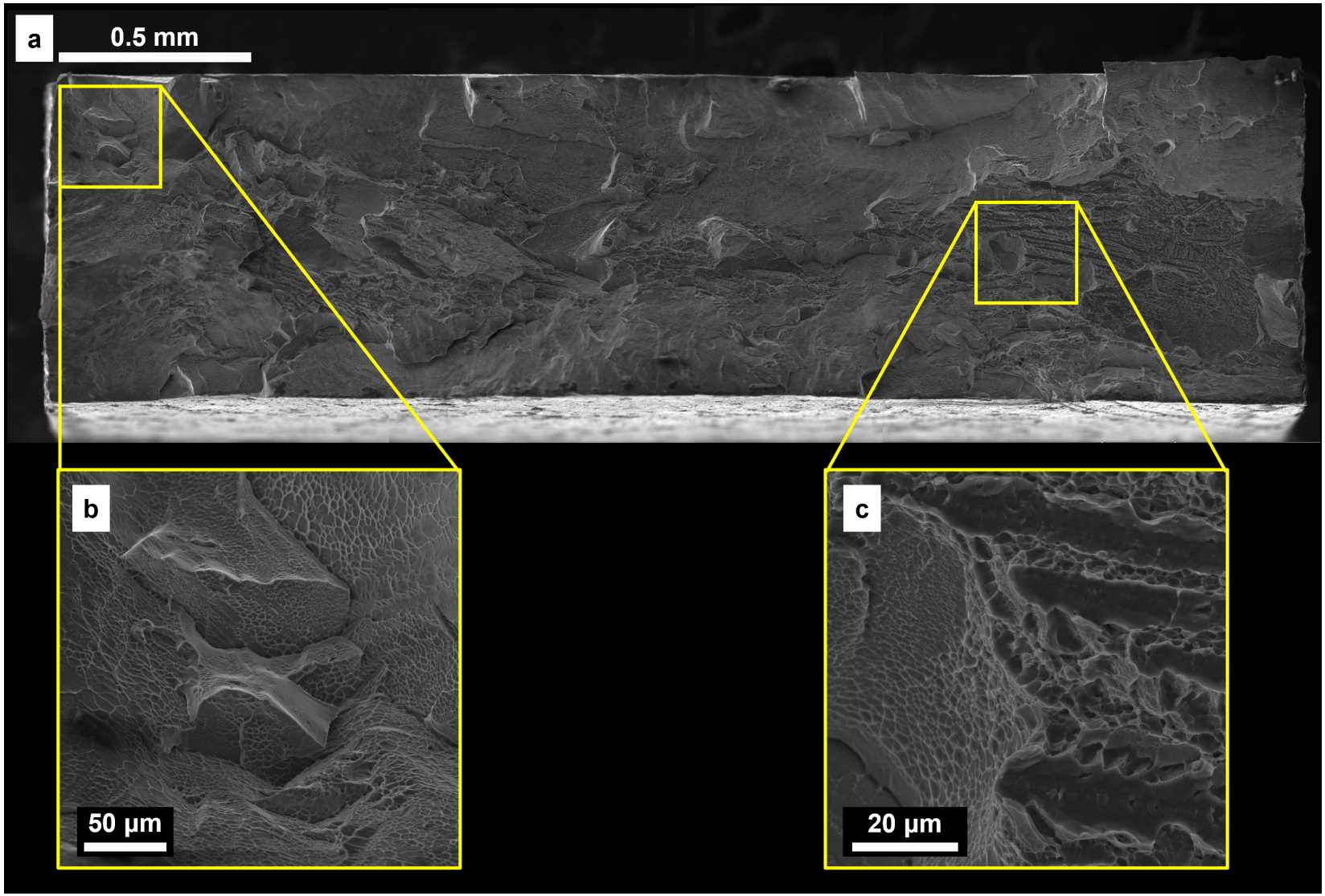

Figure D.11: (a) SE-SEM photomicrograph of the fracture surface from a TCA tensile test sample aged at 400 °C for 6 h, stitched together using multiple photomicrographs. (b, c) Higher magnification SE SEM photomicrographs illustrating mixed-mode failure including dimples and features that could be larger α-phase precipitates pulled away from the β matrix.

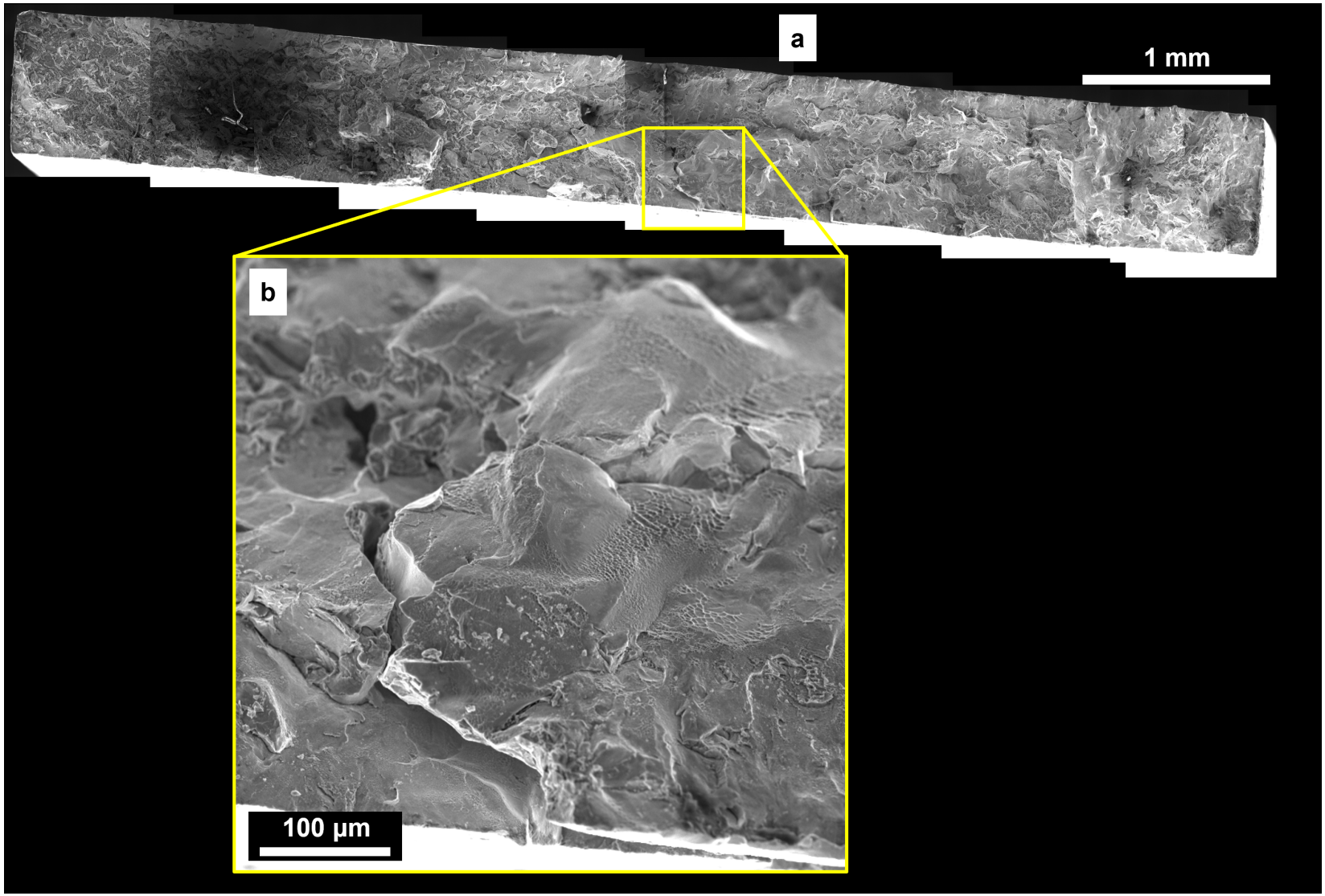

Figure D.12: (a) SE-SEM photomicrograph of the fracture surface from a TCA tensile test sample aged at 400 °C for 12 h, stitched together using multiple photomicrographs. (b) Higher magnification SE SEM photomicrographs illustrating mixed-mode failure including intergranular cracks and dimples.

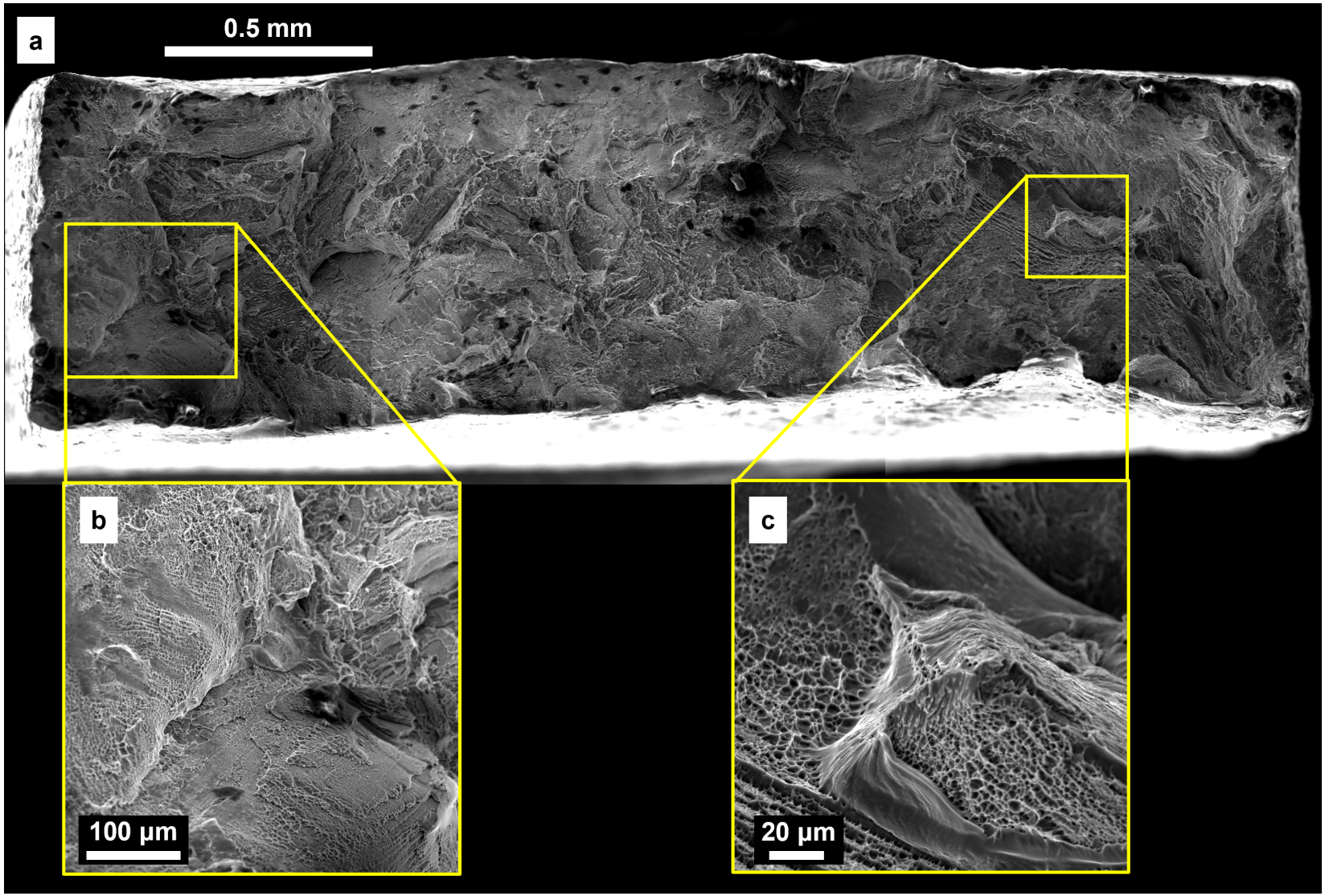

Figure D.13: (a) SE-SEM photomicrograph of the fracture surface from a TCFA tensile test sample aged at 400 °C for 0.75 h, stitched together using multiple photomicrographs. (b, c) Higher magnification SE SEM photomicrographs illustrating mixed-mode failure including dimples, tearing, and ledges.

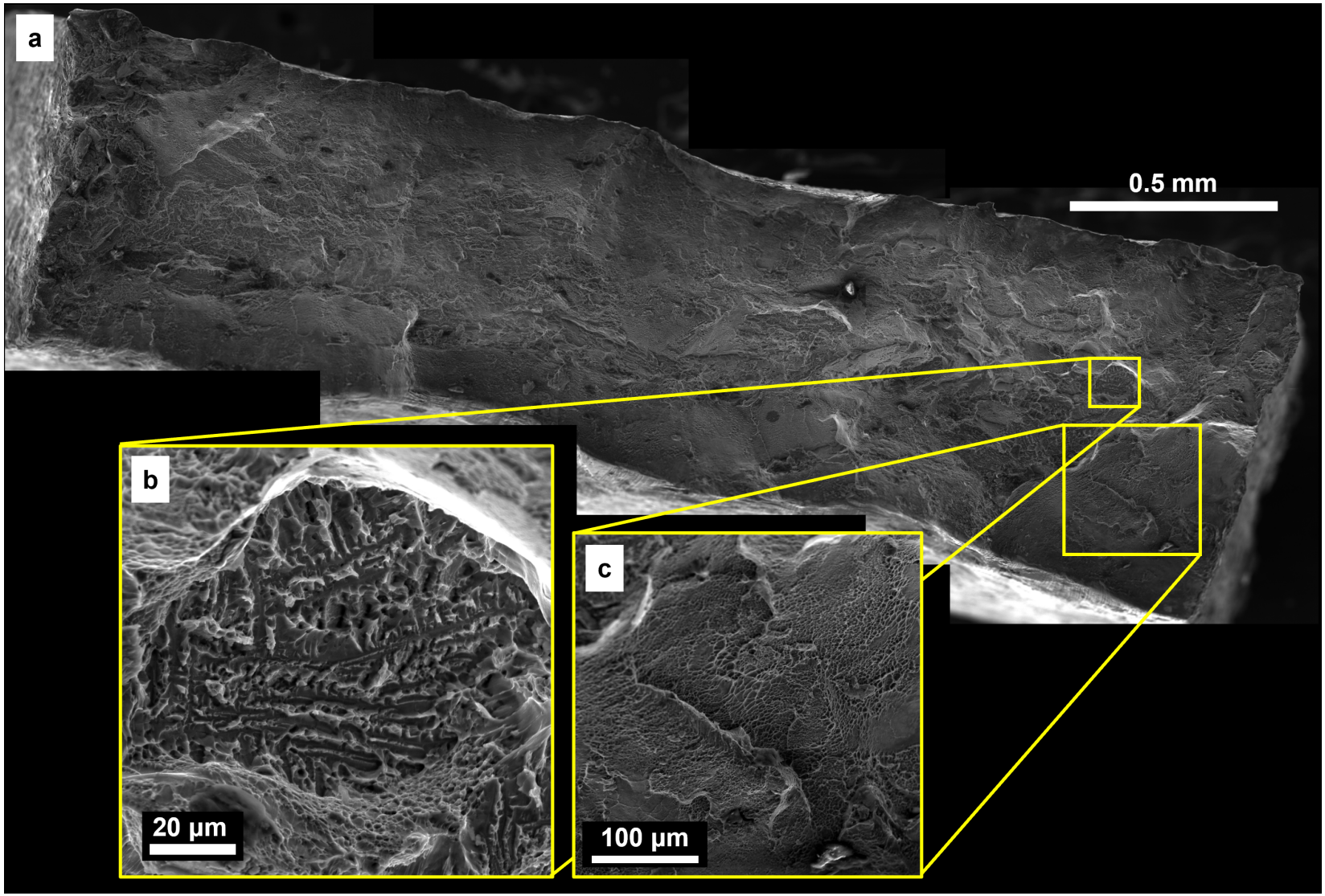

Figure D.14: (a) SE-SEM photomicrograph of the fracture surface from a TCFA tensile test sample aged at 400 °C for 1.5 h, stitched together using multiple photomicrographs. (b) Higher magnification SE SEM photomicrograph showing larger α precipitates pulled away from the more ductile β matrix, and (c) higher magnification SE SEM photomicrograph illustrating dimples and tearing.

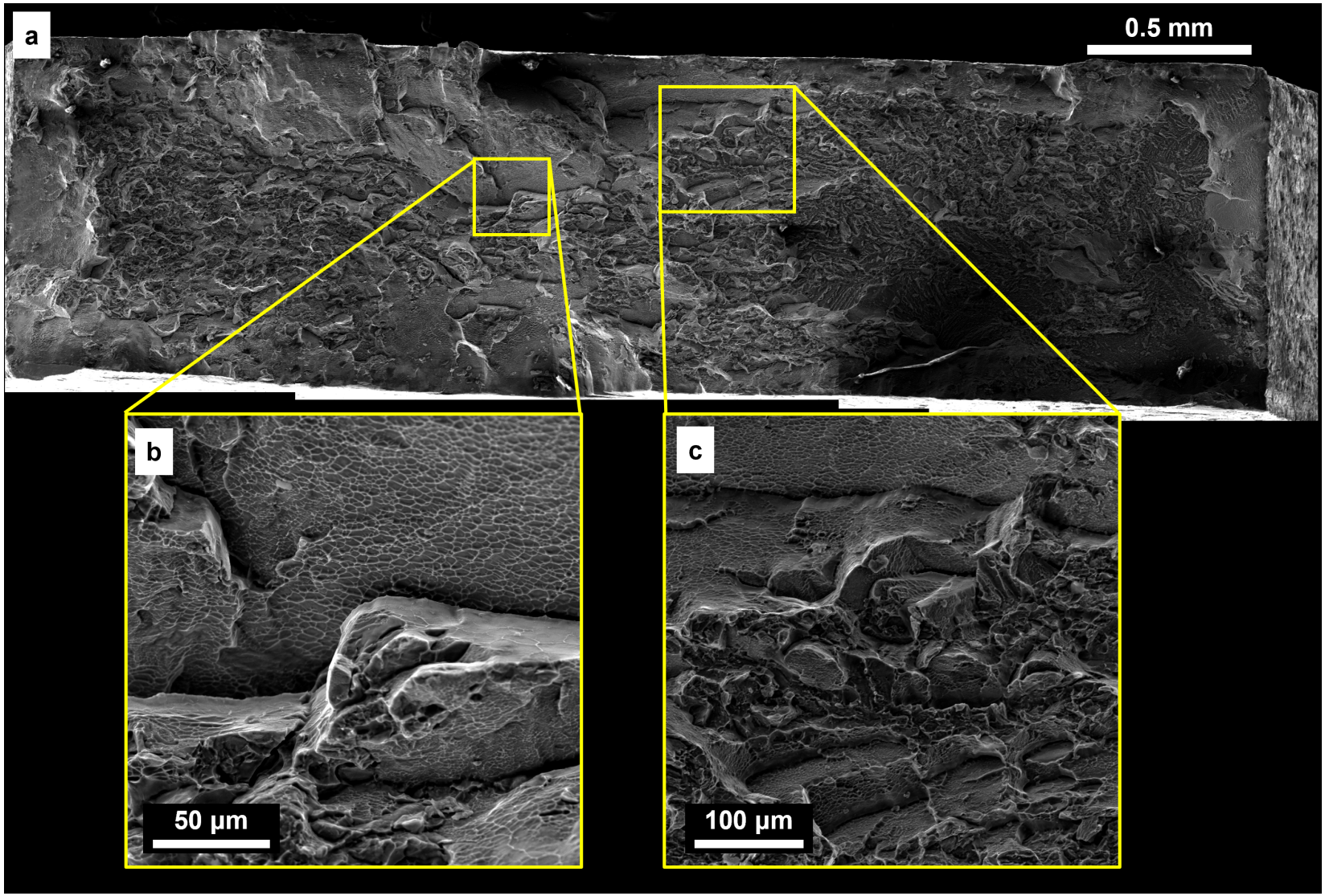

Figure D.15: (a) SE-SEM photomicrograph of the fracture surface from a TCFA tensile test sample aged at 400 °C for 6 h, stitched together using multiple photomicrographs. (b, c) Higher magnification SE SEM photomicrographs illustrating intergranular fracture and dimples.

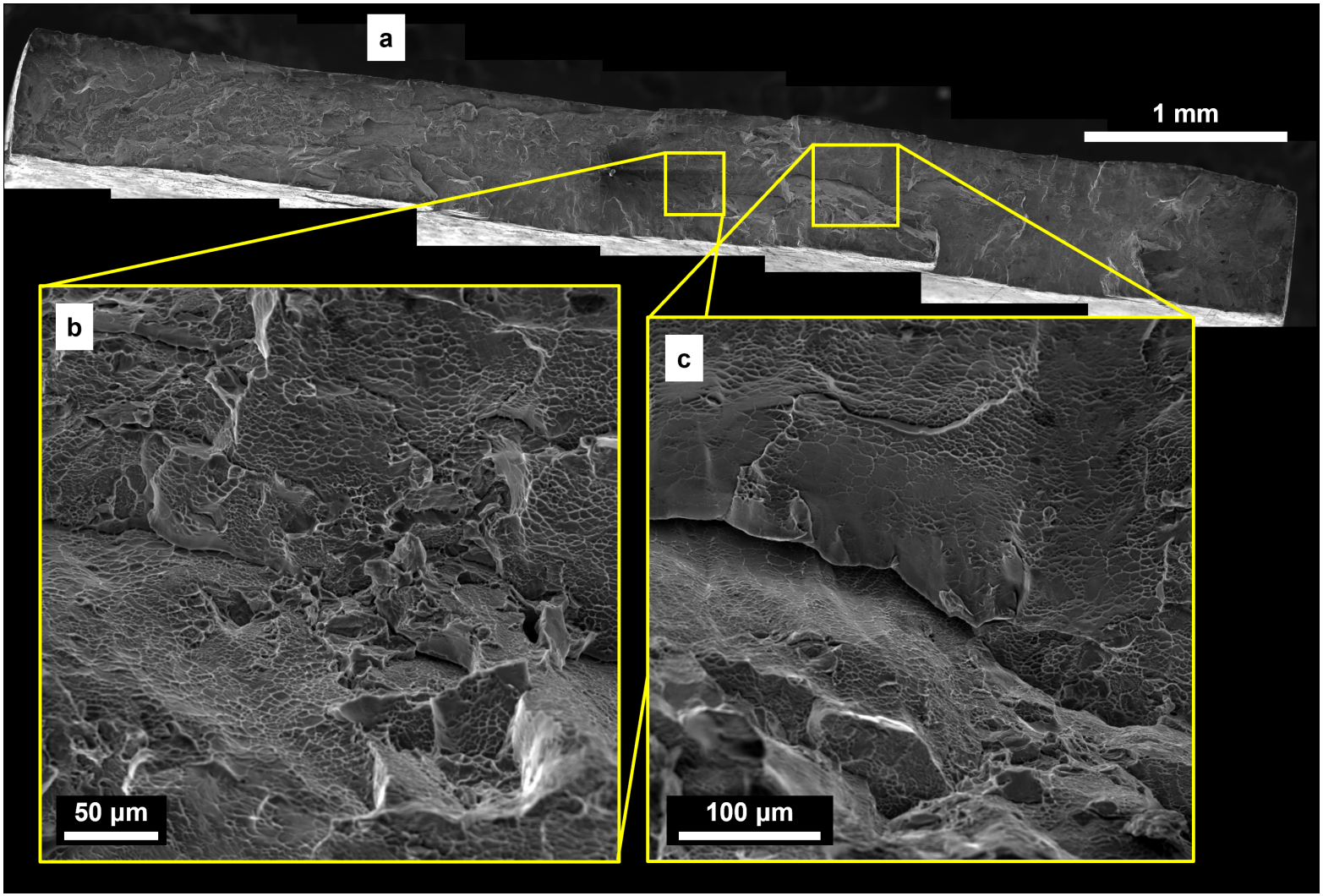

Figure D.16: (a) SE-SEM photomicrograph of the fracture surface from a TCFA tensile test sample aged at 400 °C for 12 h, stitched together using multiple photomicrographs. (b, c) Higher magnification SE SEM photomicrographs illustrating intergranular fracture and dimples.

BIBLIOGRAPHY

BIBLIOGRAPHY

[1] J. P. Immarigeon, R. T. Holt, A. K. Koul, L. Zhao, W. Wallace, and J. C. Beddoes. Lightweight materials for aircraft applications. *Materials Characterization*, 35(1):41–67, 1995.

[2] James D. Cotton, Robert D. Briggs, Rodney R. Boyer, Sesh Tamirisakandala, Patrick Russo, Nikolay Shchetnikov, and John C. Fanning. State of the Art in Beta Titanium Alloys for Airframe Applications. *JOM*, 67(6):1281–1303, June 2015.

[3] R. Kolli and Arun Devaraj. A Review of Metastable Beta Titanium Alloys. *Metals*, 8(7):506, June 2018.

[4] Arun Devaraj, Vineet V. Joshi, Ankit Srivastava, Sandeep Manandhar, Vladimir Moxson, Volodymyr A. Duz, and Curt Lavender. A low-cost hierarchical nanostructured beta-titanium alloy with high strength. *Nature Communications*, 7(1):11176, September 2016.

[5] Mitsuo Niinomi and Carl J. Boehlert. Titanium Alloys for Biomedical Applications. In Mitsuo Niinomi, Takayuki Narushima, and Masaaki Nakai, editors, *Advances in Metallic Biomaterials: Tissues, Materials and Biological Reactions*, pages 179–213. Springer Berlin Heidelberg, Berlin, Heidelberg, 2015.

[6] The Nation's Older Population Is Still Growing, Census Bureau Reports. *Press Release CB17-100*, June 2017.

[7] G Lütjering and J. C. Williams. *Titanium*. Springer, Berlin, 2 edition, 2007.

[8] R. Boyer, G. Welsch, and E. W. Collings. *Materials properties handbook: titanium alloys*. ASM International, Materials Park, Ohio, 4 edition, 2007.

[9] Yufeng Zheng, Robert E.A. Williams, Dong Wang, Rongpei Shi, Soumya Nag, Pavani Kami, John M. Sosa, Rajarshi Banerjee, Yunzhi Wang, and Hamish L. Fraser. Role of ω phase in the formation of extremely refined intragranular α precipitates in metastable β-titanium alloys. *Acta Materialia*, 103:850–858, January 2016.

[10] Tong Li, Damon Kent, Gang Sha, Hongwei Liu, Suzana G. Fries, Anna V. Ceguerra, Matthew S. Dargusch, and Julie M. Cairney. Nucleation driving force for ω-assisted formation of α and associated ω morphology in β-Ti alloys. *Scripta Materialia*, 155:149–154, October 2018.

[11] Rodney R. Boyer and Robert D. Briggs. The Use of β Titanium Alloys in the Aerospace Industry.

[12] S.L. Nyakana, J.C. Fanning, and R.R. Boyer. Quick Reference Guide for β Titanium Alloys in the 00s. *Journal of Materials Engineering and Performance*, 14(6):799–811, December 2005.

[13] K. Faller and F. H. (Sam) Froes. The use of titanium in family automobiles: Current trends. *JOM*, 53(4):27–28, April 2001.

[14] A.R. Morris. The use of titanium tubes in MSF desalination plants. *Desalination*, 31(1-3):387, October 1979.

[15] F. H. Froes, H. Friedrich, J. Kiese, and D. Bergoint. Titanium in the family automobile: The cost challenge. *JOM*, 56(2):40–44, February 2004.

[16] W.F. Smith. *Structure and Properties of Engineering Alloys*. McGraw-Hill, New York, 2 edition, 1993.

[17] Paul J. Bania. Beta titanium alloys and their role in the titanium industry. *JOM*, 46(7):16–19, July 1994.

[18] Cecil G Rhodes and James C Williams. The Precipitation of of α-Phase in Metastable β-Phase Ti Alloys. *Metallurgical Transactions A*, 6A:2103–2114, 1975.

[19] S Malinov, W Sha, and P Markovsky. Experimental study and computer modelling of the b⇒a1b phase transformation in b21s alloy at isothermal conditions. *Journal of Alloys and Compounds*, page 9, 2003.

[20] M. Naveen, R. Santhosh, M. Geetha, and M. Nageswara Rao. Experimental study and computer modelling of the β -> α + β phase transformation in Ti15-3 alloy under isothermal conditions. *Journal of Alloys and Compounds*, 616:607–613, December 2014.

[21] A J Williams, R W Cahn, and C S Barrett. The Crystallography of the β-α Transformation in Titanium. *Acta Metallurgica*, 2:117–128, January 1954.

[22] Hongmei Li. *Analysis of the deformation behavior of the hexagonal close-packed alpha phase in titanium and titanium alloys*. Doctor of Philosophy, Michigan State University, 2013.

[23] Shanoob Balachandran, Ankush Kashiwar, Abhik Choudhury, Dipankar Banerjee, Rongpei Shi, and Yunzhi Wang. On variant distribution and coarsening behavior of the α phase in a metastable β titanium alloy. *Acta Materialia*, 106:374–387, March 2016.

[24] Yufeng Zheng, Robert E.A. Williams, John M. Sosa, Talukder Alam, Yunzhi Wang, Rajarshi Banerjee, and Hamish L. Fraser. The indirect influence of the ω phase on the degree of refinement of distributions of the α phase in metastable β-Titanium alloys. *Acta Materialia*, 103:165–173, 2016.

[25] N.G. Jones, R.J. Dashwood, M. Jackson, and D. Dye. β Phase decomposition in Ti–5Al–5Mo–5V–3Cr. *Acta Materialia*, 57(13):3830–3839, August 2009.

[26] Harold Alexander, John B. Brunski, Stuart L. Cooper, Larry L. Hench, Robert W. Hergenrother, Allan S. Hoffman, Joachim Kohn, Robert Langer, Nikolaos A. Peppas, Buddy D. Ratner, Shalaby W. Shalaby, Susan A. Visser, and Ioannis V. Yannas. CHAPTER 2 - Classes of Materials Used in Medicine. In Buddy D. Ratner, Allan S. Hoffman, Frederick J. Schoen,

and Jack E. Lemons, editors, *Biomaterials Science*, pages 37–130. Academic Press, San Diego, January 1996.

[27] S. Sadeghpour, S.M. Abbasi, M. Morakabati, and S. Bruschi. Correlation between alpha phase morphology and tensile properties of a new beta titanium alloy. *Materials & Design*, 121:24–35, May 2017.

[28] Shun Guo, Qing-Kun Meng, Hong-Ping Li, and Xin-Qing Zhao. Direct evidence for competition between metastable ω and equilibrium α phases in aged β-type Ti alloys. *Rare Metals*, 33(4):390–393, August 2014.

[29] P. D. Frost, W. M. Parris, L. L. Hirsch, J. R. Doig, and C. M. Schwartz. Isothermal transformation of titanium-chromium alloys. *Trans. Amer. Soc. metals*, 46:231–256, 1954.

[30] J. C. Jamieson. Crystal Structures of Titanium, Zirconium, and Hafnium at High Pressures. *Science*, 140(3562):72–73, 1963.

[31] Yogesh K. Vohra and Philemon T. Spencer. Novel γ -Phase of Titanium Metal at Megabar Pressures. *Physical Review Letters*, 86(14):3068–3071, April 2001.

[32] L.M. Hsiung and D.H. Lassila. Shock-induced deformation twinning and omega transformation in tantalum and tantalum–tungsten alloys. *Acta Materialia*, 48(20):4851–4865, December 2000.

[33] B. S. Hickman. The formation of omega phase in titanium and zirconium alloys: A review. *Journal of Materials Science*, 4(6):554–563, June 1969.

[34] S.K. Sikka, Y.K. Vohra, and R. Chidambaram. Omega phase in materials. *Progress in Materials Science*, 27(3-4):245–310, January 1982.

[35] J. M. Silcock, M. H. Davies, and H. K. Hardy. Structure of the ω-Precipitate in Titanium–16 per cent Vanadium Alloy. *Nature*, 175(4460):731, 1955.

[36] R. Prakash Kolli, William J. Joost, and Sreeramamurthy Ankem. Phase Stability and Stress-Induced Transformations in Beta Titanium Alloys. *JOM*, 67(6):1273–1280, June 2015.

[37] J. C. Williams, D. de Fontaine, and N. E. Paton. The ω-Phase as an Example of an Unusual Shear Transformation. *Metallurgical Transactions*, 4:2701–2708, 1973.

[38] D. de Fontaine and Otto Buck. A Monte Carlo simulation of the omega phase transformation. *Philosophical Magazine*, 27(4):967–983, April 1973.

[39] A. Devaraj, S. Nag, R. Srinivasan, R.E.A. Williams, S. Banerjee, R. Banerjee, and H.L. Fraser. Experimental evidence of concurrent compositional and structural instabilities leading to ω precipitation in titanium–molybdenum alloys. *Acta Materialia*, 60(2):596–609, January 2012.

[40] T. W. Duerig, G. T. Terlinde, and J. C. Williams. Phase transformations and tensile properties of Ti-10V-2Fe-3AI. *Metallurgical Transactions A*, 11(12):1987–1998, December 1980.

[41] Yasuya Ohmori, Toshitaka Ogo, Kiyomichi Nakai, and Sengo Kobayashi. Effects of ω-phase precipitation on β->α, α″ transformations in a metastable β titanium alloy. *Materials Science and Engineering A*, pages 182–188, 2001.

[42] Frédéric Prima, Philippe Vermaut, Denis Ansel, and Jean Debuigne. ω Precipitation in a Beta Metastable Titanium Alloy, Resistometric Study. *Materials Transactions, JIM*, 41(8):1092–1097, 2000.

[43] Tong Li, Damon Kent, Gang Sha, Leigh T. Stephenson, Anna V. Ceguerra, Simon P. Ringer, Matthew S. Dargusch, and Julie M. Cairney. New insights into the phase transformations to isothermal ω and ω-assisted α in near β-Ti alloys. *Acta Materialia*, 106:353–366, March 2016.

[44] Y.B. Wang, Y.H. Zhao, Q. Lian, X.Z. Liao, R.Z. Valiev, S.P. Ringer, Y.T. Zhu, and E.J. Lavernia. Grain size and reversible beta-to-omega phase transformation in a Ti alloy. *Scripta Materialia*, 63(6):613–616, September 2010.

[45] S. Nag, R. Banerjee, R. Srinivasan, J.Y. Hwang, M. Harper, and H.L. Fraser. ω-Assisted nucleation and growth of α precipitates in the Ti–5Al–5Mo–5V–3Cr–0.5Fe β titanium alloy. *Acta Materialia*, 57(7):2136–2147, April 2009.

[46] J.I. Qazi, B. Marquardt, L.F Allard, and H.J. Rack. Phase transformations in Ti–35Nb–7Zr–5Ta–(0.06–0.68)O alloys. *Materials Science and Engineering: C*, 25(3):389–397, May 2005.

[47] Tong Li, Damon Kent, Gang Sha, Matthew S. Dargusch, and Julie M. Cairney. The mechanism of ω-assisted α phase formation in near β-Ti alloys. *Scripta Materialia*, 104:75–78, July 2015.

[48] Xingfeng Zhao, Mitsuo Niinomi, Masaaki Nakai, and Junko Hieda. Effect of Deformation-Induced ω Phase on the Mechanical Properties of Metastable β-Type Ti-V Alloys. *Materials Transactions*, 53(8):1379–1384, 2012.

[49] Yufeng Zheng, Deep Choudhuri, Talukder Alam, Robert E.A. Williams, Rajarshi Banerjee, and Hamish L. Fraser. The role of cuboidal ω precipitates on α precipitation in a Ti-20V alloy. *Scripta Materialia*, 123:81–85, October 2016.

[50] Atsushi Yamamoto and Harushige Tsubakino. Convergent Beam Dark Field Imaging Technique with its Application to Observation of Multiphase Materials. *Materials Transactions, JIM*, 39(9):989–994, 1998.

[51] B A Hatt and J A Roberts. The w-phase in zirconium base alloys. *Acta Metallurgica*, 8:575–584, 1960.

[52] Alireza Samiee, Gilberto Casillas, Mansur Ahmed, Dmytro Savvakin, Ryan Naseri, and Elena Pereloma. Formation of Deformation-Induced Products in a Metastable-β Titanium Alloy during High Temperature Compression. *Metals*, 8(2):100, January 2018.

[53] M. J. Blackburn and J. C. Williams. Phase Transformations in Ti-Mo and Ti-V Alloys. *Transactions of the Metallurgical Society of AIME*, 242:2461–2469, 1968.

[54] Y Ohmori, H Natsui, and K Nakai. Crystallographic Analysis of α Phase Formation in a Metastable β Ti Alloy. *Materials Transactions, JIM*, 39(1):49–56, 1998.

[55] G. Aurelio and A. Fernández Guillermet. Interatomic distances of the hexagonal omega structure in Ti-V alloys: neutron diffraction study and analysis of bonding related regularities. *Scripta Materialia*, 43(7):665–669, September 2000.

[56] Matthias Bönisch, Ajit Panigrahi, Mihai Stoica, Mariana Calin, Eike Ahrens, Michael Zehetbauer, Werner Skrotzki, and Jürgen Eckert. Giant thermal expansion and α-precipitation pathways in Ti-alloys. *Nature Communications*, 8(1):1429, December 2017.

[57] Mansur Ahmed, Tong Li, Gilberto Casillas, Julie M. Cairney, David Wexler, and Elena V. Pereloma. The evolution of microstructure and mechanical properties of Ti–5Al–5Mo–5V–2Cr–1Fe during ageing. *Journal of Alloys and Compounds*, 629:260–273, April 2015.

[58] V. Chandrasekaran, R. Taggart, and D.H. Polonis. An electron microscopy study of the aged omega phase in Ti-Cr alloys. *Metallography*, 11(2):183–198, April 1978.

[59] F. Prima, P. Vermaut, G. Texier, D. Ansel, and T. Gloriant. Evidence of α-nanophase heterogeneous nucleation from ω particles in a β-metastable Ti-based alloy by high-resolution electron microscopy. *Scripta Materialia*, 54(4):645–648, February 2006.

[60] S. Nag, A. Devaraj, R. Srinivasan, R. E. A. Williams, N. Gupta, G. B. Viswanathan, J. S. Tiley, S. Banerjee, S. G. Srinivasan, H. L. Fraser, and R. Banerjee. Novel Mixed-Mode Phase Transition Involving a Composition-Dependent Displacive Component. *Physical Review Letters*, 106(24):245701, June 2011.

[61] Z. Fan and A. P. Miodownik. TEM study of metastable β-phase decomposition in rapidly solidified Ti-6AI-4V alloy. *Journal of Materials Science*, 29:6403–6412, 1994.

[62] Y.K. Vohra, S.K. Sikka, S.N. Vaidya, and R. Chidambaram. Impurity effects and reaction kinetics of the pressure-induced α -> ω transformation in Ti. *Journal of Physics and Chemistry of Solids*, 38(11):1293–1296, 1977.

[63] A. K. Singh, Murali Mohan, and C. Divakar. The kinetics of pressure-induced α->ω transformation in Ti. *Journal of Applied Physics*, 53(2):1221–1223, February 1982.

[64] D Errandonea, Y Meng, M Somayazulu, and D Hausermann. Pressure-induced α->ω transition in titanium metal: a systematic study of the effects of uniaxial stress. *Physica B*, 355:116–125, 2005.

[65] M. Arul Kumar, N. Hilairet, R.J. McCabe, T. Yu, Y. Wang, I.J. Beyerlein, and C.N. Tomé. Role of twinning on the omega-phase transformation and stability in zirconium. *Acta Materialia*, 185:211–217, February 2020.

[66] Qianglong Liang, Zachary Kloenne, Yufeng Zheng, Dong Wang, Stoichko Antonov, Yipeng Gao, Yulin Hao, Rui Yang, Yunzhi Wang, and Hamish L. Fraser. The role of nano-scaled structural non-uniformities on deformation twinning and stress-induced transformation in a cold rolled multifunctional β-titanium alloy. *Scripta Materialia*, 177:181–185, March 2020.

[67] Mansur Ahmed, David Wexler, Gilberto Casillas, Orest M. Ivasishin, and Elena V. Pereloma. The influence of β phase stability on deformation mode and compressive mechanical properties of Ti–10V–3Fe–3Al alloy. *Acta Materialia*, 84:124–135, February 2015.

[68] X.L. Wang, L. Li, W. Mei, W.L. Wang, and J. Sun. Dependence of stress-induced omega transition and mechanical twinning on phase stability in metastable β Ti–V alloys. *Materials Characterization*, 107:149–155, September 2015.

[69] H. Xing and J. Sun. Mechanical twinning and omega transition by ⟨111⟩ {112} shear in a metastable β titanium alloy. *Applied Physics Letters*, 93(3):031908, July 2008.

[70] A. Jaworski and S. Ankem. The Effect of α Phase on the Deformation Mechanisms of β Titanium Alloys. *Journal of Materials Engineering and Performance*, 14(6):755–760, December 2005.

[71] S Hanada and O Izumi. Correlation of Tensile Properties, Deformation Modes, and Phase Stability in Commercial/3-Phase Titanium Alloys. *Metallurgical Transactions A*, 18A:265–271, 1986.

[72] J. P. Guibert and C. Servant. Deformation Mechanisms in a βm Alloy. volume 8, Birmingham, 1995. Titanium 95 Science and Technology.

[73] Y Ivanisenko, A Kilamametov, H Rösner, and R.Z. Valiev. Evidence of α -> ω phase transition in titanium after high pressure torsion. *International Journal of Materials Research*, 99(1):36–41, 2008.

[74] Askar Kilmametov, Yulia Ivanisenko, Boris Straumal, Alena Gornakova, Andrey Mazilkin, and Horst Hahn. The α -> ω Transformation in Titanium-Cobalt Alloys under High-Pressure Torsion. *Metals*, 8(1):1, December 2017.

[75] A.R. Kilmametov, Yu. Ivanisenko, A.A. Mazilkin, B.B. Straumal, A.S. Gornakova, O.B. Fabrichnaya, M.J. Kriegel, D. Rafaja, and H. Hahn. The α->ω and β->ω phase transformations in Ti–Fe alloys under high-pressure torsion. *Acta Materialia*, 144:337–351, February 2018.

[76] Mario J. Kriegel, Askar Kilmametov, Martin Rudolph, Boris B. Straumal, Alena S. Gornakova, Hartmut Stöcker, Yulia Ivanisenko, Olga Fabrichnaya, Horst Hahn, and David Rafaja. Transformation Pathway upon Heating of Ti-Fe Alloys Deformed by High-Pressure Torsion. *Advanced Engineering Materials*, 20(4):1700933, April 2018.

[77] M. Tane, Y. Okuda, Y. Todaka, H. Ogi, and A. Nagakubo. Elastic properties of single-crystalline ω phase in titanium. *Acta Materialia*, 61(20):7543–7554, December 2013.

[78] Ajit Panigrahi, Matthias Bönisch, Thomas Waitz, Mariana Calin, Werner Skrotzki, Jürgen Eckert, and Michael Zehetbauer. Thermal stability of hpt-induced omega phase in biocompatible Ti-16.1Nb alloys. In *Proceedings of the International Conference on Solid-Solid Phase Transformations in Inorganic Materials 2015*, page 7, June 2015.

[79] B.B. Straumal, A.R. Kilmametov, Yu. Ivanisenko, A.A. Mazilkin, R.Z. Valiev, N.S. Afonikova, A.S. Gornakova, and H. Hahn. Diffusive and displacive phase transitions in Ti–Fe and Ti–Co alloys under high pressure torsion. *Journal of Alloys and Compounds*, 735:2281–2286, February 2018.

[80] Kaveh Edalati and Zenji Horita. Phase transformations during high-pressure torsion (HPT) in titanium, cobalt and graphite. *IOP Conference Series: Materials Science and Engineering*, 63:012099, August 2014.

[81] G.K. Dey, R. Tewari, S. Banerjee, G. Jyoti, S.C. Gupta, K.D. Joshi, and S.K. Sikka. Formation of a shock deformation induced ω phase in Zr 20 Nb alloy. *Acta Materialia*, 52(18):5243–5254, October 2004.

[82] R. M. Wood. Martensitic alpha and omega phases as deformation products in a titanium-15% molybdenum alloy. *Acta Metallurgica*, 11:907–914, 1963.

[83] D. de Fontaine, N. E. Paton, and J. C. Williams. The omega phase transformation in titanium alloys as an example of displacement controlled reactions. *Acta Metallurgica*, 19(11):1153–1162, 1971.

[84] D. Choudhuri, Y. Zheng, T. Alam, R. Shi, M. Hendrickson, S. Banerjee, Y. Wang, S.G. Srinivasan, H. Fraser, and R. Banerjee. Coupled experimental and computational investigation of omega phase evolution in a high misfit titanium-vanadium alloy. *Acta Materialia*, 130:215–228, May 2017.

[85] H.P. Ng, A. Devaraj, S. Nag, C.J. Bettles, M. Gibson, H.L. Fraser, B.C. Muddle, and R. Banerjee. Phase separation and formation of omega phase in the beta matrix of a Ti–V–Cu alloy. *Acta Materialia*, 59(8):2981–2991, May 2011.

[86] Yufeng Zheng, Dipankar Banerjee, and Hamish L. Fraser. A nano-scale instability in the β phase of dilute Ti–Mo alloys. *Scripta Materialia*, 116:131–134, April 2016.

[87] E Sukedai and H Matsumoto. Annihilation behaviour under electron irradiation of athermal ω-phase crystals formed by cooling at 131K in a β-Ti-Mo alloy. *Journal of Physics: Conference Series*, 241:012106, July 2010.

[88] James Coakley, Vassili A. Vorontsov, Kenneth C. Littrell, Richard K. Heenan, Masato Ohnuma, Nicholas G. Jones, and David Dye. Nanoprecipitation in a beta-titanium alloy. *Journal of Alloys and Compounds*, 623:146–156, February 2015.

[89] E Sukedai, H Matsumoto, and H Hashimoto. Electron microscopy study on Mo content dependence of β to ω phase transformation due to cooling in Ti-Mo alloys. *Journal of Electron Microscopy*, 51:S143–S147, 2002.

[90] M Hida, E Sukedai, and H Terauchi. Microscopic approaches to isothermal transformation of incommensurate omega phase zones in Ti-20wt%Mo alloy studied by XDS, HREM and EXAFS. *Acta Metallurgica*, 36(6):1429–1441, 1988.

[91] R Pynn. The structure of the diffuse omega phase observed in Zr and Ti alloys. *Journal of Physics F: Metal Physics*, 8(1):1–13, January 1978.

[92] D. de Fontaine. Simple models for the omega phase transformation. *Metallurgical Transactions A*, 19(2):169–175, February 1988.

[93] Tong Li, Damon Kent, Gang Sha, Julie M. Cairney, and Matthew S. Dargusch. The role of ω in the precipitation of α in near-β Ti alloys. *Scripta Materialia*, 117:92–95, May 2016.

[94] H. Kubo and S. Farjami. Lattice study of the incommensurate ω phase transition in Zr-Nb alloys. *Physical Review B*, 83(13):134302, April 2011.

[95] James Coakley, Vassili A. Vorontsov, Nicholas G. Jones, Anna Radecka, Paul A.J. Bagot, Kenneth C. Littrell, Richard K. Heenan, Frédéric Hu, Andrew P. Magyar, David C. Bell, and David Dye. Precipitation processes in the Beta-Titanium alloy Ti–5Al–5Mo–5V–3Cr. *Journal of Alloys and Compounds*, 646:946–953, October 2015.

[96] M.J. Lai, T. Li, and D. Raabe. ω phase acts as a switch between dislocation channeling and joint twinning- and transformation-induced plasticity in a metastable β titanium alloy. *Acta Materialia*, 151:67–77, June 2018.

[97] S. Azimzadeh and H. J. Rack. Phase transformations in Ti-6.8Mo-4.5Fe-1.5Al. *Metallurgical and Materials Transactions A*, 29(10):2455–2467, October 1998.

[98] T. Gloriant, G. Texier, F. Sun, I. Thibon, F. Prima, and J.L. Soubeyroux. Characterization of nanophase precipitation in a metastable β titanium-based alloy by electrical resistivity, dilatometry and neutron diffraction. *Scripta Materialia*, 58(4):271–274, February 2008.

[99] James Coakley, Anna Radecka, David Dye, Paul A.J. Bagot, Tomas L. Martin, Ty J. Prosa, Yimeng Chen, Howard J. Stone, David N. Seidman, and Dieter Isheim. Characterizing nanoscale precipitation in a titanium alloy by laser-assisted atom probe tomography. *Materials Characterization*, 141:129–138, July 2018.

[100] Cheng-Lin Li, Xu-Jun Mi, Wen-Jun Ye, Song-Xiao Hui, Dong-Geun Lee, and Yong-Tai Lee. Influence of heat treatment on microstructure and tensile property of a new high strength beta alloy Ti–2Al–9.2Mo–2Fe. *Materials Science and Engineering: A*, 580:250–256, September 2013.

[101] X.H. Min, S. Emura, L. Zhang, and K. Tsuzaki. Effect of Fe and Zr additions on ω phase formation in β-type Ti–Mo alloys. *Materials Science and Engineering: A*, 497(1-2):74–78, December 2008.

[102] F Prima, J Debuigne, M Boliveau, and D Ansel. Control of omega phase volume fraction precipitated in a beta titanium alloy: Development of an experimental method. *Journal of Materials Science Letters*, 19:2219–2221, 2000.

[103] Qiang Li, Junjie Li, Guanghao Ma, Xuyan Liu, and Deng Pan. Influence of ω phase precipitation on mechanical performance and corrosion resistance of Ti–Nb–Zr alloy. *Materials & Design*, 111:421–428, December 2016.

[104] Arun Devaraj, Daniel E. Perea, Jia Liu, Lyle M. Gordon, Ty. J. Prosa, Pritesh Parikh, David R. Diercks, Subhashish Meher, R. Prakash Kolli, Ying Shirley Meng, and Suntharampillai Thevuthasan. Three-dimensional nanoscale characterisation of materials by atom probe tomography. *International Materials Reviews*, 63(2):68–101, February 2018.

[105] A. Devaraj, R.E.A. Williams, S. Nag, R. Srinivasan, H.L. Fraser, and R. Banerjee. Three-dimensional morphology and composition of omega precipitates in a binary titanium–molybdenum alloy. *Scripta Materialia*, 61(7):701–704, October 2009.

[106] Mitsuo Niinomi, Masaaki Nakai, Mandana Hendrickson, Peeyush Nandwana, Talukder Alam, Deep Choudhuri, and Rajarshi Banerjee. Influence of oxygen on omega phase stability in the Ti-29Nb-13Ta-4.6Zr alloy. *Scripta Materialia*, 123:144–148, October 2016.

[107] Yufeng Zheng, Talukder Alam, Rajarshi Banerjee, Dipankar Banerjee, and Hamish L. Fraser. The influence of aluminum and oxygen additions on intrinsic structural instabilities in titanium-molybdenum alloys. *Scripta Materialia*, 152:150–153, July 2018.

[108] D. L. Moffat and D. C. Larbalestier. The competition between the alpha and omega phases in aged Ti-Nb alloys. *Metallurgical Transactions A*, 19(7):1687–1694, July 1988.

[109] Hsueh-Chuan Hsu, Shih-Ching Wu, Shih-Kuang Hsu, Chien-Ting Li, and Wen-Fu Ho. Effects of chromium addition on structure and mechanical properties of Ti–5Mo alloy. *Materials & Design (1980-2015)*, 65:700–706, January 2015.

[110] F. Prima, P. Vermaut, T. Gloriant, J. Debuigne, and D. Ansel. Experimental evidence of elastic interaction between ω nanoparticles embedded in a metastable β titanium alloy. *Journal of Materials Science Letters*, 21:1935–1937, 2002.

[111] Yuji Ikeda and Isao Tanaka. Stability of the ω structure of transition elements. *Physical Review B*, 93(9):094108, March 2016.

[112] J. C. Williams, B. S. Hickman, and D. H. Leslie. The Effect of Ternary Additions on the Decomposition of Metastable Beta-Phase Titanium Alloys. *Metallurgical Transactions*, 2:477–484, 1971.

[113] T Hamajima, G Luetjering, and S Weissman. Microstructure and Phase Relations for Ti-Mo-Al Alloys. *Metallurgical Transactions*, 3:2805–2810, 1972.

[114] F. H. Froes, C. F. Yolton, J. M. Capenos, M. G. H. Wells, and J. C. Williams. The Relationship Between Microstructure and Age Hardening Response in the Metastable Beta Titanium Alloy Ti-11.5 Mo-6 Zr-4.5 Sn (Beta III). *Metallurgical Transactions A*, 11A:21–31, 1980.

[115] D. Kent, G. Wang, W. Wang, and M. S. Dargusch. Influence of ageing temperature and heating rate on the properties and microstructure of b-Ti alloy, Ti-6Cr-5Mo-5V-4Al. *Materials Science and Engineering A*, 531:98–106, 2012.

[116] P Barriobero-Vila, G Requena, F Warchomicka, A Stark, N Schell, and T Buslaps. Phase transformation kinetics during continuous heating of a β-quenched Ti-10V-2Fe-3Al alloy. *Journal of Materials Science*, 50(3):1412–1426, 2015.

[117] Masakazu Tane, Hiroki Nishiyama, Akihiro Umeda, Norihiko L. Okamoto, Koji Inoue, Martin Luckabauer, Yasuyoshi Nagai, Tohru Sekino, Takayoshi Nakano, and Tetsu Ichitsubo. Diffusionless isothermal omega transformation in titanium alloys driven by quenched-in compositional fluctuations. *Physical Review Materials*, 3(4):043604, April 2019.

[118] F. Sun, J. Y. Zhang, P. Vermaut, D. Choudhuri, T. Alam, S. A. Mantri, P. Svec, T. Gloriant, P. J. Jacques, R. Banerjee, and F. Prima. Strengthening strategy for a ductile metastable β-titanium alloy using low-temperature aging. *Materials Research Letters*, 5(8):547–553, November 2017.

[119] S.A. Mantri, D. Choudhuri, T. Alam, V. Ageh, F. Sun, F. Prima, and R. Banerjee. Change in the deformation mode resulting from beta-omega compositional partitioning in a Ti Mo alloy: Room versus elevated temperature. *Scripta Materialia*, 130:69–73, March 2017.

[120] Mingjia Li and Xiaohua Min. Origin of ω-phase formation in metastable β-type Ti-Mo alloys: cluster structure and stacking fault. *Scientific Reports*, 10(1):8664, December 2020.

[121] R. B. Gullberg, R. Taggart, and D. H. Polonis. On the decomposition of the beta phase in titanium alloys. *Journal of Materials Science*, 6:384–389, 1971.

[122] K. K. McCabe and S. L. Sass. The initial stages of the omega phase transformation in Ti-V alloys. *Philosophical Magazine*, 23(184):957–970, April 1971.

[123] S. Nag, R. Banerjee, and H. L. Fraser. Intra-granular alpha precipitation in Ti–Nb–Zr–Ta biomedical alloys. *Journal of Materials Science*, 44(3):808–815, February 2009.

[124] Jing Chen, Wenlong Xiao, Matthew Simon Dargusch, and Chaoli Ma. The Dependence of Isothermal ω Precipitation on the Quenching Rate in a Metastable β-Ti Alloy. *Scientific Reports*, 5(1):14632, December 2015.

[125] Yufeng Zheng, John M. Sosa, and Hamish L. Fraser. On the influence of Athermal ω and a Phase Instabilities on the Scale of Precipitation of the α Phase in Metastable β-Ti Alloys. *JOM*, 68(5):1343–1349, 2016.

[126] Yufeng Zheng, Robert E.A. Williams, John M. Sosa, Yunzhi Wang, Rajarshi Banerjee, and Hamish L. Fraser. The role of the ω phase on the non-classical precipitation of the α phase in metastable β-titanium alloys. *Scripta Materialia*, 111:81–84, January 2016.

[127] T Furuhara, T Maki, and T Makino. Microstructure control by thermomechanical processing in b-Ti±15±3 alloy. *Journal of Materials Processing Technology*, 117:318–323, 2001.

[128] Rongpei Shi, Yufeng Zheng, Rajarshi Banerjee, Hamish L. Fraser, and Yunzhi Wang. ω-Assisted α nucleation in a metastable β titanium alloy. *Scripta Materialia*, 171:62–66, October 2019.

[129] J G Niu, D H Ping, T Ohno, and W T Geng. Suppression effect of oxygen on the β to ω transformation in a β -type Ti alloy: insights from first-principles. *Modelling and Simulation in Materials Science and Engineering*, 22(1):015007, January 2014.

[130] James Coakley, Anna Radecka, David Dye, Paul A. J. Bagot, Howard J. Stone, David N. Seidman, and Dieter Isheim. Isothermal omega formation and evolution in the Beta-Ti alloy Ti-5Al-5Mo-5V-3Cr. *Philosophical Magazine Letters*, 96(11):416–424, November 2016.

[131] S. Nag, R. Banerjee, R. Srinivasan, J.Y. Hwang, M. Harper, and H.L. Fraser. ω-Assisted nucleation and growth of α precipitates in the Ti–5Al–5Mo–5V–3Cr–0.5Fe β titanium alloy. *Acta Materialia*, 57(7):2136–2147, April 2009.

[132] Tong Li, Damon Kent, Gang Sha, Matthew S. Dargusch, and Julie M. Cairney. Precipitation of the α-phase in an ultrafine grained beta-titanium alloy processed by severe plastic deformation. *Materials Science and Engineering: A*, 605:144–150, May 2014.

[133] Tong Li, Mansur Ahmed, Gang Sha, Rongpei Shi, Gilberto Casillas, Hung-Wei Yen, Yunzhi Wang, Elena V. Pereloma, and Julie M. Cairney. The influence of partitioning on the growth of intragranular α in near-β Ti alloys. *Journal of Alloys and Compounds*, 643:212–222, September 2015.

[134] H.L. Wang, Y.L. Hao, S.Y. He, T. Li, J.M. Cairney, Y.D. Wang, Y. Wang, E.G. Obbard, F. Prima, K. Du, S.J. Li, and R. Yang. Elastically confined martensitic transformation at the nano-scale in a multifunctional titanium alloy. *Acta Materialia*, 135:330–339, August 2017.

[135] H.L. Wang, Y.L. Hao, S.Y. He, K. Du, T. Li, E.G. Obbard, J. Hudspeth, J.G. Wang, Y.D. Wang, Y. Wang, F. Prima, N. Lu, M.J. Kim, J.M. Cairney, S.J. Li, and R. Yang. Tracing the coupled atomic shear and shuffle for a cubic to a hexagonal crystal transition. *Scripta Materialia*, 133:70–74, May 2017.

[136] H.L. Wang, S.A.A. Shah, Y.L. Hao, F. Prima, T. Li, J.M. Cairney, Y.D. Wang, Y. Wang, E.G. Obbard, S.J. Li, and R. Yang. Stabilizing the body centered cubic crystal in titanium alloys by a nano-scale concentration modulation. *Journal of Alloys and Compounds*, 700:155–158, April 2017.

[137] Y.L. Hao, D.L. Gong, T. Li, H.L. Wang, J.M. Cairney, Y.D. Wang, E.G. Obbard, F. Sun, F. Prima, S.J. Li, K. Du, and R. Yang. Continuous and reversible atomic rearrangement in a multifunctional titanium alloy. *Materialia*, 2:1–8, October 2018.

[138] D. R. Trinkle, M. D. Jones, R. G. Hennig, S. P. Rudin, R. C. Albers, and J. W. Wilkins. Empirical tight-binding model for titanium phase transformations. *Physical Review B*, 73(9):094123, March 2006.

[139] R. Salloom, S. A. Mantri, R. Banerjee, and S. G. Srinivasan. First principles computation of composition dependent elastic constants of omega in titanium alloys: implications on mechanical behavior. *Scientific Reports*, 11(1):12005, December 2021.

[140] W. Petry, A. Heiming, J. Trampenau, M. Alba, C. Herzig, H. R. Schober, and G. Vogl. Phonon dispersion of the bcc phase of group-IV metals. I. bcc titanium. *Physical Review B*, 43(13):10933–10947, May 1991.

[141] Hsueh-Chuan Hsu, Shih-Ching Wu, Shih-Kuang Hsu, Yu-Chih Sung, and Wen-Fu Ho. Effects of heat treatments on the structure and mechanical properties of Zr–30Ti alloys. *Materials Characterization*, 62(2):157–163, February 2011.

[142] Wen-Fu Ho, Chang-Hung Pan, Shih-Ching Wu, and Hsueh-Chuan Hsu. Mechanical properties and deformation behavior of Ti–5Cr–xFe alloys. *Journal of Alloys and Compounds*, 472(1-2):546–550, March 2009.

[143] Wen-Fu Ho. Effect of omega phase on mechanical properties of Ti-Mo alloys for biomedical applications. *Journal of Medical and Biological Engineering*, 28(1):47–51, 2008.

[144] James Coakley, Khandaker M. Rahman, Vassili A. Vorontsov, Masato Ohnuma, and David Dye. Effect of precipitation on mechanical properties in the β-Ti alloy Ti–24Nb–4Zr–8Sn. *Materials Science and Engineering: A*, 655:399–407, February 2016.

[145] A Lasalmonie and M Loubradou. The age hardening effect in Ti-6 Al-4 V due to ω and α precipitation in the β grains. *Journal of Materials Science*, 14:2589–2595, 1979.

[146] Masaaki Nakai, Mitsuo Niinomi, and Takahiro Oneda. Improvement in Fatigue Strength of Biomedical β-type Ti–Nb–Ta–Zr Alloy While Maintaining Low Young's Modulus Through Optimizing ω-Phase Precipitation. *Metallurgical and Materials Transactions A*, 43(1):294–302, January 2012.

[147] H.P. Ng, E. Douguet, C.J. Bettles, and B.C. Muddle. Age-hardening behaviour of two metastable beta-titanium alloys. *Materials Science and Engineering A*, 527:7017–7026, 2010.

[148] V Chandrasekaran, R Taggart, and D. H. Polonis. Fracture Modes in a Binary Titanium Alloy. *Metallography*, 5:235–250, 1972.

[149] J. A. Feeney and M. J. Blackburn. Effect of Microstructure on the Strength, Toughness, and Stress-Corrosion Cracking Susceptibility of a Metastable Beta Titanium Alloy (Ti-11.5Mo-6Zr-4.5Sn). *Metallurgical Transactions*, 1:3309–3323, 1970.

[150] J C Williams, B S Hickman, and H L Marcus. The effect of omega phase on the mechanical properties of titanium alloys. *Metallurgical Transactions*, 2:1913–1919, 1971.

[151] C. H. Wang, C. D. Yang, M. Liu, X. Li, P. F. Hu, A. M. Russell, and G. H. Cao. Martensitic microstructures and mechanical properties of as-quenched metastable β-type Ti–Mo alloys. *Journal of Materials Science*, 51(14):6886–6896, July 2016.

[152] G. T. Terlinde, T. W. Duerig, and J. C. Williams. Microstructure, tensile deformation, and fracture in aged ti 10V-2Fe-3Al. *Metallurgical Transactions A*, 14(10):2101–2115, October 1983.

[153] L. Lilensten, Y. Danard, C. Brozek, S. Mantri, P. Castany, T. Gloriant, P. Vermaut, F. Sun, R. Banerjee, and F. Prima. On the heterogeneous nature of deformation in a strain-transformable beta metastable Ti-V-Cr-Al alloy. *Acta Materialia*, 162:268–276, January 2019.

[154] T. W. Duerig, J. E. Allison, and J. C. Williams. Microstructural influences on fatigue crack propagation in Ti-10V-2Fe-3Al. *Metallurgical Transactions A*, 16(5):739–751, May 1985.

[155] Ahmad Zafari, Yunpeng Ding, Jianzhong Cui, and Kenong Xia. Achieving Fine Beta Grain Structure in a Metastable Beta Titanium Alloy Through Multiple Forging-Annealing Cycles. *Metallurgical and Materials Transactions A*, 47(7):3633–3648, July 2016.

[156] Xingfeng Zhao, Mitsuo Niinomi, Masaaki Nakai, Junko Hieda, Takuya Ishimoto, and Takayoshi Nakano. Optimization of Cr content of metastable β-type Ti-Cr alloys with changeable Young's modulus for spinal fixation applications. *Acta Biomaterialia*, 8(6):2392–2400, July 2012.

[157] J. M. Silcock. An X-ray examination of the ω phase in TiV, TiMo and TiCr alloys. *Acta Metallurgica*, 6:481–493, July 1958.

[158] Jin Min, Yanhua Guo, Jingzhe Niu, Juexian Cao, Zhonggang Sun, and Hui Chang. The Characteristic of Fe as a β-Ti Stabilizer in Ti Alloys. *Materials*, 14(24):7516, December 2021.

[159] Hsueh-Chuan Hsu, Shih-Kuang Hsu, Shih-Ching Wu, Chih-Jhan Lee, and Wen-Fu Ho. Structure and mechanical properties of as-cast Ti–5Nb–xFe alloys. *Materials Characterization*, 61(9):851–858, September 2010.

[160] Gyeong Ryeong Bak, Jong Woo Won, Hye-Jeong Choe, Chan Hee Park, and Yong-Taek Hyun. Effect of iron content on β->α phase transformation behavior of Ti-5Al-xFe (x=1, 2.5, 4) alloys during continuous cooling. *Journal of Materials Research and Technology*, 8(3):2887–2897, 2019.

[161] ISHIYAMA Shuji Hanada. Effect of Zr, Sn and Al Additions on Deformation Modeand Beta Phase Stability of Metastable Beta Ti Alloys. *ISIJ International*, 31:807–813, 1991.

[162] Ljerka Slokar, Tanja Matković, and Prosper Matković. Alloy design and property evaluation of new Ti–Cr–Nb alloys. *Materials & Design*, 33:26–30, January 2012.

[163] Justin A Newman, Paul D Schmitt, Scott J Toth, Fengyuan Deng, Shijie Zhang, and Garth J Simpson. Parts per Million Powder X-ray Diffraction. *Analytical chemistry*, 87(21):10950–10955, November 2015. Edition: 2015/10/22.

[164] Masahiko Morinaga, Yoshinori Murata, and Hiroshi Yukawa. Molecular Orbital Approach to Alloy Design. In *Applied Computational Materials Modeling*, pages 255–306. 2007.

[165] R.R. Hake, D.H. Leslie, and T.G. Berlincourt. Electrical resistivity, Hall effect and superconductivity of some b.c.c. titanium-molybdenum alloys. *Journal of Physics and Chemistry of Solids*, 20(3-4):177–186, August 1961.

[166] B. W. Levinger. Lattice Parameter of Beta Titanium at Room Temperature. *JOM*, 5(2):195–195, February 1953.

[167] Ervin Tal-Gutelmacher and Dan Eliezer. The hydrogen embrittlement of titanium-based alloys. *JOM*, 57(9):46–49, September 2005.

[168] G W Willie and J W Davis. Hydrogen in Titanium Alloys. Technical Report DOE/ET/52039-2, The U. S. Department of Energy, 1981.

[169] George A. Young, Jr. and John R Scully. Effects of hydrogen on the mechanical properties of a Ti-Mo-Nb-Al alloy. *Scripta METALLURGICA et MATERIALIA*, 28:507–512, 1993.

[170] J. E. Costa, J. C. Williams, and A. W. Thompson. The effect of hydrogen on mechanical properties in Ti-10V-2Fe-3Al. *Metallurgical Transactions A*, 18(8):1421–1430, August 1987.

[171] A Alvarez. Hydrogen embrittlement of a metastable β-titanium alloy. *Acta Materialia*, 52(14):4161–4175, August 2004.

[172] F H Beck. Effect of hydrogen on the mechancial properties of titanium and its alloys. Technical Report NASA CR-134796, National Aeronautics and Space Administration, 1975.

[173] Fengkai Yan, Isabelle Mouton, Leigh T. Stephenson, Andrew J. Breen, Yanhong Chang, Dirk Ponge, Dierk Raabe, and Baptiste Gault. Atomic-scale investigation of hydrogen distribution in a Ti Mo alloy. *Scripta Materialia*, 162:321–325, March 2019.

[174] Yanhong Chang, Andrew J. Breen, Zahra Tarzimoghadam, Philipp Kürnsteiner, Hazel Gardner, Abigail Ackerman, Anna Radecka, Paul A.J. Bagot, Wenjun Lu, Tong Li, Eric A. Jägle, Michael Herbig, Leigh T. Stephenson, Michael P. Moody, David Rugg, David Dye, Dirk Ponge, Dierk Raabe, and Baptiste Gault. Characterizing solute hydrogen and hydrides in pure and alloyed titanium at the atomic scale. *Acta Materialia*, 150:273–280, May 2018.

[175] Isabelle Mouton, Andrew J. Breen, Siyang Wang, Yanhong Chang, Agnieszka Szczepaniak, Paraskevas Kontis, Leigh T. Stephenson, Dierk Raabe, M. Herbig, T. Ben Britton, and Baptiste Gault. Quantification Challenges for Atom Probe Tomography of Hydrogen and Deuterium in Zircaloy-4. *Microscopy and Microanalysis*, 25(02):481–488, April 2019.

[176] G. Sundell, M. Thuvander, and H.-O. Andrén. Hydrogen analysis in APT: Methods to control adsorption and dissociation of H2. *Ultramicroscopy*, 132:285–289, September 2013.

[177] J. Takahashi, K. Kawakami, H. Otsuka, and H. Fujii. Atom probe analysis of titanium hydride precipitates. *Ultramicroscopy*, 109(5):568–573, April 2009.

[178] Daniel E. Perea, Stephan S. A. Gerstl, Jackson Chin, Blake Hirschi, and James. E. Evans. An environmental transfer hub for multimodal atom probe tomography. *Advanced Structural and Chemical Imaging*, 3(1):12, December 2017.

[179] Joshua D. Wnuk, Justin M. Gorham, Samantha G. Rosenberg, Willem F. van Dorp, Theodore E. Madey, Cornelis W. Hagen, and D. Howard Fairbrother. Electron Induced Surface Reactions of the Organometallic Precursor Trimethyl(methylcyclopentadienyl)platinum(IV). *The Journal of Physical Chemistry C*, 113(6):2487–2496, February 2009.

[180] Masahiko Ikeda, Shin-ya Komatsu, Mitsuhide Ueda, and Akihiro Suzuki. The Effect of Cooling Rate from Solution Treatment Temperature on Phase Constitution and Tensile Properties of Ti-4.3Fe-7.1Cr-3.0Al Alloy. *MATERIALS TRANSACTIONS*, 45(5):1566–1570, 2004.

[181] J. Ballor, M. Ikeda, E. J. Kautz, C. J. Boehlert, and A. Devaraj. Composition-Dependent Microstructure-Property Relationships of Fe and Al Modified Ti-12Cr (wt.%). *JOM*, 71(7):2321–2330, July 2019.

[182] E04 Committee. Test Methods for Determining Average Grain Size. Technical report, ASTM International, 2013.

[183] U Muehle, S Jansen, and L Hillmann. FIB-based target preparations of complex material systems for advanced TEM investigations. *Microscopy: Science, Technology, Applications and Education*, page 13, 2010.

[184] K. Thompson, D. Lawrence, D.J. Larson, J.D. Olson, T.F. Kelly, and B. Gorman. In situ site-specific specimen preparation for atom probe tomography. *Ultramicroscopy*, 107(2-3):131–139, February 2007.

[185] Rigaku. Integrated X-ray Powder Diffraction Software PDXL. *Rigaku Journal*, 26(1):23–27, 2010.

[186] J.L. Taylor and P. Duwez. *Trans. Amer. Soc. Met.*, 44(495), 1952.

[187] R.R. Pawar and V.T. Deshpande. *Acta Crystallogr., Sec.*

[188] Ye.S. Chebotareva and S.G. Nuzhdina. *Phys. Met. Metall.*, 36(200), 1973.

[189] Fedor F. Balakirev, Susan M. Ennaceur, Robert J. Migliori, Boris Maiorov, and Albert Migliori. Resonant ultrasound spectroscopy: The essential toolbox. *Review of Scientific Instruments*, 90(12):121401, December 2019.

[190] Luther M. Gammon, Robert D. Briggs, John M. Packard, Kurt W. Batson, Rodney Boyer, and Charles W. Domby. Metallography and Microstructures of Titanium and Its Alloys. In George F. Vander Voort, editor, *Metallography and Microstructures*, pages 899–917. ASM International, December 2004.

[191] Weilie Zhou and Zhong Lin Wang. *Scanning microscopy for nanotechnology: techniques and applications*. Springer science & business media, 2007.

[192] Baptiste Gault, Michael P Moody, Julie M Cairney, and Simon P Ringer. *Atom probe microscopy*, volume 160. Springer Science & Business Media, 2012.

[193] Julie M Cairney, Krishna Rajan, Daniel Haley, Baptiste Gault, Paul AJ Bagot, Pyuck-Pa Choi, Peter J Felfer, Simon P Ringer, Ross KW Marceau, and Michael P Moody. Mining information from atom probe data. *Ultramicroscopy*, 159:324–337, 2015.

[194] A. Devaraj, T. C. Kaspar, S. Ramanan, S. Walvekar, M. E. Bowden, V. Shutthanandan, and R. J. Kurtz. Nanoscale phase separation in epitaxial Cr-Mo and Cr-V alloy thin films studied using atom probe tomography: Comparison of experiments and simulation. *Journal of Applied Physics*, 116(19):193512, November 2014. Publisher: American Institute of Physics.

[195] Arun Devaraj, Meng Gu, R Colby, Pengfei Yan, Chong M Wang, JM Zheng, Jie Xiao, Arda Genc, JG Zhang, Ilias Belharouak, et al. Visualizing nanoscale 3d compositional fluctuation of lithium in advanced lithium-ion battery cathodes. *Nature communications*, 6(1):1–8, 2015.

[196] Michael P Moody, Leigh T Stephenson, Anna V Ceguerra, and Simon P Ringer. Quantitative binomial distribution analyses of nanoscale like-solute atom clustering and segregation in atom probe tomography data. *Microscopy research and technique*, 71(7):542–550, 2008.

[197] Yongzhou Wang. *Fundamentals of Recrystallization in Titanium Alloys*. Master of Science, University of Manchester, 2014.

[198] Tadashi Furuhara, Hiroshi Abe, Behrang Poorganji, and Tadashi Maki. Dynamic Recrystallization in Titanium Alloys during Hot Deformation. *Ti-2007 Science and Technology*, pages 913–919, 2007.

[199] S. O. Kasap. *Principles of Electronic Materials and Devices*. McGraw-Hill, 3 edition.

[200] Hee Young Kim and Shuichi Miyazaki. Chapter 1 - Martensitic Transformation Characteristics. In Hee Young Kim and Shuichi Miyazaki, editors, *Ni-Free Ti-Based Shape Memory Alloys*, pages 1–52. Butterworth-Heinemann, 2018.

[201] William D. Callister, Jr. *Materials Science and Engineering An Introduction*. John Wiley & Sons, Inc., New York, 5 edition, 2000.

[202] Y.L. Kao, G.C. Tu, C.A. Huang, and T.T. Liu. A study on the hardness variation of α- and β-pure titanium with different grain sizes. *Materials Science and Engineering: A*, 398(1-2):93–98, May 2005.

[203] D. Doraiswamy and S. Ankem. The effect of grain size and stability on ambient temperature tensile and creep deformation in metastable beta titanium alloys. *Acta Materialia*, 51(6):1607–1619, April 2003.

[204] Junshuai Wang, Wenlong Xiao, Yu Fu, Lei Ren, and Chaoli Ma. Dependence of mechanical behavior on grain size of metastable Ti–Nb–O titanium alloy. *Progress in Natural Science: Materials International*, 32(1):63–71, February 2022.

[205] Kristin Persson. Materials data on ticr2 (sg:227) by materials project, 2 2015. An optional note.

[206] P Hidnert. Thermal expansion of titanium. *Journal of Research of the National Bureau of Standards*, 30:101–105, February 1943.

[207] R. I. Jaffee. The physical metallurgy of titanium alloys. *Progress in Metal Physics*, 7:65–163, 1958.

[208] Bingjie Zhang, Yan Chong, Ruixiao Zheng, Yu Bai, Reza Gholizadeh, Mingda Huang, Dong Wang, Qiaoyan Sun, Yunzhi Wang, and Nobuhiro Tsuji. Enhanced mechanical properties in β-Ti alloy aged from recrystallized ultrafine β grains. *Materials & Design*, 195:109017, October 2020.

[209] S M. Jagadeesh Babu, Pramod S. Kataraki, and K S. Narayanaswamy. Phase transformation and microstructure evolution study in various alloy systems: An insight. *IOP Conference Series: Materials Science and Engineering*, 505(1):012149, May 2019.

[210] Changsheng Tan, Yiduo Fan, Qiaoyan Sun, and Guojun Zhang. Improvement of the Crack Propagation Resistance in an α + β Titanium Alloy with a Trimodal Microstructure. *Metals*, 10(8):1058, August 2020.

[211] T.S. Prithiv, Zachary Kloenne, Dian Li, Rongpei Shi, Yufeng Zheng, Hamish L. Fraser, Baptiste Gault, and Stoichko Antonov. Grain boundary segregation and its implications regarding the formation of the grain boundary α phase in the metastable β-Titanium Ti–5Al–5Mo–5V–3Cr alloy. *Scripta Materialia*, 207:114320, January 2022.

[212] Kristina Bartha, Josef Strasky, Anna Veverkova, Jozef Vesely, and Milos Janecek. Observation of the omega phase particles in Ti15Mo alloy by electron microscopy. *Materials Letters*, 309:131376, February 2022.

[213] Yanhong Chang, Wenjun Lu, Julien Guénolé, Leigh T. Stephenson, Agnieszka Szczpaniak, Paraskevas Kontis, Abigail K. Ackerman, Felicity F. Dear, Isabelle Mouton, Xiankang Zhong, Siyuan Zhang, David Dye, Christian H. Liebscher, Dirk Ponge, Sandra Korte-Kerzel, Dierk Raabe, and Baptiste Gault. Ti and its alloys as examples of cryogenic focused ion beam milling of environmentally-sensitive materials. *Nature Communications*, 10(1):942, December 2019.

[214] Harish Narasimhan Chakravarty. *Effect of Alloying Additions of Aluminium and Iron on the Creep Resistance of Ti-12Cr (Wt.%)*. PhD thesis, Michigan State University, 2019.

[215] Uri Argaman and Guy Makov. First-principles study of the temperature dependence of the elastic constants of hcp titanium. *Computational Materials Science*, 184:109917, November 2020.

[216] A. J. Mortlocks and D. H. Tomlm. The atomic diffusion of chromium in the titanium-chromium system. *Philosophical Magazine*, 4(41):628–643, May 1959.

[217] H Nakajima, S Ohshidat, K Nonakat, Y Yoshida, and F E Fujital. Diffusion of Fe in β Ti-Fe alloys. *Scripta Materialia*, 34(6):949–953, 1996.

[218] Hideki Araki, Toshimi Yamane, Yoritoshi Minamino, Shigeoki Saji, Yoshitake Hana, and Seung Boo Jung. Anomalous Diffusion of Aluminum in β-Titanium. *Metallurgical and Materials Transactions A*, 25(4):874–876, 1994.

[219] Yufeng Zheng, Robert E.A. Williams, Gopal B. Viswanathan, William A.T. Clark, and Hamish L. Fraser. Determination of the structure of α-β interfaces in metastable β-Ti alloys. *Acta Materialia*, 150:25–39, May 2018.

[220] Kathleen Chou and Emmanuelle A. Marquis. Oxygen effects on ω and α phase transformations in a metastable β Ti–Nb alloy. *Acta Materialia*, 181:367–376, December 2019.

[221] I I Kornilov. Solubility of the elements in titanium. *Bulletin of the Academy of Sciences of the USSR, Division of chemical science*, 3:329–335, May 1954.

[222] Graham J.C. Carpenter, Jennifer A. Jackman, John P. McCaffrey, and Reza Alani. In Situ Hydride Formation in Zirconium and Titanium during Ion Milling. *Microscopy and Microanalysis*, 1(4):175–184, August 1995.

[223] John A. Fellows, Howard E. Boyer, Hugh Baker, Edward A. Durand, Philip D. Harvey, Paul M. Unterweiser, Helen V. Bukovics, and Craig W. Kirkpatrick, editors. *METALS HANDBOOK: Fractography and Atlas of Fractographs*, volume 9. American Society for Metals, 8 edition, 1974.